Doctoral Dissertation

Doctoral Program in Aerospace Engineering (36thcycle)

Advanced Structural Concepts and Simulation for Aircraft Design & Production

By

Cesare Patuelli

******

Supervisor(s):

Prof. Enrico Cestino, Supervisor

Prof. Giacomo Frulla, Co-Supervisor

Ing. Federico Valente, Co-Supervisor

Doctoral Examination Committee:

Dr. Ameduri Salvatore , Referee, Centro Italiano Ricerche Aerospaziali (CIRA)

Prof. Sodja Jurij, Referee, Technishe Universiteit DELFT

Prof. Sergio Preidikman,Universidad Nacional de Córdoba

Prof. Marco Gherlone, Politecnico di Torino

Prof. Stefani Scarsoglio, Politecnico di Torino

Politecnico di Torino

2024

Declaration

I hereby declare that, the contents and organization of this dissertation constitute my own original work and does not compromise in any way the rights of third parties, including those relating to the security of personal data.

<div align="right">

Cesare Patuelli
2024

</div>

I would like to dedicate this thesis to my family

Acknowledgements

Abstract

This work explores the possibilities in terms of structural design offered by the advent of composite materials. Through aeroelastic tailoring, it is possible to design high aspect ratio wings with greater aeroelastic performance. The bending-torsion coupling given by oriented fibers or stiffeners can be optimized to counter aeroelastic phenomena such as flutter and divergence.

The first part of this work presents the derivation of a beam finite element with bending-torsion coupling formulation for static and dynamic analysis of wing structures with oriented fibers or stiffeners. Then the finite model is extended to nonlinear vibration analysis of pre-deformed structure through a perturbation approach. The models have been validated with a series of experimental vibration tests and by comparison of numerical and experimental results present in the literature.

The objective of the finite element model is to obtain a versatile tool for static and dynamic analysis of beam structures with bending-torsion coupling, but also for more complex analyses which requires a larger number of calculations and where these elements can be beneficial in terms of computational cost. At this scope, the presented element has been implemented in an optimization algorithm to compute the optimal curvilinear stiffeners path for beam structures. Another application for the finite element is divergence analysis, where the beam finite element structural model can be coupled with an aerodynamic model to find the equilibrium configuration of the wing structure under the aerodynamic load or the divergence condition.

Besides the study of finite elements for the simulation of beam structures with bending-torsion coupling, this thesis presents extensive work on additive manufacturing simulation. Additive manufacturing is increasingly important in the aerospace industry and could be adopted for the production of curvilinear stiffeners for box-beam structures. These geometries can be used to expand the aeroelastic design domain, and requires innovative manufacturing technologies. However, accurate

process simulations are needed to reduce the costs of low quality or failed parts generally associated to additive manufacturing. At this scope, an algorithm for additive manufacturing process simulation has been validated with industrial computed tomography and used to simulate the production of a stiffened panel and a calibrating artifact.

Contents

List of Figures

List of Tables

Chapter 1

Aeroelastic Design and Production

1.1 Introduction and Significance

Aviation sustainability is a major concern as it contributes a large amount of greenhouse gases and other pollutants. Air transport alone accounts for 1-2% CO_2 emissions related to human activities worldwide [1]. These numbers are destined to increase due to the relentless expansion of air travel. Airbus in its Global Market Forecast, expects an annual growth of 3.6% for the demand of passenger traffic over the next 20 years. Airbus also forecast demand for 40850 new passenger and freighter aircraft deliveries over the next 20 years [2]. Boeing, in its Commercial Market Outlook, highlighted how the global passenger traffic continues to recover ground lost during the pandemic and it already surpassed the pre-pandemic levels. Boeing forecast that air travel will continue growing faster than global economic activity driven by tourism demand and increased service levels, particularly in developing markets. Air traffic will more than double over the next 20 years with at a 3.7% growth, outpacing the fleet growth at 3.2%. Airlines aircraft demand is expected to reach more than 42000 units delivered by 2042 [3]. For these reasons, the National Aeronautics and Space Administration (NASA) and the European Commission, put out challenging sustainable aviation goals to reduce the environmental effects of the forecast increase in air traffic [4, 5].

The recent Paris Agreement established new goals for aviation emission target which are unlikely to be satisfied with the current trend of air traffic [6]. The urgency imposed by international agreements and regulations requires new game-changing

design concepts to improve aircraft performance in terms of fuel consumption. The augmentation of wing aspect ratio (AR) can play a crucial role for new efficient aircraft [7]. Several research works in the aerospace field established a correlation between an increased aspect ratio and a reduction in fuel consumption. According to recent studies, expanding the wingspan of conventional aircraft by 15-23% can lead to a reduction of fuel consumption estimated of 8-11% [8, 9]. The beneficial effects of augmented AR are known to the principal aircraft manufacturer, in fact, the AR of commercial transport aircraft has shown an increasing trend with extended wingspan and wingtip devices.

The main goal of this change in design is to reduce lift-induced drag and thus enhance efficiency end reduce fuel consumption [10]. Part of the aircraft drag is associated to the fiction of the boundary layer on the aircraft surfaces and it is called viscous drag. The boundary layer flow on today's large aircraft is turbulent on almost the entire wetted surface and this results in viscous drag five to ten times larger than that of laminar boundary layers. Laminar flow control and optimized airfoils for laminar boundary layers can considerably improve aircraft performance [11]. An important component of an aircraft drag is the lift-induced drag, this is a primary issue for conventional commercial aircraft constituting up to 80% of the total drag during climb and 40 % during cruise [11]. In the recent years, many daring design have been proposed to enhance aircraft efficiency through AR augmentation. Strut-Braced Wings (SBW) designed in the RHEA project [12] presented an AR of 25, while the aircraft designed in the Subsonic Ultra Green Aircraft Research (SUGAR) project adopted an AR of 19,55 [13] with a Truss-Braced Wing (TBW) configuration. NASA and Boeing are cooperating on the design of the transonic TBW concept [13–16], they stated that TBW design could reduce aircraft fuel consumption by up to 10% compared to conventional aircraft [17]. Other projects involving SBW and TBW configuration are currently ongoing and adopt high AR [18, 10, 19]. Recently, the HELIPLAT project [20], carried out at Politecnico di Torino, involved high AR wing structure for the design of an high altitude very-long endurance uninhabited air vehicle (HAVE-UAV). The most recent studies indicate that these configurations could reduce aircraft fuel burn by 10-20% in long-range missions [21–25] and by 7-10% in short range missions [18, 26, 27].

Despite the aforementioned aerodynamic benefits, the development of High Aspect Ratio Wings (HARW) is slowed by structural design issues inherent to HARW. An augmented wingspan implies higher structural flexibility and higher stress levels

at the wing root. Another problem is represented by airport terminal operations and maintenance facilities which limit the wing allowable span airport terminal operations and maintenance facilities [28]. Moreover, with the increase of wing structural flexibility, the wing becomes more susceptible to higher deflections during normal operations, this can affect the dynamic behaviour and, as a consequence, aeroelastic instabilities for HARW occurs at lower speed than in a conventional wing structure. According to Hodges and Dowell [29], for HARW, the flap bending mode, the chord bending mode, and the torsion mode may couple and result in significant structural nonlinearities. Hence, the importance of assessing the effects of nonlinearities on the aeroelastic behavior of HARW. The first studies concerning nonlinear elasticity are mainly connected to helicopter blades. These structures usually have a very high aspect ratio and can present nonlinear aeroelastic behavior possibly in transonic flow with shock and stall [30]. The interest for fixed wing aircraft nonlinear aeroelasticity increased due to the need to understand aeroelastic response in the transonic regime [31], where aerodynamic nonlinearities are observed. The advent of unmanned HARW aircraft such as the High Altitude Long Endurance (HALE) aircraft [32, 33] required more studies on the effect of geometric nonlinearities on aeroelastic behavior even in cruise conditions [34]. Moreover, a study conducted by Frulla [35] highlighted the importance of the effect of deformed equilibrium configuration in the dynamic behavior of slender wings. Aircraft wings are deflected by aerodynamic loads during normal operations, this deformations introduces non-linearities which influence the dynamic behavior and bending-twist vibrations. This coupling effect induced by the equilibrium deformation can cause critical flutter conditions into the system at a lower velocity if compared with the linear case. This amplifies the need of specific design solutions and simulation tools.

One of the possible solutions is to combine aerodynamic couplings with structural couplings and mitigate these instabilities or shift them at a higher speed [36–38]. Structural coupling can be achieved with specific materials or technologies, the introduction of innovative solutions such as Variable Angle Tow (VAT) laminates [39–45]. Other solutions are represented by the use of oriented rectilinear or curvilinear stiffeners panels [40, 46]. The design of structures with anisotropic material properties to influence wing aeroelastic properties is called aeroelastic tailoring, this thesis aims to realize reliable and efficient tools for aeroelastic tailoring design and optimization. Particularly, the problem is addressed with the derivation of a beam finite element with bending-torsion coupling formulation and its extension for

dynamic analysis with geometric nonlinearities. The finite element has been widely tested with numerical and experimental results and then adopted for optimization problems and aeroelastic analysis.

1.2 Aeroelastic Tailoring: A Short Overview

Aeroelastic tailoring is a design process in which minimum weight is the preponderant objective. Aeroelastic tailoring involves the use of structural deformation of a lifting surface to achieve desired aircraft performance [47]. Aeroelastic tailoring is a passive control where the control law is embedded within the structure in the material constitutive relations. The first example of the use of anisotropic material to enhance the performance of aerodynamic surfaces was given by Munk in 1949 [48]. He used oriented wood plates to provide a fixed pitch propeller where the blades twist elastically under the aerodynamic loads. This feature was used to keep the optimal orientation at different trust levels.

In 1969 General Dynamics proposed several applications of advanced composite materials for weight saving but also to improve transonic performance of supercritical wings. The purpose of the project was to design a wing capable of maintaining the optimal shape at both cruise and design maneuver conditions. The researchers showed that the directional properties of composites could be used to create bending-torsion coupling which can be used to control the shape of supercritical wings [49].

The most famous application of aerolastic tailoring is on the X-29 forward-swept wing demonstrator aircraft. The innovative structural layout was heavily affected by the divergence problem and needed to be controlled [50]. Weisshaar also focused on forward-swept wings, he studied the aeroelastic performance and stability properties of aircraft with sophisticated swept-forward composite wing structures [38]. His investigation revealed the possible use of composite bending-torsion elastic coupling to mitigate the undesired swept-forward wing divergence behavior. An area that attracted aeroelastic tailoring research was the wing-box laminate configuration. Lynch and Rogers [51] developed an algorithm to explore wing design using anisotropy in laminate layup for improving aeroelastic drag problems, control effectiveness, strength, divergence, and flutter without any weight penalty.

Librescu and Song [52] analyzed the static aeroelastic response and the divergence instability of a swept-forward wing with a thin-walled anisotropic composite beam structure. More recently the research is moving toward tools and algorithms for aeroelastic tailoring design and optimization. This thesis aims to be a contribute for this research field through the development and validation of specific beam finite elements for aeroelastic analysis of composite wing structures.

1.3   Metal Additive Manufacturing in Aerospace

The sustainability goals set for the next decades requires also advanced production technologies for their fulfillment. Weight reduction is a key requirement for aerospace components which, alongside the increasing complexity of mechanical parts, is setting new challenges for conventional manufacturing techniques. Additive manufacturing (AM) is increasingly present in the aerospace industry and could enable the development of new structural concepts associated to aeroelastic tailoring. A critical challenge to metal AM applications in aerospace is represented by certification. The regulatory bodies must be confident that AM systems are well known and design and inspection process can satisfy the expectations in terms of repeatability, reliability, and safety. Certifications vary based on the criticality of the proposed AM component and require connection with existing standards and the emerging ones for AM processes [53].

Additive manufacturing utilizes layer by layer built strategy based on a common feedstock, typically powder for metal processes and wire for polymers. The raw material is melted by a heat source in specific positions and solidifies to produce a layer of the final geometry [54]. AM brings several advantages to the aerospace industry, lead time and cost can be sensibly reduced and new lightweight complex components can be manufactured. Moreover, multiple components can be merged in one single part reducing the risks associated to joints failures [55, 56]. With AM technologies is possible to include internal features which can be an advantage for combustion chambers or turbine blades cooling channels [57, 58].

The aerospace sector relies heavily on machined forged and billet structures for critical structural systems. These technologies are well known and guarantee high certainty in final product quality. However, these manufacturing techniques add substantial direct production costs and indirect costs due to high manufacturing lead

times. Moreover, the material waste is considerably high, typical buy-to-fly rations can vary from 20:1 [59] to 40:1 [60]. Due to their nature, the additive manufacturing process produces little to no waste with the possibility to recycle unused material. The buy-to-fly ratios in this case are between 1:1 and 3:1 [61].

Additive manufacturing is a complex procedure that involves many physical processes at different scales. The process is influenced by a large number of process parameters which can heavily affect the final quality of the produced parts [62]. Despite the continuous improvement in understanding the effect of process parameters, AM is not able to guarantee consistency in the quality of the produced parts and this leads to difficulties in the certification process for the use of AM for critical aerospace components. Further disadvantages of AM include limited materials, uncertainty in material properties, specific design constraints inherent to AM, post-processing requirements, waste generation (used powder, build plates, failed builds), increased requirements of design skills to allow lower-mass components with feasible complex designs, often utilizing time-consuming topology optimization software workflows, as well as the need for strict quality control and certification of the process [63, 53].

Despite the drawbacks mentioned, the technical advantages over traditional manufacturing methods are clear. AM process simulation can be a useful method to make the AM process more predictable and therefore limit the waste given by failed or poor quality components. Several studies are already moving toward this key aspect of AM and this thesis aims to contribute to this topic with the implementation of AM process simulation for the production of aerospace components.

1.4 Objective of the work

The primary objective of this work is to develop and validate efficient simulation tools to enlarge the design space for next generation aircraft structures. The main problems addressed are the development of a beam finite element with bending-torsion coupling formulation for aeroelastic tailoring design and the validation of AM simulation theory. These problems are connected by a possible application of AM process for the production of curvilinear or complex-shape stiffeners given by topology optimization for aeroelastic performance.

This work aims also to expand the use of beam finite elements with bending-torsion coupling formulation to dynamic analysis in the presence of geometric nonlinearities. Moreover, this thesis aims to develop an efficient procedure for topology optimization of structures with bending-torsion couplings and for divergence analysis.

1.5   Structure of the thesis

The present work is organized as follows. Chapter 2 presents the derivation of the beam finite element with bending-torsion coupling. The equations of motion are derived and the finite element mass and stiffness matrix are derived with Galerkin's method. The finite element is derived through the definition of specifically derived shape functions which include the bending-torsion coupling.

The extension of the beam finite element with bending-torsion coupling to the nonlinear field is presented in Chapter 3. Two nonlinear models are derived, the first includes only the geometrical effects, while the second is derived through a perturbation method and includes also the stiffness effects.

In Chapter 4 an equivalent single layer for stiffened panel is experimentally validated for the modal analysis of stiffened and composite box-beams.

In Chapter 5 the beam finite element with bending-torsion coupling is validated with numerical and experimental evidence for static and dynamic analysis. This chapter presents also the numerical and experimental validation of the nonlinear version of the finite element for nonlinear dynamic analysis of pre-deformed structures.

Chapters 6 and 7 presents two applications of the finite element derived. The first consists in an optimization of the curvilinear stiffeners path with constraints on bending and torsion and for AM production. In the second, divergence analysis is performed coupling the structural analysis with the beam finite element and an aerodynamic analysis. This procedure is validated with experimental results of composite structures.

Chapter 8 presents an overview of AM process simulation and presents the simulation strategy adopted in this thesis. In this chapter, an application of AM production to oriented stiffened panels based on the results of Chapter 6 is presented. Moreover, the theory implemented in the simulation software is validated with the

simulation of the production of a metal component and a results comparison with an industrial computed tomography performed on the actual part.

Chapter 9 summarizes the results obtained in this work and draws some concluding remarks.

1.6   Contribution of the thesis

The main contributions of the present work are summarized hereto:

- The derivation of a beam finite element with bending-torsion coupling formulation for static and dynamic analysis of box-beam structures with rectilinear or curvilinear stiffened panels or composite fibers.

- The derivation of two models for the dynamic analysis of box-beam structures with bending-torsion couplings in the presence of geometric nonlinearities.

- The experimental validation of an equivalent single layer for stiffened panels for dynamic analysis. The validation showed good accuracy and extended the use of this model also for the modal analysis of stiffened panels box-beam structures.

- The experimental and numerical validation of the derived finite element for the static and dynamic problems of composite beams, stiffened and composite thin-walled box-beam, variable stiffness beams, and pre-deformed beams.

- The development of an optimization procedure for the design of box-beam structures with curvilinear stiffness in the presence of bending-torsion performance constraints as well as AM constraints.

- A procedure for divergence analysis of composite wing structures using the derived finite element and an aerodynamic analysis performed with the Vortex Lattice Method. The results obtained have been validated with experimental results.

- The validation of an AM process simulation algorithm with experimental results obtained with an industrial computed tomography.

The above-mentioned contribution has led to the publication listed below:

Journal Paper

1. Patuelli, C., Polla, A., Cestino, E. et al. Experimental and Numerical Dynamic Behavior of Bending-Torsion Coupled Box-Beam. J. Vib. Eng. Technol. 11, 3451–3463 (2023).

2. Patuelli, C.; Cestino, E.; Frulla, G. A Beam Finite Element for Static and Dynamic Analysis of Composite and Stiffened Structures with Bending-Torsion Coupling. Aerospace 2023, 10, 142.

3. Patuelli, C.; Cestino, E.; Frulla, G.; Valente, F. Optimization of Curvilinear Stiffener Beam Structures Simulated by Beam Finite Elements with Coupled Bending–Torsion Formulation. Materials 2023, 16, 3391.

4. Patuelli, C.; Cestino, E.; Frulla, G.; Valente, F.; Servetti, G.; Esposito, F.; Barbero, L. FEM Simulation of AlSi10Mg Artifact for Additive Manufacturing Process Calibration with Industrial-Computed Tomography Validation. Materials 2023, 16, 4754.

5. Patuelli, C.; Cestino, E.; Frulla, G. A Nonlinear Beam Finite Element with Bending–Torsion Coupling Formulation for Dynamic Analysis with Geometric Nonlinearities. Aerospace 2024, 11, 255.

Conference Paper

1. Cesare Patuelli, Enrico Cestino and Giacomo Frulla. "Aeroelastic Analysis through Non-Linear Beam Finite Elements with Bending-Torsion Coupling Formulation," AIAA 2024-1073. AIAA SCITECH 2024 Forum. January 2024.

Chapter 2

Beam Finite Element with Bending-Torsion Coupling Derivation

This chapter presents the derivation of a beam finite element for static and dynamic analysis of beam structures with material bending-torsion couplings. A specific set of shape functions is derived in order to establish the relation between the bending and torsional nodal degree of freedom of a two-node beam element. These functions are derived considering Timoshenko's hypothesis and imposing the torsional moment constant along the element. The second hypothesis connects the bending and torsional behavior and can be considered satisfied for small elements. The stiffness and mass matrices are obtained through Galerkin's method starting from the linear equilibrium equation. The beam finite element has been tested with a static analysis and compared with numerical and analytical results. Moreover, an LDV modal analysis has been performed on a beam structure with oriented composite panels and on a beam structure with oriented stiffened aluminum panels.

2.1 Overview on Beam Structures Models with Bending-Torsion Coupling

In this section, we provide an overview of the analytical and numerical methods for static and dynamic analysis of beam structures with bending-torsion coupling. Many types of this class of models are present in literature, each one addressed to a specific kind of coupling, shape, or analysis. Hollowell [64] conducted an analytical and experimental investigation to determine the aeroelastic flutter and divergence behaviour of unswept, rectangular wings simulated by graphite/epoxy, cantilevered plates with various amounts of bending-torsion stiffness coupling. The analytical approach incorporated a Rayleigh-Ritz formulation.

Hong and Chopra [65] investigated the aeroelastic stability of flap bending, lead-lag bending, and torsion of a composite rotor blade in hover using a finite element theory based on Hamilton's principle. The energy and governing differential equations were derived for moderately large deflections. The blade was discretized into beam elements with fifteen nodal degrees of freedom. The study revealed that stiffness coupling terms affect heavily blade dynamic stability.

Dokumaci [66] presented an exact determination of coupled bending and torsion vibration characteristics for beams with a single cross-sectional symmetry and explained the effect of bending-torsion couplings on the natural frequencies and modes.

Banerjee [67] derived the explicit expressions for the coupled bending-torsional dynamic stiffness matrix of a uniform beam element by solving the governing differential equation of the beam. Numerical evidence demonstrated the accuracy of results for a cantilever beam with a substantial amount of bending torsion coupling. However, the coupling was given by the distance between the mass and the elastic axis and not by the material orientation. Later, Banerjee et al. [68] developed an exact dynamic stiffness matrix for free vibration analysis of composite beams using symbolic computation. The derived dynamic stiffness matrix was used with the Wittrick-Williams algorithm to compute the natural frequencies and mode shapes of composite beams with bending torsion coupling.

Smith and Chopra [69] presented a direct analytical beam formulation for predicting the elastic stiffness and the corresponding deformation behavior of tailored

composite wing boxes. The model has been validated with numerical and experimental results showing a good precision in predicting beam deformations within 10 percent of detailed finite element solutions.

Chandra [70] developed a Vlasov-type linear theory to analyze the structural response of composite I-section beams with elastic couplings. The theoretical study has been validated with experimental results under bending and torsional loads. Another work [71] investigated the vibration of rotating composite box beams, with governing equations derived using a Newtonian approach. In this case, the bending-shear and the extension shear coupling were the main couplings affecting the vibration frequencies.

Hashemi and Richard [72] developed a Dynamic Finite Element (DFE) formulation for the vibration analysis of bending-torsion coupled beams. They found the exact solutions for the differential equations governing the uncoupled vibrations, then they used these solutions as basis functions for the frequency-dependent shape function that can be used to find the nodal approximations of variables. The Dynamic Stiffness Matrix is then obtained with the Principle of Virtual Work (PVW).

Jung et al [73] proposed a refined structural model based on a mixed forces and displacements method for the analysis of composite rotor blades with elastic couplings. The theory accounts for the effect of elastic couplings, warping, shell thickness, and transverse shear deformation. They developed a first-order shear deformation theory deriving the beam force-displacement relations with a semi-complementary energy functional. Bending and torsion-related warping and shear correction factors were obtained in closed form. The theory was validated against experimental data and finite element results.

Wenbin et al. [74] formulated a finite element-based analysis for nonhomogeneous, initially curved, and twisted anisotropic beams from geometrically nonlinear three-dimensional elasticity. The strain field is formulated through the decomposition of the rotation tensor and is given in terms of one-dimensional generalized strains and a three-dimensional warping displacement obtained from the formulation. The warping is found via the variational asymptotic method. Numerical results presented the variation of classical and nonclassical couplings as the initial twist and curvature are varied.

Mohri et al. [75] investigated a theoretical and numerical model to study the behavior of open cross-section beams in the presence of large torsion. This model

takes into account large torsion, warping, pre-buckling deformation, and flexural-torsional coupling. The model is implemented into a two nodes and seven nodal degrees of freedom beam element. The model has been derived for linear and non-linear analysis carried out with Newton-Raphson iterative method.

More recently Babuska et al. [76] presented a weak-form approach to the development of a bend-twist coupled composite laminate beam element. The beam element was tested for static and dynamic analysis and compared with analytical and shell element solutions.

Most of the works already published in literature concerning structural models for beam structures with specific couplings found their application in static and dynamic analysis of wings or rotor blades. This highlights the great interest in this class of models for the design of these structures. However, many of the models presented are based on analytical formulation and can be challenging when it comes to actual applications. A beam finite element considering the bending-torsion coupling caused by the anisotropy of the material can be a very versatile tool for simulation and optimization in the early phases of wing structure design. For this reason, the derivation Bending-Torsion Coupling beam finite Element (BTCE) is addressed in the present chapter. The model here presented establishes a relation between bending and torsion in the presence of material coupling by means of specific shape functions. These functions are obtained by applying the beam element boundary conditions and introducing the hypothesis of constant torsional moment along the element length. The stiffness and mass matrices are then derived using Galerkin's method. The BTCE has been tested against shell finite elements and experimental results showing great accuracy for static and dynamic analysis.

2.2   Basic assumption on the beam model

The motion of a beam element can be described by three translational displacements and three rotations on each section. Three Euler's angles can be used to describe the rotation of the beam from the undeformed condition to the deformed condition. We consider an initially straight beam represented in Figure 2.1. Two coordinate systems are introduced: the coordinate system xyz for the undeformed geometry and the orthogonal curvilinear coordinate system 123 for the deformed geometry. Let s to be the curvilinear abscissa. Let $\mathbf{i_x}$, $\mathbf{i_y}$, and $\mathbf{i_z}$ denote the unit vectors of the coordinate

system xyz while $\mathbf{i_1}$, $\mathbf{i_2}$, and $\mathbf{i_3}$ denote the unit vectors of the coordinate system 123. Let $u(s,t)$, $v(s,t)$, and $w(s,t)$ be the component of the elastic displacements with respect to the centroid of the beam at an arbitrary abscissa s. The three Euler angles ψ, θ, and φ are used to describe the rotation from the undeformed position to the deformed one. First, the angle ψ about the z axis is applied to the xyz system to obtain the intermediate coordinate system x_1y_1z. Second, the x_1y_1z system is rotated by an angle θ about the y_1 axis to the second intermediate system $1y_1z_2$ and finally, the system $1y_1z_2$ is rotated by the angle φ about the 1 axis to obtain the 123 coordinate system. The consecutive rotations are represented in Figure 2.2
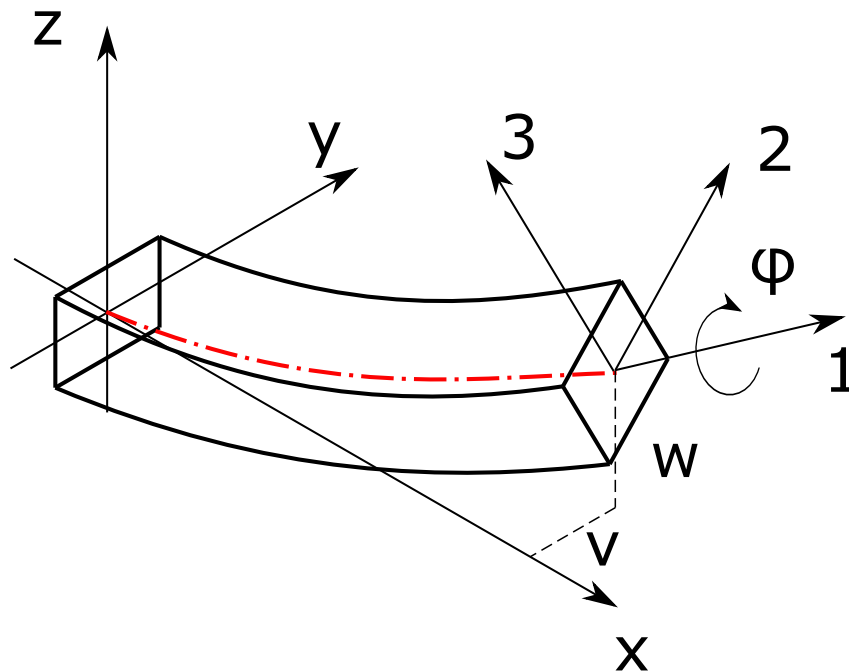
Fig. 2.1 Coordinate System
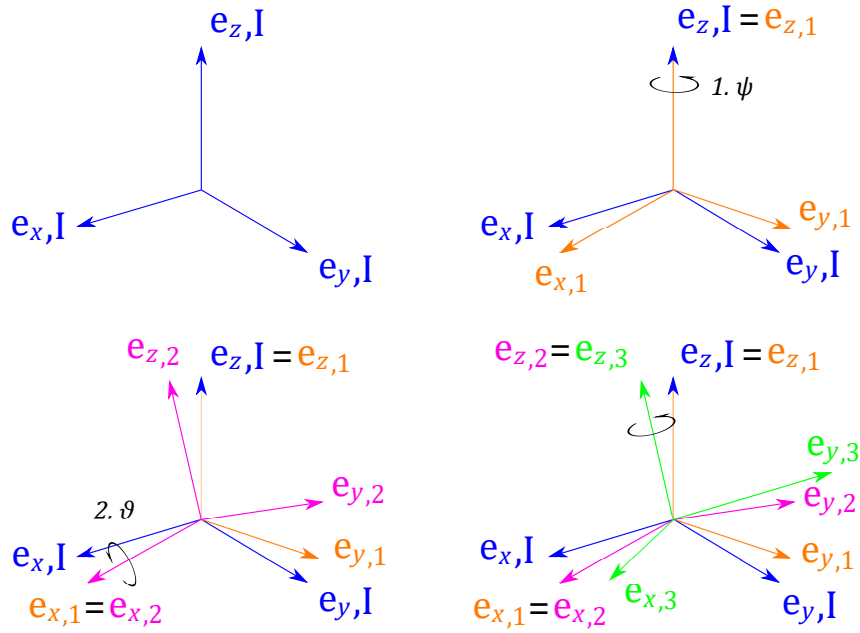
Fig. 2.2 Exemplification of the three successive counterclockwise rotations defined to align the inertial system to the deformed system.

The successive counter-clockwise rotations define a transformation matrix reported in Equation 2.1.

$$[T] = \begin{bmatrix} cos\vartheta cos\psi & cos\vartheta sin\psi cos\varphi + sin\vartheta sin\varphi & cos\vartheta sin\psi sin\varphi - sin\vartheta cos\varphi \\ -sin\psi & cos\psi cos\varphi & cos\psi sin\varphi \\ sin\vartheta cos\psi & sin\vartheta sin\psi cos\varphi - cos\vartheta sin\varphi & sin\vartheta sin\psi sin\varphi + cos\vartheta cos\varphi \end{bmatrix}$$

(2.1)

The angular velocity ω of the centroidal frame with respect to the inertial frame can be written as

$$\begin{aligned} \omega(s,t) &= \dot{\psi} i_z + \dot{\vartheta} i_{y1} + \dot{\varphi} i_1 \\ &= (\dot{\varphi} - \dot{\psi} sin\vartheta) i_1 + (\dot{\psi} cos\vartheta sin\varphi + \dot{\vartheta} cos\varphi) i_2 \\ &\quad + (\dot{\psi} cos\vartheta cos\varphi - \dot{\vartheta} sin\varphi) i_3 \end{aligned}$$

(2.2)

Where the dots denote the time derivative. The components of the curvature ρ_1, ρ_2 and ρ_3 can be obtained by replacing the time derivative with spatial derivatives, denoted with the prime, into Equation 2.2 according to Love's kinetic analogy.

$$
\begin{aligned}
\rho(s,t) &= \psi' i_z + \vartheta' i_{y1} + \varphi' i_1 \\
&= (\varphi' - \psi' \sin\vartheta) i_1 + (\psi' \cos\vartheta \sin\varphi + \vartheta' \cos\varphi) i_2 \\
&\quad + (\psi' \cos\vartheta \cos\varphi - \vartheta' \sin\varphi) i_3 \\
&= \rho_1 i_1 + \rho_2 i_2 + \rho_3 i_3
\end{aligned}
\tag{2.3}
$$

The motion of the beam is described by six generalized displacements, three translations (u, v, w) and, three rotations (ψ, ϑ, φ). The equations of motion are derived neglecting the extension of the neutral axis, the shear deformation, and the warping of the cross-section. These hypothesis are applicable to the cases studied in this thesis, but this model would not be applicable for beams subject to large centrifugal forces (e. g. helicopter rotor blades), beams with highly deformed cross-sections, and to beams with twisting-extension or bending-extension couplings due to anisotropy. With these assumptions, only three generalized displacements are independent.

The extension of the beam can be written as

$$
e = \sqrt{(1+u')^2 + v'^2 + w'^2} - 1
\tag{2.4}
$$

The inextensibility constraint equation can be written as

$$
(1+u')^2 + v'^2 + w'^2 = 1
\tag{2.5}
$$

Moreover, the angles $\psi(s,t)$ and $\vartheta(s,t)$ can be rewritten as a function of the derivatives u', v', w' as

$$
\tan\psi = \frac{v'}{1+u'}
\tag{2.6a}
$$

$$
\tan\vartheta = -\frac{w'}{\sqrt{(1+u')^2 + v'}}
\tag{2.6b}
$$

The variations of curvature are derived according to Pai [77]. The coefficients of the transformation matrix [T] are obtained with a Taylor expansion up to order two to the coefficients reported in Equation 2.1.

$$T_{31} = -w', \tag{2.7a}$$

$$T_{21} = -v', \tag{2.7b}$$

$$T_{32} = -\varphi, \tag{2.7c}$$

$$T_{22} = 1, \tag{2.7d}$$

$$T_{33} = 1, \tag{2.7e}$$

$$T_{23} = \varphi, \tag{2.7f}$$

From Equation 2.7, the expressions of the curvature components retaining only second order terms are

$$\rho_1 = \varphi' + v''w', \tag{2.8a}$$

$$\rho_2 = -w'' + v''\varphi, \tag{2.8b}$$

$$\rho_3 = v'' + w''\varphi, \tag{2.8c}$$

2.3   Derivation of the equation of motion

In this section, the derivation of the equation of motion of the beam is outlined. The equations of motion are obtained by means of the extended Hamilton's principle expressed in Equation 2.9.

$$\int_{t1}^{t2} (\partial T - \partial \pi + \partial W_{nc}) \, dt = 0 \tag{2.9}$$

$$\partial w(x,t) = 0 \quad t = t_1, t_2 \tag{2.10}$$

$$\partial v(x,t) = 0 \quad t = t_1, t_2 \tag{2.11}$$

$$\partial \phi(x,t) = 0 \quad t = t_1, t_2 \tag{2.12}$$

where ∂T is the variation of kinetic energy, $\partial \pi$ is the variation of the potential energy and ∂W_{nc} is the virtual work of the non-conservative forces.

2.3.1   Variation of the potential energy

According to [77], the variation of the potential energy is given by:

$$\partial \pi = \int_0^L (M_1 \partial \rho_1 + M_2 \partial \rho_2 + M_3 \partial \rho_3)\, ds \tag{2.13}$$

where M_1, M_2, and M_3 are the moments with respect to the principal directions, while $\partial \rho_1$, $\partial \rho_2$, and $\partial \rho_3$ are the variations of the curvatures and can be written as

$$\partial \rho_1 = \partial \varphi' + \partial v'' w' + v'' \partial w', \tag{2.14a}$$

$$\partial \rho_2 = \partial(-w'') + \partial v'' \varphi + v'' \partial \varphi, \tag{2.14b}$$

$$\partial \rho_3 = \partial v'' + \partial w'' \varphi + w'' \partial \varphi, \tag{2.14c}$$

Considering the beam inextensible, the contribution of the forces normal to the section is neglected.

Substituting Equation 2.14 into Equation 2.13 one obtains the following expression:

$$\begin{aligned}
\partial \pi = \int_0^L (&M_1 \partial \varphi' + M_2 v'' \partial \varphi + M_3 w'' \partial \varphi + \\
&+ M_1 w' \partial v'' + M_2 \varphi \partial v'' + M_3 \partial v'' + \\
&+ M_1 v'' \partial w' + M_2 \partial(-w'') + M_3 \varphi \partial w'')\, ds
\end{aligned} \tag{2.15}$$

The terms containing the variations of the derivative of the generalized displacements can be integrated by parts to obtain the terms associated with the variation of the generalized displacements and the boundary conditions. After some algebraical manipulation, it is possible to obtain the following:

$$\partial \pi = \int_0^L \left[\left(-M_1' + M_2 v'' + M_3 w'' \right) \partial \varphi + \left(M_1'' w''' + M_2'' \varphi'' + M_3'' \right) \partial v + \right.$$
$$\left(-M_1' v''' - M_2'' + M_3'' \varphi'' \right) \partial w \right] ds + \left[M_1 \partial \varphi + \left(M_1 w' + M_2 \varphi + M_3 \right) \partial v' + \right.$$
$$\left. - \left(M_1 w' + M_2 \varphi + M_3 \right)' \partial v + \left(M_2 + M_3 \varphi \right) \partial w' - \left(M_2 + M_3 \varphi \right)' \partial w \right]_0^L$$

$$\text{(2.16)}$$

Knowing that for a bend-twist coupled beam, the resultant of the moment can be written as in Equation 2.17, the terms associated with the variation of the generalized displacements can be obtained as in 2.18

$$M_1 = GJ_t \rho_1 + K \rho_2, \tag{2.17a}$$

$$M_2 = EI_2 \rho_2 + K \rho_1, \tag{2.17b}$$

$$M_3 = EI_3 \rho_3, \tag{2.17c}$$

$$\partial \varphi : -GJ_t (\varphi'' + v''' w'') + K(w''' - v''' \varphi' + v'' \varphi') + (EI_3 - EI_2) v'' w'', \tag{2.18a}$$

$$\partial v : EI_3 v'''' + (EI_3 - EI_2) w'''' \varphi'' + GJ_t (\varphi'' w''' + w'' \varphi''') + \\ + K(\varphi'' \varphi' + \varphi'' \varphi'' - w''' w''' - w'' w''''), \tag{2.18b}$$

$$\partial w : EI_2 w'''' + (EI_3 - EI_2) \varphi'' v'''' - GJ_t v''' \varphi'' - K(\varphi''' + v'''' w''), \tag{2.18c}$$

2.3.2   Equations of motion

Assuming that the mass and the moments of inertia of the structure are constant in time, the variation of the mass is assumed a higher-order effect that can be neglected. Moreover, the center of gravity of the structure is assumed coincident with the x-axis and the centroid of the section. Denoting $j = \rho I_p$ the mass moment of inertia about the beam axis and f_φ, f_w, and f_v the generalized forces. The governing equations of the beam with bending-torsion coupling are given as follows

$$j\ddot{\varphi} - GJ_t(\varphi'' + v'''w'') + K(w''' - v'''\varphi' + v''\varphi') + (EI_3 - EI_2)v''w'' = f_\varphi, \quad (2.19\text{a})$$

$$m\ddot{v} + EI_3 v'''' + (EI_3 - EI_2)w''''\varphi'' + GJ_t(\varphi''w''' + w''\varphi''') +$$
$$+ K(\varphi''\varphi' + \varphi''\varphi'' - w'''w''' - w''w'''') = f_v, \quad (2.19\text{b})$$

$$m\ddot{w} + EI_2 w'''' + (EI_3 - EI_2)\varphi''v'''' - GJ_t v'''\varphi'' - K(\varphi''' + v''''w'') = f_w, \quad (2.19\text{c})$$

Which can be also written considering only the first-order terms to obtain 2.20

$$j\ddot{\varphi} - GJ_t \varphi'' + Kw''' = f_\varphi, \quad\quad\quad (2.20\text{a})$$

$$m\ddot{v} + EI_3 v'''' = f_v, \quad\quad\quad (2.20\text{b})$$

$$m\ddot{w} + EI_2 w'''' - K\varphi''' = f_w, \quad\quad\quad (2.20\text{c})$$

2.4   Finite Element Formulation

This section presents the derivation of a beam finite element with bending-torsion coupling stiffness and mass matrices. A two-node beam finite element with six degrees of freedom per node, represented in Figure 2.3, is considered for the derivation. One of the hypotheses for the derivation of the beam equations of motion obtained in the previous section was the inextensibility of the beam. For this reason, the axial deformation is neglected and the equations concerning the axial degree of freedom u will not be discussed, and the nodal degrees of freedom are reduced to five per node.

The equations of motion 2.20 can be rewritten as:

$$\rho A \frac{\partial^2 v}{\partial t^2} + EI_z \frac{\partial^2}{\partial x^2}\left(\frac{\partial^2 v}{\partial x^2}\right) = f_v \quad\quad (2.21\text{a})$$

$$\rho A \frac{\partial^2 w}{\partial t^2} + EI_y \frac{\partial^2}{\partial x^2}\left(\frac{\partial^2 w}{\partial x^2}\right) - K\frac{\partial}{\partial x}\left(\frac{\partial^2 \varphi}{\partial x^2}\right) = f_w \quad\quad (2.21\text{b})$$

$$\rho I_p \frac{\partial^2 \varphi}{\partial t^2} - GJ_t \frac{\partial}{\partial x}\left(\frac{\partial \varphi}{\partial x}\right) + K\frac{\partial}{\partial x}\left(\frac{\partial^2 w}{\partial x^2}\right) = f_\varphi \quad\quad (2.21\text{c})$$
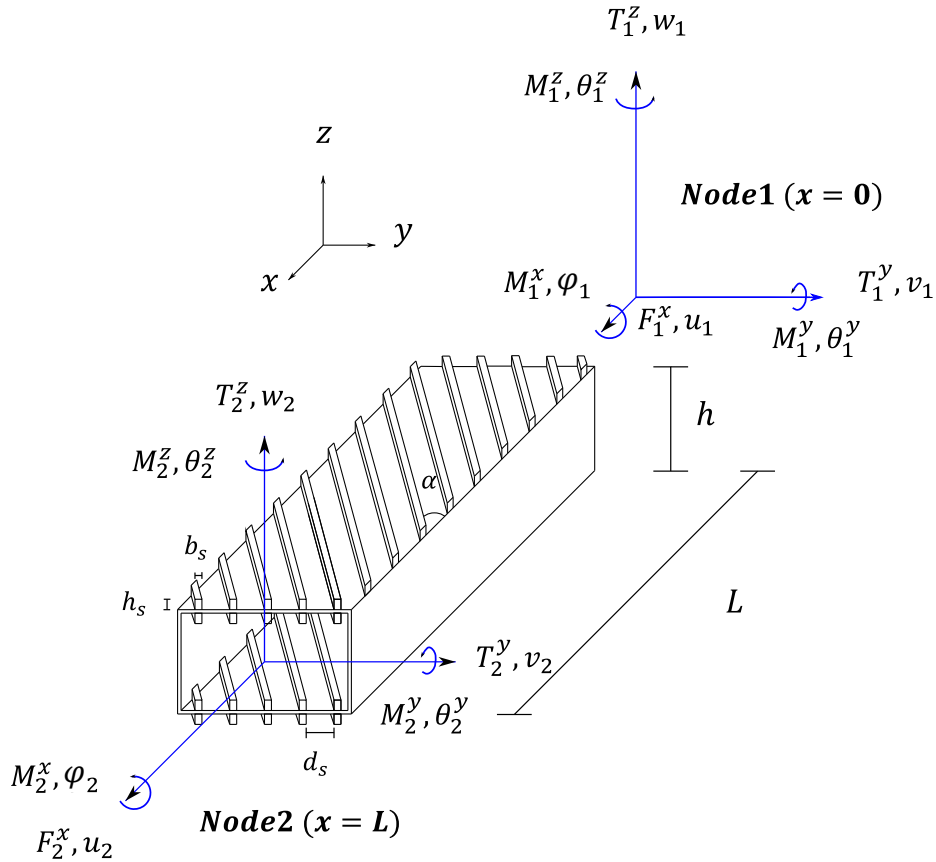
Fig. 2.3 Beam element reference system with dimensions, nodal degrees of freedom. and resultants

2.4.1 Galerkin's method

Galerkin's method can be used to derive the stiffness and mass matrices for the beam finite element with bending torsion formulation. The method starts with the partial differential equation of motion 2.21. The maximum spatial partial derivative order for $w(s,t)$, $v(s,t)$, and $\varphi(s,t)$ are denoted with p, q, and r respectively. $w(s,t)$, $v(s,t)$, and $\varphi(s,t)$ must be expressed as a series of functions with one or more terms. For the case here considered this means:

$$v(x,t) = \sum_{j=i}^{N} \xi_j(t)\phi_{vj}(x) \tag{2.22a}$$

$$w(x,t) = \sum_{j=i}^{N} \xi_j(t)\phi_{wj}(x) \qquad (2.22b)$$

$$\varphi(x,t) = \sum_{j=i}^{N} \xi_j(t)\phi_{\varphi j}(x) \qquad (2.22c)$$

According to [78], for use in Galerkin's method, the functions ϕ_i must possess the following characteristics

- Each function must satisfy all boundary conditions.

- Each function must be respectively at least q, s, t times differentiable. The qth derivative of at least one function must be nonzero.

- If more than one function is used, it must be chosen from a complete set of functions.

- The set of functions must be linearly independent.

Once the shape functions are defined, the set of functions must be multiplied by a residual function R_e and integrated over the beam length. Imposing the solution of Equation 2.23 equal to zero, the error between the approximation introduced with the shape functions and the solution of the problem is minimized.

$$\int_0^L \phi_j R_e dx = 0 \qquad (2.23)$$

The results of this process consent to obtain the mass matrix $[M]$ and the stiffness matrix $[K]$ for a beam finite element.

2.4.2   Shape functions

Polynomials are a typical choice for this class of problems as approximate solutions since they satisfy all the requirements for Galerkin's method. For the presented case, the approximate solutions as a function of the position can be written as follows:

$$v(x) = c_1 + c_2 x + c_3 x^2 + c_4 x^3 \qquad (2.24a)$$

$$w(x) = c_5 + c_6 x + c_7 x^2 + c_8 x^3 \tag{2.24b}$$

$$\varphi(x) = c_9 + c_{10} x + c_{11} x^2 \tag{2.24c}$$

The coefficients c_i can be obtained by applying the boundary conditions listed in Table 2.1. Boundary conditions (1-8) give the classical Hermite's polynomials for $v(x)$ and $w(x)$, while boundary conditions (9-11) result in an expression for $\varphi(x)$ which link bending and torsion through the coupling coefficient K.

Table 2.1 Boundary conditions for a two-nodes element.

$x = 0$	$x = L$
$v = v_1$ ①	$v = v_2$ ②
$v' = \theta_1^z$ ③	$v' = \theta_2^z$ ④
$w = w_1$ ⑤	$w = w_2$ ⑥
$w' = -\theta_1^y$ ⑦	$w' = -\theta_2^y$ ⑧
$\varphi = \varphi_1$ ⑨	$\varphi = \varphi_2$ ⑩

As additional constraint the torsional moment is considered constant over the length.

$$M_x' = 0 \; ⑪ \tag{2.25}$$

$$v(x) = \left[1 - 3\frac{x^2}{L^2} + 2\frac{x^3}{L^3}\right] v_1 + \left[x - 2\frac{x^2}{L} + \frac{x^3}{L^2}\right] \theta_1^z + \\ + \left[3\frac{x^2}{L^2} - 2\frac{x^3}{L^3}\right] v_2 + \left[-\frac{x^2}{L} + \frac{x^3}{L^2}\right] \theta_2^z \tag{2.26a}$$

$$w(x) = \left[1 - 3\frac{x^2}{L^2} + 2\frac{x^3}{L^3}\right] w_1 - \left[x - 2\frac{x^2}{L} + \frac{x^3}{L^2}\right] \theta_1^y + \\ + \left[3\frac{x^2}{L^2} - 2\frac{x^3}{L^3}\right] w_2 - \left[-\frac{x^2}{L} + \frac{x^3}{L^2}\right] \theta_2^y \tag{2.26b}$$

$$\varphi(x) = \left[1 - \frac{x}{L}\right]\varphi_1 + \left[\frac{6K}{GJ_tL^3}(x^2 - Lx)\right]w_1 + \left[\frac{3K}{GJ_tL^2}(Lx - x^2)\right]\theta_1^y +$$
$$+ \left[\frac{x}{L}\right]\varphi_2 + \left[\frac{6K}{GJ_tL^3}(Lx - x^2)\right]w_2 + \left[\frac{3K}{GJ_tL^2}(Lx - x^2)\right]\theta_2^y \qquad (2.26c)$$

Equations 2.26 can be written as the product of the shape functions array times the nodal degrees of freedom column matrix.

$$v(x) = \{N_v(x)\}\{q_v\}^T \qquad (2.27a)$$

$$w(x) = \{N_w(x)\}\{q_w\}^T \qquad (2.27b)$$

$$\varphi(x) = \{N_\psi(x)\}\{q_\varphi\}^T \qquad (2.27c)$$

Where $\{q_v\}$, $\{q_w\}$, and $\{q_\varphi\}$ are defined as follow

$$\{q_v\} = \{v_1, \theta_1^z, v_2, \theta_2^z\} \qquad (2.28a)$$

$$\{q_w\} = \{w_1, \theta_1^y, w_2, \theta_2^y\} \qquad (2.28b)$$

$$\{q_\psi\} = \{\varphi_1, w_1, \theta_1^y, \varphi_2, w_2, \theta_2^y\} \qquad (2.28c)$$

and $\{N_v(x)\}$, $\{N_w(x)\}$, and $\{N_\varphi(x)\}$ are defined as

$$\{N_v(x)\} = \{N_{v1}, N_{v2}, N_{v3}, N_{v4}\} \qquad (2.29a)$$

$$\{N_w(x)\} = \{N_{w1}, N_{w2}, N_{w3}, N_{w4}\} \qquad (2.29b)$$

$$\{N_\varphi(x)\} = \{N_{\varphi1}, N_{\varphi2}, N_{\varphi3}, N_{\varphi4}, N_{\varphi5}, N_{\varphi6}\} \qquad (2.29c)$$

The terms N_{ij} are summarized in Table 2.2

Table 2.2 Shape Functions for Bending-Torsion Coupled Beam Element.

$\{N_v(x)\}$		$\{N_w(x)\}$		$\{N_\varphi(x)\}$	
N_{v1}	$\left[1-3\dfrac{x^2}{L^2}+2\dfrac{x^3}{L^3}\right]$	N_{w1}	$\left[1-3\dfrac{x^2}{L^2}+2\dfrac{x^3}{L^3}\right]$	N_{φ_1}	$\left[1-\dfrac{x}{L}\right]$
N_{v2}	$\left[x-2\dfrac{x^2}{L}+\dfrac{x^3}{L^2}\right]$	N_{w2}	$-\left[x-2\dfrac{x^2}{L}+\dfrac{x^3}{L^2}\right]$	N_{φ_2}	$\left[\dfrac{6K}{GJ_tL^3}\left(x^2-Lx\right)\right]$
N_{v3}	$\left[3\dfrac{x^2}{L^2}-2\dfrac{x^3}{L^3}\right]$	N_{w3}	$\left[3\dfrac{x^2}{L^2}-2\dfrac{x^3}{L^3}\right]$	N_{φ_3}	$\left[\dfrac{3K}{GJ_tL^2}\left(Lx-x^2\right)\right]$
N_{v4}	$\left[-\dfrac{x^2}{L}+\dfrac{x^3}{L^2}\right]$	N_{w4}	$-\left[-\dfrac{x^2}{L}+\dfrac{x^3}{L^2}\right]$	N_{φ_4}	$\left[\dfrac{x}{L}\right]$
				N_{φ_5}	$\left[\dfrac{6K}{GJ_tL^3}\left(Lx-x^2\right)\right]$
				N_{φ_6}	$\left[\dfrac{3K}{GJ_tL^2}\left(Lx-x^2\right)\right]$

2.4.3   Stiffness and mass matrices

Once a set of shape functions compliant with Galerkin's method has been defined, the approximate solution for the equations of motion can be written as follows:

$$v^{(e)} = N_{v1}v_1 + N_{v2}\theta_1^z + N_{v3}v_2 + N_{v4}\theta_2^z = \{N_v(x)\}\{q_v(t)\}^T \tag{2.30a}$$

$$w^{(e)} = N_{w1}w_1 + N_{w2}\theta_1^y + N_{w3}w_2 + N_{w4}\theta_2^y = \{N_w(x)\}\{q_w(t)\}^T \tag{2.30b}$$

$$\varphi^{(e)} = N_{\varphi 1}\varphi_1 + N_{\varphi 2}w_1 + N_{\varphi 3}\theta_1^y + N_{\varphi 4}\varphi_2 + N_{\varphi 5}w_2 + N_{\varphi 6}\theta_2^y = \{N_\varphi(x)\}\{q_\varphi(t)\}^T \tag{2.30c}$$

Where the shape functions N_i are only space-dependent while the nodal degrees of freedom q_i are only time-dependent. Substituting the approximate solutions 2.30 into the partial differential equation of motion 2.21, a residual function is obtained.

$$R_v^e = \rho A\frac{\partial^2 v^{(e)}}{\partial t^2} + EI_z\frac{\partial^2}{\partial x^2}\left(\frac{\partial^2 v^{(e)}}{\partial x^2}\right) - f_v \tag{2.31a}$$

$$R_w^e = \rho A\frac{\partial^2 w^{(e)}}{\partial t^2} + EI_y\frac{\partial^2}{\partial x^2}\left(\frac{\partial^2 w^{(e)}}{\partial x^2}\right) - K\frac{\partial}{\partial x}\left(\frac{\partial^2 \varphi^{(e)}}{\partial x^2}\right) - f_w \tag{2.31b}$$

$$R_\varphi^e = \rho I_p\frac{\partial^2 \varphi^{(e)}}{\partial t^2} - GJ_t\frac{\partial}{\partial x}\left(\frac{\partial \varphi^{(e)}}{\partial x}\right) + K\frac{\partial}{\partial x}\left(\frac{\partial^2 w^{(e)}}{\partial x^2}\right) - f_\varphi \tag{2.31c}$$

The residual functions 2.31 can be multiplied times the shape functions associated with the respective generalized displacement variable and integrated over the length. Imposing the solution of the integral equal to zero, the error between the exact solution and the approximate solution is minimized and the stiffness and mass matrices can be derived.

$$\int_0^L \{N_v\}R_v^e dx = 0 \tag{2.32a}$$

$$\int_0^L \{N_w\}R_w^e dx = 0 \tag{2.32b}$$

$$\int_0^L \{N_\varphi\}R_\varphi^e dx = 0 \tag{2.32c}$$

The Equations 2.31 can be substituted into Equations 2.32 to obtain

$$\int_0^L \{N_v\}\rho A \frac{\partial^2 v^{(e)}}{\partial t^2} dx + \int_0^L \{N_v\}EI_z \frac{\partial^2}{\partial x^2}\left(\frac{\partial^2 v^{(e)}}{\partial x^2}\right) dx - \int_0^L \{N_v\}f_v dx = 0 \tag{2.33a}$$

$$\int_0^L \{N_w\}\rho A \frac{\partial^2 w^{(e)}}{\partial t^2} dx + \int_0^L \{N_w\}EI_y \frac{\partial^2}{\partial x^2}\left(\frac{\partial^2 w^{(e)}}{\partial x^2}\right) dx +$$
$$- \int_0^L \{N_w\}K \frac{\partial}{\partial x}\left(\frac{\partial^2 \varphi^{(e)}}{\partial x^2}\right) dx - \int_0^L \{N_w\}f_w dx = 0 \tag{2.33b}$$

$$\int_0^L \{N_\varphi\}\rho I_p \frac{\partial^2 \varphi^{(e)}}{\partial t^2} dx - \int_0^L \{N_\varphi\}GJ_t \frac{\partial}{\partial x}\left(\frac{\partial \varphi^{(e)}}{\partial x}\right) dx +$$
$$+ \int_0^L \{N_\varphi\}K \frac{\partial}{\partial x}\left(\frac{\partial^2 w^{(e)}}{\partial x^2}\right) dx - \int_0^L \{N_\varphi\}f_\varphi dx = 0 \tag{2.33c}$$

Integrating two times by parts the second member of Equation 2.33 and one time the third member of Equation 2.33b and 2.33c, Equation 2.33 becomes:

$$\int_0^L \{N_v\}\rho A \frac{\partial^2 v^{(e)}}{\partial^2 t}dx + \int_0^L \{N_v\}''EI_z\left(\frac{\partial^2 v^{(e)}}{\partial x^2}\right)dx =$$

$$= \int_0^L \{N_v\}f_v dx - \{N_v\}EI_z\frac{\partial}{\partial x}\left(\frac{\partial^2 v^{(e)}}{\partial x^2}\right)\bigg|_0^L + \{N_v\}'EI_z\left(\frac{\partial^2 v^{(e)}}{\partial x^2}\right)\bigg|_0^L$$

$$\text{(2.34a)}$$

$$\int_0^L \{N_w\}\rho A \frac{\partial^2 w^{(e)}}{\partial t^2}dx + \int_0^L \{N_w\}''EI_y\frac{\partial^2 w^{(e)}}{\partial x^2}dx - \int_0^L \{N_w\}''K\frac{\partial \varphi^{(e)}}{\partial x}dx =$$

$$= \int_0^L \{N_w\}f_w dx - \{N_w\}EI_y\frac{\partial}{\partial x}\left(\frac{\partial^2 w^{(e)}}{\partial x^2}\right)\bigg|_0^L + \{N_w\}K\left(\frac{\partial^2 \varphi^{(e)}}{\partial x^2}\right)\bigg|_0^L +$$

$$\{N_w\}'EI_y\left(\frac{\partial^2 w^{(e)}}{\partial x^2}\right)\bigg|_0^L - \{N_w\}'K\left(\frac{\partial \varphi^{(e)}}{\partial x}\right)\bigg|_0^L$$

$$\text{(2.34b)}$$

$$\int_0^L \{N_\varphi\}\rho A \frac{\partial^2 \varphi^{(e)}}{\partial^2 t}dx + \int_0^L \{N_\varphi\}'GJ_t\left(\frac{\partial \varphi^{(e)}}{\partial x}\right)dx - \int_0^L \{N_\varphi\}'K\left(\frac{\partial^2 w^{(e)}}{\partial x^2}\right)dx =$$

$$= \int_0^L \{N_\varphi\}f_\varphi dx + \{N_\varphi\}GJ_t\left(\frac{\partial \varphi^{(e)}}{\partial x}\right)\bigg|_0^L - \{N_\varphi\}K\left(\frac{\partial^2 w^{(e)}}{\partial x^2}\right)\bigg|_0^L$$

$$\text{(2.34c)}$$

The right part of Equations 2.34 can be rewritten to obtain the element nodal forces and moments.

$$\int_0^L \{N_v\}f_v dx + \left\{\begin{array}{c} N_{v1}\left[-EI_z\frac{\partial}{\partial x}\left(\frac{\partial^2 v^{(e)}}{\partial x^2}\right)\right]\bigg|_0^L \\ N_{v2}\left[-EI_z\frac{\partial}{\partial x}\left(\frac{\partial^2 v^{(e)}}{\partial x^2}\right)\right]\bigg|_0^L \\ N_{v3}\left[-EI_z\frac{\partial}{\partial x}\left(\frac{\partial^2 v^{(e)}}{\partial x^2}\right)\right]\bigg|_0^L \\ N_{v4}\left[-EI_z\frac{\partial}{\partial x}\left(\frac{\partial^2 v^{(e)}}{\partial x^2}\right)\right]\bigg|_0^L \end{array}\right\} + \left\{\begin{array}{c} N_{v1}'EI_z\left(\frac{\partial^2 v^{(e)}}{\partial x^2}\right)\bigg|_0^L \\ N_{v2}'EI_z\left(\frac{\partial^2 v^{(e)}}{\partial x^2}\right)\bigg|_0^L \\ N_{v3}'EI_z\left(\frac{\partial^2 v^{(e)}}{\partial x^2}\right)\bigg|_0^L \\ N_{v4}'EI_z\left(\frac{\partial^2 v^{(e)}}{\partial x^2}\right)\bigg|_0^L \end{array}\right\}$$

$$\text{(2.35a)}$$

$$\int_0^L \{N_w\} f_w \, dx + \begin{Bmatrix} N_{w1} \left[-EI_y \frac{\partial}{\partial x} \left(\frac{\partial^2 w^{(e)}}{\partial x^2} \right) + K \frac{\partial^2 \varphi^{(e)}}{\partial x^2} \right] \Big|_0^L \\ N_{w2} \left[-EI_y \frac{\partial}{\partial x} \left(\frac{\partial^2 w^{(e)}}{\partial x^2} \right) + K \frac{\partial^2 \varphi^{(e)}}{\partial x^2} \right] \Big|_0^L \\ N_{w3} \left[-EI_y \frac{\partial}{\partial x} \left(\frac{\partial^2 w^{(e)}}{\partial x^2} \right) + K \frac{\partial^2 \varphi^{(e)}}{\partial x^2} \right] \Big|_0^L \\ N_{w4} \left[-EI_y \frac{\partial}{\partial x} \left(\frac{\partial^2 w^{(e)}}{\partial x^2} \right) + K \frac{\partial^2 \varphi^{(e)}}{\partial x^2} \right] \Big|_0^L \end{Bmatrix} +$$

$$+ \begin{Bmatrix} N_{w1}' \left(EI_y \frac{\partial^2 w^{(e)}}{\partial x^2} - K \frac{\partial \varphi^{(e)}}{\partial x} \right) \Big|_0^L \\ N_{w2}' \left(EI_y \frac{\partial^2 w^{(e)}}{\partial x^2} - K \frac{\partial \varphi^{(e)}}{\partial x} \right) \Big|_0^L \\ N_{w3}' \left(EI_y \frac{\partial^2 w^{(e)}}{\partial x^2} - K \frac{\partial \varphi^{(e)}}{\partial x} \right) \Big|_0^L \\ N_{w4}' \left(EI_y \frac{\partial^2 w^{(e)}}{\partial x^2} - K \frac{\partial \varphi^{(e)}}{\partial x} \right) \Big|_0^L \end{Bmatrix}$$

$$(2.35b)$$

$$\int_0^L \{N_\varphi\} f_\varphi \, dx + \begin{Bmatrix} N_{\varphi 1} \left[GJ_t \frac{\partial \varphi^{(e)}}{\partial x} - K \frac{\partial^2 w^{(e)}}{\partial x^2} \right] \Big|_0^L \\ N_{\varphi 2} \left[GJ_t \frac{\partial \varphi^{(e)}}{\partial x} - K \frac{\partial^2 w^{(e)}}{\partial x^2} \right] \Big|_0^L \\ N_{\varphi 3} \left[GJ_t \frac{\partial \varphi^{(e)}}{\partial x} - K \frac{\partial^2 w^{(e)}}{\partial x^2} \right] \Big|_0^L \\ N_{\varphi 4} \left[GJ_t \frac{\partial \varphi^{(e)}}{\partial x} - K \frac{\partial^2 w^{(e)}}{\partial x^2} \right] \Big|_0^L \\ N_{\varphi 5} \left[GJ_t \frac{\partial \varphi^{(e)}}{\partial x} - K \frac{\partial^2 w^{(e)}}{\partial x^2} \right] \Big|_0^L \\ N_{\varphi 6} \left[GJ_t \frac{\partial \varphi^{(e)}}{\partial x} - K \frac{\partial^2 w^{(e)}}{\partial x^2} \right] \Big|_0^L \end{Bmatrix} \qquad (2.35c)$$

Knowing that:

$$\begin{cases} -EI_z\dfrac{\partial}{\partial x}\left(\dfrac{\partial^2 v^{(e)}}{\partial x^2}\right) = T_y \\[2ex] EI_z\left(\dfrac{\partial^2 v^{(e)}}{\partial x^2}\right) = M_z \\[2ex] -EI_y\dfrac{\partial}{\partial x}\left(\dfrac{\partial^2 w^{(e)}}{\partial x^2}\right)+K\dfrac{\partial^2 \varphi^{(e)}}{\partial x^2} = T_z \\[2ex] -EI_y\dfrac{\partial^2 w^{(e)}}{\partial x^2}+K\dfrac{\partial \varphi^{(e)}}{\partial x} = M_y \\[2ex] GJ_t\dfrac{\partial \varphi^{(e)}}{\partial x}-K\dfrac{\partial^2 w^{(e)}}{\partial x^2} = M_x \end{cases} \tag{2.36}$$

and that the shape functions and their derivatives assume the following values for the first node ($x = 0$) and the second node ($x = L$) of the element:

$$\begin{cases} N_{v1}(0) = 1, N_{v1}(L) = 0, N'_{v1}(0) = 0, N'_{v1}(L) = 0 \\ N_{v2}(0) = 0, N_{v2}(L) = 0, N'_{v2}(0) = 1, N'_{v2}(L) = 0 \\ N_{v3}(0) = 0, N_{v3}(L) = 1, N'_{v3}(0) = 0, N'_{v3}(L) = 0 \\ N_{v4}(0) = 0, N_{v4}(L) = 0, N'_{v4}(0) = 0, N'_{v4}(L) = 1 \end{cases} \tag{2.37}$$

$$\begin{cases} N_{w1}(0) = 1,\ N_{w1}(L) = 0,\ N'_{w1}(0) = 0,\ N'_{w1}(L) = 0 \\ N_{w2}(0) = 0,\ N_{w2}(L) = 0,\ N'_{w2}(0) = -1,\ N'_{w2}(L) = 0 \\ N_{w3}(0) = 0,\ N_{w3}(L) = 1,\ N'_{w3}(0) = 0,\ N'_{w3}(L) = 0 \\ N_{w4}(0) = 0,\ N_{w4}(L) = 0,\ N'_{w4}(0) = 0,\ N'_{w4}(L) = -1 \end{cases} \tag{2.38}$$

$$\begin{cases} N_{\varphi 1}(0) = 1,\ N_{\varphi 1}(L) = 0 \\ N_{\varphi 2}(0) = 0,\ N_{\varphi 2}(L) = 0 \\ N_{\varphi 3}(0) = 0,\ N_{\varphi 3}(L) = 0 \\ N_{\varphi 4}(0) = 0,\ N_{\varphi 4}(L) = 1 \\ N_{\varphi 5}(0) = 0,\ N_{\varphi 5}(L) = 0 \\ N_{\varphi 6}(0) = 0,\ N_{\varphi 6}(L) = 0 \end{cases} \tag{2.39}$$

Equation (2.40) are obtained.

$$\int_0^L \{N_v\} \rho A \frac{\partial^2 v^{(e)}}{\partial t^2} dx + \int_0^L \{N_v\}'' E I_z \left(\frac{\partial^2 v^{(e)}}{\partial x^2} \right) dx = \int_0^L \{N_v\} f_v dx + \begin{Bmatrix} -T_1^y \\ -M_1^z \\ T_2^y \\ M_2^z \end{Bmatrix}$$

$$(2.40a)$$

$$\int_0^L \{N_w\} \rho A \frac{\partial^2 w^{(e)}}{\partial t^2} dx + \int_0^L \{N_w\}'' E I_y \frac{\partial^2 w^{(e)}}{\partial x^2} dx - \int_0^L \{N_w\}'' K \frac{\partial \varphi}{\partial x} dx = \int_0^L \{N_w\} f_w dx + \begin{Bmatrix} -T_1^z \\ -M_1^y \\ T_2^z \\ M_2^y \end{Bmatrix}$$

$$(2.40b)$$

$$\int_0^L \{N_\varphi\} \rho I_p \frac{\partial^2 \varphi^{(e)}}{\partial t^2} dx + \int_0^L \{N_\varphi\}' G J_t \frac{\partial \varphi^{(e)}}{\partial x} dx - \int_0^L \{N_\varphi\}' K \frac{\partial^2 w^{(e)}}{\partial x^2} dx = \int_0^L \{N_\varphi\} f_\varphi dx + \begin{Bmatrix} -M_1^x \\ 0 \\ 0 \\ M_2^x \\ 0 \\ 0 \end{Bmatrix}$$

$$(2.40c)$$

where T_1^y, T_2^y, T_1^z, T_2^z, M_1^z, M_2^z, M_1^y, M_2^z, M_1^z and M_2^x are the nodal loads of the beam finite element associated to the boundary conditions.

Substituting the expression of the approximate solutions (2.30) into Equation (2.40), one obtains:

$$\int_0^L \rho A \{N_v\} \{N_v\} \{\ddot{q}_v\} dx + \int_0^L E I_z \{N_v\}'' \{N_v\}'' \{q_v\} dx =$$

$$= \int_0^L \{N_v\} f_v dx + \begin{Bmatrix} -T_1^y \\ -M_1^z \\ T_2^y \\ M_2^z \end{Bmatrix} \qquad (2.41a)$$

$$\int_0^L \rho A\{N_w\}\{N_w\}\{\ddot{q}_w\}dx + \int_0^L EI_y\{N_w\}''\{N_w\}''\{q_w\}dx - \int_0^L K\{N_w\}''\{N_\varphi\}'\{q_\varphi\}dx =$$

$$= \int_0^L \{N_w\}f_w dx + \begin{Bmatrix} -T_1^z \\ -M_1^y \\ T_2^z \\ M_2^y \end{Bmatrix}$$

(2.41b)

$$\int_0^L \rho I_P\{N_\varphi\}\{N_\varphi\}\{\ddot{q}_\varphi\}dx + \int_0^L GJ_t\{N_\varphi\}'\{N_\varphi\}'\{q_\varphi\}dx - \int_0^L K\{N_\varphi\}'\{N_w\}''\{q_w\}dx =$$

$$= \int_0^L \{N_\varphi\}f_\varphi dx + \begin{Bmatrix} -M_1^x \\ 0 \\ 0 \\ M_2^x \\ 0 \\ 0 \end{Bmatrix}$$

(2.41c)

Equations (2.41) can be rewritten in the matrix form as follows:

$$[M_v]\{\ddot{q}_v\} + [K_v]\{q_v\} = \{p_v\} + \begin{Bmatrix} -T_1^y \\ -M_1^z \\ T_2^y \\ M_2^z \end{Bmatrix}$$

(2.42a)

$$[M_w]\{\ddot{q}_w\} + [K_w]\{q_w\} - [K_{w\varphi}]\{q_\varphi\} = \{p_w\} + \begin{Bmatrix} -T_1^z \\ -M_1^y \\ T_2^z \\ M_2^y \end{Bmatrix}$$

(2.42b)

$$[M_\varphi]\{\ddot{q}_\varphi\} + [K_\varphi]\{q_\varphi\} - [K_{\varphi w}]\{q_w\} = \{p_\varphi\} + \begin{Bmatrix} -M_1^x \\ 0 \\ 0 \\ M_2^x \\ 0 \\ 0 \end{Bmatrix} \qquad (2.42c)$$

The matrices in Equation (2.42) are defined as follows

$$[K_v] = \int_0^L EI_z\{N_v\}''\{N_v\}''dx = \frac{EI_z}{L^3} \begin{bmatrix} 12 & 6L & -12 & 6L \\ & 4L^2 & -6L & 2L^2 \\ & & 12 & -6L \\ & & & 4L^2 \end{bmatrix} \qquad (2.43)$$

$$[K_w] = \int_0^L EI_y\{N_w\}''\{N_w\}''dx = \frac{EI_y}{L^3} \begin{bmatrix} 12 & -6L & -12 & -6L \\ & 4L^2 & 6L & 2L^2 \\ & & 12 & 6L \\ & & & 4L^2 \end{bmatrix} \qquad (2.44)$$

$$[K_\varphi] = \int_0^L GJ_t\{N_\varphi\}'\{N_\varphi\}'dx = \begin{bmatrix} \dfrac{GJ_t}{L} & 0 & 0 & -\dfrac{GJ_t}{L} & 0 & 0 \\ & \dfrac{12K^2}{GJ_tL^3} & -\dfrac{6K^2}{GJ_tL^2} & 0 & -\dfrac{12K^2}{GJ_tL^3} & -\dfrac{6K^2}{GJ_tL^2} \\ & & \dfrac{3K^2}{GJ_tL} & 0 & \dfrac{6K^2}{GJ_tL^2} & \dfrac{3K^2}{GJ_tL} \\ & & & \dfrac{GJ_t}{L} & 0 & 0 \\ & & & & \dfrac{12K^2}{GJ_tL^3} & \dfrac{6K^2}{GJ_tL^2} \\ & & & & & \dfrac{3K^2}{GJ_tL} \end{bmatrix}$$

$$(2.45)$$

$$[K_{w\varphi}] = \int_0^L K\{N_w\}''\{N_\varphi\}'dx = \begin{bmatrix} 0 & \dfrac{12K}{GJ_tL^3} & -\dfrac{6K}{GJ_tL^2} & 0 & -\dfrac{12K}{GJ_tL^3} & -\dfrac{6K}{GJ_tL^2} \\ -\dfrac{1}{L} & -\dfrac{6K}{GJ_tL^2} & \dfrac{3K}{GJ_tL} & \dfrac{1}{L} & \dfrac{6K}{GJ_tL^2} & \dfrac{3K}{GJ_tL} \\ 0 & -\dfrac{12K}{GJ_tL^3} & \dfrac{6K}{GJ_tL^2} & 0 & \dfrac{12K}{GJ_tL^3} & \dfrac{6K}{GJ_tL^2} \\ \dfrac{1}{L} & -\dfrac{6K}{GJ_tL^2} & \dfrac{3K}{GJ_tL} & -\dfrac{1}{L} & \dfrac{6K}{GJ_tL^2} & \dfrac{3K}{GJ_tL} \end{bmatrix}$$

$$(2.46)$$

$$[K_{\varphi w}] = \int_0^L K\{N_\varphi\}'\{N_w\}''dx = \begin{bmatrix} 0 & -\dfrac{1}{L} & 0 & \dfrac{1}{L} \\ \dfrac{12K^2}{GJ_tL^3} & -\dfrac{6K^2}{GJ_tL^2} & -\dfrac{12K^2}{GJ_tL^3} & -\dfrac{6K^2}{GJ_tL^2} \\ -\dfrac{6K^2}{GJ_tL^2} & \dfrac{3K^2}{GJ_tL} & \dfrac{6K^2}{GJ_tL^2} & \dfrac{3K^2}{GJ_tL} \\ 0 & \dfrac{1}{L} & 0 & -\dfrac{1}{L} \\ -\dfrac{12K^2}{GJ_tL^3} & \dfrac{6K^2}{GJ_tL^2} & \dfrac{12K^2}{GJ_tL^3} & \dfrac{6K^2}{GJ_tL^2} \\ -\dfrac{6K^2}{GJ_tL^2} & \dfrac{3K^2}{GJ_tL} & \dfrac{6K^2}{GJ_tL^2} & \dfrac{3K^2}{GJ_tL} \end{bmatrix}$$

$$(2.47)$$

$$[M_v] = \int_0^L \rho A\{N_v\}\{N_v\}dx = \dfrac{\rho AL}{210}\begin{bmatrix} 78 & 11L & 27 & \dfrac{-13L}{2} \\ & 2L^2 & \dfrac{13L}{2} & \dfrac{-3L^2}{2} \\ & & 78 & -11L \\ & & & 2L^2 \end{bmatrix}$$

$$(2.48)$$

$$[M_w] = \int_0^L \rho A\{N_w\}\{N_w\}dx = \frac{\rho AL}{210} \begin{bmatrix} 78 & -11L & 27 & \dfrac{13L}{2} \\ & 2L^2 & -\dfrac{13L}{2} & \dfrac{-3L^2}{2} \\ & & 78 & 11L \\ & & & 2L^2 \end{bmatrix} \qquad (2.49)$$

$$[M_\varphi] = \int_0^L \rho A\{N_\varphi\}\{N_\varphi\}dx = \rho I_p \begin{bmatrix} \dfrac{L}{3} & -\dfrac{K}{2GJ_t} & \dfrac{KL}{4GJ_t} & \dfrac{L}{6} & \dfrac{K}{2GJ_t} & \dfrac{KL}{4GJ_t} \\ & \dfrac{6K^2}{5GJ_t^2 L} & \dfrac{3K^2}{5GJ_t^2} & -\dfrac{K}{2GJ_t} & \dfrac{6K^2}{5GJ_t^2 L} & \dfrac{3K^2}{5GJ_t^2} \\ & & \dfrac{3K^2 L}{10GJ_t^2} & \dfrac{KL}{4GJ_t} & \dfrac{3K^2}{5GJ_t^2} & \dfrac{3K^2 L}{10GJ_t^2} \\ & & & \dfrac{L}{3} & \dfrac{K}{2GJ_t} & \dfrac{KL}{4GJ_t} \\ & & & & \dfrac{6K^2}{5GJ_t^2 L} & \dfrac{3K^2}{5GJ_t^2} \\ & & & & & \dfrac{3K^2 L}{10GJ_t^2} \end{bmatrix}$$

$$(2.50)$$

It is now possible to define the array *q* which includes all the nodal degrees of freedom for a two-node element as:

$$q = \{v_1, w_1, \varphi_1, \theta_1^y, \theta_1^z, v_2, w_2, \varphi_2, \theta_2^y, \theta_2^z\} \qquad (2.51)$$

The finite element global stiffness matrix [K] and mass matrix [M] can be obtained by combining matrices (2.43) to (2.50) with the sum of the members involving the same degrees of freedom.

$$[K] = \begin{bmatrix} \dfrac{12EI_z}{L^3} & 0 & 0 & 0 & \dfrac{6EI_z}{L^2} & -\dfrac{12EI_z}{L^3} & 0 & 0 & 0 & \dfrac{6EI_z}{L^2} \\ & K_1 & 0 & K_2 & 0 & 0 & -K_1 & 0 & K_2 & 0 \\ & & \dfrac{GJ_t}{L} & \dfrac{K}{L} & 0 & 0 & 0 & -\dfrac{GJ_t}{L} & -\dfrac{K}{L} & 0 \\ & & & K_3 & 0 & 0 & -K_2 & -\dfrac{K}{L} & K_4 & 0 \\ & & & & \dfrac{4EI_z}{L} & -\dfrac{6EI_z}{L^2} & 0 & 0 & 0 & \dfrac{2EI_z}{L} \\ & & & & & \dfrac{12EI_z}{L^3} & 0 & 0 & 0 & -\dfrac{6EI_z}{L^2} \\ & & & & & & K_1 & 0 & -K_2 & 0 \\ & & & & & & & \dfrac{GJ_t}{L} & \dfrac{K}{L} & 0 \\ & & & & & & & & K_3 & 0 \\ & & & & & & & & & \dfrac{4EI_z}{L} \end{bmatrix}$$

$$\tag{2.52}$$

with

$$K_1 = \frac{12(EI_y GJ_t - K^2)}{GJ_t L^3} \quad K_2 = \frac{6(K^2 - EI_y GJ_t)}{GJ_t L^2}$$

$$\tag{2.53}$$

$$K_3 = \frac{4EI_y GJ_t - 3K^2}{GJ_t L} \quad K_4 = \frac{2EI_y GJ_t - 3K^2}{GJ_t L}$$

$$[M] = \begin{bmatrix}
\dfrac{13AL\rho}{35} & 0 & 0 & 0 & \dfrac{11AL^2\rho}{210} & -\dfrac{9AL\rho}{70} & 0 & 0 & 0 & -\dfrac{13AL^2\rho}{420} \\[1em]
 & M_1 & -\dfrac{I_pK\rho}{2GJ_t} & M_2 & 0 & 0 & M_3 & -\dfrac{I_pK\rho}{2GJ_t} & M_4 & 0 \\[1em]
 & & \dfrac{I_pL\rho}{3} & \dfrac{I_pKL\rho}{4GJ_t} & 0 & 0 & \dfrac{I_pK\rho}{2GJ_t} & \dfrac{I_pL\rho}{6} & \dfrac{I_pKL\rho}{4GJ_t} & 0 \\[1em]
 & & & M_5 & 0 & 0 & -M_4 & \dfrac{I_pKL\rho}{4GJ_t} & M_6 & 0 \\[1em]
 & & & & \dfrac{AL^3\rho}{105} & \dfrac{13AL^2\rho}{420} & 0 & 0 & 0 & -\dfrac{AL^3\rho}{140} \\[1em]
 & & & & & \dfrac{13AL\rho}{35} & 0 & 0 & 0 & -\dfrac{11AL^2\rho}{210} \\[1em]
 & & & & & & M_1 & \dfrac{I_pK\rho}{2GJ_t} & -M_2 & 0 \\[1em]
 & & & & & & & \dfrac{I_pL\rho}{3} & \dfrac{I_pKL\rho}{4GJ_t} & 0 \\[1em]
 & & & & & & & & M_5 & 0 \\[1em]
 & & & & & & & & & \dfrac{AL^3\rho}{105}
\end{bmatrix}$$

$$(2.54)$$

with

$$M_1 = \frac{6I_pK^2\rho}{5GJ_t^2L} + \frac{13AL\rho}{35} \qquad M_2 = -\frac{3I_pK^2\rho}{5GJ_t^2} - \frac{11AL^2\rho}{210} \qquad M_3 = -\frac{6I_pK^2\rho}{5GJ_t^2L} + \frac{9AL\rho}{70}$$

$$M_4 = -\frac{3I_pK^2\rho}{5GJ_t^2} + \frac{13AL^2\rho}{420} \qquad M_5 = \frac{3I_pK^2L\rho}{10GJ_t^2} + \frac{AL^3\rho}{105} \qquad M_6 = \frac{3I_pK^2L\rho}{10GJ_t^2} - \frac{AL^3\rho}{140}$$

$$(2.55)$$

It is worth noting that if the configuration is uncoupled and K is equal to 0, the matrices [K] and [M] are the standard Hermitian beam element uncoupled matrices.

Chapter 3

Introduction of Geometric Non-Linear Effects in the BTCE Formulation

3.1   Introduction and Motivation

High aspect ratio slender wings can improve the aerodynamic efficiency of modern aircraft. However, these structures are more prone to high deformations which introduce geometric non-linearities that can influence the aeroelastic performance. the importance of aerodynamic and structural geometrical non-linearities in the aeroelastic behavior of high-aspect-ratio wings has been established by Patil and Hodges [79]. Patil et al. [80] studied the effects of structural geometric non-linearities on the flutter behavior of high aspect-ratio wings they presented the changes in structural and aeroelastic characteristics of a steady state deflection of a wing. Their study revealed a significant change in the structural frequencies and a significant reduction in the flutter speed. Frulla and Cestino [35], investigated an

equivalent configuration derived from the HELIPLAT HAVE-UAV (high-altitude very-long endurance unmanned air vehicle) wing structure. With this study, they assessed the presence of non-linearities induced by the slenderness of the wing structure and proposed a modified wing configuration to highlight these effects on flutter behavior.

Detailed coupled computational fluid dynamics and finite element method formulation for aeroelastic analysis and formulation have been widely studied [28]. These models can be very sophisticated and can involve a large number of calculations which is not efficient during early design stages. Low-order aeroelastic models allow for a reduction of computational cost granting similar prediction capabilities of higher-order models. A popular approach for non-linear elasticity consists of geometrically exact beam formulation. Hodges [81, 82] presented an intrinsic formulation for non-linear dynamics of initially curved and twisted anisotropic beams. Geometrically exact beam models use equivalent beam properties derived from finite element models [83, 84]. These formulations found an application in several works involving flexible wing structures. Drela [85] used a non-linear beam model to develop an integrated model for aerodynamic and structural simulation of flexible aircraft, while Patil [86] presented a theory for flight dynamic analysis of highly flexible wing configuration accounting for geometrically non-linear structural deformations. Recently, Ritter [87] and Medeiros [88] developed a new class of low-order structural models that relies on high-order modal expansions, these models require non-linear static analysis of a FEM to determine the modal expansion terms. Another model has been presented by Bruni et al. [89], who used an expansion of the partial differential equations for beam dynamics up to the third order, the solution was obtained with Galerkin's method and with a multi-modal approach. With this model, they explored the effects of static deflection, external trim, gust loads, and aerodynamic stalls.

The variety of structural models for static and dynamic non-linear analysis of beam structures present in literature employ different solutions to simulate specific conditions, some models consider only one-dimensional finite elements as in [90] while other developed models that include all the degrees of freedom. Yang et al. [91] developed a six-degree of freedom beam element including material non-linearities, they described a procedure for non-linear static analysis which consists of a piecewise linearization of the response quotations and iterations at each incremental step to achieve equilibrium. Surana et al. [92] presented a formulation for a three-dimensions curved beam element with geometric non-linearities using a Lagrangian

approach and verified the accuracy of the formulation against literature results of non-linear static analysis. More recently, Duan and Li [93] developed a three-dimensional beam element for dynamic analysis with geometric non-linearities, the derivation is based on the co-rotational formulation. The model showed good results under large deflection and rotations, but small strains are assumed.

Low-order structural models can be further developed to consider also material couplings and expand the aeroelastic design domain. Cestino et al. [94] studied flutter instability of high aspect ratio wings and considered the phenomenon as the sum of two effects, the Geometrical Effect (GE) given by the deformed geometry and the Stiffness Effect (SE), which is the effect caused by the loads at the equilibrium condition on the differential stiffness matrix. They demonstrated that the GE represents the main contribution to the non-linear dynamic analysis of slender structures and that the results of flutter analysis are verified by experimental evidence either when considering only GE or when accounting also for SE.

In this chapter, a procedure to perform dynamic analysis in the presence of geometric non-linearities with the derived BTCE is presented. A first formulation for the BTCE allows for the consideration of both non-linear effects, the GE and the SE (BTCE-NL) through a perturbation approach. Moreover, a simplified approach including only the GE (BTCE-GE) has been developed considering a deformed equilibrium-dependent transformation matrix to account for the orientation of a deformed BTCE model.

3.2   Models Derivation

In this section, the BTCE derived in [95] is used to develop two procedures for modal analysis of pre-deformed structures. The first procedure considers only the geometrical effects given by the deformed configuration while the second procedure uses a perturbation approach to include non-linear effects in the beam element stiffness matrix.
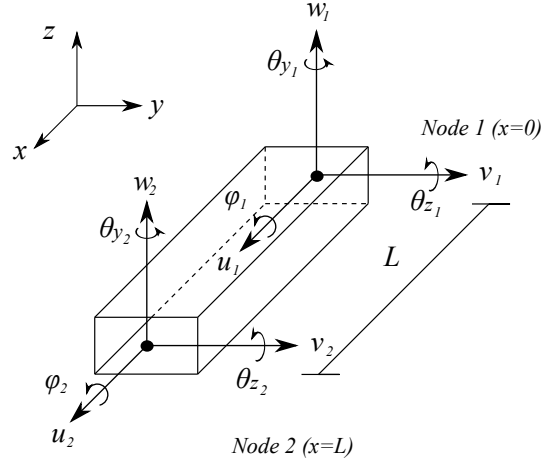
Fig. 3.1 Beam Element Reference System

3.2.1   Geometrical Effect (BTCE-GE)

The BTCE stiffness and mass matrices $[K_{el}]$ and $[M_{el}]$ can be obtained through Galerkin's method following the procedure described in the second chapter of this thesis. The BTCE formulation allows to consider the bending-torsion coupling given by oriented fibres or stiffeners for a slender box-beam in CAS configuration. This coupling is obtained through the shape functions reported in Table 2.2 derived with the hypothesis of the constant torsional moment along the beam element. To perform a dynamic analysis of a pre-deformed structure considering only the geometrical effects, the beam can be discretized in finite elements with position and orientation given by a known equilibrium configuration. This can be achieved with the rotation of the mass and stiffness matrices with an opportune transformation matrix $[T]$ defined in Equation (3.1):

$$[T] = \begin{bmatrix} T_{11} & T_{12} & T_{13} \\ T_{21} & T_{22} & T_{23} \\ T_{31} & T_{32} & T_{33} \end{bmatrix} \qquad (3.1)$$

The members T_{ij} for an inextensible beam are reported in Equation (3.2) according to the derivation presented in [77]. The T_{ij} are obtained with Taylor's expansion truncated at the second order, this introduces the hypothesis of moderate-to-large deformations with deflections between 10% and 15% of the beam length. This

correspond to a 2-5 meters deflection considering the wingspan of typical HARW which can range from 39 m (RHEA-Short Range) to 62 m (RHEA-Mid Range).

$$
\begin{cases}
T_{11} = 1 - \dfrac{1}{2}v'^2 - \dfrac{1}{2}w'^2 \\[2mm]
T_{12} = v' \\[2mm]
T_{13} = w' \\[2mm]
T_{21} = -v' - w'\varphi \\[2mm]
T_{22} = 1 - \dfrac{1}{2}v'^2 - \dfrac{1}{2}\varphi^2 \\[2mm]
T_{23} = \varphi \\[2mm]
T_{31} = -w' + \varphi v' \\[2mm]
T_{32} = -\varphi - v'w' \\[2mm]
T_{33} = 1 - \dfrac{1}{2}w'^2 - \dfrac{1}{2}\varphi^2
\end{cases}
\tag{3.2}
$$

v, w, and φ are the displacement variables function of the coordinate x. The known deformed configuration can be denoted with v_0, w_0, and φ_0. For a two-node finite element represented in Figure 3.1, the equilibrium deformation can be expressed as the product of shape functions times the nodal degrees of freedom of the element as represented in Equation (3.3), the suffix 0 denotes the equilibrium value of the degree of freedom.

$$
\begin{cases}
w_0(x) = N_{w1}(x)w_{01} + N_{w2}(x)\theta_{y01} + N_{w3}(x)w_{02} + N_{w4}(x)\theta_{y02} \\[2mm]
v_0(x) = N_{v1}(x)v_{01} + N_{v2}(x)\theta_{z01} + N_{v3}(x)v_{02} + N_{v4}(x)\theta_{z02} \\[2mm]
\varphi_0(x) = N_{\varphi1}(x)\varphi_{01} + N_{\varphi2}(x)w_{01} + N_{\varphi3}(x)\theta_{y01} + N_{\varphi4}(x)\varphi_{02} + N_{\varphi5}(x)w_{02} + \\[2mm]
\qquad + N_{\varphi6}(x)\theta_{y02}
\end{cases}
\tag{3.3}
$$

Substituting Equation (3.3) into Equation (3.2), the transformation matrix is obtained for each element of the structure. However, the members T_{ij}, vary along the beam element length. The orientation of the element can be obtained by evaluating the T_{ij} at the first node of the beam element. This procedure introduces the hypothesis that the deformations along the element are negligible and can be considered straight. Once the matrix $[T]$ is obtained, the finite element mass and stiffness matrices

in local coordinates $[K_{el}]$ and $[M_{el}]$ can be rotated according to the orientation of the deformed structure with Equations (3.4) and (3.5). The oriented element can be assembled to solve the eigenvalue problem (3.6) computing the corresponding eigenvectors solution of Equation (3.7) with the global stiffness and mass matrices $[K_g]$ and $[M_g]$.

$$[K_g] = [T]^T [K_{el}][T] \tag{3.4}$$

$$[M_g] = [T]^T [M_{el}][T] \tag{3.5}$$

$$det\left([K_g] - \omega_n^2 [M_g]\right) = 0 \tag{3.6}$$

$$([K_g] - \omega_n^2 [M_g])\phi_n = 0 \tag{3.7}$$

3.2.2   Introduction of Stiffness Effect (BTCE-NL)

The second model developed in this chapter takes into account the stiffness effect of an equilibrium-deformed configuration. Consider a uniform straight orthotropic inextensible beam, the Cartesian coordinate system xyz describes the undeformed geometry, and the Cartesian system $\xi\eta\zeta$ describes the deformed geometry (Figure 3.2). The derivation uses the generalized Hamilton's Principle reported in Equation (3.8).

$$\int_{t_1}^{t_2} \left(\partial T - \partial \pi + \partial W_{nc}\right) dt = 0 \tag{3.8}$$

$$\partial w(x,t) = 0 \quad t = t_1, t_2 \tag{3.9}$$

$$\partial v(x,t) = 0 \quad t = t_1, t_2 \tag{3.10}$$

$$\partial \phi(x,t) = 0 \quad t = t_1, t_2 \tag{3.11}$$
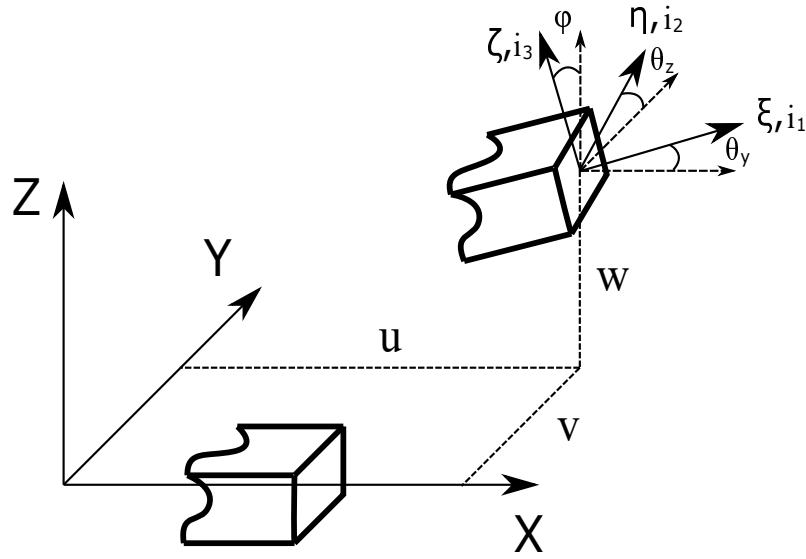
Fig. 3.2 Beam Reference System

where ∂T is the kinetic energy and ∂W_{nc} are the non conservative terms. The variation of the elastic energy $\partial \pi$ can be written as in Equation (3.12) according to [77].

$$\partial \pi = \int_0^L (M_1 \partial \rho_1 + M_2 \partial \rho_2 + M_3 \partial \rho_3)\, ds = 0 \qquad (3.12)$$

with the moment resultants:

$$\begin{cases} M_1 = GJ\rho_1 + K\rho_2 \\ M_2 = EI_2\rho_2 + K\rho_1 \\ M_3 = EI_3\rho_3 \end{cases} \qquad (3.13)$$

The curvatures ρ_1, ρ_2 and ρ_3 are obtained from the transformation matrix [T] according to [77] with a Taylor expansion truncated at the second order.

$$\begin{cases} \rho_1 = \varphi' + v''w' \\ \rho_2 = -w'' + v''\varphi \\ \rho_3 = v'' + w''\varphi \end{cases} \qquad (3.14)$$

the assumption that allows to obtain linear equations is to consider the displacement variables as the sum of an equilibrium term denoted with the suffix 0 and a perturbation term.

$$\begin{cases} \varphi = \varphi_0 + \tilde{\varphi} \\ w = w_0 + \tilde{w} \\ v = v_0 + \tilde{v} \end{cases} \tag{3.15}$$

substituting Equation (3.15) in Equation (3.14) and neglecting the equilibrium terms, Equation (3.14) becomes:

$$\begin{cases} \rho_1 = \tilde{\varphi}' + v_0'' \tilde{w}' + w_0' \tilde{v}'' \\ \rho_2 = -\tilde{w}'' + v_0'' \tilde{\varphi} + \varphi_0 \tilde{v}'' \\ \rho_3 = \tilde{v}'' + w_0'' \tilde{\varphi} + \varphi_0 \tilde{w}'' \end{cases} \tag{3.16}$$

the differential of the curvatures can be written as:

$$\begin{cases} \partial \rho_1 = \partial \tilde{\varphi}' + v_0'' \partial \tilde{w}' + w_0' \partial \tilde{v}'' \\ \partial \rho_2 = \partial (-\tilde{w})'' + v_0'' \partial \tilde{\varphi} + \varphi_0 \partial \tilde{v}'' \\ \partial \rho_3 = \partial \tilde{v}'' + w_0'' \partial \tilde{\varphi} + \varphi_0 \partial \tilde{w}'' \end{cases} \tag{3.17}$$

With these considerations is it possible to substitute Equation (3.16) and Equation (3.17) into Equation (3.12). Considering only the perturbation terms it is possible to obtain Equation (3.18). The three members of Equation (3.12) are presented separately for the sake of clarity.

$$\begin{cases} M_1 \partial \rho_1 = \left[GJ \left(\tilde{\varphi}' + v_0'' \tilde{w}' + w_0' \tilde{v}'' \right) + K(-\tilde{w}' + v_0'' \tilde{\varphi} + \varphi_0 \tilde{v}'') \right] \partial \rho_1 \\ M_2 \partial \rho_2 = \left[EI_2(-\tilde{w}'' + v_0'' \tilde{\varphi} + \varphi_0 \tilde{v}'') + K(\tilde{\varphi}' + v_0'' \tilde{w}' + w_0' \tilde{v}'') \right] \partial \rho_2 \\ M_3 \partial \rho_3 = \left[EI_3(\tilde{v}'' + w_0'' \tilde{\varphi} + \varphi_0 \tilde{w}'') \right] \partial \rho_3 \end{cases} \tag{3.18}$$

Equation (3.18) can be written in matrix form as

$$
\begin{cases}
M_1 \partial \rho_1 = \{\partial \tilde{d}\}\{\ 1 \quad 0 \quad w_0' \quad v_0'' \quad 0\ \}^T \{\ GJ \quad K \quad GJw_0' + K\varphi_0 \quad GJv_0'' \quad Kv_0'' \ \}\{\tilde{d}\}^T \\
M_2 \partial \rho_2 = \{\partial \tilde{d}\}\{\ 0 \quad 1 \quad \varphi_0 \quad 0 \quad v_0'' \ \}^T \{\ K \quad EI_2 \quad EI_2\varphi_0 + Kw_0' \quad Kv_0'' \quad EI_2v_0'' \ \}\{\tilde{d}\}^T \\
M_3 \partial \rho_3 = \{\partial \tilde{d}\}\{\ 0 \quad -\varphi_0 \quad 1 \quad 0 \quad w_0'' \ \}^T \{\ 0 \quad -EI_3\varphi_0 \quad EI_3 \quad 0 \quad EI_3w_0'' \ \}\{\tilde{d}\}^T
\end{cases}
$$

$$(3.19)$$

with $\{\partial \tilde{d}\}$ and $\{\tilde{d}\}$ defined as in Equations (3.20) and (3.21)

$$
\{\partial \tilde{d}\} = \{\ \partial \tilde{\varphi}' \quad \partial(-\tilde{w}'') \quad \partial \tilde{v}'' \quad \partial \tilde{w}' \quad \partial \tilde{\varphi}\ \} \tag{3.20}
$$

$$
\{\tilde{d}\} = \{\ \tilde{\varphi}' \quad (-\tilde{w}'') \quad \tilde{v}'' \quad \tilde{w}' \quad \tilde{\varphi}\ \} \tag{3.21}
$$

the vectors containing only equilibrium terms can be multiplied obtaining:

$$\begin{cases} M_1 \partial \rho_1 = \{\partial \tilde{d}\} \begin{bmatrix} GJ & K & GJw_0' + K\varphi_0 & GJv_0'' & Kv_0'' \\ 0 & 0 & 0 & 0 & 0 \\ GJw_0' & Kw_0' & w_0'(GJw_0' + K\varphi_0) & GJv_0''w_0' & Kv_0''w_0' \\ GJv_0'' & Kv_0'' & v_0''(GJw_0' + K\varphi_0) & GJ(v_0'')^2 & K(v_0'')^2 \\ 0 & 0 & 0 & 0 & 0 \end{bmatrix} \{\tilde{d}\}^T \\[3em] M_2 \partial \rho_2 = \{\partial \tilde{d}\} \begin{bmatrix} 0 & 0 & 0 & 0 & 0 \\ K & EI_2 & EI_2\varphi_0 + Kw_0' & Kv_0'' & EI_2v_0'' \\ K\varphi_0 & EI_2\varphi_0 & \varphi_0(EI_2\varphi_0 + Kw_0') & Kv_0''\varphi_0 & EI_2v_0''\varphi_0 \\ 0 & 0 & 0 & 0 & 0 \\ Kv_0'' & EI_2v_0'' & v_0''(EI_2\varphi_0 + Kw_0') & K(v_0'')^2 & EI_2(v_0'')^2 \end{bmatrix} \{\tilde{d}\}^T \\[3em] M_3 \partial \rho_3 = \{\partial \tilde{d}\} \begin{bmatrix} 0 & 0 & 0 & 0 & 0 \\ 0 & -EI_3\varphi_0^2 & -EI_3\varphi_0 & 0 & -EI_3w_0''\varphi_0 \\ 0 & -EI_3\varphi_0 & EI_3 & 0 & EI_3w_0'' \\ 0 & 0 & 0 & 0 & 0 \\ 0 & -EI_3\varphi_0w_0'' & EI_3w_0'' & 0 & EI_3(w_0'')^2 \end{bmatrix} \{\tilde{d}\}^T \end{cases}$$

$$(3.22)$$

Equation (3.12) can be rewritten in the matrix form as:

$$\partial \pi = \int_0^L \{\partial \tilde{d}\}[\tilde{C}]\{\tilde{d}\}^T ds = 0 \qquad (3.23)$$

The matrix $[\tilde{C}]$ is obtained with the sum of the matrices in Equation (3.22).

$$
[\tilde{C}] = \begin{bmatrix}
GJ & K & GJw_0' + K\varphi_0 & GJv_0'' & Kv_0'' \\
 & EI_2 + EI_3\varphi_0^2 & EI_2\varphi_0 + Kw_0' - EI_3\varphi_0 & Kv_0'' & EI_2v_0'' - EI_3w_0''\varphi_0 \\
 & & EI_3 + GJ(w_0')^2 + K\varphi_0w_0' + EI_2(\varphi_0)^2 + Kw_0'\varphi_0 & GJv_0''w_0' + Kv_0'\varphi_0 & EI_2v_0''\varphi_0 + EI_3w_0'' + Kv_0''w_0' \\
 & & & GJ(v_0'')^2 & K(v_0'')^2 \\
 & & & & EI_2(v_0'')^2 + EI_3(w_0'')^2
\end{bmatrix}
$$

$$(3.24)$$

The displacement variables can be expressed as a set of space-dependent shape functions $[N(x)]$ which multiplies the time-dependent nodal degrees of freedom $\{\tilde{q}\}$. In this case, the shape functions used are the ones that include the bending torsion coupling derived in the previous chapter and reported in Table 2.2.

$$
\tilde{d} = [N(x)]\{\tilde{q}(t)\}^T \tag{3.25}
$$

Substituting the shape functions into equation (3.23) it can be rewritten as:

$$
\partial \pi = \partial \{\tilde{q}\} \left(\int_0^L [N(x)]^T [\tilde{C}][N(x)] ds \right) \{\tilde{q}\}^T = 0 \tag{3.26}
$$

where the non-linear stiffness matrix is expressed as:

$$
[\tilde{K}] = \left(\int_0^L [N(x)]^T [\tilde{C}][N(x)] ds \right) \tag{3.27}
$$

The result of the integral reported in equation 3.27 is a 10×10 symmetric matrix dependent on the equilibrium configuration nodal displacements and rotations. A symbolic calculator can give the exact equations for the member of the matrix which are not reported in this thesis due to their extension. A known equilibrium configuration can be used to compute the non-linear stiffness matrix $[\tilde{K}]$ and solve the eigenvalue problem by computing the corresponding eigenvector solution of the equations. The mass matrix $[M]$ can be assembled using the linear BTCE formulation since the effect of non-linear terms is negligible.

Chapter 4

Equivalent Single Layer for Stiffened Panels

In this chapter, the Equivalent Single Layer (ESL) model developed by Danzi [96] is presented. The model can be applied to stiffened structures to obtain a layer with mechanical properties equivalent to the stiffeners. With this homogenization, it is possible to consider a symmetric stiffened panel as a laminate with orthotropic mechanical properties. However, the model was only validated for static analysis [97] and a dynamic analysis validation for the BTCE application was needed. The first part of the chapter briefly describes the ESL. The second part of the chapter presents an experimental validation of the ESL model.

4.1   Equivalent Single Layer Model

The bending torsion coupling effect can be achieved with oriented composite materials, but also with stiffened panels. However, for an efficient simulation, the stiffeners must be reduced to an ESL with equivalent mechanical properties. The stiffeners can be considered as an ESL with orthotropic properties following the work done

by Danzi et al. [96, 44, 97]. According to Nemeth [98], a kinematic equivalence is imposed between the strains of the stiffeners and the corresponding plate strains. Furthermore, the plate stresses resultants are related to the beam forces and moments with a static equivalence. The condition of kinematic and static equivalence is called direct compatibility. The variation of the stress resultants across the width of the stiffeners is considered negligible. The direct compatibility can be derived for a family of equally spaced rectilinear stiffeners with d_s being the stiffeners spacing and oriented with an angle Ψ_s with respect to the x-axis of the plate. The stiffeners are considered symmetric and perfectly bonded to the skin. In addition to direct compatibility, the bending of the stiffener in the plane parallel to the plate mid-plane is considered negligible and thus, the variation of the strains across the width of the ESL can be neglected. Furthermore, it is presumed that the eccentric stiffener contributes only half of the in-plane shearing strain and half of the change in the surface twist of the equivalent stiffener layer. To establish the static equivalence between the repetitive stiffened panel and the equivalent plate elements, the stress resultants of the equivalent plate have to be equal to the beam forces and moments of the beam following Timoshenko's hypothesis for the straight beam. After some algebraic manipulation, the stress resultants of the stiffeners layer can be written as:

$$N_x^{stiff} = \frac{E_s A_s}{d_s}\left(\varepsilon_{xx}^0 + \bar{z}k_{xx}\right) \qquad N_{xy}^{stiff} = \frac{k_y G_s A_s}{d_s}\left(\gamma_{xy}^0 + \bar{z}k_{xy}\right)$$

$$M_x^{stiff} = \frac{E_s A_s \bar{z}}{d_s}\left(\varepsilon_{xx}^0 + \frac{E_s I_{yy}}{d_s}\bar{z}k_{xx}\right) \quad M_{xy}^{stiff} = \frac{k_y G_s A_s \bar{z}}{2d_s}\gamma_{xy}^0 + \frac{G_s J_t}{2d_s}k_{xy} \qquad (4.1)$$

$$Q_{xz}^{stiff} = \frac{k_z G_s A_s}{d_s}\gamma_{xy}^0$$

The constitutive equations for the stiffeners in terms of the strain expressed in the equivalent plate can be written as follows:

$$\left\{\begin{array}{c} N_x \\ N_y \\ N_{xy} \end{array}\right\} = \left[\begin{array}{ccc} \dfrac{E_s A_s}{d_s} & 0 & 0 \\ 0 & 0 & 0 \\ 0 & 0 & \dfrac{k_y G_s A_s \bar{z}}{4d_s} \end{array}\right] \left\{\begin{array}{c} \varepsilon_{xx}^0 \\ \varepsilon_{yy}^0 \\ \gamma_{xy}^0 \end{array}\right\} + \left[\begin{array}{ccc} \dfrac{E_s A_s \bar{z}}{d_s} & 0 & 0 \\ 0 & 0 & 0 \\ 0 & 0 & \dfrac{k_y G_s A_s \bar{z}}{4d_s} \end{array}\right] \left\{\begin{array}{c} k_{xx}^0 \\ k_{yy}^0 \\ k_{xy}^0 \end{array}\right\} \qquad (4.2)$$

$$
\begin{Bmatrix} M_x \\ M_y \\ M_{xy} \end{Bmatrix} = \begin{bmatrix} \dfrac{E_s A_s \bar{z}}{d_s} & 0 & 0 \\ 0 & 0 & 0 \\ 0 & 0 & \dfrac{k_y G_s A_s \bar{z}}{4 d_s} \end{bmatrix} \begin{Bmatrix} \varepsilon_{xx}^0 \\ \varepsilon_{yy}^0 \\ \gamma_{xy}^0 \end{Bmatrix} + \begin{bmatrix} \dfrac{E_s I_s}{d_s} & 0 & 0 \\ 0 & 0 & 0 \\ 0 & 0 & \dfrac{G_s J_t}{24} \end{bmatrix} \begin{Bmatrix} k_{xx}^0 \\ k_{yy}^0 \\ k_{xy}^0 \end{Bmatrix} \quad (4.3)
$$

$$
\begin{Bmatrix} Q_{xy} \\ Q_{xz} \end{Bmatrix} = \begin{bmatrix} 0 & 0 \\ 0 & \dfrac{k_y G_s A_s}{2 d_s} \end{bmatrix} \begin{Bmatrix} \gamma_{xz} \\ \gamma_{yz} \end{Bmatrix} \quad (4.4)
$$

Finally, a rotation must be performed to align the beam reference system to the plate reference system (x, y, z), then one can obtain the expression of the stiffness matrices of the usual Reissner-Mindlin plate:

$$
\overline{Q}_{11}^{stiff} = \frac{E_s b_s}{d_s} \cos^2 \Psi_s \left(\cos^2 \Psi_s + \tau_y^s \sin^2 \Psi_s \right)
$$

$$
\overline{Q}_{12}^{stiff} = \frac{E_s b_s}{d_s} \cos^2 \Psi_s \sin^2 \Psi_s \left(1 - \tau_y^s \right)
$$

$$
\overline{Q}_{16}^{stiff} = \frac{E_s b_s}{d_s} \cos \Psi_s \sin \Psi_s \left(\cos^2 \Psi_s - \frac{\tau_y^s}{2} \cos 2\Psi_s \right)
$$

$$
\overline{Q}_{22}^{stiff} = \frac{E_s b_s}{d_s} \sin^2 \Psi_s \left(\sin^2 \Psi_s + \tau_y^s \cos^2 \Psi_s \right)
$$

$$
\overline{Q}_{26}^{stiff} = \frac{E_s b_s}{d_s} \cos \Psi_s \sin \Psi_s \left(\sin^2 \Psi_s + \frac{\tau_y^s}{2} \cos 2\Psi_s \right) \quad (4.5)
$$

$$
\overline{Q}_{66}^{stiff} = \frac{E_s b_s}{d_s} \left(\cos^2 \Psi_s \sin^2 \Psi_s + \frac{\tau_y^s}{4} \cos^2 \Psi_s \right)
$$

$$
\overline{Q}_{44}^{stiff} = \frac{E_s b_s \tau_z^{stiff}}{d_s} \sin^2 \Psi_s
$$

$$
\overline{Q}_{45}^{stiff} = \frac{E_s b_s \tau_z^{stiff}}{d_s} \sin \Psi_s \cos \Psi_s
$$

$$
\overline{Q}_{55}^{stiff} = \frac{E_s b_s \tau_z^{stiff}}{d_s} \cos^2 \Psi_s
$$

Where $\tau_y^s = \dfrac{k_y^2 G_s}{E_s}$, $\tau_z^s = \dfrac{k_z^2 G_s}{E_s}$ are the in-plane and transverse shear-deformation parameters, k_y^2 and k_z^2 are the respective correction factor, E_s is the Young's Modulus of the stiffener, b_s and d_s are the stiffeners width and spacing respectively. It should be noted that the resulting matrix $\left[\overline{Q}\right]$ for the straight stiffener is singular; particularly, from the equation in (2) is worth noting that, the rank is 2. If one aims to derive the equivalent properties of the UD material, one has:

$$E_{11} = \left(\frac{E_s b_s}{d_s}\right)_{el-12}; \; E_{22} = 0; \; \nu_{12} = 0; \; G_{12} = \frac{\tau_y^s}{4}\left(\frac{E_s b_s}{d_s}\right)_{el-12}; \; G_{13} = \tau_z^s\left(\frac{E_s b_s}{d_s}\right)_{el-12}; \; G_{23} = 0$$

$$(4.6)$$

Further details concerning equations (4.1)-(4.6), can be found in [96] and [98].

4.2 ESL Dynamic Validation

The validation of the ESL for the dynamic analysis consisted of the application of the ESL to a SHELL Model (EQM from hereinafter) of a metal-stiffened structure. The characteristic frequencies obtained with the EQM have been compared with numerical and experimental results. Moreover, a composite structure has been tested with a similar procedure to show that the coupling effect introduced with oriented composite fibers is similar to the one obtained with oriented stiffeners.

4.2.1 Box-Beam Stiffened Structure

The first structure considered is an aluminum beam represented in Figure 4.1 and presented in [97]. The beam is composed of two stiffened symmetric panels with stiffeners oriented at $25°$ glued to two C-shaped spars with constant cross-sections 20 *mm*, 40 *mm* wide, and with a thickness equal to 2 *mm*. The stiffened panels are 2 *mm* thick and 50 *mm* wide, with symmetric rectangular stiffeners with base $b_s = 3 \, mm$ and height $h_s = 4 \, mm$. The number of stiffeners is $N_s = 6$ defining a ratio $d_s = b/N_s = 8.33$. The beam is 1200 *mm* long, but 100 *mm* are used to constrain the structure, and thus the useful length is 1100 *mm*. The material is a 6060 aluminum alloy with mechanical properties reported in Table 4.1

Table 4.1 Al6060 mechanical and physical properties.

Property	Value
Young's Modulus, E [MPa]	58000
Shear Modulus, G [MPa]	21805
Poisson's ratio, ν	0.33
Mass Density, ρ $[kg/dm^3]$	2.66
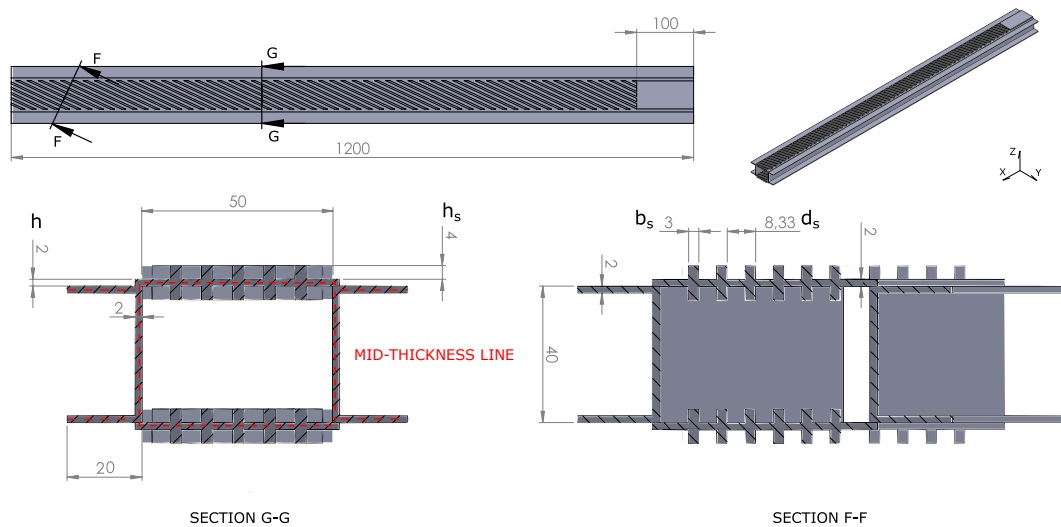
Fig. 4.1 Aluminium Stiffened Beam

Dynamic numerical and experimental tests have been performed on real and digital models of the structure with cantilever configuration. The finite element model which includes the ESL formulation is a SHELL model of the aluminum box-beam with the stiffened panels modeled as laminates. The equivalent mechanical properties of the ESL can be computed with Equation 4.6 and are reported in Table 4.2. The results of a modal analysis obtained with the EQM have been tested against experimental results and against a TETRA4 finite element model with a full representation of the stiffeners. The finite element models have been constrained imposing all the nodal displacements equal to zero for the nodes highlighted in Figure 4.2B.

Table 4.2 Equivalent Single Layer Material Properties.

Property	Value
Longitudinal Young's Modulus, E_1 [MPa]	20,888.36
Transverse Young's Modulus, E_2 [MPa]	0
Shear Modulus, G_{12} [MPa]	1636.03
Poisson's ratio, ν	0
Mass Density, ρ [kg/dm^3]	0.99
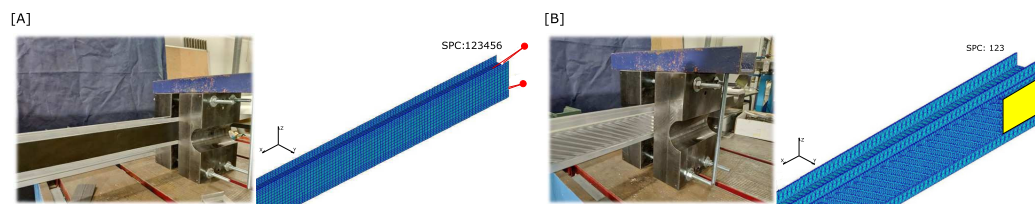
Fig. 4.2 Experimental and numerical boundary conditions

4.2.2 Box-Beam Composite Structure

The second beam presented the same configuration already considered by Cestino et. al [99] for static analysis. The structure represented in Figure 4.3 presents two carbon fiber reinforced polymer (CRFP) panels with four unidirectional (UD) T700 carbon/epoxy prepreg layers with fibers oriented at 18°. The total thickness is 1 *mm*. The lateral plates are obtained with C-shaped spars of 6060 aluminum alloy with section 20 *mm* high, 40 *mm* wide, and thickness equal to 2 *mm*. The mechanical properties of the carbon/epoxy prepreg are reported in Table 4.3. The beam is 1450 *mm* long with bolted metal extensions which allow to constraint of the beam without useful length penalties.

The experimental results for the composite beam have been tested against a SHELL finite element model with composite panels described by a laminate model. The finite element model has been constrained with the rigid body element which connects the nodes corresponding to the position of the bolts to two fixed points as represented in Figure 4.2A.
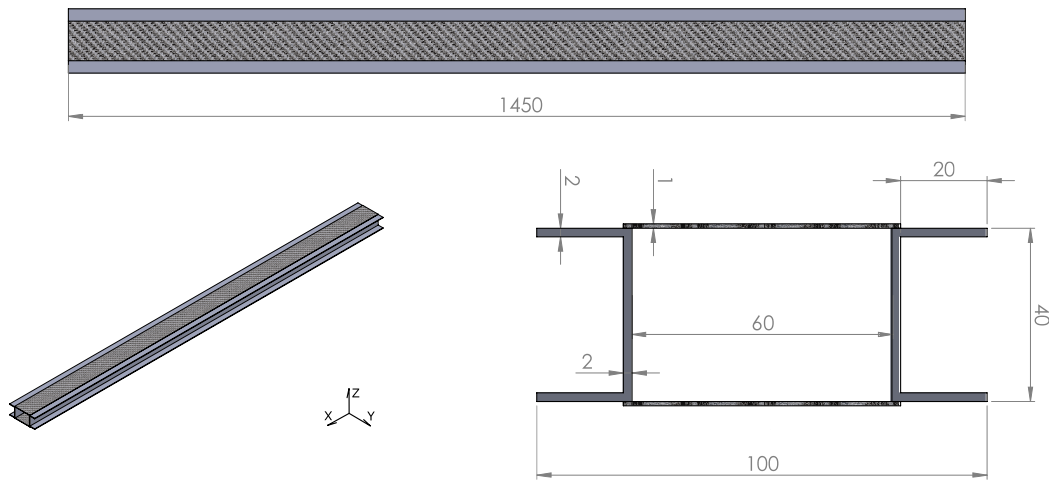
Fig. 4.3 UD Carbon FRP Beam - Geometry and dimension in mm

Table 4.3 UD T700/Epoxy mechanical and physical properties.

Property	Value
Longitudinal Young's Modulus, E1 [MPa]	118000
Transverse Young's Modulus, E2 [MPa]	9938
Shear Modulus, G12 [MPa]	3400
Poisson's ratio, v	0.33
Mass Density, ρ $[kg/dm^3]$	1.60

4.2.3 Experimental Procedure

The dynamic behavior of the two beams has been investigated with an experimental modal analysis. For this experimental test, a Laser Doppler Vibrometer (LDV) apparatus has been used. LDV uses the Doppler effect of a laser beam reflected by a vibrating surface to determine its speed during a period of time. This technology is particularly interesting for experimental modal analysis due to the absence of contacts and additional masses. However, some drawbacks are represented by the constraint imposed by the mutual position of the test component and the laser scanning head. The device used is a Polytec PSV-500 scanning laser head with a control box and a signal amplifier. The excitation of the beam was given by an electrodynamic shaker K200xE01 and measured with a load cell. The measurement chain, represented in Figure 4.4, consists of an input signal generated by the control box and managed by the PSV software. The signal is amplified and sent to the electrodynamic shaker. An impedance head is installed between the shaker and the test piece with cyanoacrylate

Table 4.4 Experimental parameters used for modal testing

Property	Aluminium Beam	Carbon UD FRP Beam
Resolution Points	36	34
Frequency Span [kHz]	0-2	0-2
Window Span [kHz]	0-1	0-1
Spectral Lines	6400	6400
Averaging Complex	8	8
Shaker Amplitude [V]	0.025	0.1
Vibrometer Sensibility [mm/s]	50	100

glue and it provides acceleration and force signal to the LDV front-end. The sample vibrations are measured in predetermined scanning points on the beam structure, multiple scanning points allow to capture the dynamic behavior of the tested structure. After a single scanning cycle, the PSV software computes the resulting frequency response function (FRF) and sends it to the PC for visualization and storage.

The excitation of the test piece is obtained through a periodic chirp signal, which consists of a continuous sweep in a defined frequency range. The frequency range was set based on the FE simulations in order to observe all the modes relevant to the experimental activity. For each scanning point, the system repeats the data acquisition as many times as the number of complex averages chosen. With this method, the data are cleaned from eventual noise. Two different experimental sessions are prepared for the box beam: TEST1 and TEST2. The shaker was fixed to an independent aluminum rigid frame which was positioned behind the beam structure at a distance indicated in Table 4.5. The experimental parameters used during the experimental modal analysis are listed in Table 4.4.

Table 4.5 Shaker position from clamped end

Beam	TEST1: Position [mm]	TEST2: Position [mm]
Aluminium	1120	700
Carbon FRP	1450	960
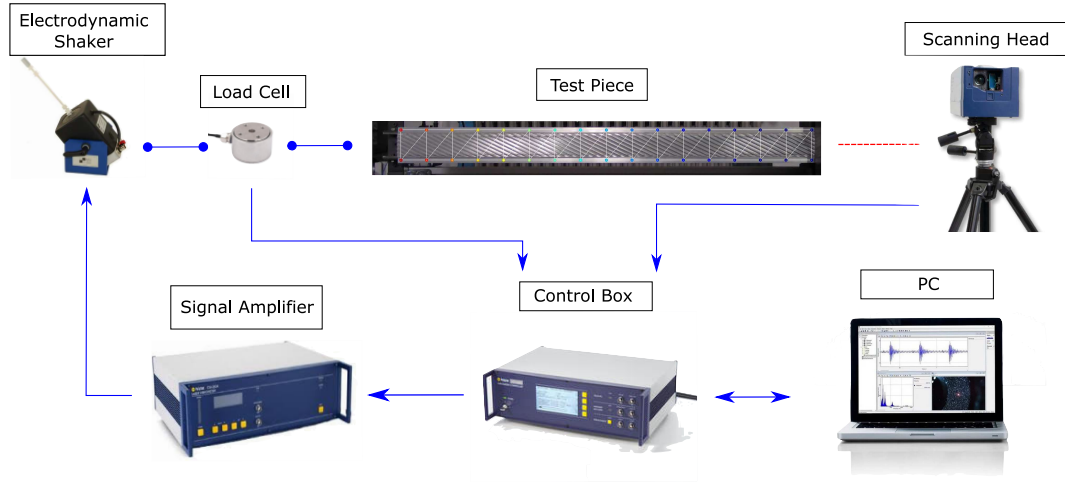
Fig. 4.4 Measurement Chain

The experimental results are compared with the numerical ones in terms of natural frequencies and mode shapes. the natural frequencies prediction accuracy is evaluated by computing the relative difference with equation 5.6. The mode shapes are compared with the Modal Assurance Criterion (MAC). MAC is a statistical indicator used to evaluate the similarity between two sets of mode shapes. A value equal to one indicates complete similarity, while a value equal to zero indicates no similarity [100, 95]. The MAC value for the *i*-th mode of the mode set *A* and the *j*-th mode of the mode set *B* is given by equation 4.7.

$$MAC_{ij} = \frac{|\Phi_A^{iT}\Phi_B^{j}|^2}{\left(\Phi_A^{iT}\Phi_A^{j}\right)\left(\Phi_B^{iT}\Phi_B^{j}\right)} \tag{4.7}$$

4.2.4   Box-Beam Stiffened Structure Results

The test with the excitation at the tip of the beam (TEST1) revealed four global vibration modes below 600 Hz in accordance with the numerical simulations. The experimental and numerical Frequency Response Functions (FRF) are reported in Figure 4.5. However, the peak between 400 Hz and 500 Hz revealed a mode shape inconsistent with the boundary conditions applied. This anomaly is probably connected to the reduced number of scanning points chosen or to a not perfect constraint which can affect the accuracy of the measurement. On the other hand, a higher number of scanning points increases the acquisition time. Moreover, the

scanning points are positioned on the free portion of the C-shaped spars and this could cause the detection of local modes. Another discrepancy is related to the failed detection of the torsional mode, expected close to 400 Hz according to the numerical simulations. This was probably caused by the position of the shaker exciting at the center of the structure and thus preventing the torsional degree of freedom excitation.

The second test with the shaker positioned at 700 mm from the clamped edge gave better results. In this case, the torsional mode was correctly captured, but the anomaly already discussed in the previous paragraph was still present.
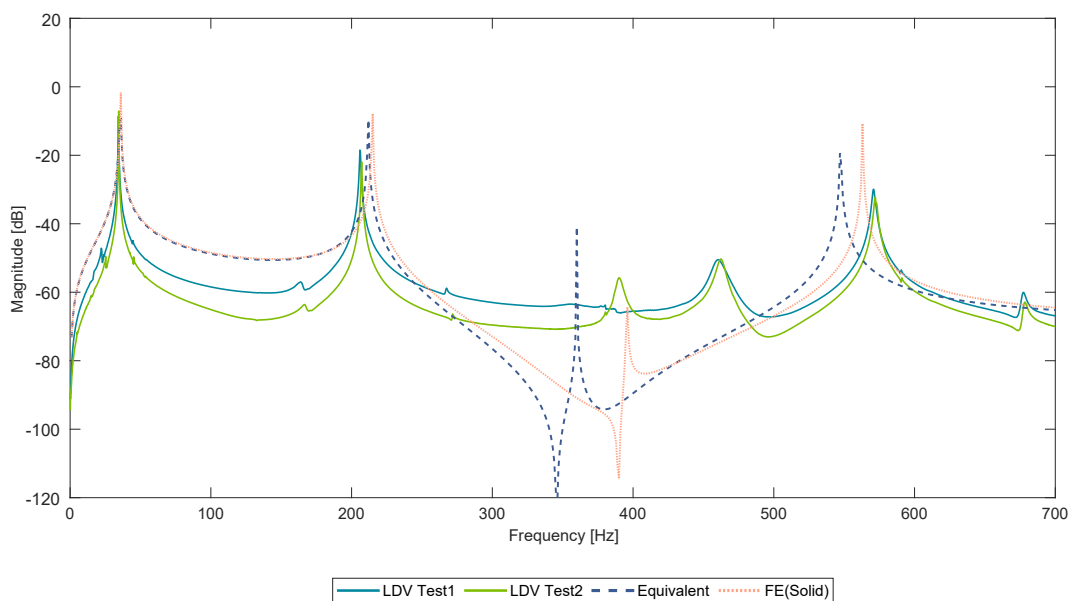
Fig. 4.5 FRF Comparison for Box-Beam Stiffened Structure

The frequencies obtained during the second test have been compared to the frequencies obtained with the EQM and the TETRA4 model, the results are reported in Table 4.6. The relative errors between the TETRA4 model and experimental modal frequency are less than 4%. The EQM predicted characteristic frequencies within the 5% of relative error if compared to the experimental results. The torsional mode frequency was slightly underestimated and presented a relative error equal to 7.59%. This difference is due to the ESL approximation which alters the behavior of the stiffeners.

The mode shapes obtained for the four modes are reported in Figure 4.6. The first, second, and fourth modes are bending modes coupled with torsion. It is possible to observe that the fringe lines are inclined with respect to the vertical direction. The

Table 4.6 Natural frequencies [Hz] for the aluminum beam compared to numerical and EQM procedure.

	Aluminium Beam				
Mode	Experimental [Hz]	Num. SOLID [Hz]	Relative diff. [%]	Num. (EQM) [Hz]	Relative diff. [%]
1	34.53	35.82	3.74	35.59	3.07
2	206.90	214.80	3.82	211.77	2.35
3	390.25	395.44	1.33	360.62	7.59
4	571.10	563.14	1.39	547.54	4.12

third mode is a torsional mode with a small bending coupling. A more quantitative mode comparison is given by the MAC matrices reported in Figure 4.7. The matrices relative to TEST1 reveal that the anomaly is very similar in mode shape with the third bending mode due to the not-zero off-diagonal values. Moreover, the comparison with the EQM confirmed that no correlation exists between the observed anomaly and the numerical modes. The MAC matrices for TEST2 confirmed the accuracy of the EQM in predicting the experimental mode shapes which results coincident with the experimental results.
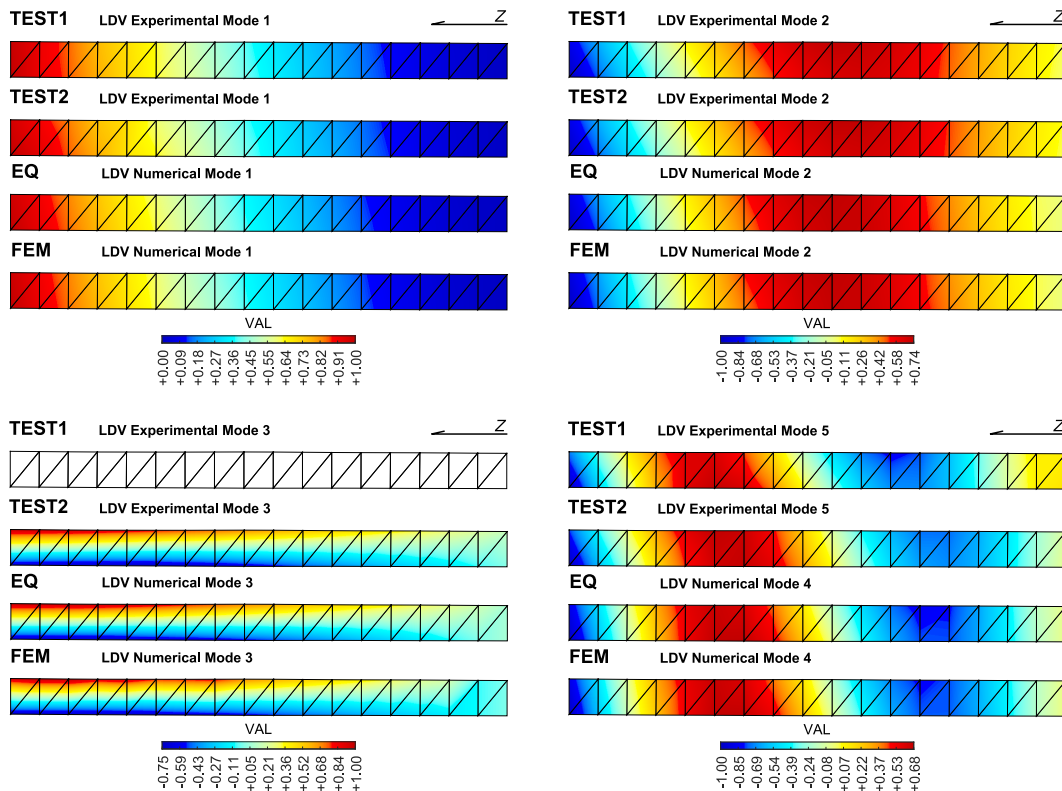
Fig. 4.6 Natural Mode Shape Comparison of the first modes of the aluminum beam: Every mode is compared with relative experimental, numerical, and equivalent model results.
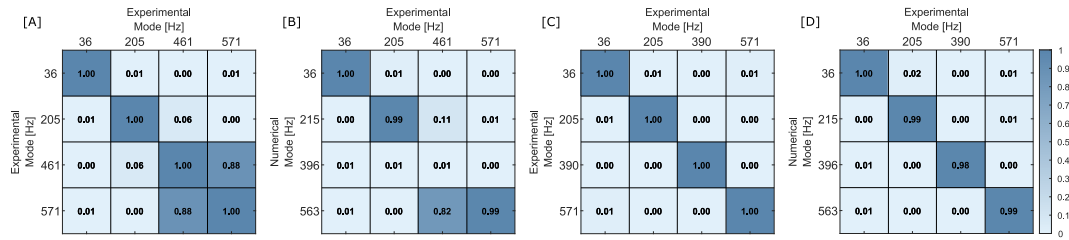
Fig. 4.7 MAC matrices for the comparison of mode shapes for aluminum beam. (A) Auto-MAC of TEST1 experimental modes, (B) MAC of TEST1 experimental and numerical modes, (C) Auto-MAC of TEST2 experimental modes, (D) MAC of TEST2 experimental and numerical modes.

4.2.5 Box-Beam Composite Structure Results

The experimental FRF curves are reported in Figure 4.8. The tests presented a similar FRF with a good correlation with the one obtained with the SHELL finite element model. Minor reported differences can be attributed to the hypothesis of perfectly glued components. This hypothesis brings over stiffness and causes the prediction of slightly higher frequencies of the natural modes. The FRF presents some noise after 300 Hz, this is related to the local vibrations of the carbon fiber panels and the chosen experimental parameters.
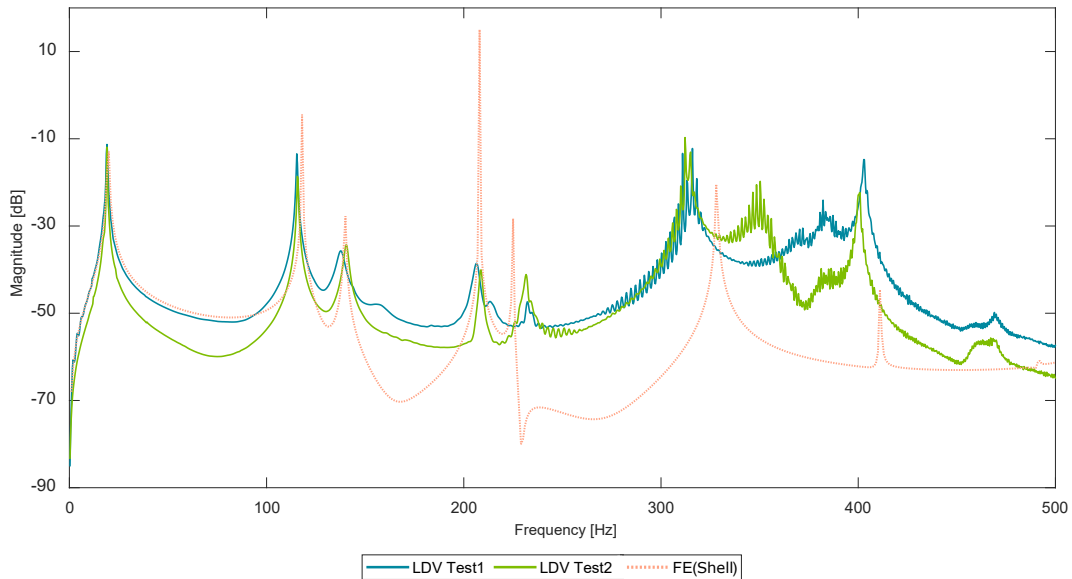
Fig. 4.8 FRF Comparison for Box-Beam Composite Structure

The frequencies obtained during TEST1 and TEST2 have been compared to the numerical results reported in Table 4.7. The measured natural frequencies presented a relative error lower than 4%.

Table 4.7 Natural frequencies [Hz] for an UD Carbon FRP beam compared to the numerical procedure. Relative difference with experimental frequency as reference value within parentheses.

	UD Carbon FRP Beam		
Mode	**Experimental [Hz]**	**Num. SHELL [Hz]**	**Relative diff. [%]**
1	19.06	19.65	3.10
2	115.30	118.05	2.39
3	140.15	139.71	0.31
4	207.50	208.00	0.24

The mode shapes represented in Figure 4.9 show a good correlation between experimental and numerical results. This is confirmed by the MAC matrices in Figure 4.10 that reveal complete agreement of the numerical results with TEST1 and TEST2. It is worth noting that the non-zero off-diagonal values indicate a certain degree of similarity between the third bending mode and the torsional mode.
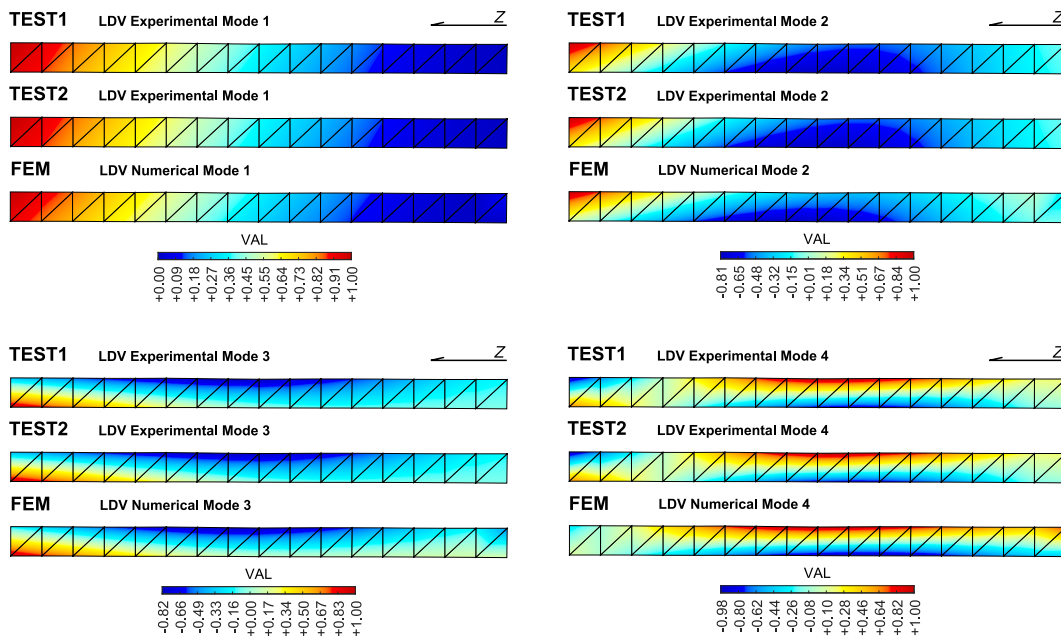
Fig. 4.9 Natural Mode Shape Comparison of the first modes of the UD carbon FRP beam: Every mode is compared with relative experimental and numerical results.
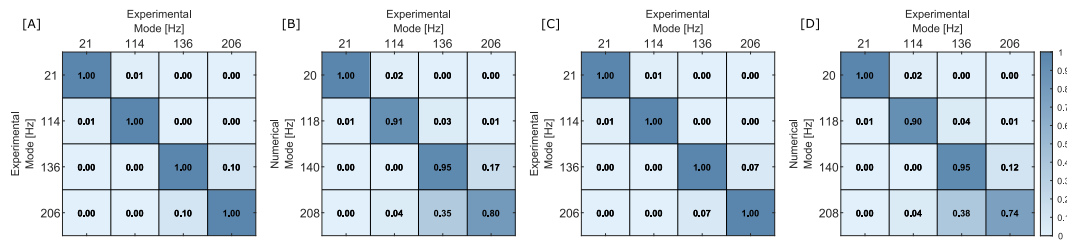
Fig. 4.10 MAC matrices for the comparison of mode shapes for UD carbon FRP beam. (A) Auto-MAC of TEST1 experimental modes, (B) MAC of TEST1 experimental and numerical modes, (C) Auto-MAC of TEST2 experimental modes, (D) MAC of TEST2 experimental and numerical modes.

4.3   Summary and Conclusions

The ESL model validation has been completed with the dynamic analysis validation. The ESL model, applied to an aluminum stiffened box-beam structure revealed a good level of accuracy for characteristic frequency prediction but also for the mode shapes. The torsional frequencies presented some differences with respect to the experimental results, these discrepancies can be attributed to the constraint modelization. The effect of constraint can be further investigated to assess the accuracy of the ESL for the torsional frequencies. These findings allow to apply the concept of ESL to the computation of thin-walled box-beam stiffness coefficients for dynamic analysis.

Chapter 5

BTCE Validation

Some of the contents and derivation presented in this chapter have been previously published in *Aerospace* 2023 and in *Journal of Vibration Technology* 2022.

C. Patuelli, E. Cestino, e G. Frulla, «A Beam Finite Element for Static and Dynamic Analysis of Composite and Stiffened Structures with Bending-Torsion Coupling», Aerospace, vol. 10, fasc. 2, p. 142, feb. 2023.

C. Patuelli, A. Polla, E. Cestino, e G. Frulla, «Experimental and Numerical Dynamic Behavior of Bending-Torsion Coupled Box-Beam», J. Vib. Eng. Technol., nov. 2022.

In this chapter, several numerical and experimental tests are presented. The BTCE has been tested for static and dynamic analysis of beam structures with different characteristics. The tests included composite and aluminum box-beam structures, variable stiffness structures, and oriented stiffeners panel structures. The first part of the chapter presents some of the relations and surrogate models applied for the simulation of the structures.

5.1 Circumferentially Asymmetric Stiffness Configuration

For a generic beam, the relation between the force resultants and the deformations can be derived as in [97], and expressed as:

$$\begin{Bmatrix} F_x \\ M_x \\ M_y \\ M_z \end{Bmatrix} = \begin{bmatrix} C_{00} & 0 & 0 & 0 \\ 0 & C_{11} & C_{12} & 0 \\ 0 & C_{12} & C_{22} & 0 \\ 0 & 0 & 0 & C_{33} \end{bmatrix} \begin{Bmatrix} \varepsilon_x \\ \rho_1 \\ \rho_2 \\ \rho_3 \end{Bmatrix} \tag{5.1}$$

The beam considered is a thin-walled beam with a closed cell section. The bending-torsion coupling effect is given by the oriented stiffeners. The stiffened panels can be considered as a laminate composed of two symmetric ESL with orthotropic properties and an isotropic aluminum mid-layer. According to the Classical Laminate Theory (CLT), the stiffness matrix can be divided into three sub-matrices called A, B, and D, where A represents the laminate extensional stiffness, B is the bending-stretching coupling stiffness and D is the laminate bending stiffness. The beam considered has a Circumferentially Asymmetric Configuration (CAS) and the stiffness coefficients can be computed with Equation 5.2.

$$C_{00} = \oint A_{11}^* ds \tag{5.2a}$$

$$C_{11} = \frac{4\Omega^2}{\oint \left(1/A_{66}^* \right) ds} + 4 \oint D_{66}^* ds \tag{5.2b}$$

$$C_{12} = 2\Omega \frac{\oint \left(A_{16}^*/A_{66}^* \right) z ds}{\oint \left(1/A_{66}^* \right) ds} - 2 \oint D_{16}^* \frac{dy}{ds} ds \tag{5.2c}$$

$$C_{22} = \oint z^2 \left(A_{11}^* - \frac{A_{16}^{*2}}{A_{66}^*} \right) ds + \frac{\left[\oint \left(A_{16}^*/A_{66}^* \right) z ds \right]^2}{\oint \left(1/A_{66}^* \right) ds} + \oint D_{11}^* \left(\frac{dy}{ds} \right)^2 ds \tag{5.2d}$$

$$C_{33} = \oint y^2 \left(A_{11}^* - \frac{A_{16}^{*2}}{A_{66}^*} \right) ds + \frac{\left[\oint \left(A_{16}^*/A_{66}^* \right) y ds \right]^2}{\oint \left(1/A_{66}^* \right) ds} + \oint D_{11}^* \left(\frac{dz}{ds} \right)^2 ds \tag{5.2e}$$

Ω is the area enclosed by the midline of the contour section according to the classical Bredt theory, A_{ij}^* and D_{ij}^* are the coefficient of the reduced laminate extensional stiffness matrix and reduced laminate bending stiffness matrix respectively. They are obtained from the coefficients of matrices [A] and [B] in the case of symmetric lamination with Equation (5.3) according to [97].

$$A^*_{11} = A_{11} - \frac{A^2_{12}}{A_{22}} \quad A^*_{16} = A_{16} - \frac{A_{12}A_{26}}{A_{22}} \quad A^*_{66} = A_{11} - \frac{A^2_{26}}{A_{22}}$$

(5.3)

$$D^*_{11} = D_{11} - \frac{D^2_{12}}{D_{22}} \quad D^*_{16} = D_{16} - \frac{D_{12}D_{26}}{D_{22}} \quad D^*_{66} = D_{66} - \frac{D^2_{26}}{D_{22}}$$

These relations allow to compute the mechanical properties of a CAS beam in the presence of laminates and composite materials. Stiffened symmetric panels can be considered as laminates as described in the previous chapter and therefore introduced for this class of structures. Moreover, the dynamic validation of the ESL model allows to extend its application also for dynamic analysis of CAS structures simulation.

5.2 Box-Beam Stiffened Structure

The first structure considered is an aluminum beam represented in Figure 4.1 and presented in [97]. The beam has been already described in the previous chapter where it was used for the dynamic analysis validation of the ESL model. However, a further step is the application of the concept of ESL to the computation of the stiffness of a beam element. At this scope, the stiffened panels have been considered as laminate with equivalent mechanical properties reported in Table 4.2 in order to obtain the corresponding laminate extensional and bending stiffness matrices. Then, with equations 5.3 and 5.2 the stiffness coefficients can be computed and applied to a BTCE element, with the exception of the axial stiffness due to the hypothesis of inextensibility.

Static and dynamic numerical and experimental tests have been performed on real and digital models of the structure with cantilever configuration. The BTCE model was obtained by assembling ten two-nodes beam finite elements with the presented formulation. The degrees of freedom of the first node have been imposed equal to zero for the cantilever configuration. The stiffness coefficients of the beam elements reported in Table 5.1 can be obtained with the procedure described in the previous paragraph. The BTCE model has been tested against two FE models solved with NASTRAN, the first model used solid TETRA10 elements for an exact geometric representation (Figure 5.1) while the second used SHELL elements with

the stiffened panels modeled as laminates and the stiffeners as an ESL. The finite element models have been constrained imposing all the degrees of freedom of nodes corresponding to the first 100 *mm* of the length equal to zero.

Table 5.1 Beam Section Stiffness Coefficients

Coefficient	Value [N mm^2]
C_{11}	5.79×10^9
C_{22}	1.41×10^{10}
C_{33}	2.17×10^{10}
C_{12}	1.44×10^9

(A)

(B)   (C)
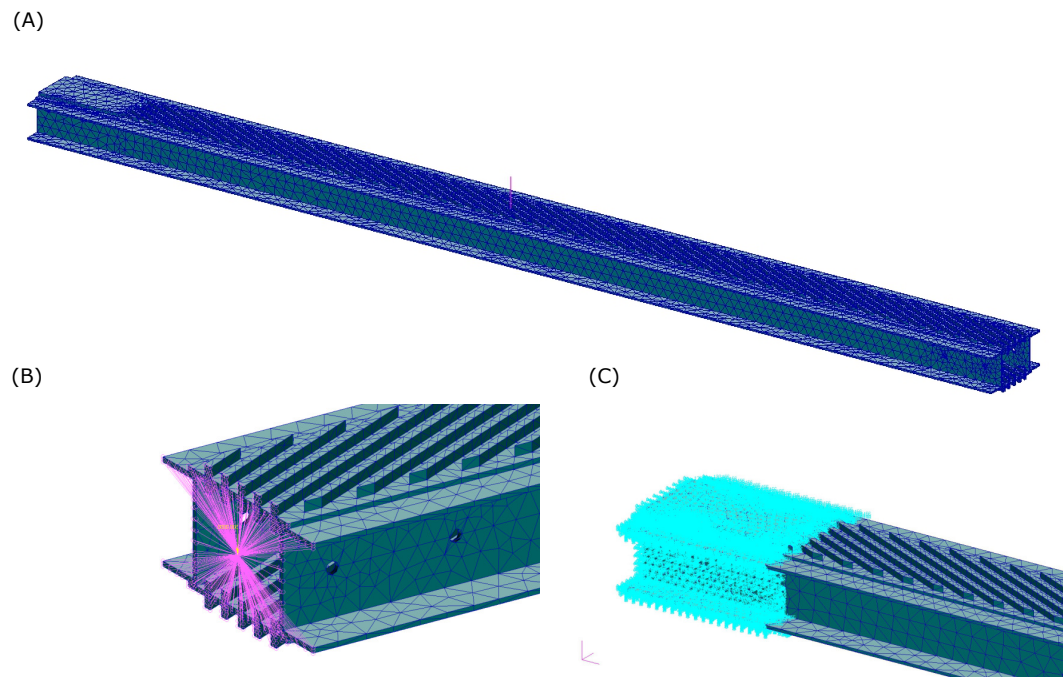
Fig. 5.1 (**A**) TETRA10 FE model, (**B**) Detail of the MPC for free end load application, (**C**) Detail of the constrained nodes.

5.2.1 Static Analysis

Static analysis for an FE model consists of the solution of the linear static problem 5.12.

$$[K_T]\{q\} = \{f\};\tag{5.4}$$

where $[K_T]$ is the global stiffness matrix obtained assembling the FE stiffness matrices, $\{q\}$ is the nodal degrees of freedom array, and $\{f\}$ is the nodal forces array. For the presented test, the load cases chosen are reported in Table 5.2. They consist of three concentrated loads applied at the free end of the beam as shown in Figure 5.1.

Table 5.2 Load cases for linear static analysis, loads applied at the free end of the beam

Name	Value
Load Case 1	$T_z = 500$ [N]
Load Case 2	$M_y = 5 \times 10^4$ [N mm]
Load Case 3	$M_x = 5 \times 10^4$ [N mm]

A first test has been performed for an uncoupled case setting the coupling term C_{12} equal to zero. The BTCE in the uncoupled case has been tested against the TETRA10 model, but also against the analytical results obtained with the Principle of Virtual Works (PVW) which gives the following expression for the determination of the tip deformations:

$$w_{T_z} = \frac{T_z L^3}{3C_{22}}\tag{5.5a}$$

$$w_{M_y} = -\frac{M_y L^2}{2C_{22}}\tag{5.5b}$$

$$\varphi_{M_x} = \frac{M_x L}{C_{11}}\tag{5.5c}$$

The results of this static analysis are summarized in Table 5.3. The accuracy of the BTCE is evaluated by computing the relative difference with the reference value. The relative difference can be computed with Equation 5.6.

$$Rel.Diff.\% = \frac{|Result_{reference} - Result|}{Result_{reference}} \cdot 100\tag{5.6}$$

Table 5.3 Static analysis results comparison for Load Case 1, 2, and 3 for the uncoupled configuration

Static Analysis Results Comparison ($C_{12} = 0$)			
Load Case 1			
Tip Displacement	PVW	BTCE	Rel. Diff. [%]
w [mm]	15.69	15.69	0
Load Case 2			
Tip Displacement	PVW	BTCE	Rel. Diff. [%]
w [mm]	-2.14	-2.14	0
Load Case 3			
Tip Displacement	PVW	BTCE	Rel. Diff. [%]
φ_x [rad]	0.95×10^{-2}	0.95×10^{-2}	0

The analytical results are in agreement with the results obtained with the BTCE model. A second test has been performed for the coupled case comparing the BTCE with the TETRA10 model solved with NASTRAN. The results are summarized in Table 5.4 and in Figures 5.2, 5.3, and 5.4.

Table 5.4 Static analysis results comparison for Load Case 1, 2, and 3 for the coupled configuration

Static Analysis Results Comparison				
Load Case 1				
	TETRA10	BTCE	Rel. Diff. [%]	Mean Rel. Diff. [%]
w [mm]	15.77	16.09	2.06	1.49
φ_x [rad]	5.68×10^{-3}	5.45×10^{-3}	4.13	3.50
Load Case 2				
	TETRA10	BTCE	Rel. Diff. [%]	Mean Rel. Diff. [%]
w [mm]	-2.13	-2.19	2.84	3.18
φ_x [rad]	1.03×10^{-3}	0.99×10^{-3}	4.23	3.65
Load Case 3				
	TETRA10	BTCE	Rel. Diff. [%]	Mean Rel. Diff. [%]
w [mm]	0.57	0.54	4.13	3.18
φ_x [rad]	9.24×10^{-3}	9.74×10^{-3}	5.39	5.48

The results obtained with a TETRA10 model for the three load cases confirmed the accuracy of the BTCE model with a relative difference of the tip values and a mean relative difference evaluated in all the nodes mostly under 5%.
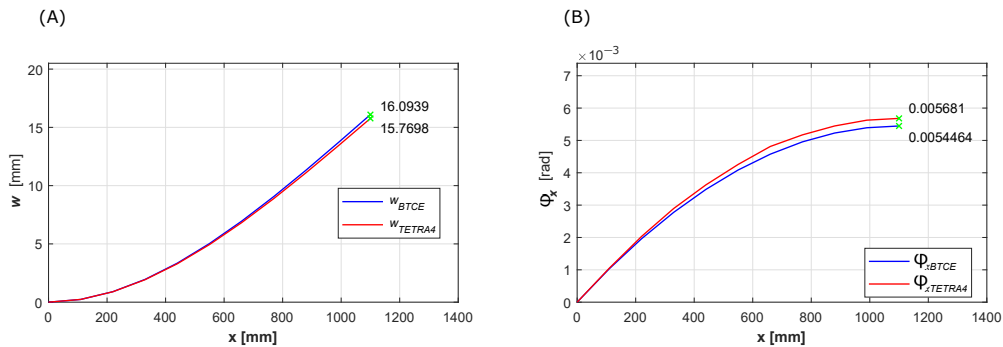
Fig. 5.2 Load Case 1 Results Comparison, (**A**) Deflection along z-axis, (**B**) Torsion Angle.
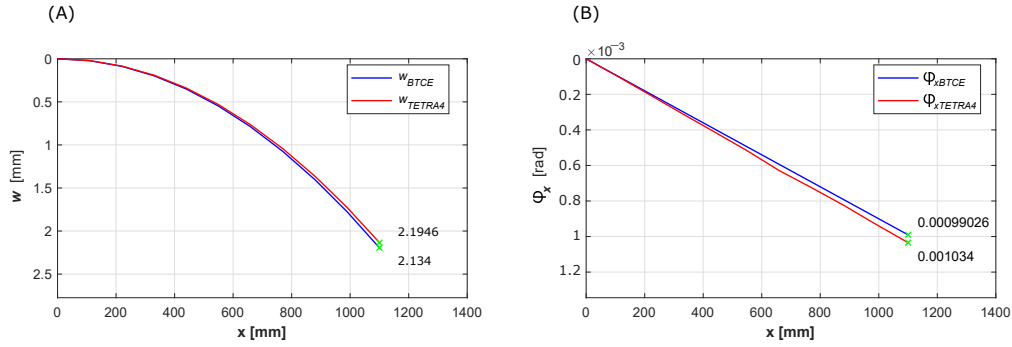
Fig. 5.3 Load Case 2 Results Comparison, (**A**) Deflection along z-axis, (**B**) Torsion Angle.
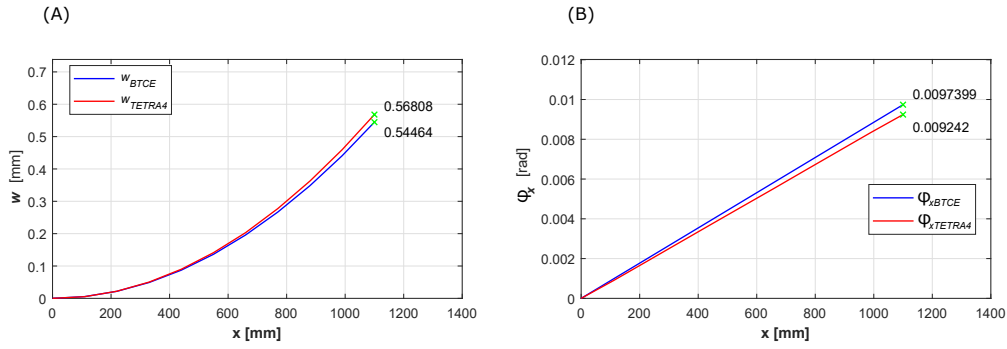
Fig. 5.4 Load Case 3 Results Comparison, (**A**) Deflection along z-axis, (**B**) Torsion Angle.

5.2.2 Modal Analysis

The BTCE model has been tested for the dynamic case with a modal analysis. The eigenvalue problem 5.7 has been solved by computing the corresponding eigenvectors solution of Equation 5.8 and giving a graphical representation of the results.

$$det\left([K_T] - \omega_n^2[M_T]\right) = 0 \tag{5.7}$$

$$\left([K_T] - \omega_n^2[M_T]\right)\phi_n = 0 \tag{5.8}$$

The BTCE model for the stiffened beam has been preliminary tested considering the coupling term $C_{12} = 0$ and comparing the characteristic frequencies obtained with the analytical solution described in [78], where the natural frequencies are computed with Equation 5.9 and 5.10 for bending and torsion modes respectively.

$$\omega_i = (\alpha_i L)^2 \sqrt{\frac{C_{22/33}}{mL^4}} \qquad (5.9)$$

$$\omega_i = \frac{(2i - L)\pi}{2L} \sqrt{\frac{C_{11}}{\rho I_P}} \qquad (5.10)$$

where L is the length of the beam, m is the mass per unit length, i is the number of the mode and the non-dimensional product $\alpha_i L$ assumes the value 1.8719, 4.69409 and 7.85476 for the 1st, 2nd and 3rd bending mode respectively according to [78]. To obtain the corresponding frequency values expressed in Hertz, the ω_i were divided by 2π.

A second modal analysis has been performed including the bending-torsion coupling given by the stiffeners. The results have been compared with the TETRA10 FE model and with experimental results collected with an LDV system represented in Figure 5.5 and with the procedure described in Chapter 3.
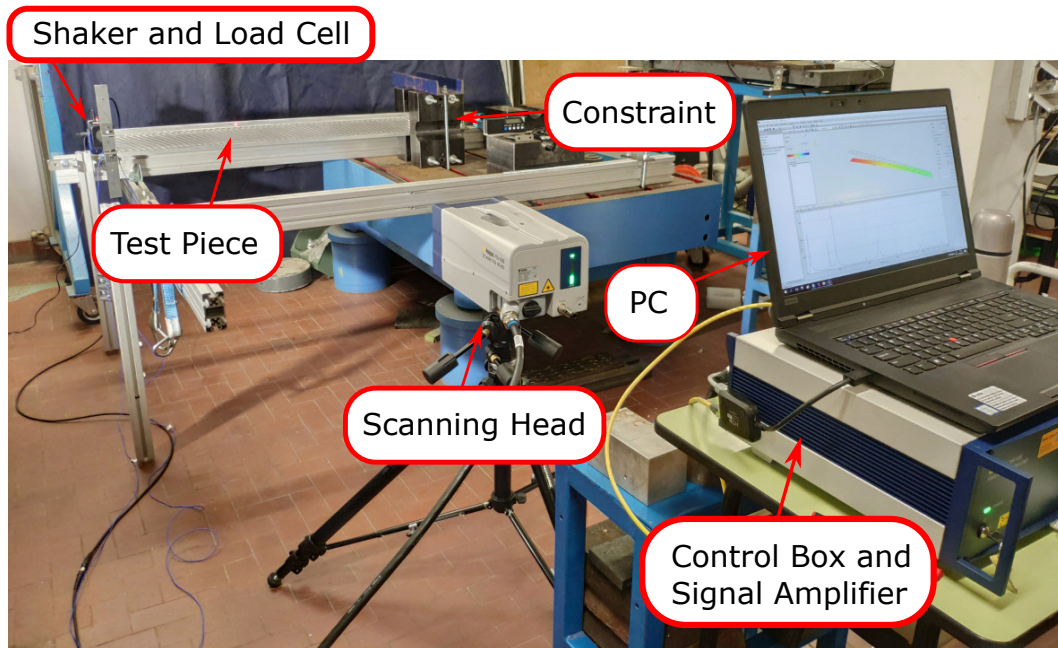
Fig. 5.5 Experimental Setup for Experimental Modal Analysis

The performance of the BTCE model has been evaluated in terms of natural frequencies and mode shapes prediction capabilities. The accuracy of the results

has been assessed by computing the relative differences with Equation 5.6, while the similarities between the numerical and the experimental mode shape have been evaluated with the modal assurance criterion 5.14. For the comparison of the mode shapes obtained with the BTCE model and the TETRA10 FE model, all the degrees of freedom have been considered. For the comparison between the BTCE model and the experiment, only the components of the eigenvector observed during the physical tests were considered, that is, the out-of-plane component along the z-axis.

A convergence study on the computed natural frequencies has been performed considering a number of elements varying from 3 to 50. The results are represented in Figure 5.6 in terms of natural frequency normalized with respect to the convergence value. It is possible to observe that the first three natural frequencies converge rapidly with the increase in the number of elements and their curves result coincident in Figure 5.6, while the fourth, fifth and sixth mode require more elements to converge. However, the natural frequency computed for Mode 6 with 10 elements is only 0.026% greater than the convergence value.
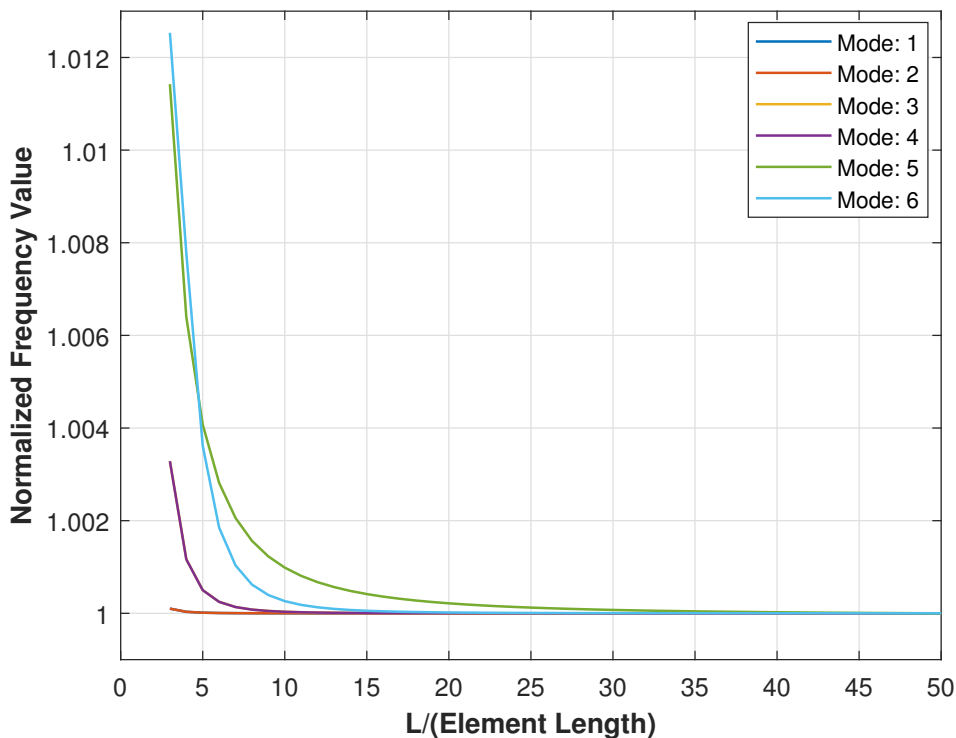
Fig. 5.6 BTCE Modal Analysis Results convergence study (Test Case 1).

The natural frequencies computed for the uncoupled case are resumed in Table 5.5. The results obtained with equation 5.9 and 5.10 are almost coincident with the numerical results predicted with the BTCE model. The comparison between the FE models reported in Table 5.6 revealed a good agreement between the present theory and the TETRA10 FE model solved with NATRAN, with a relative error lower than 5% for most of the natural frequencies computed. The 6th natural frequency presents a higher relative difference equal to 9.29%. The correlation with the experimental results reported in Table 5.7 is generally good. The relative error is around 5% for the 1st and the 5th modes, but with a considerably higher difference for the 3rd and the 6th modes. The discrepancies are caused by the approximations introduced when the cross-section of the beam is reduced to its mid-thickness line with effects on the stiffness coefficients and the inertia properties of the beam.

Table 5.5 Natural frequencies [Hz] comparison for uncoupled BTCE model ($C_{12} = 0$) and analytical results

Analytical Results Comparison			
Mode	Analytical [Hz]	Num. BTCE [Hz]	Rel. Diff. [%]
1	36.31	36.31	0
2	45.02	45.02	0
3	227.55	227.57	7.20×10^{-3}
4	282.10	282.12	7.20×10^{-3}
5	410.88	411.31	1.03×10^{-1}
6	637.18	628.34	2.54×10^{-2}

Table 5.6 Natural frequencies [Hz] comparison of a TETRA10 FE model and a coupled bending-torsion BTCE model.

	Numerical Results Comparison		
Mode	Num. TETRA10 [Hz]	Num. BTCE [Hz]	Rel. Diff. [%]
1	36.73	35.85	2.40
2	47.11	45.02	4.44
3	219.57	224.51	2.25
4	285.29	282.12	1.11
5	399.36	411.47	3.03
6	574.83	628.24	9.29

Table 5.7 Natural frequencies [Hz] comparison of experimental results and a coupled bending-torsion BTCE model.

	Experimental Results Comparison		
Mode	Experimental [Hz]	Num. BTCE [Hz]	Rel. Diff. [%]
1	34.53	35.85	3.82
2	-	45.02	-
3	206.900	224.51	8.5
4	-	282.12	-
5	390.25	411.47	5.43
6	571.10	628.24	10.00

The mode shapes obtained with the BTCE model are graphically represented in figure 5.7. The representation is limited to the three eigenvectors components involved in the modes investigated, the in-plane component v, the out-of-plane component w, and the rotation about the x-axis (torsion) φ_x. The representation highlights the coupling effect for the first, third, and fifth modes which are mainly bending modes, and for the sixth mode which is mainly torsional. It is worth noting that the second and fourth modes are in-plane bending modes and result correctly not influenced by the coupling term C_{12} and result uncoupled. Similar conclusions can be inferred by observing the comparison of mode shape reported in Figures 5.8–5.13, where the mode shapes and the coupling effects are in accordance with the results obtained for the TETRA10 model. Minor differences are reported for the torsional

degree of freedom in the coupled mode, .Furthermore, the mode shapes are in good agreement with the experimental results for the z component of the eigenvectors.
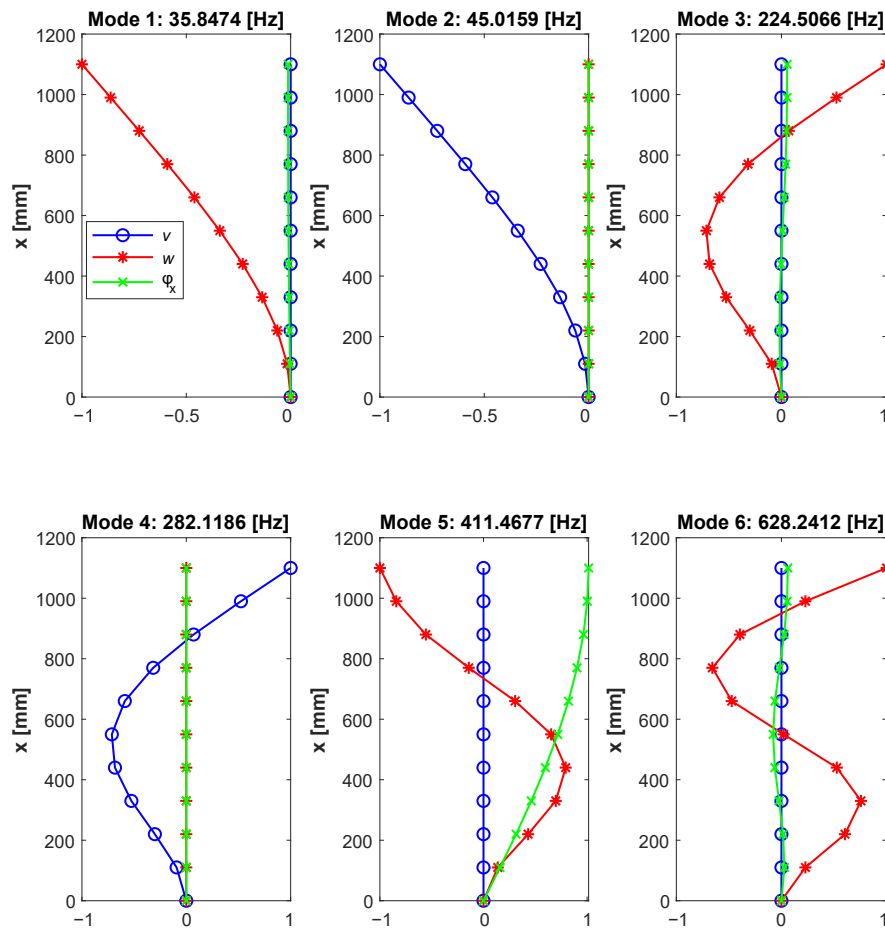
Fig. 5.7 BTCE Modal Analysis Results with eigenvectors components along the z and y-axis and rotational component along the x-axis.
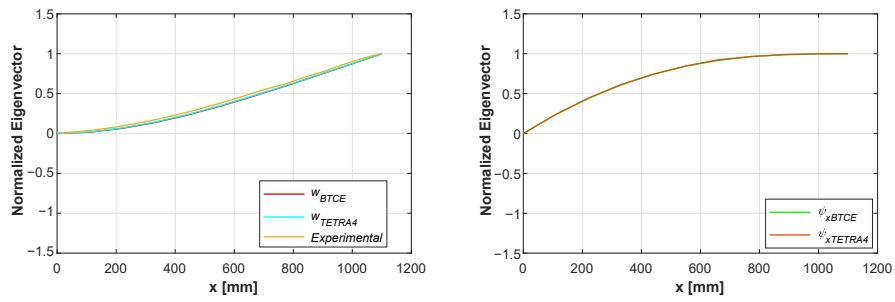
Fig. 5.8 First Mode Shape Comparison between BTCE, TETRA10 and Experimental results.
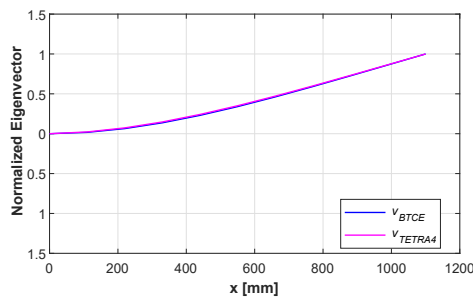
Fig. 5.9 Second Mode Shape Comparison between BTCE and TETRA10 results.
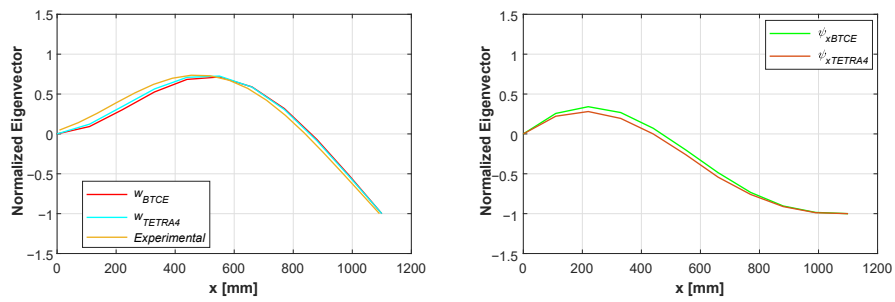
Fig. 5.10 Third Mode Shape Comparison between BTCE, TETRA10 and Experimental results.
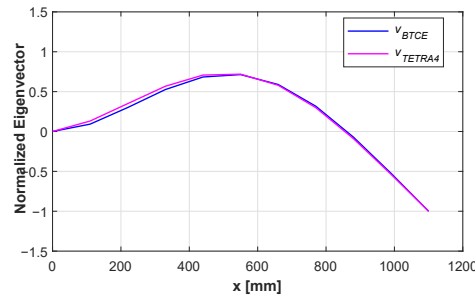
Fig. 5.11 Fourth Mode Shape Comparison between BTCE and TETRA10 results.
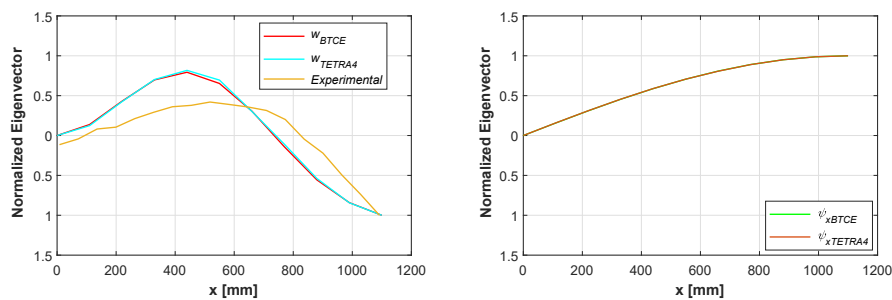
Fig. 5.12 Fifth Mode Shape Comparison between BTCE, TETRA10 and Experimental results.
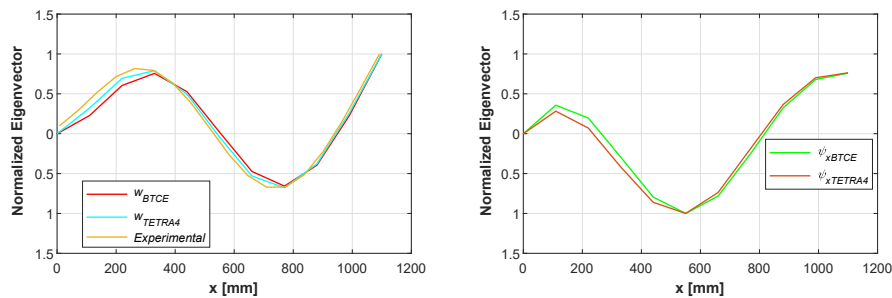
Fig. 5.13 Sixth Mode Shape Comparison between BTCE, TETRA10 and Experimental results.

The MAC matrices computed for the mode shape comparisons are reported in Figure 5.14. The BTCE model showed a very good accordance with the TETRA10 model. The MAC matrices highlight the similarity between the third and the fifth modes. This effect was expected since the torsional mode (Mode 5) is coupled with the bending degrees of freedom through the term C_{12}. The out-of-plane bending component of the fifth mode is similar to the same component of the second bending

mode (Mode 3) as can be observed in Figures 5.10 and 5.12. The same coupling effect can be observed in the MAC matrix which compares the experimental results with the BTCE model. The MAC value for the out-of-diagonal elements is higher because only the vertical component of the eigenvector is considered in this comparison. The lower similarity between the fifth BTCE mode and the corresponding experimental mode is probably related to the low number of acquisition points along the beam axis during the physical test.
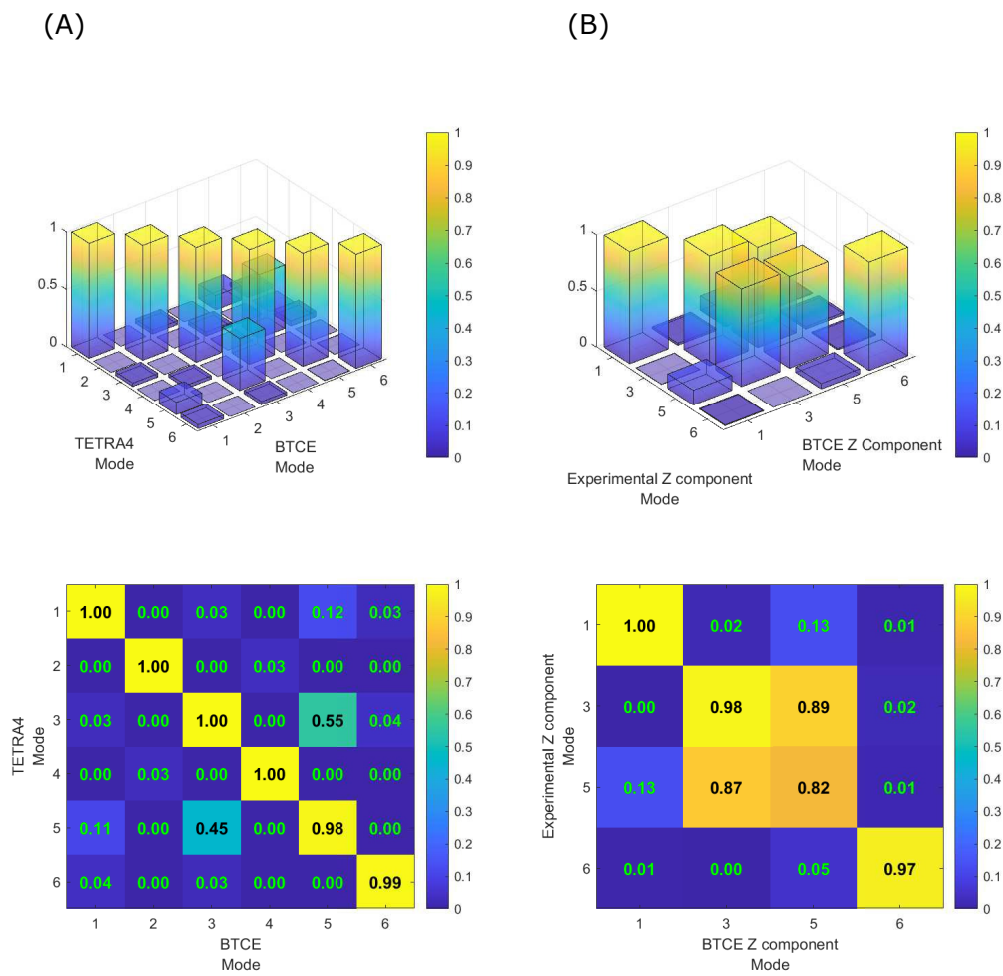
Fig. 5.14 (**A**) MAC matrix for TETRA10-BTCE mode shapes comparison; (**B**) MAC matrix for Experimental -BTCE Z component of mode shapes comparison.

5.3   Composite Box-beam Structure

The second test case considered for the BTCE validation is a CAS composite box-beam structure described in [101, 71]. This test case allowed to validate the BTCE model also for composite materials. The dimensions and mechanical properties of the composite beam are reported in Table 5.8. The cross-sectional stiffness of the BTCE has been computed with Equation 5.1 for two different layups, with six layers oriented at $30°$ and $45°$. The FE model with the presented elements was obtained by assembling 10 two-node elements and imposing the degrees of freedom of the first node equal to zero.

Table 5.8 CAS cantilever graphite/epoxy box beam properties

Property	Value
Width [mm]	24.21
Depth [mm]	13.46
Length [mm]	762
Ply thickness [mm]	0.127
E_{11} [GPa]	142
$E_{22} = E_{33}$ [GPa]	9.8
$G_{12} = G_{13}$ [GPa]	6.0
G_{23} [GPa]	4.83
$\nu_{12} = \nu_{13}$	0.42
ν_{23}	0.5

5.3.1   Modal Analysis

The results of the modal analysis performed on the CAS composite box-beam structure are reported in Table 5.9. The results have been compared to experimental data reported in [71] and numerical results from [101]. The results are in good agreement with numerical and experimental results. The comparison between the BTCE model and the experimental results revealed a relative difference lower than 7% for the twisted vertical bending modes. The accuracy was slightly lower for the predicted frequencies of the first horizontal bending mode, with a relative difference of 13.81% for the lamination at $45°$. The accordance with numerical results reported

in [101] is generally good, with a relative difference for the predicted frequencies lower than 7%.

Table 5.9 Comparison of frequencies (Hz) with numerical results and experimental data

Layup	Mode	BTCE	[101]	[71]
$[30]_6$ CAS	1TV	20.20	19.92	20.96
			(1.41%)	(3.63%)
	2TV	126.47	124.73	128.36
			(1.40%)	(1.47%)
	1HB	35.108	37.62	38.06
			(6.68%)	(7.78%)
$[45]_6$ CAS	1TV	15.63	14.69	16.67
			(6.40%)	(6.24%)
	2TV	97.92	92.02	96.15
			(6.41%)	(1.84%)
	1HB	25.41	25.13	29.48
			(1.11%)	(13.81%)

TV = Twisted Vertical bending. HB = Horizontal Bending.

5.4 Non-uniform stiffness wind turbine blade

The previous test case involved only structures with a uniform stiffness and section. However, many structures present variable sections and, for composite structures, different laminations along the beam length. The National Renewable Energy Laboratory (NREL) presented a 5MW horizontal axis wind turbine (HAWAT) [102] with a variable stiffness wind turbine blade represented in Figure 5.15. The structure is 61.5 m long with a total mass of 17.740 kg, the cross-sectional stiffness properties are reported in Figure 5.16. The wind turbine blade properties are defined in [102] for 49 sections along its axis, for this reason, the BTCE model has been assembled using 48 elements. The model has been constrained imposing all the first node degrees of freedom equal to zero.
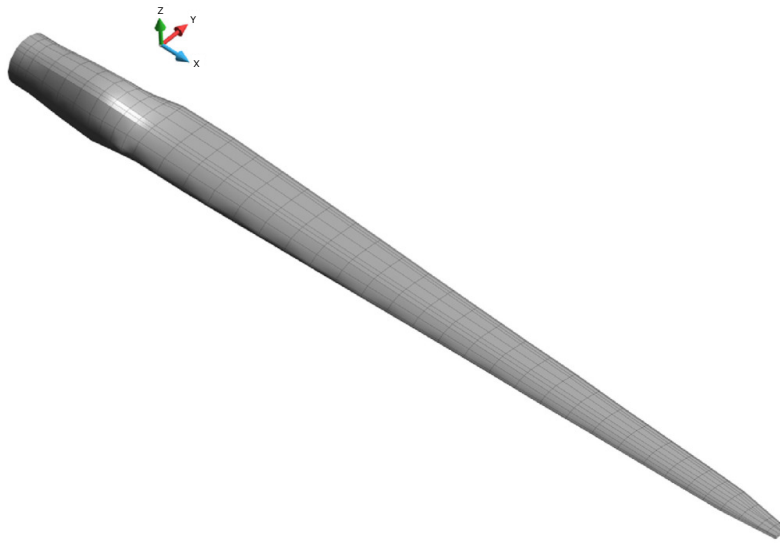
Fig. 5.15 NREL 5MW HAWAT blade.
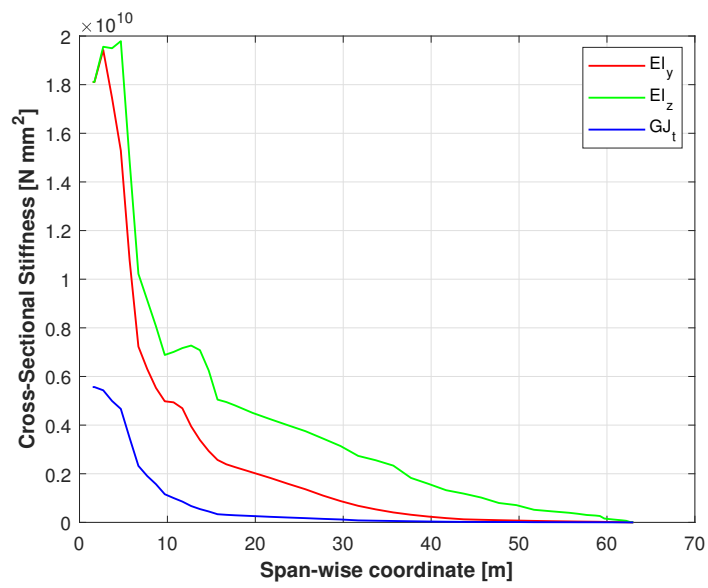
Fig. 5.16 Cross-Sectional Stiffness properties of NREL 5 MW HAWT blade

5.4.1 Modal Analysis

A modal analysis of the wind turbine blade has been performed to predict the first five natural frequencies of the structure. The results of the modal analysis performed on the BTCE model of the NREL 5MW HAWAT blade described in [102] are reported in Table 5.10. The results have been compared with the natural frequency obtained with Rayleigh theory, with Timoshenko theory, and with Bernoulli theory reported in [103]. The values computed with the BTCE model have been compared also with the results obtained with two software developed by NREL [103], B-Modes and FAST, with the results obtained by Jeong et al. [104] using BEM-ABAQUS commercial software and with the results obtained by Li et al. [105] where a geometrically exact beam theory was used.

Table 5.10 Natural frequency comparisons for the different beam theories and results for NREL 5 MW HAWT blade in the flap-wise (F) and edge-wise (E) directions of a single blade without an aerodynamic force.

Mode	BTCE [Hz]	Rayleigh [103] [Hz]	B Modes [103] [Hz]	FAST [103] [Hz]	[105] [Hz]	[104] [Hz]	Timoshenko [103] [Hz]	Bernoulli [103] [Hz]
1	0.68 F	0.68 (0%)	0.69 (1.44%)	0.68 (0%)	0.67 (1.49%)	0.68 (0%)	0.67 (1.49%)	0.68 (0%)
2	1.09 E	1.11 (1.80%)	1.12 (2.68%)	1.10 (0.91%)	1.11 (1.80%)	1.10 (0.91%)	1.09 (0%)	1.11 (1.80%)
3	1.95 F	1.98 (1.51%)	2.00 (2.5%)	1.94 (0.52%)	1.92 (1.56%)	1.98 (1.51%)	1.95 (0%)	3.05 (36%)
4	4.04 E	4.10 (1.46%)	4.12 (1.94%)	4.00 (1.00%)	3.96 (2.02%)	3.99 (1.25%)	3.98 (1.51%)	3.91 (3.32%)
5	4.51 F	4.45 (1.35%)	4.69 (3.84%)	4.43 (1.81%)	4.43 (1.81%)	4.66 (3.28%)	4.42 (2.04%)	4.21 (7.13%)

The BTCE model showed great accordance with other beam theories and commercial software results, with a relative difference below 5% for the computed natural frequencies. The error is considerably higher when the BTCE model is compared to the Bernoulli theory, however, the natural frequencies computed with the Bernoulli theory for the third and the fifth frequencies are not in accordance with the other theories or commercial solvers.
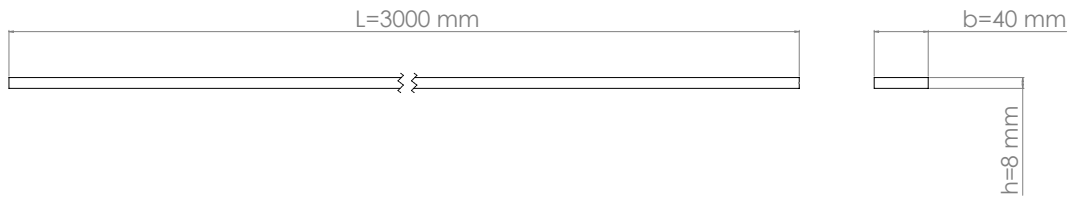
Fig. 5.17 Beam Dimensions

Table 5.11 Aluminium 6060 Mechanical Properties

Property	Value
E	61000 [MPa]
ν	0.3
ρ	2675 Kg/m^3

5.5   Isotropic Beam with Equilibrium Deformation

The models derived in Chapter 3 have been validated through experimental modal analysis. The tests have been performed on a rectangular section aluminum 6060 beam with dimensions $L = 3000$ *mm*, $b = 40$ *mm*, and $h = 8$ *mm* (Figure 5.17) and mechanical properties listed in Table 5.11. The beam has been clamped in four different positions to gather data from four cases respectively with useful lengths $L_1 = 1000$ *mm*, $L_2 = 1500$ *mm*, $L_3 = 2000$ *mm*, and $L_4 = 2500$ *mm* (Figure 5.18). Defined the ratio $\lambda = \mu/L$ with μ equal to the tip deflection, one of the scopes of the experimental test is to understand at which level of λ the geometric non-linear effects have an influence on the beam mode shapes and characteristic frequencies determining the need of a non-linear modal analysis. The other objective of the experimental testing is to verify the accuracy of the presented models in predicting characteristic frequencies and mode shapes.

The beam has been investigated with four experimental tests with similar equipment. The structure has been clamped between two steel blocks to guarantee a rigid constraint (Figure 5.19) at the first section of the beam. Ten poly-lactic acid (PLA) targets (Figure 5.19) have been placed along the span to acquire data at ten equidistant stations. The number of targets has been limited to ten units to keep the additional weight negligible. More targets can be added to improve the acquisition resolution, but mass and inertia must be considered and can alter the non-linear effects observed. Each target presents two vertical surface for signal acquisition

where a squared piece of reflective tape has been positioned to improve the surface reflectiveness. The acquisition has been performed with a Polytec PSV-500 Laser Doppler Vibrometer (LDV) system while the excitation has been obtained with an electrodynamic shaker K200xE01. The shaker has been placed at 550 *mm* from the constraint and perpendicular to the beam axis as represented in Figure 5.19. The objective was to excite only the edgewise degree of freedom because edgewise and torsional characteristic frequencies are the most affected by flapwise deflection, moreover, the torsional modes should be visible only when the non-linear coupling effect becomes important according to [79]. The experimental validation considers the case where the coupling term K is equal to 0. This allows to reduce the number of variables and keeps the interpretation of the results straightforward. Moreover, the term K induces bending torsion deformations, this means that a mode shape that involves the torsional degree of freedom, determine also a flap-wise displacement which needs a 3D LDV system to be detected.

Four numerical models have been defined for experimental result comparison. Two models have been created with MATLAB and use the BTCE finite element. One uses the formulation accounting for the geometrical effect (BTCE-GE), while the second uses the non-linear BTCE (BTCE-NL). Two additional models have been defined in PATRAN and solved with NASTRAN starting with an undeformed configuration, both used SHELL elements to describe the beam geometry but one was solved with SOL103 and the second one was solved with the non-linear solution SOL106. The linear modal analysis has been performed on the undeformed configuration to obtain linear mode shapes and frequencies for the result comparison. The choice behind the use of SHELL finite elements is the possibility of adding bending-torsion coupling terms which is possible for the BTCE but not for conventional beam elements. The BTCE models have been obtained by assembling 10 elements which represent the 10 segments described by the targets positioned on the experimental beam. The first node has been constrained imposing the translations and the rotations equal to 0. For the BTCE-GE model, the modal analysis has been performed using the linear stiffness matrix rotated with the equilibrium configuration dependent transformation matrix $[T]$ reported in 3.1. The BTCE-NL model uses the stiffness matrix derived from Equation 3.27, which depends on the equilibrium static deformation. The mass of each element has been lumped at the nodes and a linear static analysis determined the equilibrium deformation used to complete the element stiffness matrix and perform the non-linear modal analysis. Alterna-
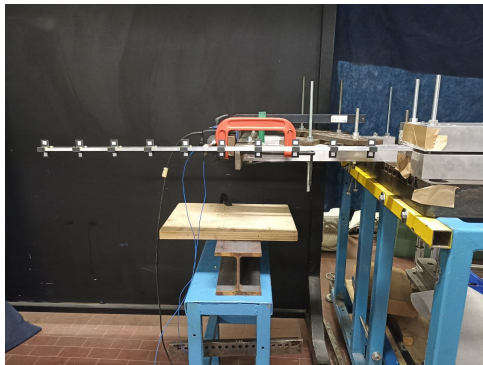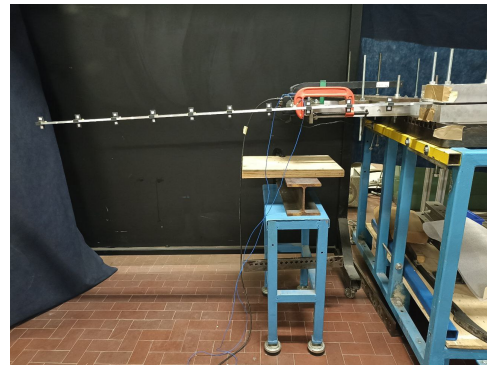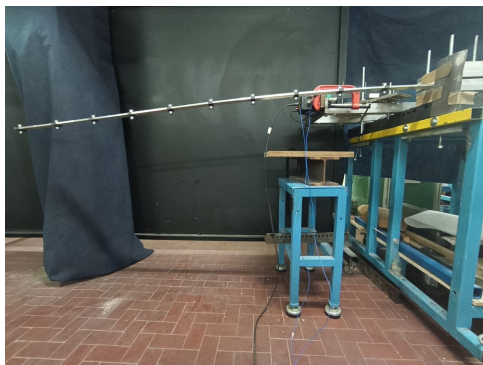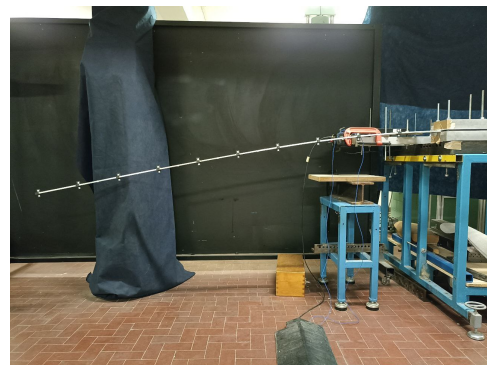
Fig. 5.18 Experimental setup: L=1000 mm (A), L=1500 mm (B), L=2000 mm (C), L=2500 mm (D)
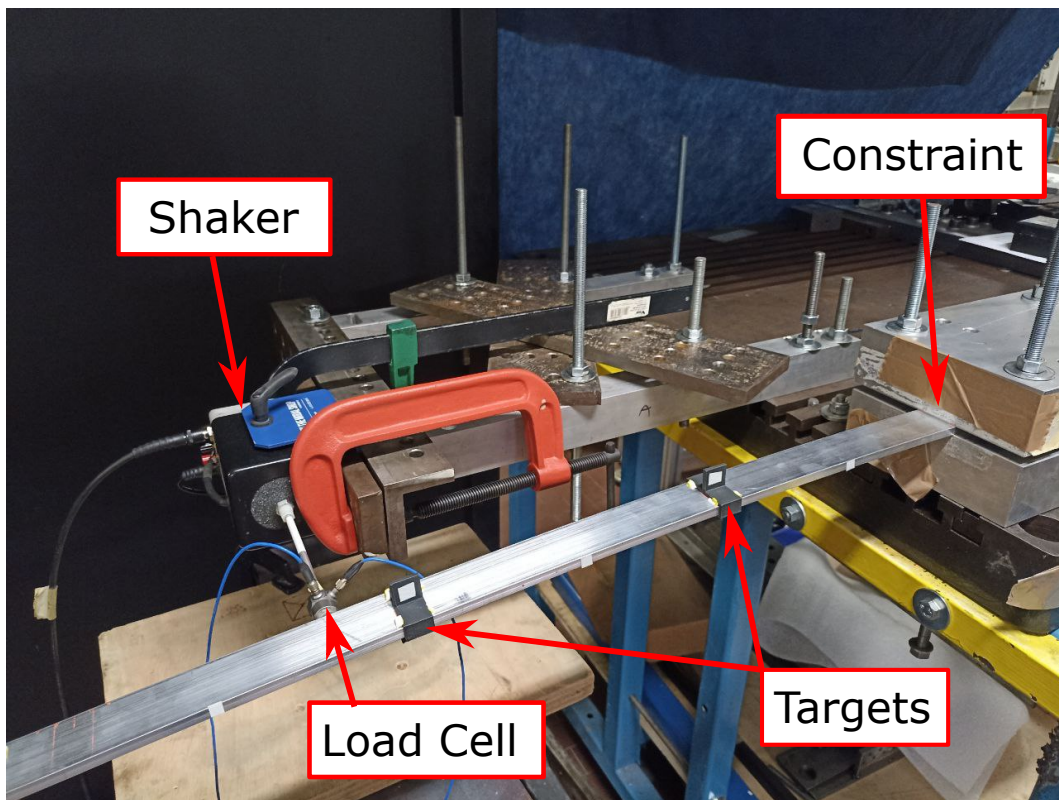
Fig. 5.19 Experimental Setup

tively, the deformed configuration can be obtained with a non-linear static analysis performed with NASTRAN. The linear static analysis for a vertical load does not present edge-wise displacements or rotation, while the non-linear static analysis has a small in-plane component v_0 and θ_{z0} which can be considered negligible. The SHELL elements have been created with 10 mm QUAD4 elements and then solved with SOL103 for the linear modal analysis in the undeformed configuration as a reference. The model has been completed with an inertial load to perform also the non-linear modal analysis SOL106 that accounts for preload. The numerical models results have been compared with the experimental results in terms of mode shapes and characteristic frequencies. The linear analysis has been performed to understand at which level of deformation it becomes unreliable and a non-linear formulation is needed. The dynamic behavior of the non-linear BTCE has been compared in terms of predicted natural frequencies and mode shapes. The accuracy of the natural frequencies was evaluated in terms of relative difference. The similarity between the FE models and the experimental mode shapes has been evaluated with the Modal Assurance Criterion (MAC). Equation (4.7) has been applied to the experimental and numerical mode shapes computed to obtain the MAC matrices. The mode sets of the experimental mode shapes have been compared with themselves computing the Auto MAC, which may indicate the existence of similarities between different mode shapes and thus the presence of couplings between the degrees of freedom. The couplings, if present, should show the same pattern for experimental and non-linear numerical modes. When the structure does not present couplings, the expected matrices for experimental and numerical linear and non-linear modes should be diagonal.

5.5.1   Static Analysis Results

The non-linear finite element derived depends on the equilibrium deformation under static load. The deformation can be obtained through linear or non-linear static analysis. In this research, a linear static analysis is used to determine the initial equilibrium deformation for the load cases considered during the experimental tests on the isotropic beam. The results of the deflection at the tip have been compared with the result of a SHELL model of the beam solved with SOL106 and experimental results, the accuracy has been evaluated by computing the relative difference between

Table 5.12 Comparison of experimental deflection measured at the tip with linear and non-linear static analysis results

Beam Length [mm]	Experimental [mm]	BTCE [mm]	SHELL SOL106 [mm]	$\mu/L\%$
1000	10	10	10	1.1 %
		0%	0%	
1500	54	51	51	3.7 %
		5.5%	5.5%	
2000	166	162	160	8.3 %
		2.4%	3.6%	
2500	367	395	386	14.68 %
		7.6%	5.2%	

numerical and experimental results. The comparison is reported in Table 5.12 with the relative difference for each result.

5.5.2   Experimental Modal Analysis Results

The Frequency Response Functions (FRF) obtained through experimental modal analysis are reported in Figure 5.20. The experimental and numerical results for the characteristic frequencies are reported in Table 5.13. For a beam length equal to 1000 *mm*, the first torsional mode was not detected, while for a length of 1500 *mm*, the torsional mode was detected but the peak was significantly smaller than the others. This confirms that the coupling between edgewise bending and torsion is weak for deformations below 5%. On the other hand for bigger deformations, the excitation of the edgewise degree of freedom provoked also the detection of the first torsional mode coupled with the edgewise bending mode.

The frequencies reported in Table 5.13 show a good accordance with the predicted values and the experimental results. In this case, both linear and non-linear models can be used to determine the characteristic frequencies of the structures. The relative difference between predicted and observed frequencies, reported within parenthesis in Table 5.13, is generally below 5% with some exceptions compatible with the approximations introduced with the derivation of the BTCE models. Moreover, the differences between the BTCE-GE model and the BTCE-NL model are minimal, confirming the findings reported in [94] concerning the major contribution of the geometrical effect in this class of analysis.

Table 5.13 Experimental and numerical natural frequencies results comparison for the isotropic beam

	L=1000mm				
Mode	Exp	Analytical LIN [Hz]	SOL103 [Hz]	BTCE-GE[Hz]	BTCE-NL [Hz]	SOL106 [Hz]
1E	30.86	30.86	30.84	30.85	30.85	30.83
		(0%)	(0.06%)	(0.03%)	(0.03%)	(0.03%)
2E	190.14	193.37	191.93	193.36	193.34	191.8
		(1.7%)	(0.94%)	(1.67%)	(1.68%)	(0.87%)
3E	525.68	541.45	531.55	541.57	541.56	530.87
		(3%)	(1.12%)	(3.02%)	(3.02%)	(0.98%)
4E	1001.56	1061.02	1025.7	1062.01	1062.00	1023.4
		(5.94%)	(2.41%)	(6.03%)	(6.03%)	(2.18%)
1T	/	271.34	279.95	271.67	271.71	264.02
	L=1500mm				
Mode	Exp	Analytical LIN [Hz]	SOL103 [Hz]	BTCE-GE [Hz]	BTCE-NL [Hz]	SOL106 [Hz]
1E	14.38	13.71	13.71	13.68	13.66	13.68
		(4.66%)	(4.66%)	(4.87%)	(5.01%)	(4.87%)
2E	88.20	85.94	85.67	85.87	85.82	85.55
		(2.56%)	(2.89%)	(2.64%)	(2.7%)	(3.0%)
3E	245.08	240.64	238.69	240.67	240.63	238.5
		(1.81%)	(2.61%)	(1.80%)	(1.82%)	(2.68%)
4E	477.42	471.56	464.43	471.85	471.86	463.79
		(1.23%)	(2.72%)	(1.16%)	(1.16%)	(2.85%)
1T	171.02	180.89	186.14	181.43	181.61	176.0
		(5.75%)	(8.84%)	(6.08%)	(6.19%)	(2.91%)
	L=2000mm				
Mode	Exp	Analytical LIN [Hz]	SOL103 [Hz]	BTCE-GE [Hz]	BTCE-NL [Hz]	SOL106 [Hz]
1E	7.71	7.71	7.71	7.62	7.56	7.60
		(0%)	(0%)	(1.17%)	(1.95%)	(1.43%)
2E	50.20	48.34	53.12	48.13	48.02	47.96
		(3.71%)	(5.82%)	(4.12%)	(4.34%)	(4.46%)
3E	133.20	135.36	134.75	133.67	134.12	131.9
		(1.62%)	(1.15%)	(0.35%)	(0.69%)	(0.98%)
4E	273.24	265.25	262.99	265.15	265.15	262.49
		(2.92%)	(3.75%)	(2.96%)	(2.96%)	(3.93%)
1T	140.92	135.67	139.42	138.89	138.99	135.96
		(3.72%)	(1.06%)	(1.44%)	(1.37%)	(3.52%)
	L=2500mm				
Mode	Exp	Analytical LIN [Hz]	SOL103 [Hz]	BTCE-GE [Hz]	BTCE-NL [Hz]	SOL106 [Hz]
1E	4.86	4.94	4.94	4.71	4.61	4.68
		(1.65%)	(1.65%)	(3.18%)	(5.42%)	(3.7%)
2E	31.94	30.94	30.94	30.44	30.27	30.29
		(3.13%)	(3.13%)	(3.33%)	(5.73%)	(5.44%)
3E	89.81	86.63	86.39	85.76	85.82	85.54
		(3.54%)	(3.81%)	(4.51%)	(4.44%)	(4.86%)
4E	176.06	169.76	168.84	169.16	169.19	168.04
		(3.58%)	(4.1%)	(3.92%)	(3.90%)	(4.56%)
1T	112.94	108.53	111.44	113.62	114.71	110.97
		(3.9%)	(1.33%)	(0.60%)	(1.57%)	(1.74%)
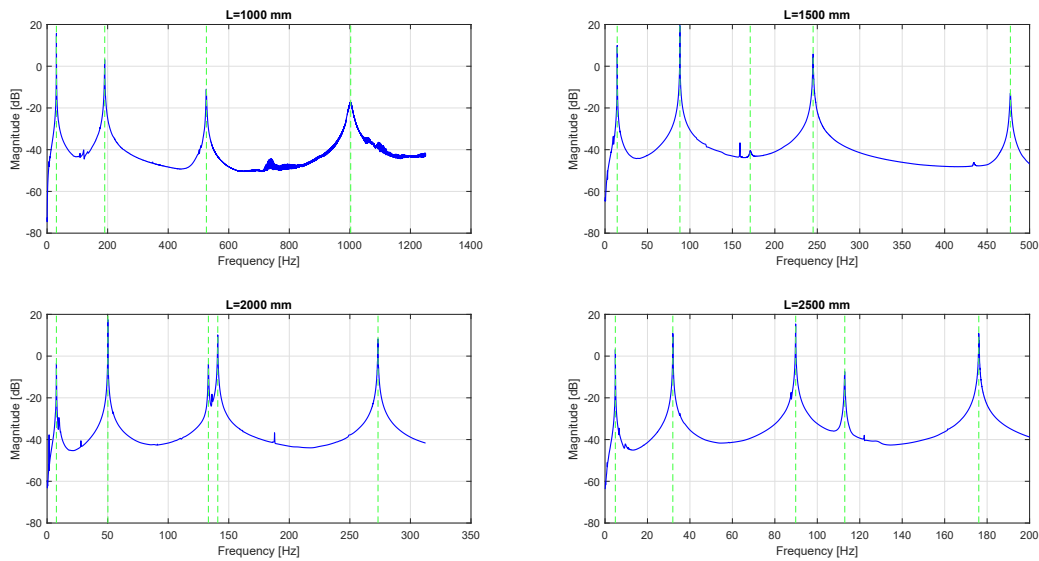
Fig. 5.20 Experimental FRF

The experimental Auto MAC matrices are reported in Figures 5.21(A), 5.22(A), 5.23(A), and 5.24(A). The modes order is based on the frequency value, from the mode with the lowest frequency to the one with the highest. With this convention for L=1000 mm and L=1500 mm, the torsional mode occupies the third position, while for the other cases it is placed in the fourth position. The remaining modes represent the edgewise modes. In figure 5.21, it is possible to notice the absence of the torsional mode. As already stated, when nonlinear effects are not present, edgewise displacement and torsion are not coupled, thus exciting the edgewise displacement, the torsional mode can not be observed. On the other hand, the numerical modes predicted five uncoupled modes as expected. For L=1500 mm, the experimental Auto MAC matrix reported in Figure 5.22(A) revealed a certain level of coupling between the torsional mode and the second and third edgewise modes, this coupling is not detected by the linear FE models while is present in the nonlinear FE models MAC matrices. The experimental and nonlinear FE models MAC matrices present some differences in the out-of-diagonal values. In this case, the torsional mode presented a small peak in the FRF because the nonlinear effects are present but not very relevant with a 3.7% of deflection. Moreover, the number of targets is relatively low and can cause some discrepancies. However, it is possible to conclude that for L=1500 mm the nonlinear effects are present and can be predicted with the nonlinear BTCE models, but linear modal analysis can be a reasonable

approximation for this level of deflection. The Auto MAC matrices for L=2000 mm
and L=2500 mm are reported in Figure 5.23(A) and 5.24(A). The pattern given by the
experimental results is correctly predicted by the nonlinear models, moreover, these
cases, highlight the lack of accuracy obtained when linear models are considered
for modal analysis of structures with moderate deformations. Figures 5.21, 5.22,
5.23, and 5.24 presents also the comparison between the experimental modes and
the numerical modes calculated with linear and nonlinear FE models. Ideally, if the
numerical modes are coincident with the experimental modes, the MAC matrices
should be identical to the Auto MAC experimental matrices. In general, it is possible
to affirm that the mode shapes predicted with the nonlinear BTCE model are in good
accordance with experimental modes, moreover, they are confirmed by the results of
the SHELL FE model solved with NASTRAN SOL106. In the first case (L=1000
mm), the torsional mode was not detected and for this reason ,the comparison with
the numerical counterpart is not reported in Figure 5.21. The MAC matrices for
the beam with L=1500 mm reveal a high similarity with experimental results when
nonlinear modal analysis is used, while the similarity is considerably lower when
nonlinear effects are not considered. This is even more evident for L=2000 mm and
L=2500 mm. The fourth case presented a relatively low similarity for the fourth
mode (Figure 5.24) which corresponds to the third edgewise mode coupled with
the torsional mode. This is probably connected to the resolution obtained with the
chosen number of targets and can be improved by considering more acquisition
points. However, the objective was to keep the mass of the targets negligible for all
the cases considered and for this reason, the number of acquisition points has been
kept constant throughout all the experimental activity.

5.6   Box-Beam Composite Structure with Equilibrium Deformation

A numerical comparison has been performed for a case with bending-torsion cou-
pling, the reference structure is a box-beam structure with a circumferentially asym-
metric stiffness (CAS) laminated composite configuration. The structure is the
same used in [106], the section is represented in Figure 5.25. The beam is obtained
with a unidirectional T700 carbon-epoxy layer bonded onto wooden spars with
fibers oriented at 24°. The structural box has the following dimensions: length,
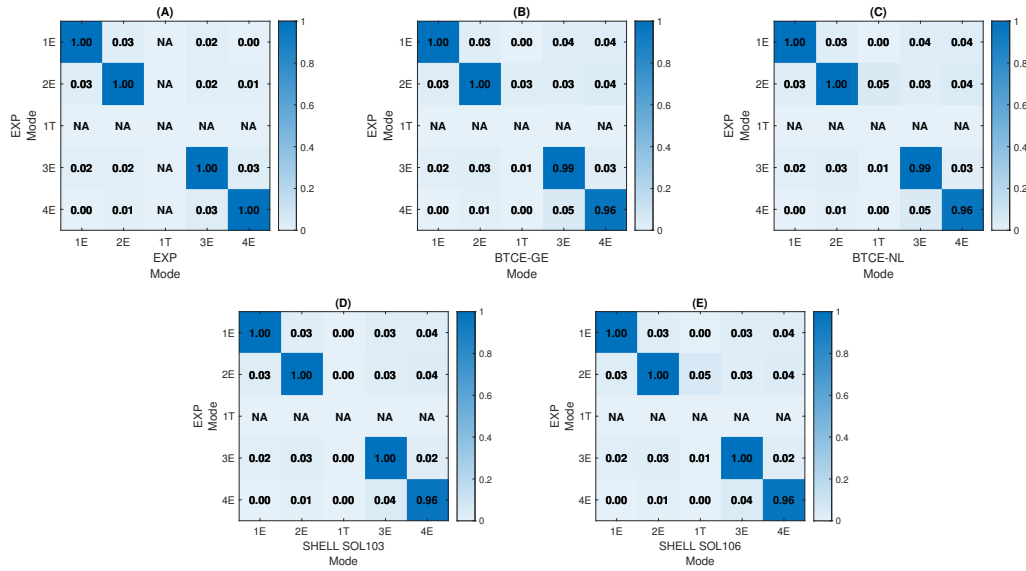
Fig. 5.21 MAC L=1000 mm, comparison with Experimental Mode Shapes: Auto MAC (A), BTCE-GE (B), BTCE-NL (C), SHELL SOL 103 (D), SHELL SOL 106 (E)
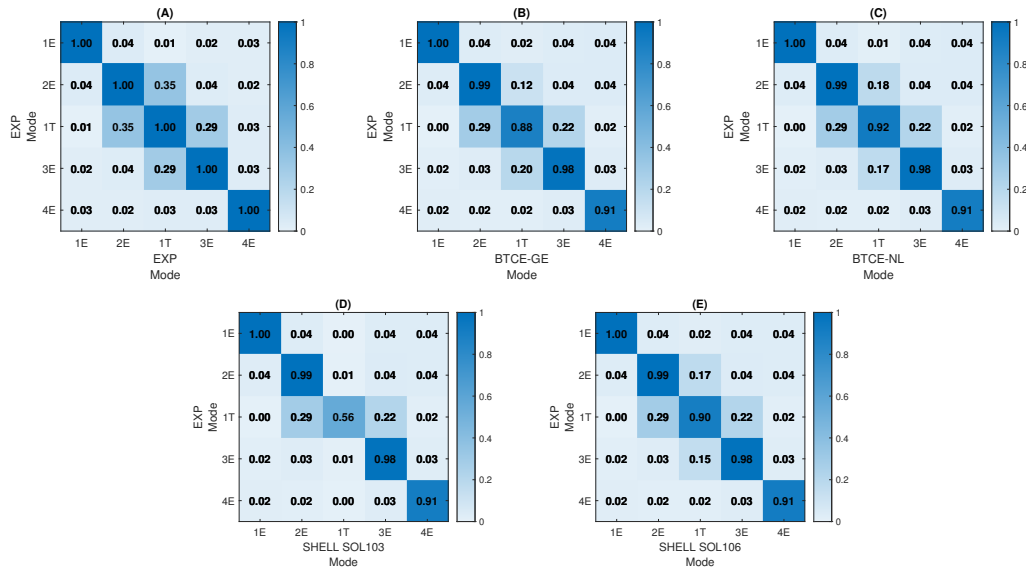
Fig. 5.22 MAC L=1500 mm, comparison with Experimental Mode Shapes: Auto MAC (A), BTCE-GE (B), BTCE-NL (C), SHELL SOL 103 (D), SHELL SOL 106 (E)
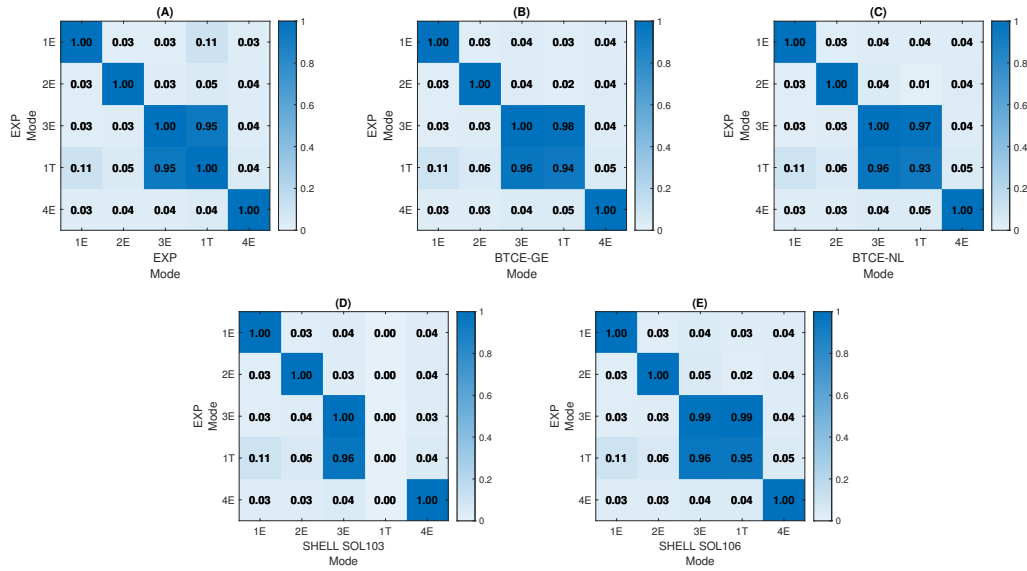
Fig. 5.23 MAC L=2000 mm, comparison with Experimental Mode Shapes: Auto MAC (A), BTCE-GE (B), BTCE-NL (C), SHELL SOL 103 (D), SHELL SOL 106 (E)
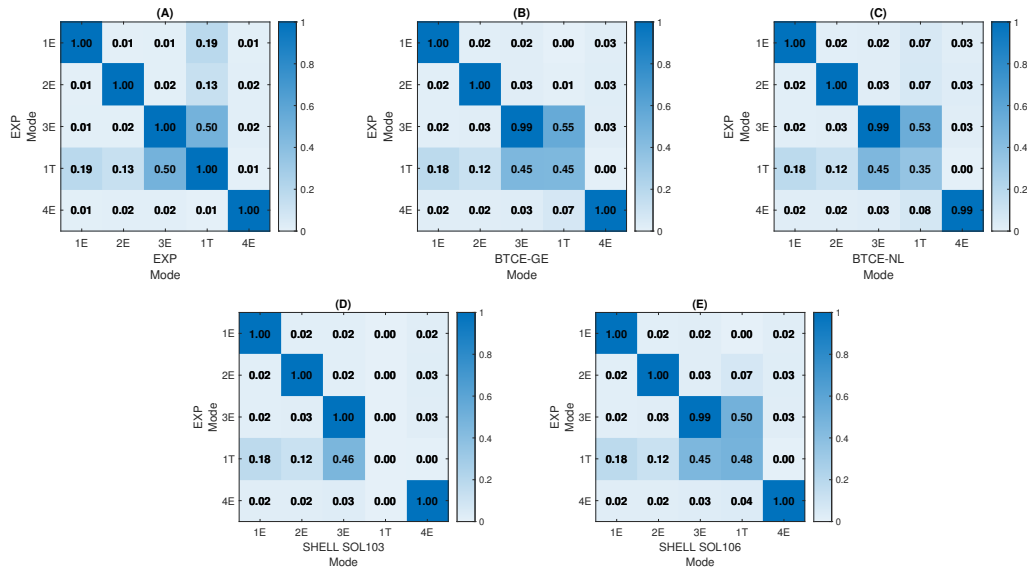
Fig. 5.24 MAC L=2500 mm, comparison with Experimental Mode Shapes: Auto MAC (A), BTCE-GE (B), BTCE-NL (C), SHELL SOL 103 (D), SHELL SOL 106 (E)

Table 5.14 Cantilever composite beam material and properties

T700 Property	Value	Wood Property	Value
E_{11}	118.4 GPa	E_{11}	16.6 GPa
E_{22}	8.7 GPa	E_{22}	8 GPa
$G_{12} = G_{13}$	3.4 GPa	$G_{12} = G_{13}$	3.4 GPa
$v_{12} = v_{13}$	0.31	$v_{12} = v_{13}$	0.31

$L = 522\,mm$; width, $w = 20\,mm$; height, $h = 2,8\,mm$; upper and lower panel thickness, $t = 0.2\,mm$; mass per unit length, $m = 1.095 \times 10^{-5}\,kg/mm$; torsional unit inertia, $Ip = 4.75 \times 10^{-4}\,kg/mm$. The mechanical properties of the material are listed in Table 5.14.
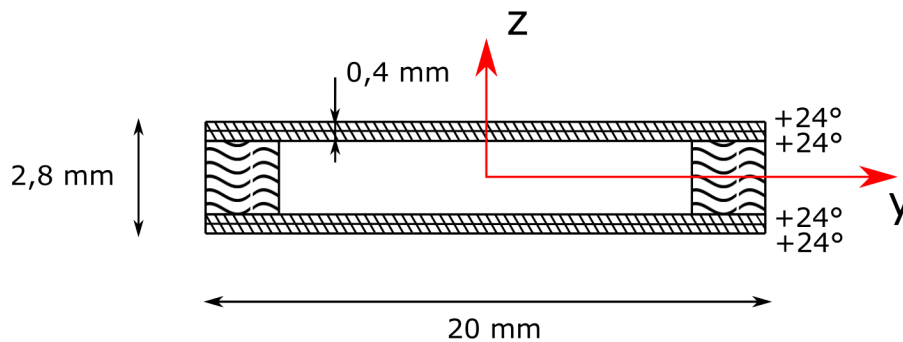
Fig. 5.25 Composite Box-Beam Section

The reference model has been defined in PATRAN with SHELL elements (Figure 5.26) while a beam model with the formulation presented in this thesis has been obtained by assembling 10 BTCE. The load condition chosen for the numerical comparison is a concentrated tip load. The load has been incremented to reach different deformation levels and observe the limits of validity of the presented model. The deformation has been evaluated with a nonlinear static analysis, then a nonlinear modal analysis has been performed for each load case and the numerical results have been compared in terms of characteristic frequencies. The deformed configuration used to orient and compute the nonlinear beam finite element has been retrieved from the nonlinear static analysis performed with NASTRAN. The first eight characteristic frequencies have been computed for the two FE models and normalized with the
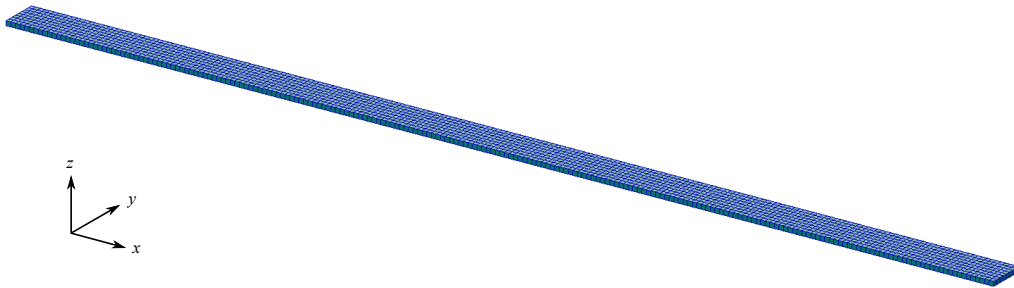
Fig. 5.26 Composite Box-Beam SHELL model

value obtained with a linear modal analysis of the undeformed configuration. The normalized frequencies have been compared for each mode at different deformation levels.

5.6.1   Numerical Modal Analysis Results

The results of the numerical modal analysis of the composite box-beam structure described by [106] are represented in Figures 5.27, 5.28, 5.29, and 5.30. Eight load cases have been considered for a maximum deflection $\lambda = 28.55\%$, six of them correspond to a deflection below 10% and can help to observe more precisely at which point the nonlinear effects cause the deviation from the linear results. The results of the simulation performed with the BTCE models have been compared to the frequencies obtained with a SHELL model solved with NASTRAN SOL106. For this comparison, the first eight modes have been investigated. In this case, the comparison is performed on the frequencies computed with the nonlinear models normalized with their linear counterparts computed for the undeformed configuration, with this method the variation of the characteristic frequency is highlighted. The material orientation causes the flapwise bending-torsion coupling, while the deflection causes the edgewise bending-torsion coupling, for this reason, all the modes involve the three degrees of freedom. However, one component of the eigenvector has a considerably higher value than the other, for this reason, the modes where flapwise bending is the major effect will be denoted with the letter F, while the modes where the edgewise bending component is the predominant will be denoted with the letter E and the mainly torsional modes will be denoted with the letter T as previously.
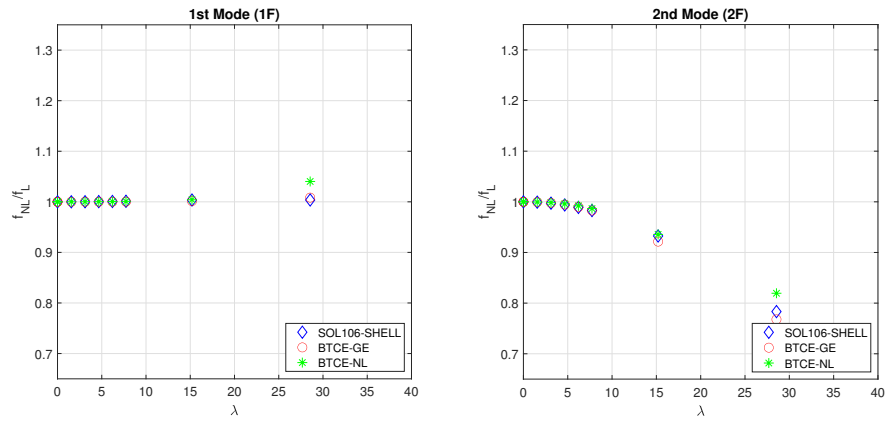
Fig. 5.27 FE Models results comparison for 1st and 2nd Modes
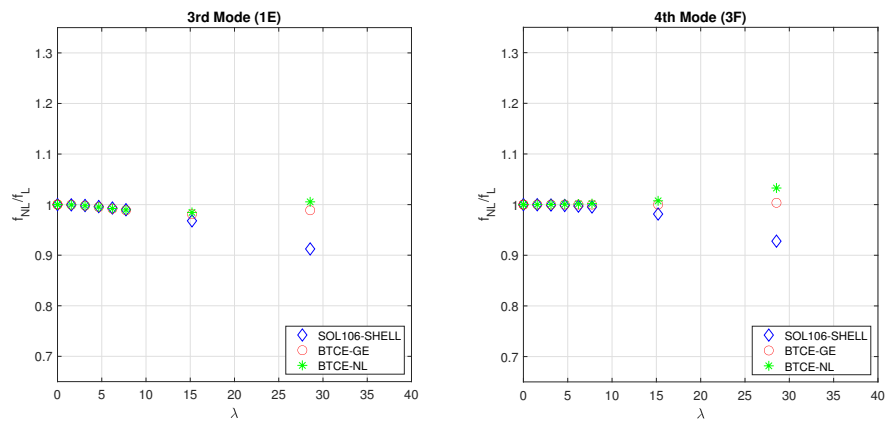
Fig. 5.28 FE Models results comparison for 3rd and 4th Modes
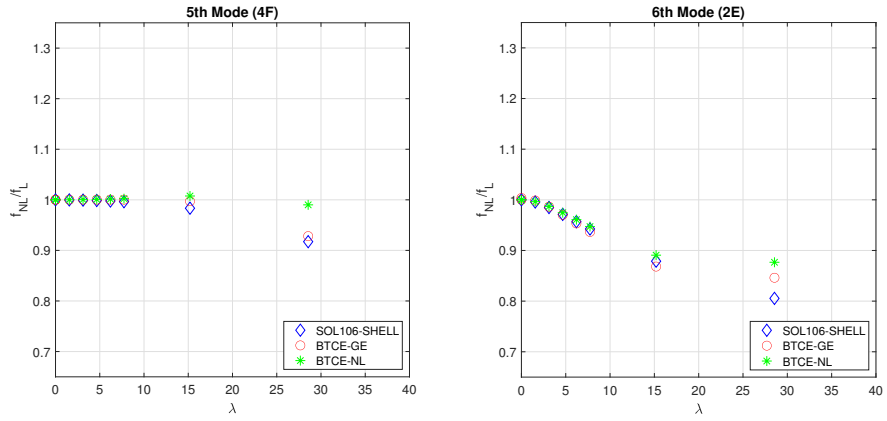
Fig. 5.29 FE Models results comparison for 5th and 6th Modes
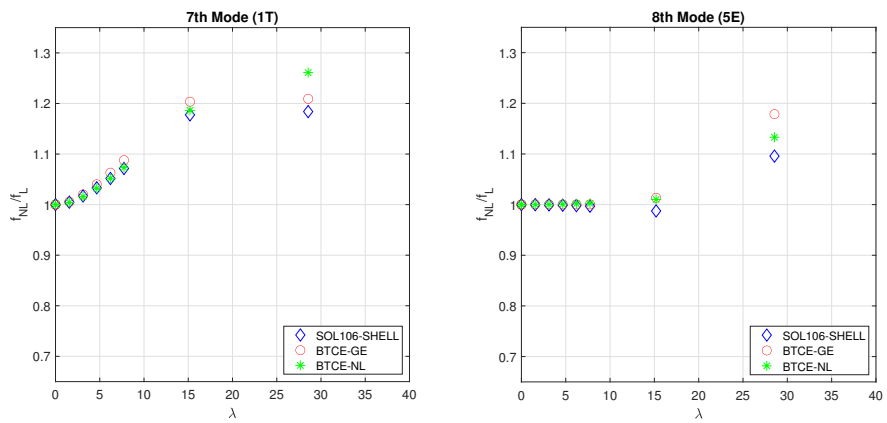
Fig. 5.30 FE Models results comparison for 7th and 8th Modes

The results show a good correlation between the BTCE models and the SHELL FE model. The 1st, 2nd, 5th, and 7th modes presented very similar results even for large displacements. The 3rd, 4th, 6th, and 8th modes present some discrepancies when the deformations are bigger than 15%. A less accurate prediction of characteristic frequencies can be attributed to many factors. First of all the number and the nature of the finite element used brings approximations that are necessary to lower the computational costs but can influence the results. Secondly, the hypothesis of inextensibility adopted for the BTCE could be not verified for for large nonlinear deformations. Moreover, the curvatures and the rotation matrix are obtained under the hypothesis of moderate-to-large displacements. Finally, the perturbation introduced for the nonlinear formulation is small and the expression used for the perturbation and the rotation matrices are truncated in the second order. For large deformations, higher-order terms may be considered. This comparison shows that the BTCE models could be used for nonlinear analysis of pre-deformed structures with deflection below 15% with results comparable to the characteristic modes of a SHELL FE model of the same structure solved with NASTRAN SOL106. Moreover, the results show that the differences between BTCE-GE and BTCE-NL are minimal up to a deflection of 15% and increase for larger deformations. The models here presented can be further improved with an experimental test involving coupled structures to assess the performance and correctly evaluate the influence of geometrical and stiffness effects.

5.7   Summary and Conclusions

The beam finite element with bending-torsion coupling formulation derived in Chapter 2 underwent validation for the static case by simulating an aluminum beam with stiffened panels in a cantilever configuration, subjected to three different load configurations at the free end. The inclusion of oriented stiffeners enabled the attainment of a noticeable bending-torsion coupling effect, accurately depicted in the results of both static and modal analyses. Comparison between the results of the static analysis and those from a TETRA10 FE model in identical configurations revealed relative differences below 5% for most load cases considered, with discrepancies primarily arising from approximations made when reducing the beam's cross-section to its mid-thickness line, affecting stiffness coefficients. Validation for the dynamic case

involved modal analysis in a cantilever configuration, with results compared to experimental and TETRA10 FE model outcomes. Relative errors were generally below 5% for numerical comparisons but higher, up to 10%, for experimental comparisons due to approximations introduced by the BTCE model's cross-section reduction and constraints during experimental tests. Mode shapes obtained using the present theory were compared with the TETRA10 FE model and experimental mode shapes using the modal assurance criterion, showing close agreement despite minor discrepancies attributed to the limited number of scanning points during experimental tests. The finite element was further tested for modal analysis of an NREL 5MW HAWT blade and a CAS graphite/epoxy cantilever box beam with varying layups, with natural frequencies compared to numerical and experimental results. Results exhibited good alignment with the BTCE model, affirming its compatibility with such structures. Overall, the coupled beam finite element was validated through numerical and experimental evidence across various structures, showcasing its effectiveness in capturing coupling effects induced by oriented stiffeners or composite material. Its consistency with kinematics and equilibrium equations extends its applicability beyond box-section beams, offering the potential for nonlinear static and dynamic analysis and addressing aeroelastic problems involving fluid-structure interactions or aerodynamic tailoring.

Chapter 3 introduced two models for dynamically analyzing beam structures with bending-torsion coupling in the presence of geometric nonlinearities. Experimental testing was conducted to verify the level of deflection necessary to observe appreciable nonlinear effects and assess the accuracy of nonlinear analysis with the BTCE models. These experiments utilized an LDV system on an aluminum beam constrained at four different lengths, allowing for the study of nonlinear effects at varying deformation levels. Results indicated that geometric nonlinearities had minimal effects on the structure's characteristic frequencies, with both linear and nonlinear numerical models predicting frequencies generally within a 5% error margin. Regarding mode shapes, it was found that for deformations below 3.7%, mode shapes exhibited low levels of coupling, and linear numerical models were suitable for studying structures under these conditions. However, for deformations of 8.3% or 14.7%, significant differences in mode shapes were observed due to nonlinear couplings, accurately predicted by the derived BTCE models. Minor discrepancies between observed and predicted modes were attributed to the relatively low number of scanning points, affecting resolution, and the reliance of BTCE models on equilib-

rium solutions computed with linear static analysis, which may be less accurate for higher deformations. Experimental findings suggested that stiffness effects played a minor role in the analyzed scenarios, and the BTCE-GE model could sufficiently predict characteristic modes and frequencies. The BTCE models were also tested on a composite structure with bending-torsion coupling, showing good agreement with results obtained from a SHELL FE model solved with NASTRAN SOL106. The presented model's application can be extended to studying the aeroelastic performances of wing structures. Moreover, the bending-torsion coupling formulation allows for the optimization of material orientation to achieve desired dynamic properties, even in the presence of geometric nonlinearities.

Chapter 6

Optimization of Curvilinear Stiffener Path

Some of the contents and derivation presented in this chapter have been previously published in *Materials* 2023.

Patuelli, C.; Cestino, E.; Frulla, G.; Valente, F. Optimization of Curvilinear Stiffener Beam Structures Simulated by Beam Finite Elements with Coupled Bending–Torsion Formulation. Materials 2023, 16, 3391.

6.1   Introduction and Motivation

The orientation of anisotropic materials is the most relevant design variable for aeroelastic tailoring problems. The design process to find the optimal configuration can be very demanding in terms of computational cost, especially if the curvilinear path is considered and the design space is sensibly increased. Recently, many authors investigated the problem of optimization for aeroelastic tailoring. Haftka [107] investigated the properties of parametric constraints for flutter optimization showing that the the parametric continuous flutter constraint can be replaced by the equivalent minimum value constraint for a more efficient optimization. Martins and Alonso [108] developed an integrated aero-structural method for the design of aerospace vehicles. They used a high-fidelity parametric model with a large number of design variables for the optimization of a supersonic business jet assessing the accuracy of the sensitivity information obtained with the procedure. Stroud et al. [109]

presented an approach for the reliability-based optimization of metallic wing plates to meet strength and flutter requirements. The design variable was the thickness distribution, while the constraints were the weight and the probability of failure. Maute et al. [110] presented a topology optimization methodology for the design of aeroelastic structures, accounting for the fluid-structure interaction. The optimization results showed the significant influence of the design dependency of the loads on the optimal layout of flexible structures when compared with results that assumed a constant aerodynamic load. Kameyama et al. [37] examined the effects of laminate configurations on flutter and divergence characteristics of composite plate wings with different sweep angles and performed an optimization to find the minimum weight design, with constraints on the flutter and divergence speeds. Equivalent models or beam elements can be adopted for more efficient optimization problems during early design stages. Danzi et al. [44] used an equivalent continuum plate model to obtain an optimal configuration through a topology optimization problem, where the design variables became the orientation of the stiffeners at prescribed points. In the present chapter, the BTCE developed in this thesis, is used for the optimization of the stiffeners curvilinear path for box-beam structures. The BTCE can be a versatile and efficient tool for topological optimization under different load cases and constraints.

6.2   Optimization Problem

The structure chosen for the optimization is based on the aluminum stiffened box-beam structure introduced in the previous chapters. The structure, represented in Figure 6.1, is a generic box-beam structure with a length $L = 1100\,mm$ and composed of two stiffened panels with a width of $b = 50\,mm$ connected with two C-shaped spars with dimensions $20\,mm\,x\,40\,mm$. The stiffeners dimensions are $h_s = 4\,mm$ and $b_s = 3\,mm$. The distance between the stiffeners is $d_s = b/N = 8.33\,mm$, with $N = 6$ the number of stiffeners. The orientation of the stiffeners follows a curvilinear path which varies linearly with Equation 6.1 from the orientation at the first section of the beam ϑ_1 to the orientation at the end section ϑ_2. The C-shaped spars and the mid-layer of the stiffened panels are $s = 2\,mm$ thick. The material considered for the structural analysis was an Al6060 aluminum alloy, with its properties listed in Table 5.11.
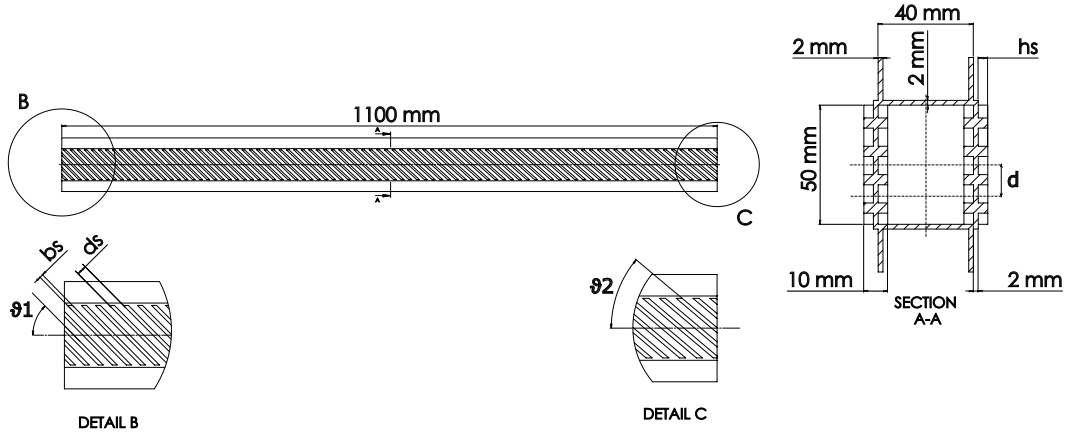
Fig. 6.1 Beam structure geometry.

$$\vartheta(x) = \vartheta_1 + \frac{(\vartheta_2 - \vartheta_1)}{b} x \qquad (6.1)$$

The stiffener orientations evaluated at the prescribed control points with equation 6.1 constitute the design variables of the topology optimization. The linear variation of the curvature has been selected according to [111–113].

The optimization problem for the static bending-torsion considers two different conditions described in Equations 6.2 and 6.3. For the first case, a load can be considered applied in the section shear center of the beam with stiffeners oriented at $0°$ and the objective of the optimization is to obtain a specific coupling effect described by target values of torsion and deflection and achieved through the root and tip orientation of the stiffeners. The second case considers a vertical load applied at a distance $d = 13$ mm from the shear center. In this situation, the vertical load is combined with a torsional moment and the objective is to obtain a configuration able to nullify the torsional angle at the tip. In both cases, the objective is the maximization of the strain energy in Equation 6.4 where $[K]$ is the global stiffness matrix, $\{u\}$ is the vector of nodal displacements, and $\{p\}$ is the vector of nodal moments and forces. The static solution and the strain energy were obtained with a 100-element BTCE model constrained at one end. The optimization was carried out with the MATLAB optimization algorithm "fmincon" which generated randomly 200 initial couples ϑ_1, ϑ_2 for the static analysis. The allowable orientations ranged from ϑ_{lb} to ϑ_{ub}, which represented the lower and upper boundaries of the problem. The stiffness coefficients C_{11}, C_{12}, C_{22}, and C_{33} were computed with Equation 5.2; the

CLT matrices were obtained by considering the stiffeners as equivalent orthotropic materials, and with properties computed with Equation 4.6 and listed in Table 5.11. For each element, the stiffener orientations were considered equal to the mean angle between the angles at the element nodes.
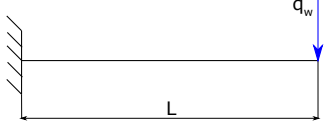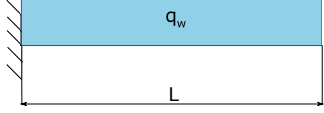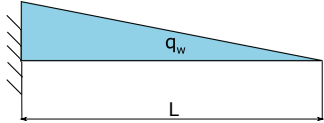
$$
\begin{cases}
max \ \dfrac{1}{2}\{u\}^T [K] \{u\} \\
subject \ to \ [K]\{u\} = \{p\} \\
\vartheta_{lb} \leq \vartheta_{1,2} \leq \vartheta_{ub} \\
|\varphi_{tip}| \geq |\varphi_0| \\
|w_{tip}| \leq |w_0|
\end{cases}
\tag{6.2}
$$

$$
\begin{cases}
max \ \dfrac{1}{2}\{u\}^T [K] \{u\} \\
subject \ to \ [K]\{u\} = \{p\} \\
\vartheta_{lb} \leq \vartheta_{1,2} \leq \vartheta_{ub} \\
\varphi_{tip} = 0°
\end{cases}
\tag{6.3}
$$

$$
\frac{1}{2}\{u\}^T [K] \{u\}
\tag{6.4}
$$

The load cases (LC) considered for the optimization are listed in Table 6.1. For each load case, the force F is equal to 41.37 kg, in accordance with the load considered in [44].

Table 6.1 Load cases descriptions

Load Case	Equation	Graphical Representation
LC1	$q_w = F$	
LC2	$q_w = F/L$	
LC3	$q_w = \dfrac{F}{L}\left(1 - \dfrac{x}{L}\right)$	

The cases with the load applied at the shear center are denoted with LCi_C, while the cases with the load applied at $d = 13\,mm$ from the shear center are denoted with LCi_U. The constraints applied for each optimization are listed in Table 6.2, and those related to the cases LCi_C were the same used in [44]. An additional case is represented by the case $LC1_{AM}$ where the load case LC1 is applied, but the design domain is modified in order to avoid or minimize the use of support structures during an additive manufacturing (AM) process. In general, the minimum overhang angle for a production without the need of support structure is $40°$, for this reason the optimization domain has been reduced to angles larger than $40°$. In general, it is not possible to determine "a priori" if the imposed constraints will be satisfied within the design space: the desired minimum torsion angle could be impossible to achieve with the imposed constraints on the deflection and vice-versa. Subsequent optimization cycles can be performed to refine the optimization, but for the scope of this work, the configuration with the highest strain energy that was closer to the constraints was considered the best solution. As an example of the application for beam structure design optimization, the optimal values related to ϑ_1 and ϑ_2 for each load case were rounded to the nearest angle with a precision of $0.5°$, defining a set of design solutions with a slight variation in final deflections. Such a variation was considered acceptable for the scope of this work. A feasible design was so generated. The chosen configurations were subsequently simulated with three different FE models: a 10 BTCE model, a SHELL FE model, and a TETRA10 FE model, following the

procedure and the FE modeling used in the previous chapters. For each model, the applied load was discretized with 10 concentrated loads positioned at element nodes for the BTCE and applied at the section centroid for the SHELL and the TETRA10 models. The three models were constrained at one end, imposing all the degrees of freedom equal to 0. The BTCE and the SHELL models consisted of ten sections. Each section considered a constant stiffener orientation equal to the mean value of the orientation angle at the section ends. The stiffened plates were considered laminates for the BTCE and the SHELL models, where the curvilinear stiffeners were modeled as an equivalent single layer. Their mechanical properties were computed by means of Equation 4.6.

Table 6.2 Optimizations loads, design limits, and constraints.

Optimization	Load Applied	$[\vartheta_{lb} \; \vartheta_{ub}]$	Constraints $[\varphi_0 \; w_{ub}]$
$LC1_C$	LC1	$[-45° \; 45°]$	$[0.287° \; 14\,mm]$
$LC2_C$	LC2	$[-45° \; 45°]$	$[0.08° \; 4.6\,mm]$
$LC3_C$	LC3	$[-45° \; 45°]$	$[0.03° \; 1.1\,mm]$
$LC1_{AM}$	LC1	$[40° \; 90°]$	$[0.2° \; 17\,mm]$
$LC1_U$	LC1 $d = 13\,mm$	$[-45° \; 45°]$	$\varphi_{tip} < \times 10^{-5}[rad]$
$LC2_U$	LC2 $d = 13\,mm$	$[-45° \; 45°]$	$\varphi_{tip} < \times 10^{-5}[rad]$
$LC3_U$	LC3 $d = 13\,mm$	$[-45° \; 45°]$	$\varphi_{tip} < \times 10^{-5}[rad]$

6.3 Optimization Results

The optimization procedure revealed that many configurations can produce a deformation within the constraints under the specified loads. However, it is possible to determine the configurations that achieved the highest strain energy values. The optimization results are presented in Figures 6.2-6.8. The green circles represent the configuration within the constraints with the highest strain energy value, the blue circles represent the solutions with a tip deformation and a torsion angle with a 5% relative difference with respect to the best solution. The red circles represent the non-convergent solutions or configurations with tip deflections and torsion angles with a relative difference with respect to the best solution greater than 5%. The cases $LC1_U$, $LC2_U$, and $LC3_U$ where the load is positioned outside the shear center and

Fig. 6.2 Optimization results for the $LC1_C$ configuration.

a tip torsion angle equal to zero is required, revealed an interesting pattern for the acceptable configurations. For each of these load cases, the solutions lay on a line at a similar level of strain energy. The optimal solutions are listed in Table 6.3

Table 6.3 Optimal solutions.

Optimization	Applied Load	$[\vartheta_1 \; \vartheta_2]$	w_{tip} [mm]	φ_{tip} [°]
$LC1_C$	LC1	$[30.77° \; 29.96°]$	-13.98	-0.26
$LC2_C$	LC2	$[18.32° \; 21.95°]$	-4.60	-0.08
$LC3_C$	LC3	$[12.50° \; -0.11°]$	-1.10	-0.01
$LC1_{AM}$	LC1	$[45.45° \; 40.24°]$	-15.93	0.2
$LC1_U$	LC1 $d = 13\,mm$	$[30.16° \; -45°]$	-11.88	$|\varphi_{tip}| < 0.01$
$LC2_U$	LC2 $d = 13\,mm$	$[25.10° \; -45°]$	-4.39	$|\varphi_{tip}| < 0.01$
$LC3_U$	LC3 $d = 13\,mm$	$[23.88° \; -45°]$	-1.15	$|\varphi_{tip}| < 0.01$

The optimal orientations for the cases LCi_C were approximated to the nearest value within $0.5°$. Due to the similarities between the optimal solutions for the cases

Fig. 6.3 Optimization results for the $LC2_C$ configuration.
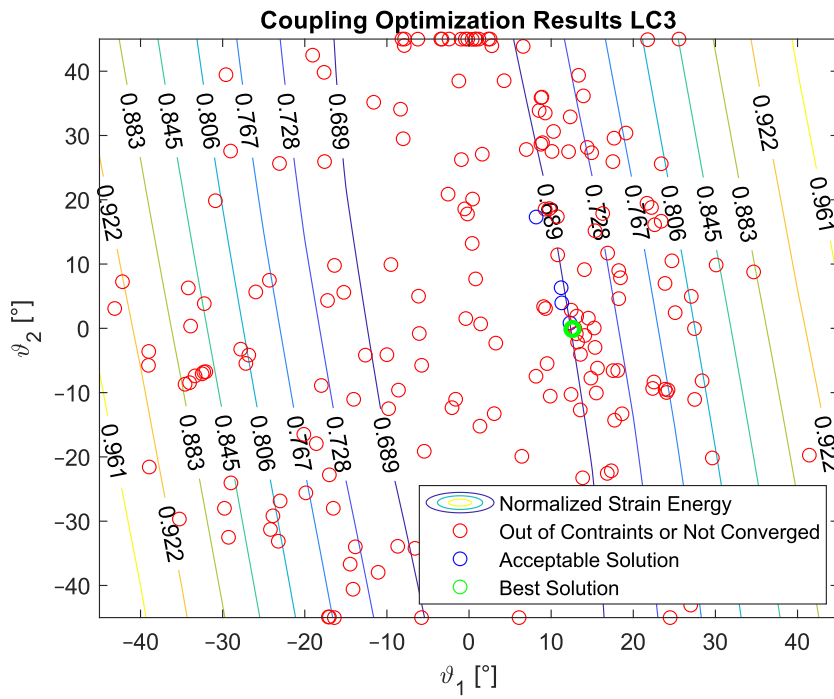
Fig. 6.4 Optimization results for the $LC3_C$ configuration.
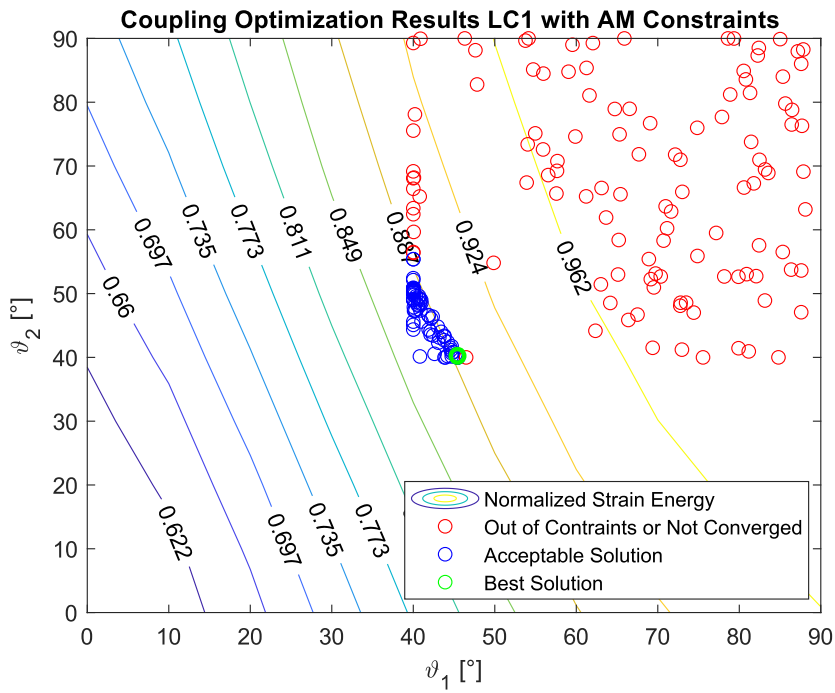
Fig. 6.5 Optimization results for the LC_{AM} configuration.
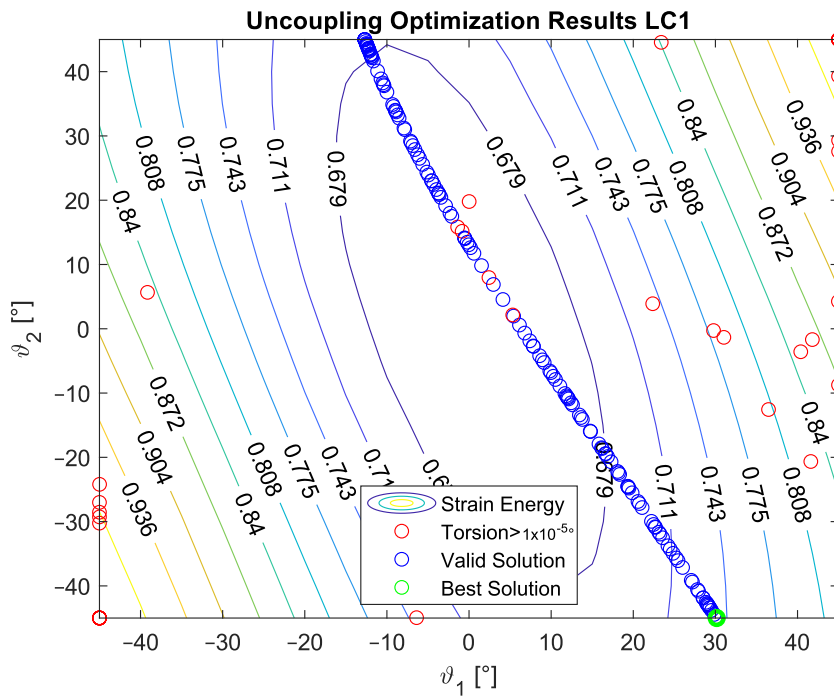
Fig. 6.6 Optimization results for the $LC1_U$ configuration.
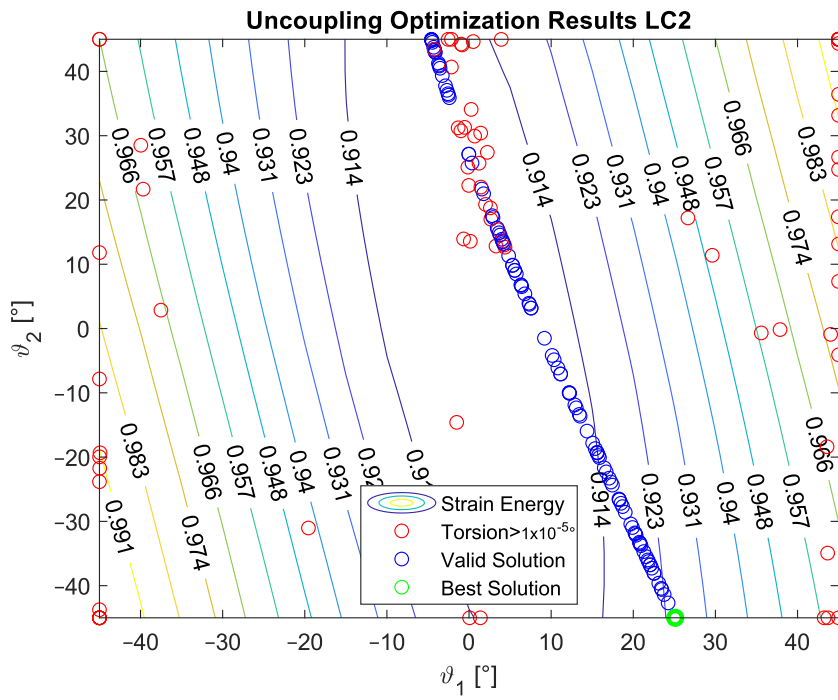
Fig. 6.7 Optimization results for the $LC2_U$ configuration.
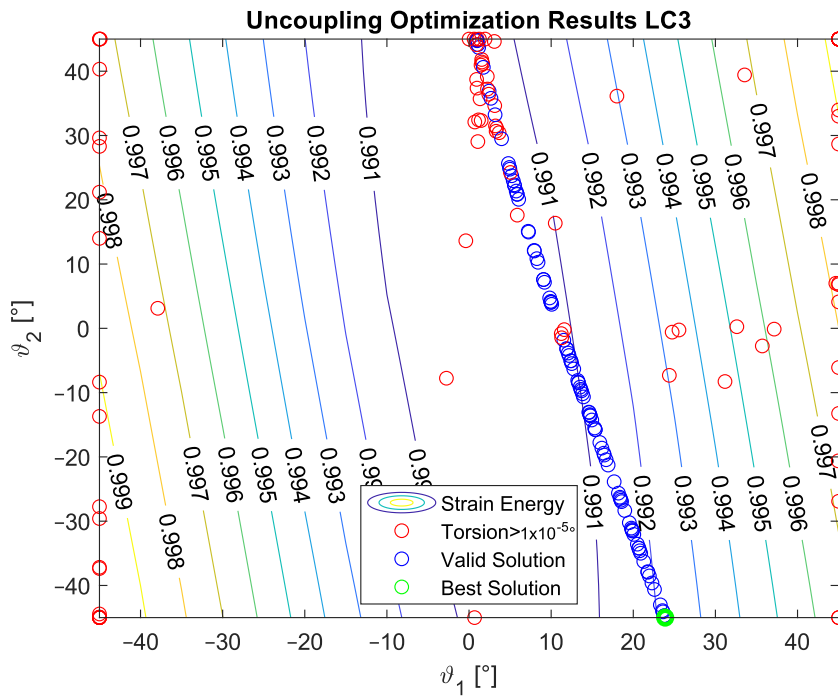
Fig. 6.8 Optimization results for the $LC3_U$ configuration.

LCi_U a single test configuration was chosen. The resulting configurations are listed in Table 6.4 and represented in Figure 6.9A-E. Three different FE models were created for each one of the geometries selected. The reference model consists of a TETRA10 FE model with three-dimensional stiffeners. Another model is obtained with SHELL elements, the beam is divided into ten segments where the orientation of the stiffeners is assumed constant and equal to the mean value between the segment ends orientation. The stiffened panels are considered laminates with two symmetric ESL for the stiffeners and a mid isotropic layer. The mechanical properties of the ESL are computed with Equation 4.6. The third model consists of a BTCE model with the same class of elements used for the optimization. The beam is divided into ten sections corresponding to ten beam finite elements. The stiffness coefficients of the element are computed with Equation 5.2 using the same hypothesis considered for the SHELL FE model. The results obtained with the different FE models are reported in Figures 6.10-6.23 and in Table 6.5 where the relative difference is computed to evaluate the accuracy with respect to the reference model.

Table 6.4 Configurations derived from optimal solutions.

Optimization	Load Applied	$[\vartheta_1 \ \vartheta_2]$
$LC1_C$	LC1	$[31° \ 30°]$
$LC2_C$	LC2	$[18.5° \ 22°]$
$LC3_C$	LC3	$[12.5° \ 0°]$
$LC1_{AM}$	LC1	$[45.5° \ 40°]$
$LC1_U$	LC1 $d = 13\,mm$	$[25° \ -45°]$
$LC2_U$	LC2 $d = 13\,mm$	$[25° \ -45°]$
$LC3_U$	LC3 $d = 13\,mm$	$[25° \ -45°]$

The geometries obtained from the optimal solutions produced a deformation compliant with the design constraints in the majority of the cases considered. Some differences with respect to the deformations results reported in Table 6.4 are present, these differences are linked to the approximations of ϑ_1 and ϑ_2 introduced in the design procedure. In particular, the case $LC2_C$ violated the imposed constraints on the deflection.
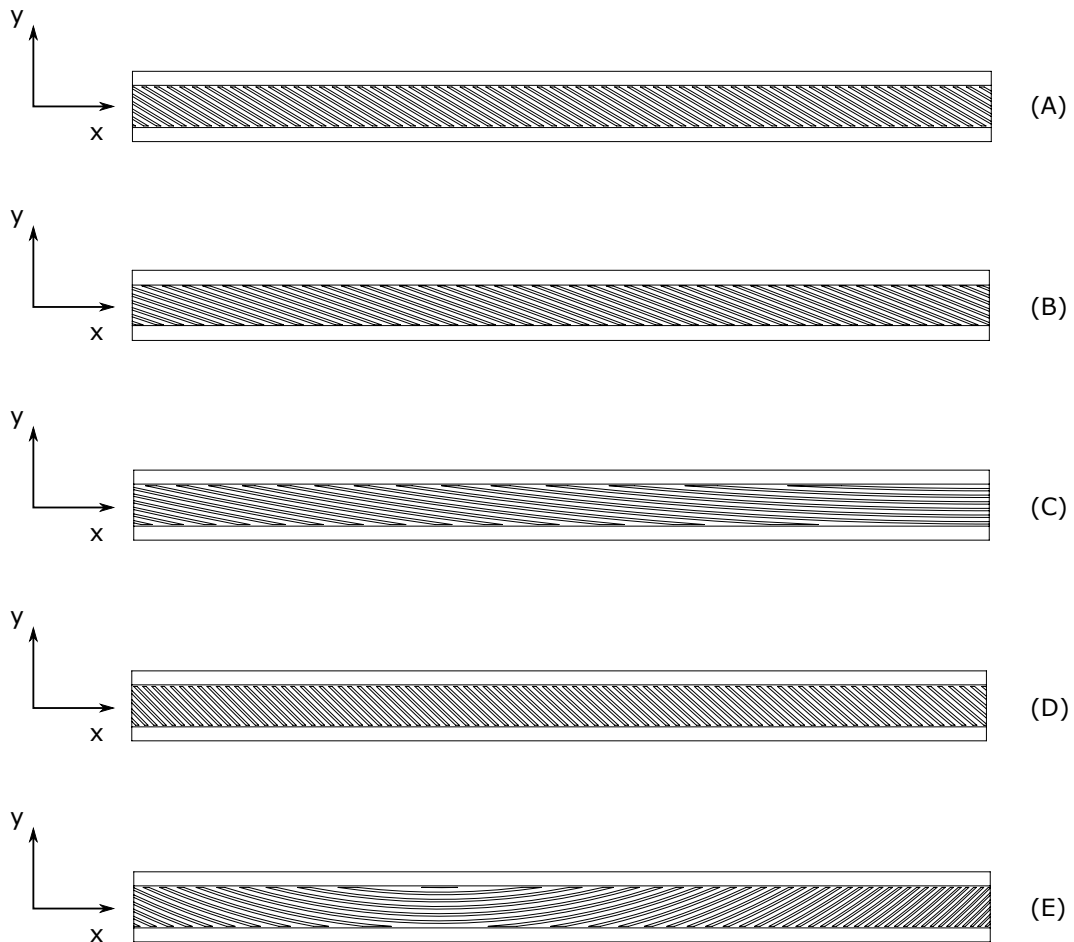
Fig. 6.9 Configuration derived from optimal solutions: (A) $LC1_C$, (B) $LC2_C$, (C) $LC3_C$, (D) $LC1_AM$, and (E) LCi_U.

The BTCE model showed a good agreement with the other FE models with a relative difference generally below 6% with respect to the TETRA10 FE and below 10% if compared with the SHELL FE model results. The developed beam element considered the stiffeners straight along the element length; moreover, an equivalent single-layer material was adopted to describe the stiffened panel behaviors. In addition, the beam element section was considered non-deformable. However, the BTCE model demonstrated good fidelity in representing the static behavior of a box-beam structure with curvilinear stiffener panels. This was a very interesting result for a tool useful in the preliminary design environment.
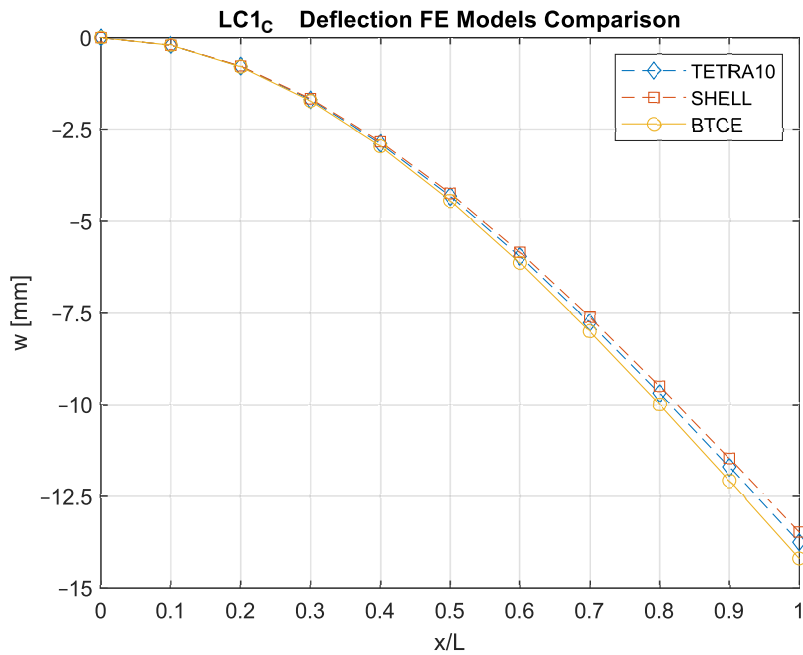
Fig. 6.10 $LC1_C$ deflection results comparison between the TETRA10 FE model, the SHELL FE model, and the BTCE model
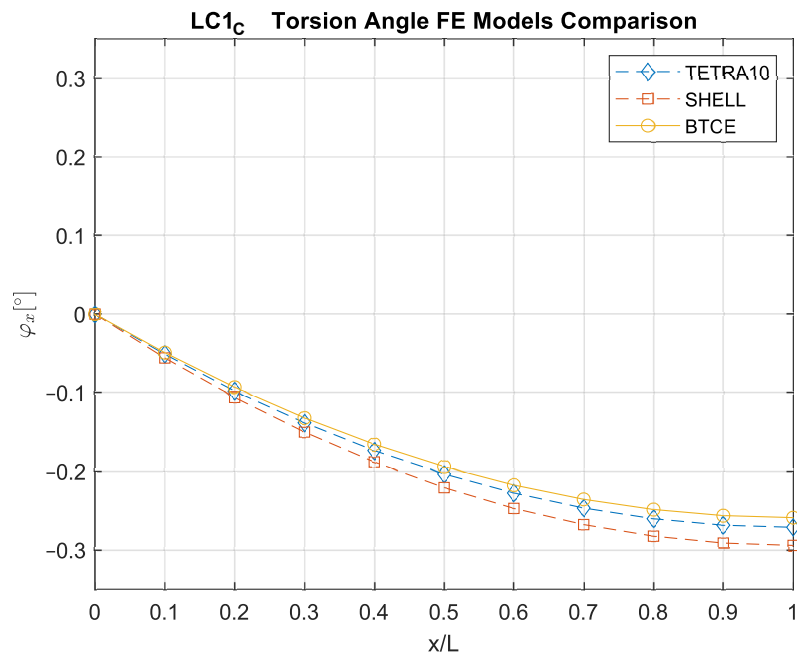
Fig. 6.11 $LC1_C$ torsion results comparison between the TETRA10 FE model, the SHELL FE model, and the BTCE model
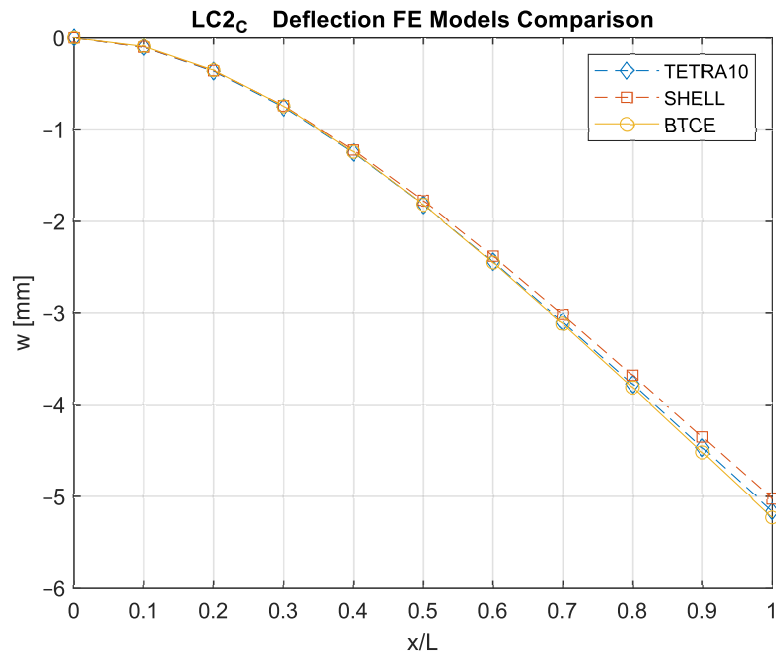
Fig. 6.12 *LC2$_C$* deflection results comparison between the TETRA10 FE model, the SHELL FE model, and the BTCE model
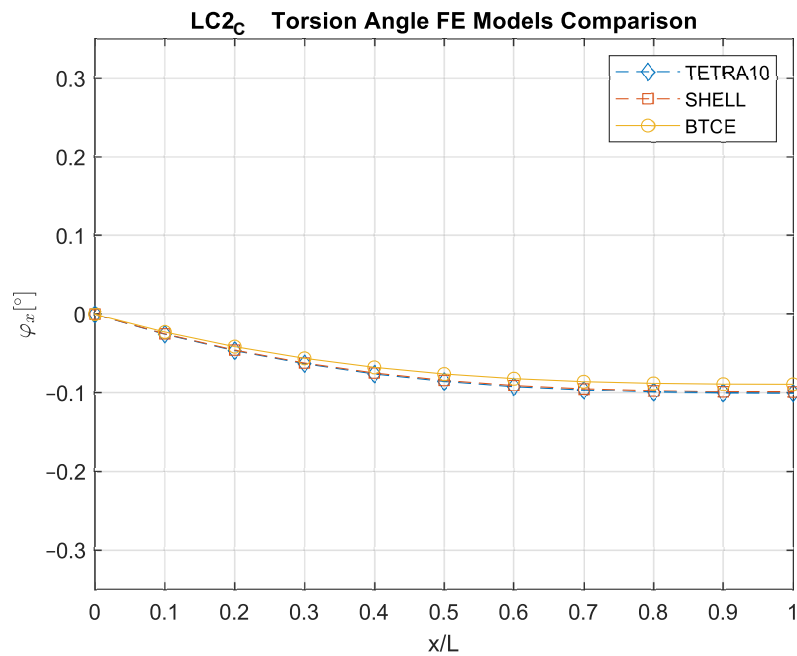
Fig. 6.13 *LC2$_C$* torsion results comparison between the TETRA10 FE model, the SHELL FE model, and the BTCE model
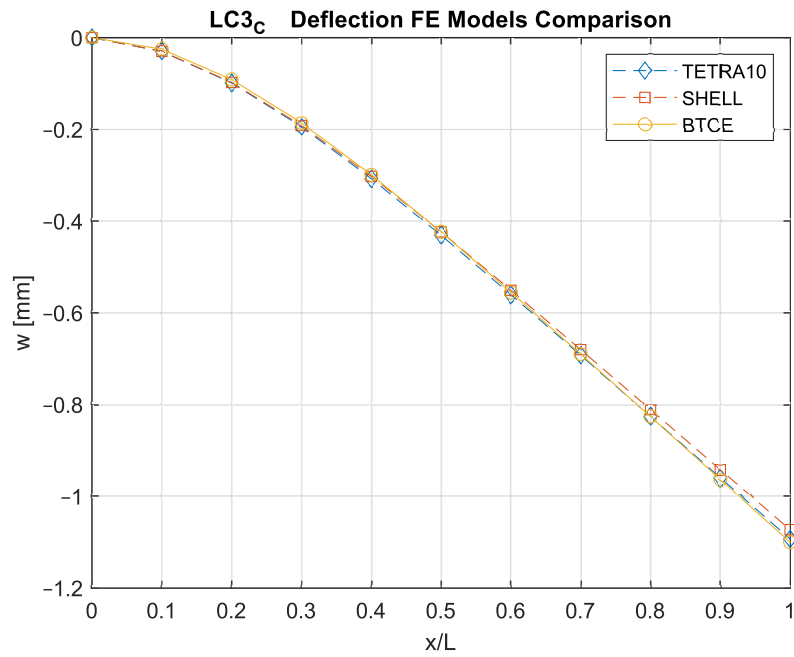
Fig. 6.14 *LC3$_C$* deflection results comparison between the TETRA10 FE model, the SHELL FE model, and the BTCE model
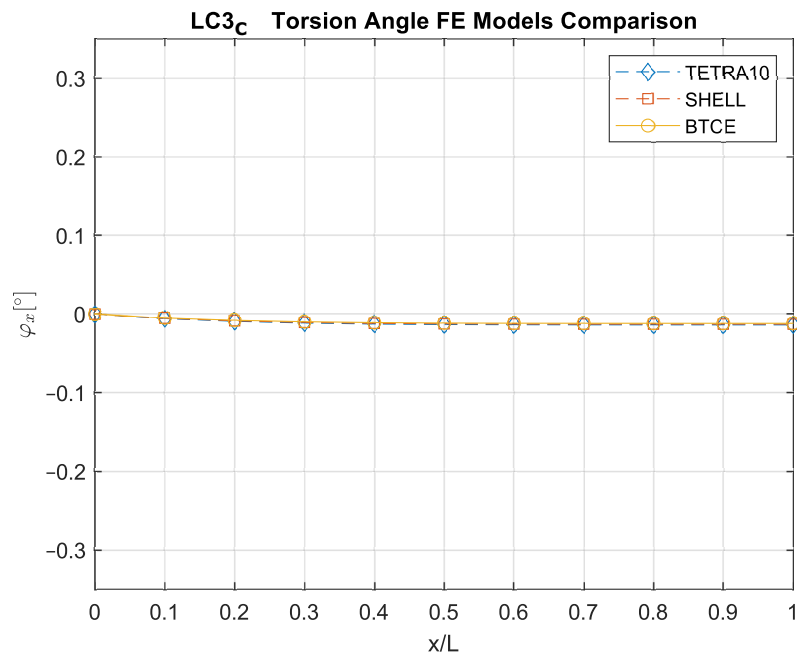
Fig. 6.15 *LC3$_C$* torsion results comparison between the TETRA10 FE model, the SHELL FE model, and the BTCE model
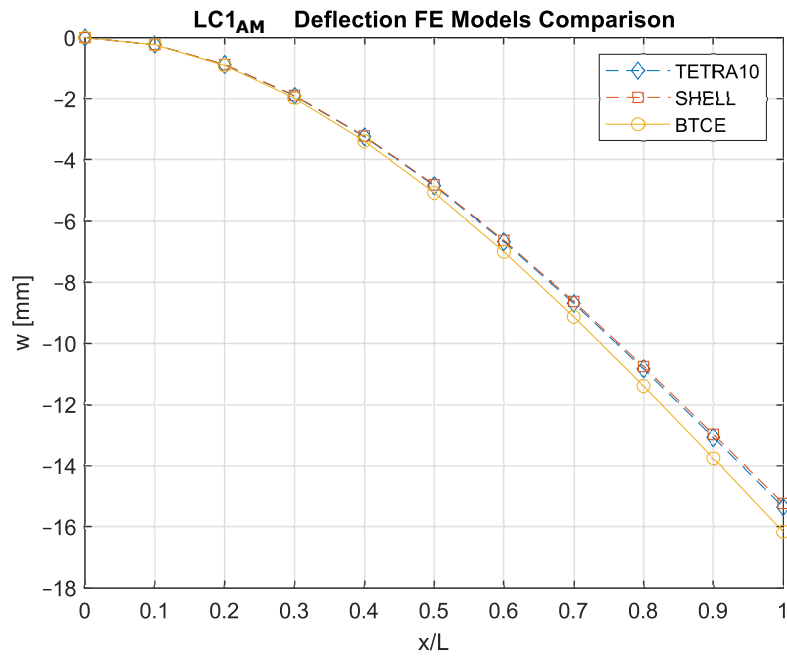
Fig. 6.16 $LC1_{AM}$ deflection results comparison between the TETRA10 FE model, the SHELL FE model, and the BTCE model
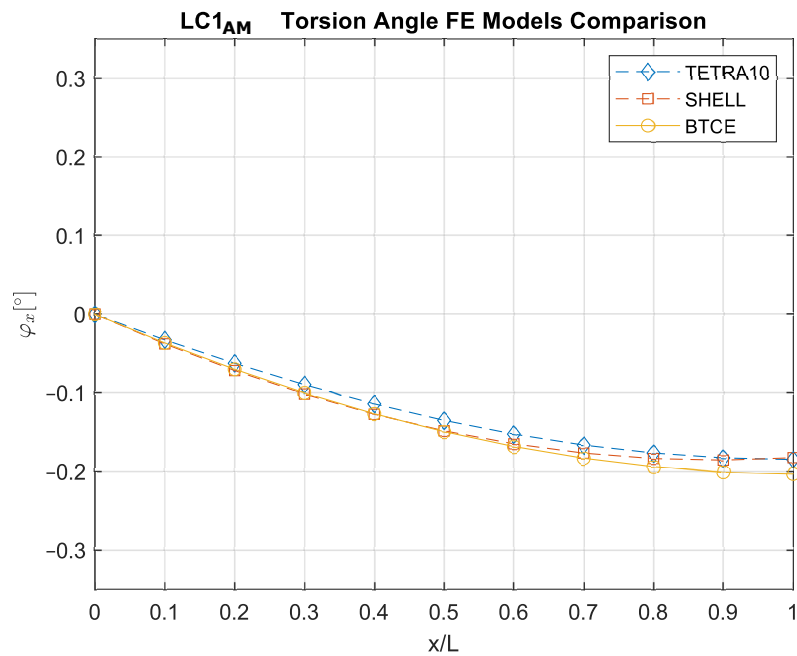
Fig. 6.17 $LC1_{AM}$ torsion results comparison between the TETRA10 FE model, the SHELL FE model, and the BTCE model
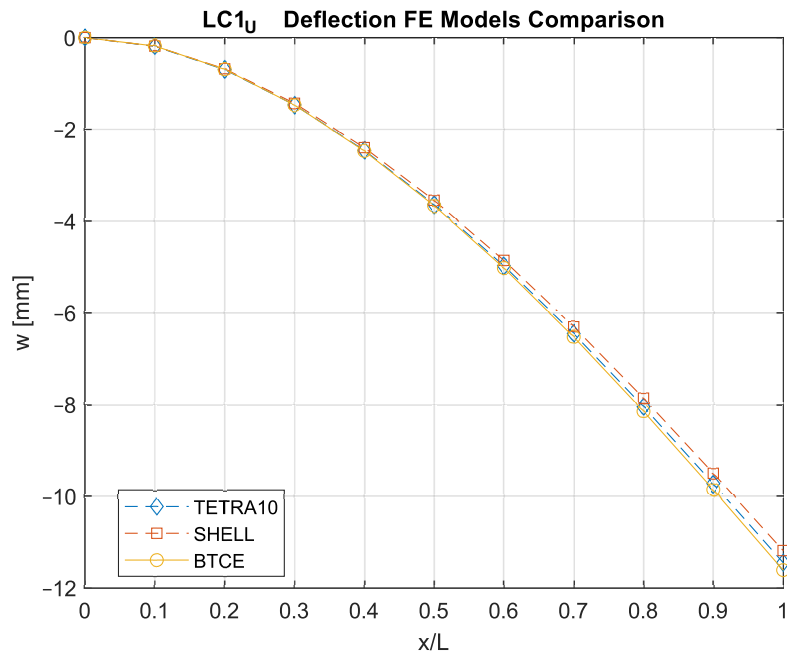
Fig. 6.18 $LC1_U$ deflection results comparison between the TETRA10 FE model, the SHELL FE model, and the BTCE model
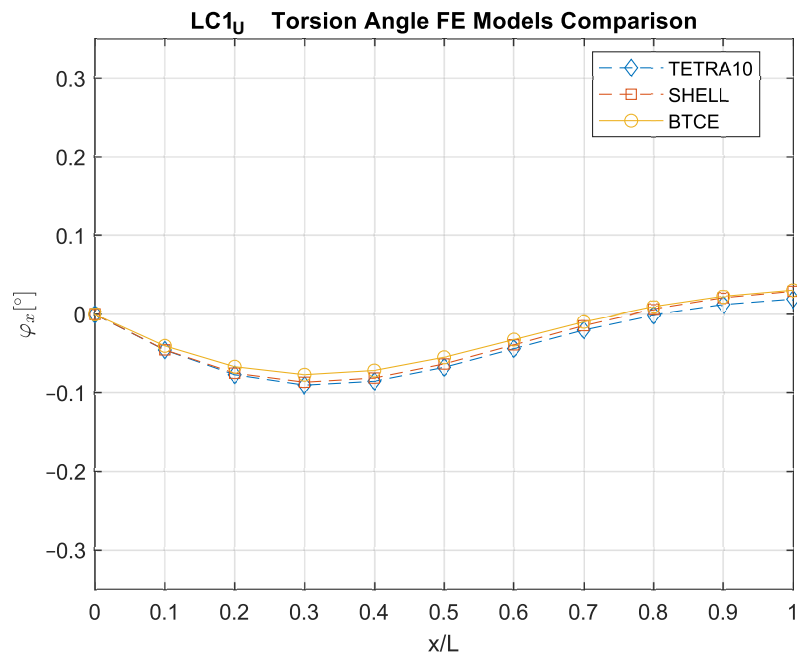
Fig. 6.19 $LC1_U$ torsion results comparison between the TETRA10 FE model, the SHELL FE model, and the BTCE model
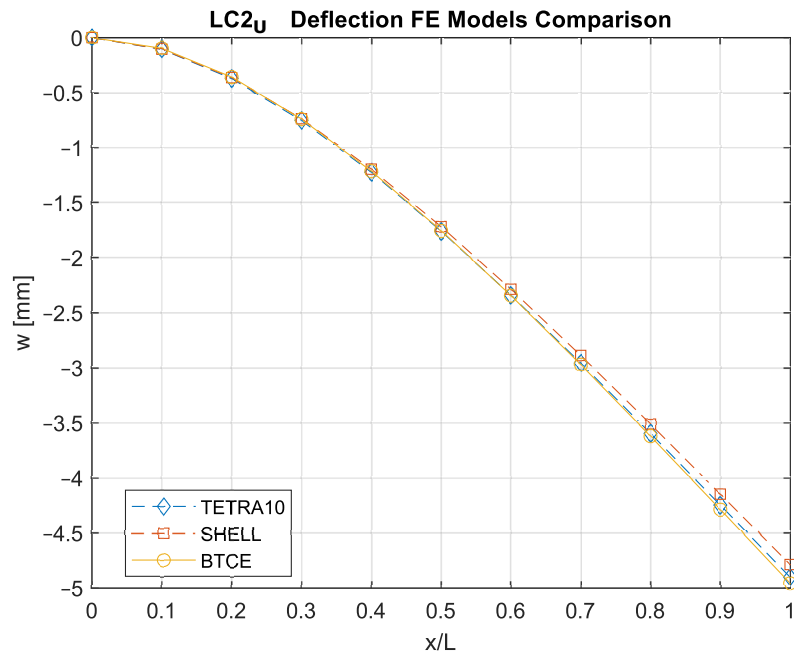
Fig. 6.20 $LC2_U$ deflection results comparison between the TETRA10 FE model, the SHELL FE model, and the BTCE model
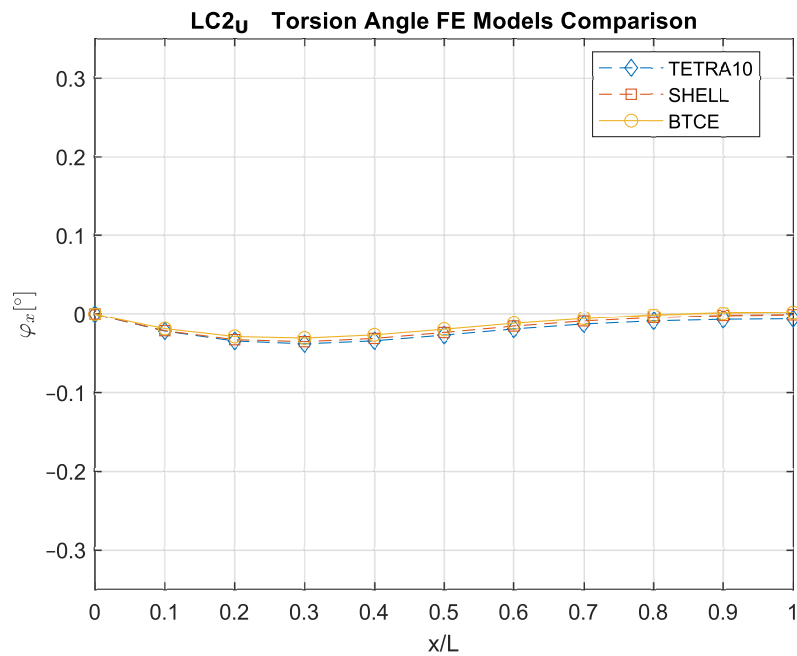
Fig. 6.21 $LC2_U$ torsion results comparison between the TETRA10 FE model, the SHELL FE model, and the BTCE model
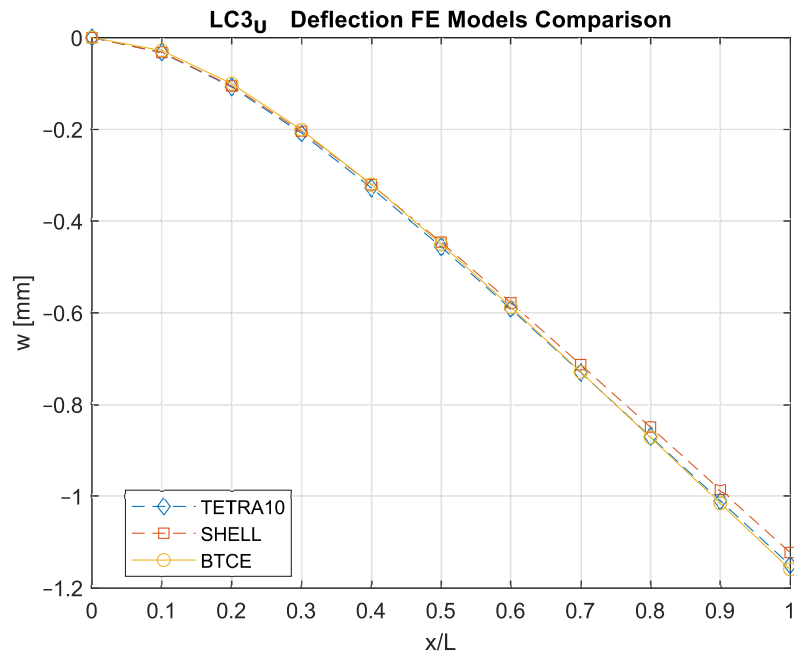
Fig. 6.22 $LC3_U$ deflection results comparison between the TETRA10 FE model, the SHELL FE model, and the BTCE model
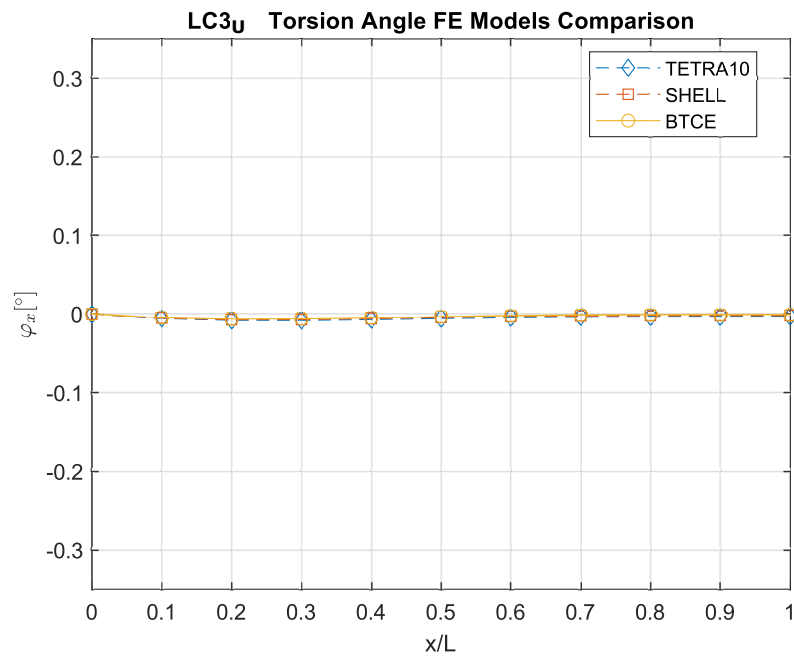
Fig. 6.23 $LC3_U$ torsion results comparison between the TETRA10 FE model, the SHELL FE model, and the BTCE model

Table 6.5 Configurations derived from optimal solutions.

		Load Positioned in the Shear Center		
Load Case	**DOF**	**BTCE**	**SHELL**	**TETRA10**
LC1	w [mm]	-14.20	-13.47 (5.4%)	-13.75 (3.3%)
	φ_x [°]	-0.26	-0.29 (10.3%)	-0.27 (3.7%)
LC2	w [mm]	-5.23	-5.03 (4.0%)	-5.16 (1.4%)
	φ_x [°]	-0.09	-0.10 (10.3%)	-0.10 (3.7%)
LC3	w [mm]	-1.10	-1.07 (0.9%)	-1.09 (0.9%)
	φ_x [°]	-0.01	-0.01 (0%)	-0.01 (0%)
LC1 AM	w [mm]	-16.17	-15.24 (6.1%)	-15.34 (5.4%)
	φ_x [°]	-0.20	-0.18 (11.1%)	-0.19 (5.26%)
		Load Positioned Outside the Shear Center		
Load Case	**DOF**	**BTCE**	**SHELL**	**TETRA10**
LC1	w [mm]	-11.61	-11.19 (3.8%)	-11.45 (1.4%)
	φ_x [°]	0.03	0.03 (0%)	0.02 (50%)
LC2	w [mm]	-4.96	-4.79 (3.5%)	-4.90 (1.2%)
	φ_x [°]	$-0.01 < \varphi_x < 0.01$	$-0.01 < \varphi_x < 0.01$	$-0.01 < \varphi_x < 0.01$
LC3	w [mm]	-1.10	-1.07 (0.9%)	-1.09 (0.9%)
	φ_x [°]	$-0.01 < \varphi_x < 0.01$	$-0.01 < \varphi_x < 0.01$	$-0.01 < \varphi_x < 0.01$

6.4   Summary and Conclusions

The utilization of a beam finite element with bending-torsion formulation for optimizing stiffener paths in box-beam structures with curvilinear stiffened panels was introduced and validated. Optimization efforts were directed towards three distinct load cases applied along the beam axis, including a typical scenario associated with geometric constraints in additive manufacturing (AM) processes. The objective of the optimization procedure was maximizing strain energy under prescribed loads while ensuring the selected configuration met global constraints for maximum vertical deflection and minimum torsional angle. This approach facilitated achieving the highest level of bending-torsion coupling. A secondary optimization focused on the same load cases but positioned at one-fourth of the beam width, introducing an additional torsional moment. Here, the aim was to minimize the bending-torsion effect, thereby maximizing strain energy while maintaining a torsion angle of zero at the tip. The outcomes of the optimization process were translated into beam structure designs to evaluate their structural performance and verify the BTCE ability to accurately represent deformations under static loads of beam structures with curvilinear stiffeners. For each design, TETRA10 FE, SHELL FE, and BTCE models were created, and static analyses were conducted. Comparisons among these different FE models demonstrated the BTCE precision, with relative differences in deformation results generally below 6% when compared to TETRA10 FE models and below 10% when compared to SHELL FE models. Discrepancies between models were attributed to assumptions made during the BTCE derivation, such as straightening stiffeners along the element length and reducing them to an equivalent single layer, as well as considering the beam element section as non-deformable. The potential of the BTCE as both an optimization and static analysis tool for beam structures with curvilinear stiffeners was confirmed. Furthermore, the ability to achieve specific configurations capable of enhancing or reducing the bending-torsion effect was demonstrated. Additionally, an optimal configuration addressing geometric constraints for AM production, featuring a self-supporting structure to minimize post-production machining, was investigated.

Chapter 7

BTCE Divergence Analysis of Structures with Bending-Torsion Coupling

Some of the contents and derivation presented in this chapter have been previously published in *AIAA SCITECH 2024 Forum*.

C. Patuelli, E. Cestino, and G. Frulla. Aeroelastic analysis through non-linear beam finite elements with bending-torsion coupling formulation.In AIAA SCITECH 2024 Forum, 2024.

7.1   Introduction and Motivation

High aspect ratio structures are particularly affected by aeroelastic phenomena like divergence and flutter. Moreover, large deformations can introduce non-linear structural effects which can further alter the aeroelastic behavior of wing structures [79]. Divergence is a typical aeroelastic instability involving torsion deformation which can potentially increase and become critical. Bending-torsion flutter is an aeroelastic dynamic instability that causes increasing amplitude oscillation and can become dangerous for structural integrity. However, aeroelastic phenomena can be controlled through the use of aeroelastic tailoring. Sherrer et al. [114] used aeroelastic tailoring to increase the divergence speed of composite forward-swept wing and validated the results with wind tunnel tests. Guo [115] demonstrated

aeroelastic tailoring to significantly reduce the weight of aircraft structures and increase up to 30% of the flutter speed. Librescu and Song [52] adopted a thin-walled anisotropic composite beam model to study the sub-critical static aeroelastic response and the divergence instability of swept-forward aircraft wing structures. Li et al. [116] presented a rapid computational fluid dynamics-based aeroelastic tool that used a reduced order model for aerodynamics that is updated for any modification of the structure by using the structural dynamics reanalysis method.

Aeroelastic analysis requires the interaction between aerodynamic and structural analysis. Coupled computational fluid dynamics and finite element method formulation for aeroelastic analysis can be used for detailed simulations [81]. These models are generally very advanced and usually require a large computational power which is not efficient for early design stage optimization. For this reason, low-order structural models can help to reduce the computational cost and guarantee similar accuracy for preliminary optimization. Geometrically exact beam formulation is a popular approach [81, 82] and has been used in several works for highly deformed wing structure analysis. Drela [85] used beam elements with non-linear formulation to develop an aerodynamic and structural simulation model for flexible aircraft, while Patil [86] presented a theory for flight-dynamic analysis of highly flexible wing configurations accounting for geometric non-linearities. More recently, a new class of low-order structural models relying on high-order modal expansion has been developed [87, 117]. However, these models require non-linear static responses of a Finite Element Model (FEM) to identify modal expansion terms.

Anisotropic materials can be adopted to enhance the aeroelastic performances of wing box structures according to the concept of aeroelastic tailoring [118, 36]. This technique demonstrates important advantages when combined with composite material where the lay-ups can be optimized to mitigate the aeroelastic phenomena. Other aeroelastic tailoring techniques involve functionally graded materials [119–121], variable angle tow [122, 111], or curvilinear stiffener panels [111, 40]. Aeroelastic tailoring relies on the structural couplings introduced with a specific orientation of composite fibers or stiffeners to modify the aeroelastic properties of a wing structure. The optimization of these structures can be very demanding in terms of time and computational costs, for this reason, equivalent models with beam finite elements can be adopted during early design stages. The problem encouraged the development of aeroelastic prediction methods that account for the nonlinear effects on highly flexible structures [123–125], but the introduction of a nonlinear

beam finite elements that account for the material bending torsion coupling could be a benefit for this class of analysis.

The beam finite element with bending torsion coupling formulation developed in this thesis can be efficiently adopted as a structural model for divergence analysis. In this chapter, a structural analysis performed using a BTCE model is coupled with aerodynamic analysis to compute the divergence speed of wing structures with oriented composite fibers or stiffeners. The use of the model presented in this chapter is not limited to divergence analysis, but it can be used to compute the equilibrium configuration of wing structures under aerodynamic loads.

7.2   Divergence Analysis Model

The model presented in this chapter is based on iterations of structural and aerodynamic simulation to find equilibrium configurations. When an equilibrium configuration is not reached, it means that the speed considered is above the divergence speed. The model can consider wing structures with sweep angle, dihedral angle, variable chord, and different airfoils. Once the geometry is described, the initial configuration can be used as input for the aerodynamic model alongside the aerodynamic parameters such as air density, flight speed, and vortices. The aerodynamic analysis is performed with Athena Vortex Lattice (AVL). AVL is a software created by Mark Drela from MIT Aero & Astro and Harold Youngren. The software is based on the numerical method Vortex Lattice Method (VLM). VLM calculates lift curve slope, induced drag, and lift distribution for a given wing configuration. The wing is modeled with horseshoe vortices distributed along the span and chord. These vortices produce a lift according to Biot-Savart Law, Kutta-Joukovsky theorem, Herman von Helmholtz theory, and Prandtl lifting-line theory. The wing structure geometry is described, in the aerodynamic model, with panels delimited by defined sections. AVL computes the resultant forces acting on each panel and its vertical (lift) and horizontal (drag) components. These components can be used to obtain the loads acting on the nodes of the structural model and therefore to obtain the corresponding deformations. The structural model consists of beam elements (BTCE) with nodes coincident with the position of the sections defined in the aerodynamic model, with this method the displacement of the nodes corresponds to the displacement of the aerodynamic section. Each element represents a portion of the wing structure

which can present different geometry, stiffness properties, materials or play angle with respect to other areas of the wing. These differences can be represented with finite elements associating the different characteristics of the wing portion to the corresponding element. The aerodynamic resultants are computed at the center of the wing panel and must be transformed in nodal forces, this can be achieved with an interpolation of the panel loads. Each element has an orientation in the space given by the initial geometry with sweep angle, dihedral angle and, rigid angle in addition to the deformation caused by the aerodynamic loads. For this reason, the element and the nodal loads should be oriented with a transformation matrix to obtain the system in global coordinates and therefore obtain the deformations in the global reference system. The linear static system can be solved to obtain the nodal displacements and rotation which describe the new deformed geometry and therefore the input for a new aerodynamic analysis. The process is iterated with the deformed geometry until the deformed configuration does not change the aerodynamic loads of the previous iteration and thus equilibrium is reached or until the deformations become too large indicating that the system is in divergence condition. The analysis workflow is summarized in Figure 7.1.

7.3   Aeroelastic Divergence of Coupled Graphite/Epoxy Cantilever Plates

The divergence analysis model has been tested on beam structures with bending-torsion coupling given by oriented fibers. The test case consists of graphite/epoxy cantilever plates with different fiber orientations. The plates are the same studied by Hollowell and Dungundji [64], they conducted an analytical and experimental investigation to determine the aeroelastic divergence behavior of unswept, rectangular wings simulated by graphite/epoxy, cantilevered plates with various bending-torsion stiffness coupling represented in Figure 7.2. The plates have an effective length $l = 305 \ mm$ and a chord $c = 76 \ mm$ for an aspect ratio $AR = 8$. The total thickness is six plies.

The plates were laminated with a midplane symmetric stacking sequence, and the graphite/epoxy tape used for the experimental models was Hercules ASI/3501-6 with

Initial Configuration

⎧ Wingspan
⎪ Sweep Angle
⎪ Dihedral Angle
⎪ Chord
⎨ Vortices
⎪ Airfoils
⎪ Incidence
⎪ Air Density
⎩ Flight Speed

AVL → Aerodyanmic Loads → FEM

Deformed Geometry

Is the new geometry different from the previous one?

Yes

No

END
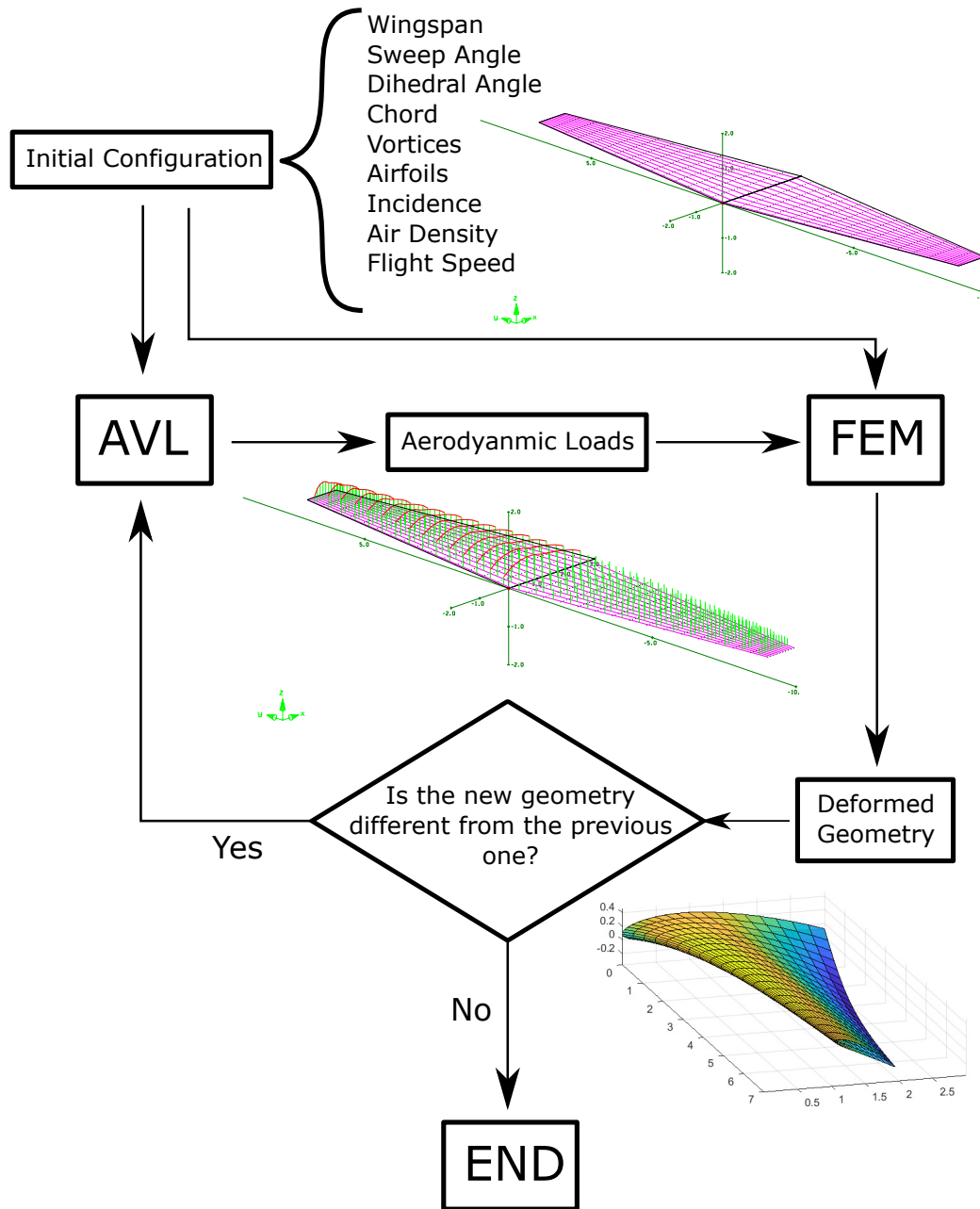
Fig. 7.1 Analysis workflow.
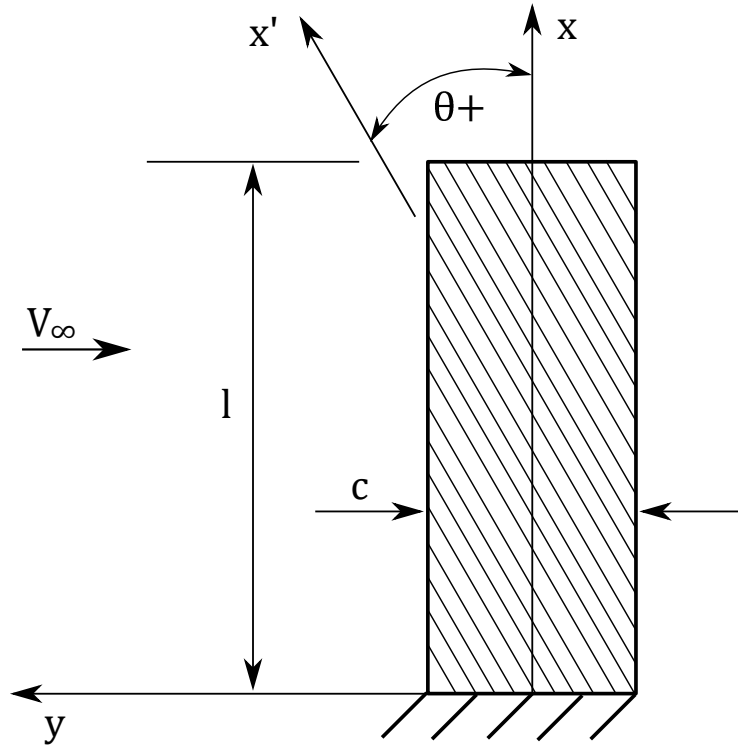
Fig. 7.2 Plate Layout

mechanical properties listed in Table 7.1, with the orthotropic engineering constants it is possible to obtain the off-axis lamina modulus components Q_{ij}.

The laminate flexural and torsional stiffness can be obtained with equation 7.1 according to [126, 127].

$$GJ_t = 4c \left(D_{66} - \frac{D_{26}^2}{D_{2}2} \right) \tag{7.1a}$$

$$K = 2c \left(D_{11} - \frac{D_{12}D_{26}}{D_{2}2} \right) \tag{7.1b}$$

$$EI_y = c \left(D_{11} - \frac{D_{12}^2}{D_{2}2} \right) \tag{7.1c}$$

$$EI_z = E_L \frac{c^3 t}{12} \tag{7.1d}$$

Table 7.1 Hercules ASI/3501-6

Property	In-plane loading	Out-of-plane loading
E_L [MPa]	130×10^3	98×10^3
E_T [MPa]	10.5×10^3	7.9×10^3
ν_{LT}	0.28	0.28
G_{LT} [MPa]	6.0×10^3	5.6×10^3
Ply Thickness [m]	0.134×10^{-3}	
Density [kg/m^3]	1520	

Table 7.2 Flexural moduli for laminates [Nm]

Laminate	D_{11}	D_{12}	D_{16}	D_{22}	D_{26}	D_{66}
$[0_2/90]_s$	4.125	0.096	0	0.490	0	0.243
$[\pm45/0]$	1.550	0.928	0.437	1.404	0.437	1.075
$[+45_2/0]_s$	1.550	0.928	0.946	1.404	0.946	1.075
$[-45_2/0]_s$	1.550	0.928	-0.946	1.404	-0.946	1.075
$[+30_2/0]_s$	2.704	0.720	1.180	0.666	0.459	0.866
$[-30_2/0]_s$	2.704	0.720	-1.180	0.666	-0.459	0.866

Where the flexural modulus D_{ij} for an n-play laminate with arbitrary ply angle orientation was obtained from Equation 7.2, l is the lamina length and t is the lamina total thickness.

$$D_{ij} = \sum_{k=1}^{n} Q_{ij}^{(\theta_k)} \left[z_k^3 - z_{k-1}^3 \right] / 3 \tag{7.2}$$

Where $Q_{ij}^{(\theta_k)}$ is the off-axis lamina modulus of the k-th ply, θ_k the ply angle of the k-th ply, and z_k the distance up from the midplane to the upper surface of the k-th ply. The flexural moduli computed for the six laminates investigated are reported in Table 7.2

The divergence analysis is performed with multiple simulations at increasing flight speed until the structure presents divergence, and then the divergence speed value is refined with the bisection method. The lift curve slope $Cl_\alpha = \partial C_l / \partial \alpha$ can

Table 7.3 Divergence velocities [m/s]

Laminate	Experimental	Analytical $(CL_\alpha = 2\pi)$	Analytical (CL_{α_r})	BTCE $(CL_\alpha = 2\pi)$	BTCE (CL_{α_r})
$[0_2/90]_s$	flutter	22.3	25.0	22.62	24.34
$[\pm45/0]$	>32.0	infinite	no divergence	>32.0	>32.0
$[+45_2/0]_s$	flutter	infinite	no divergence	>32.0	>32.0
$[-45_2/0]_s$	12.5	9.9	11.1	11.56	12.44
$[+30_2/0]_s$	flutter	infinite	no divergence	>32.0	>32.0
$[-30_2/0]_s$	11.7	10.2	11.5	11.12	11.94

be assumed equal to 2π, however, this approximation can reduce the accuracy for small AR. The divergence analysis has been performed considering also an empirical correction of Cl_α of the airfoil which is reduced with a coefficient equal to 0.8 according to [128].

7.3.1   Divergence Analysis Result

The results obtained are summarized in Table 7.3. The first three columns report the experimental and analytical results presented in [64], while the last two columns present the results obtained with the procedure here presented computed for $Cl_\alpha = 2\pi$ and for Cl_{α_r}.

The $[0_2/90]_s$,$[-45_2/0]_s$ and $[-30_2/0]_s$ which have a negative or null bending-torsion coefficient presented divergence at a certain speed. The plate with lamination $[0_2/90]_s$ can be used as a reference case, the plate has straight fibers and therefore bending, and torsion are uncoupled, during the experimental tests reported in [64] the specimen experienced flutter right before divergence and this affected the detection of the divergence velocities. However, as shown in Figure 7.3, the numerical results here presented are in accordance with the previously published analytical results. The lamination $[-45_2/0]_s$ present to a negative bending-torsion stiffness D_{16}, for this reason, the section of the beam increases the incidence when the aerodynamic loads cause a deflection. This coupling determines a reduction of the divergence speed with respect to the straight lamination as shown in Figure 7.4. The results present some differences if compared to the analytical divergence velocities, however, they seem to be more in agreement with the experimental evidence. The test case with
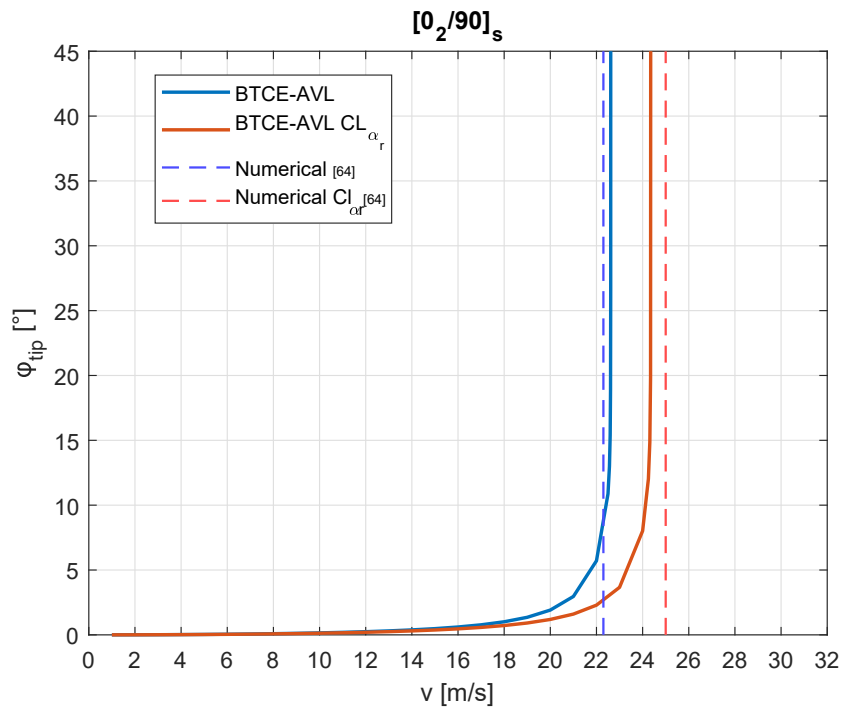
Fig. 7.3 Results comparison plate $[0_2/90]_s$

lamination $[-30_2/0]_s$ has the most negative bending-torsion stiffness D_{16} which reduce further the divergence velocity as shown in Figure 7.5. In this case, there is good accordance with both experimental and analytical results.

7.3.2   Deformation Results

The procedure presented can be applied also to compute the equilibrium deformation of plates with bending torsion coupling subject to aerodynamic loads. Hollowell [129] studied the effect of angle of attack on tip deflection and rotation of coupled graphite/epoxy cantilever plates with different laminations. In particular studied the laminations $[\pm 45/0]$ and $[-45/0]_s$. The results obtained have been compared with the equilibrium deformations obtained with the BTCE model and are presented in Figures 7.6-7.9.

For the lamination $[\pm 45/0]$ the results concerning the tip deflection are in good agreement with the experimental data, the deflection predicted with the BTCE model has a good level of accuracy even for high levels of deformation up to 50%. Some discrepancies are present in the case where $\alpha_0 = 6°$ for high deformations. The
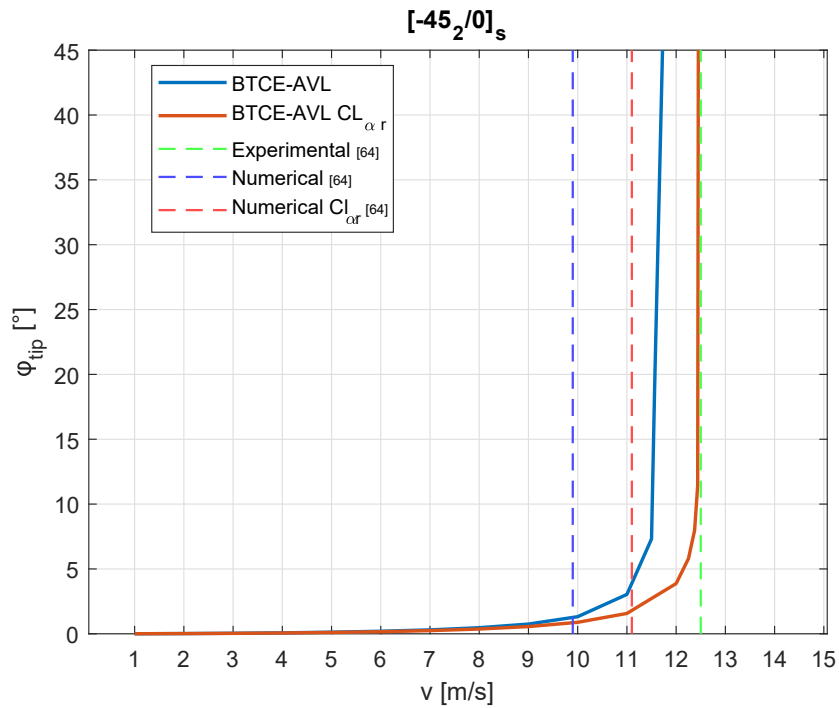
Fig. 7.4 Results comparison plate $[-45_2/0]_s$
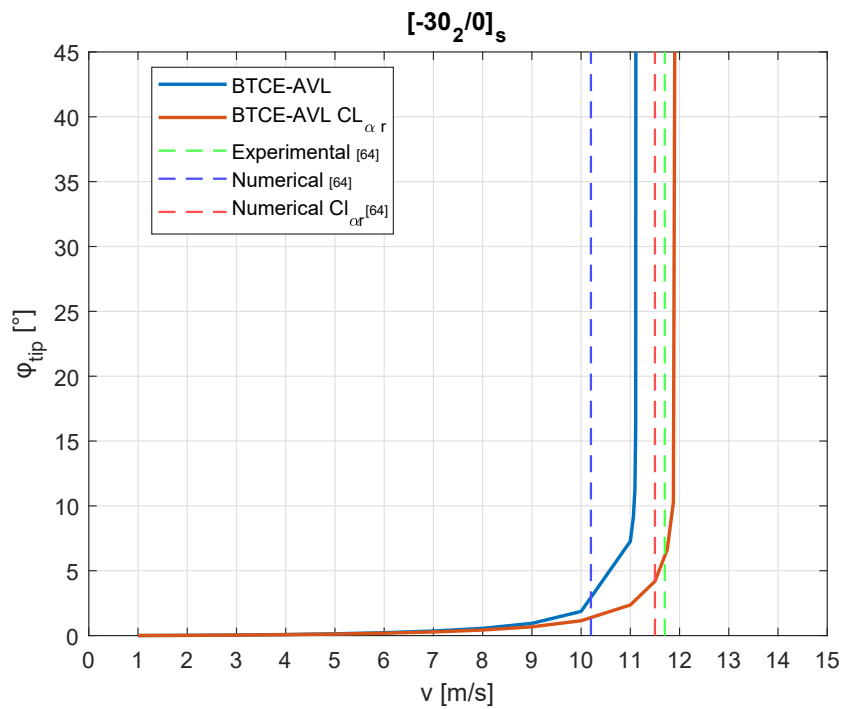
Fig. 7.5 Results comparison plate $[-30_2/0]_s$
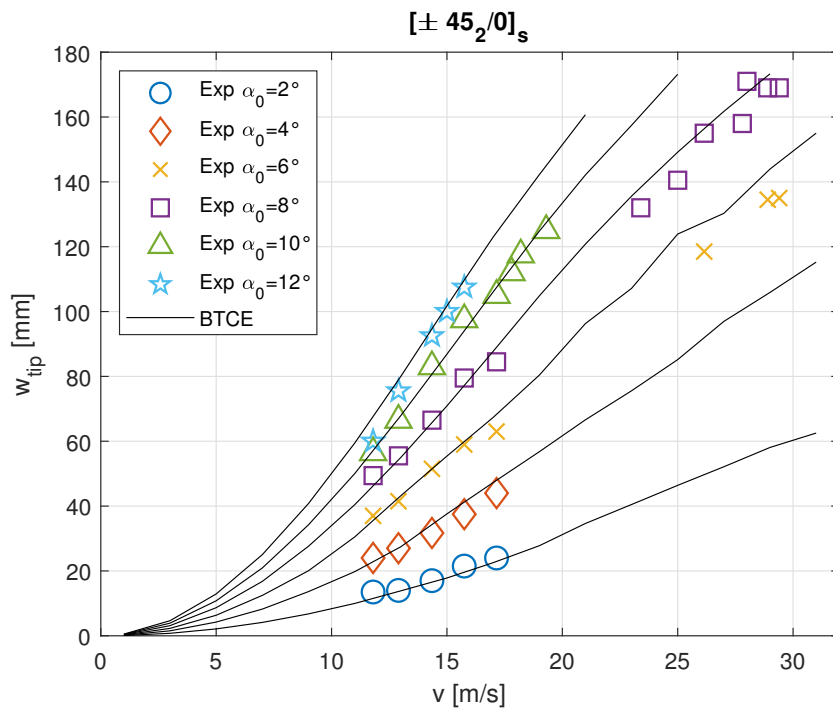
Fig. 7.6 Tip deflection at different angle of attack $[\pm 45/0]$
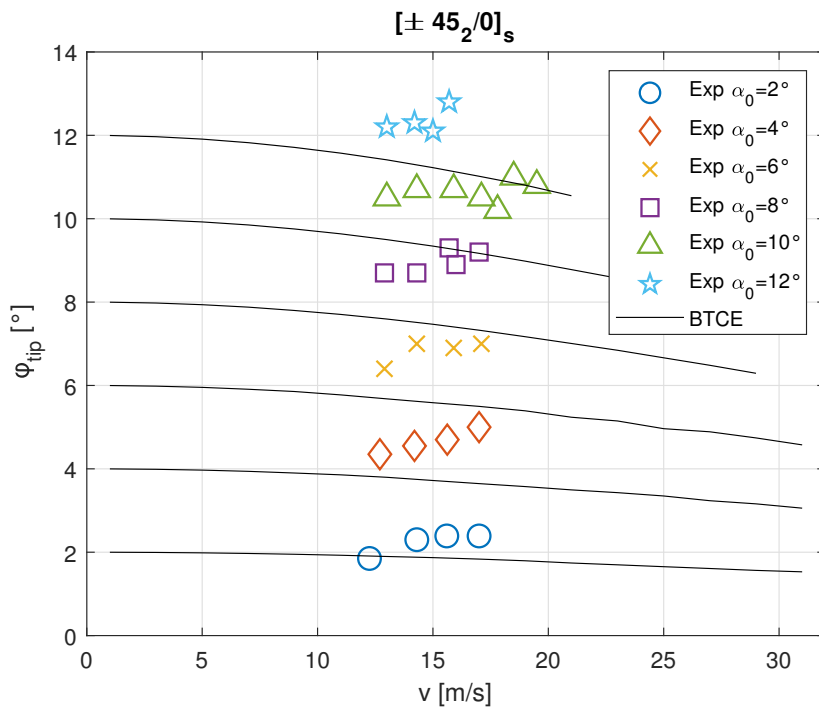
Fig. 7.7 Tip rotation at different angle of attack $[\pm 45/0]$
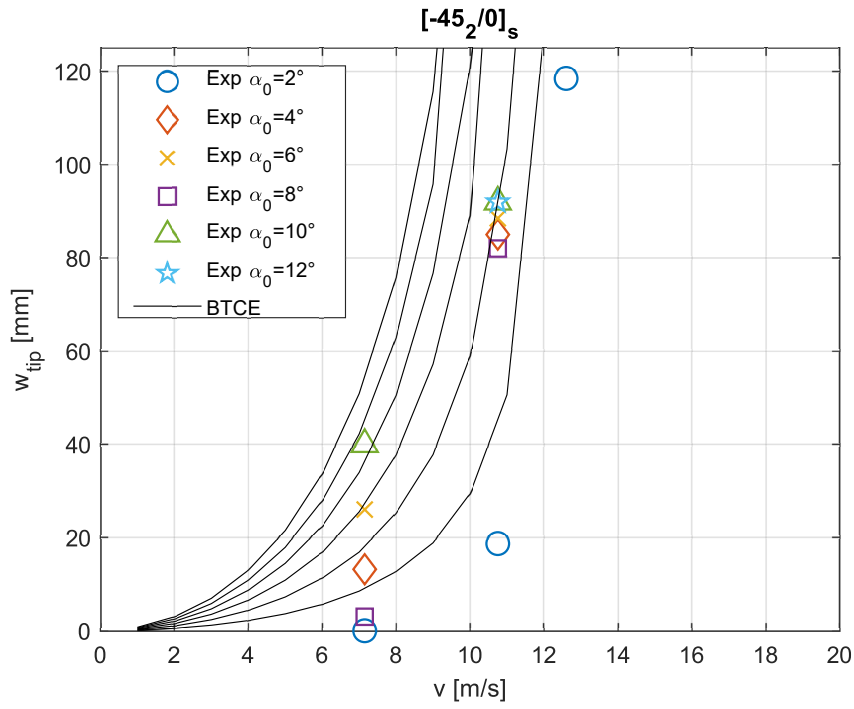
Fig. 7.8 Tip deflection at different angle of attack $[-45_2/0]_s$
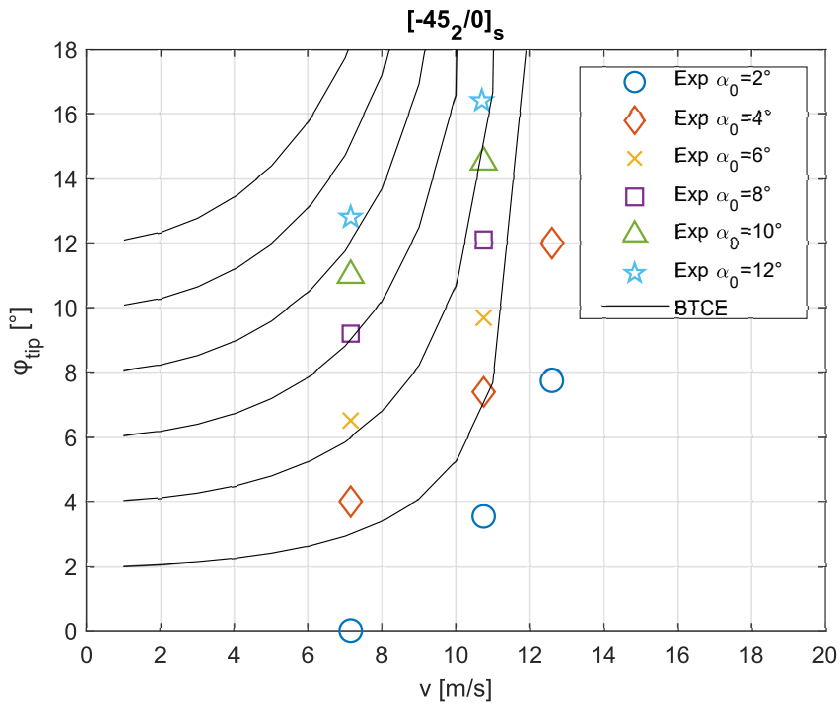
Fig. 7.9 Tip rotation at different angle of attack $[-45_2/0]_s$

tip rotation predicted with the BTCE tends to decrease with the speed, while the experimental tip rotation remains constant or slightly increases. Divergent tendencies of both the tip lateral deflections and angle of attack for the $[-45/0]_s$ are evident in Figures 7.8 and 7.9. The trend predicted with the BTCE model where similar to the experimental results presented in [129], however, the numerical and experimental results did not correlate. Finally, the numerical data appear to diverge faster than the experimental data. The case with $[\pm45/0]$ lamination presents a small coupling term, thus a difference in the actual lamination with respect to the model can affect sensibly the results. Moreover, Hollowell in [129] reported some difficulties in measure the tip rotation angle due to buffeting.

7.4   Effect of Curvilinear Lamination

The BTCE model presented in this thesis can be used for the simulation of variable stiffness structures. The previous chapter presented an application for curvilinear stiffeners path optimization demonstrating the capabilities of the structural model. In this section, the same principle can be applied to composite fiber orientation to show that curvilinear lamination can be adopted to improve the aeroelastic performance of a composite wing structure. The structure chosen is the same used in the previous section but with the fibers' orientation varying linearly with equation 7.3 with θ_1 denoting the orientation at the root section of the beam and θ_2 the angle at the end section of the beam (Figure 7.10).

$$\theta(x) = \theta_1 + \frac{\theta_2 - \theta_1}{l}x \tag{7.3}$$

The divergence speed has been computed for the possible configuration with curvilinear lamination with θ_1 and θ_2 varying from $-90°$ to $90°$. The divergence speed for the configuration with $\theta_1 = \theta_2 = 0°$ is taken as a reference value. The results are reported in Figure 7.11, where the divergence speed is normalized with respect to the reference value. A divergence speed value equal to three times the reference divergence speed has been considered as the limit for the calculation.

It is possible to notice that most of the curvilinear laminations with an initial negative orientation are not beneficial in terms of divergence speed, while the con-
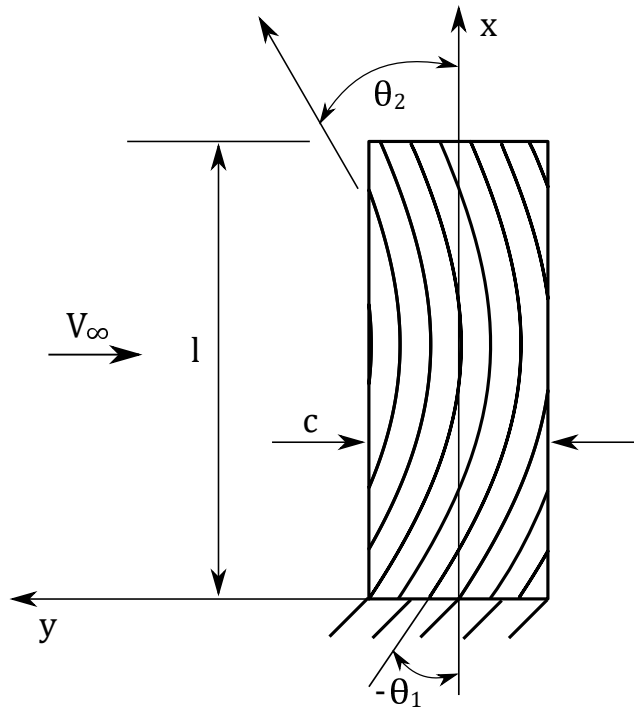
Fig. 7.10 Curvilinear lamination
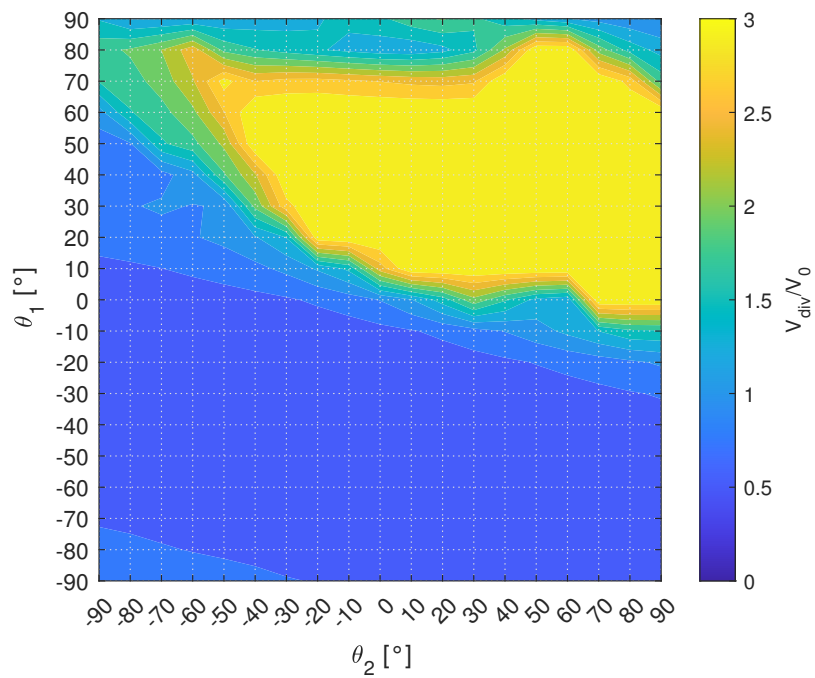
Fig. 7.11 Normalized divergence speed for curvilinear lamination

figurations with an initial positive orientation present many possible designs that present a higher divergence speed.

7.5   Summary and Conclusions

This chapter demonstrates the capabilities of a beam finite element incorporating bending-torsion coupling for static aeroelastic analysis. This approach involves structural analysis using a BTCE model alongside aerodynamic analysis based on VLM, with validation against experimental and analytical literature results. The divergence velocities predicted align well with experimental data, although for lamination $[-45_2/0]_s$, the tip deflection and rotation did not correlate with experimental findings. The methodology was also applied to various curvilinear laminations to assess their impact on static aeroelastic analysis outcomes and explore potential applications of the BTCE. The BTCE emerges as a versatile analytical tool suitable for integration into aerodynamic analyses and static aeroelastic investigations. Moreover, it allows for the use of curvilinear lamination, enabling the manipulation of design variables to achieve specific aeroelastic performance objectives. Future advancements may involve the integration of optimization algorithms to address optimization challenges and expand their applicability to flutter analysis.

Chapter 8

Laser Powder Bed Fusion Process Monitoring and Simulation

This chapter presents an overview of Laser Powder Bed Fusion (LPBF) process simulation. The simulation is applied to a section of curvilinear stiffener panel obtained from the topological optimization performed in Chapter 6. The introduction of complex geometries require the use of advanced technologies such as AM production. However, the high costs associated to this manufacturing technique impose the needs of accurate simulations to improve the knowledge of process parameters and to reduce the number of failed or low quality parts. At this scope, a multi-scale simulation method is briefly presented. This method, implemented in the software AMTOP® developed by ITACAe Srl, has been used for the simulation of a test artifact and the deformation caused by the residual stress relief. The artifact has been manufactured with LPBF technology and the deformations were measured through industrial Computed Tomography (iCT). Numerical and experimental data are compared to assess the precision of the simulation.

8.1 Additive Manufacturing Simulation Literature Overview

The importance of additive manufacturing is increasing due to its effectiveness in the field of lightweight structure design. Topology optimization is a technique that allows to reduce the weight of the structures with almost no stiffness penalty. However, the optimized geometries are often complex or not suitable for traditional manufacturing technologies like casting, extrusion, or machining. Lattice structures are another feature that is increasingly present in AM design due to their performance in weight reduction and heat exchange applications, however, this kind of geometries requires AM to be manufactured [130]. AM technologies for metals, such as selective laser melting (SLM) allow to manufacture of complex geometries with high precision and can significantly enlarge the design space. However, SLM can be considered as a series of micro-welding processes and carries the same problems related to residual stresses and deformations [131], [132]. The SLM process consists of a thin layer of metal powder spread with a roller and heated with a laser beam. The laser beam follows a scanning path based on the manufacturer's process parameters. The molten powder cools down and consolidates building the layer of the part. After consolidation, the process is iterated lowering the part and building the subsequent layer. As already stated, SLM-processes present issues related to residual stresses, for this reason, SLM produced parts with complex geometries often present undesired deformations or defects. This uncertainty of the process can limit the industrial development of such a technology [133]. The outcome of an AM process and its quality are strictly connected to the right set of process parameters. The characteristics of the powder, its morphology and, size distribution, are also relevant for the choice of process parameters [134]. Trial-and-error or empirical methods are widely spread among manufacturers, who rely on design of experiment (DOE) [135] to find a suitable set of parameters. The measurement of the distortions is an effective method to evaluate the quality of the production [136]; however a DOE can require tens of specimens and can become time and cost expensive. Moreover, the results may be not extendable to different geometries [63].

For these reasons, analytical methods can be an efficient alternative to calculate temperatures, stresses, and final deformation and to correlate them with process parameters [137]. These methods are suitable for simple geometries and features

but show their limits when the complexity increases. Understanding the physical mechanisms occurring during the melting process in SLM production is crucial for the comprehension of the effect that the process parameters have on the manufactured part. Several studies [138–141] investigated single aspects of the SLM process such as melting pool, scan speed, size of the laser beam, build height effect, and inner layer time. These design variables are strictly related to the residual stresses and subsequent distortion on the final part. The residual stresses can be calculated with different analytical or numerical approaches. Analytical methods can be useful to understand the effects of the process parameters on the physical phenomena, a reliable method considers the eigenfunctions approach [137] that can calculate the temperature and the stresses that occur at different layers. The method can give a good result in terms of physical variable fields, however, it is more convenient to use a numerical approach when using complex geometries.

A popular numerical method used for AM process simulation is the Finite Element Method (FEM) which can be used also for process parameter identification. This technique allows also the simulation of the process on different scales. Detailed micro or meso-scale models can used to study the scanning path or the melt pool [142, 143], while macro-scale models can be used to study the temperature evolution and the residual stresses during the process [144, 116, 145–147]. The heating processes occurring during different AM processes have been the subject of several studies allowing us to understand the micro-scale physical phenomena and the importance of micro and mesoscale modeling. Geng et al. [148] published a study of AM micro-scale processes, they combined FE with a microscopic phase field (PF) model to determine the temperature distribution field during a melting phase process for a wire arc additive manufacturing process, moreover, they studied the effects of the microstructure evolution. The PF model can be combined also with computational fluid dynamics and it proved to be effective in predicting the chemical composition through concentration field equations and grain morphology. This allowed for the determination of the quality of the microstructure by the temperature evolution and it allowed for the identification of the columnar dendritic spacing. All these evaluations can be useful to determine optimized process parameters such as laser speed and power. Cattenone et al. [149] used FE analysis to determine the distortions and residual stresses at the meso and macro-scale. The study, validated with experimental results, investigated the process parameters and the modeling method, moreover, it determined the importance of constitutive material models as

well as the meshing strategy and the time step in the local temperature distribution calculation. The result of the research was an FE analysis capable of predicting defects and distortion of an object manufactured with fused deposition modeling (FDM) with a coefficient of variation of 12.2%. Song et al. [150] simulated a laser direct energy deposition (LDED) AM process using FE implemented in Abaqus AM module. The research established the importance of the surrounding powder bed but also of the building plate thickness and its geometry constraint effects. The powder bed thickness becomes increasingly relevant for small features; in this case, also the FE mesh must be carefully evaluated. Another important finding was that the time step for the thermal analysis can be incremental without compromising the final result and saving time for the calculation.

The use of AM process simulation for complex geometries is limited for industrial applications due to the excessive calculation time. The reason is that the direct modeling of laser scan lines requires a considerable number of nodes for a high-fidelity representation and a small time increment. The works done by Van Belle [151] and Price [152] reported run times of tens to hundreds of hours for medium-size models. These limits increased the need for reliable and fast simulation for the determination of the optimal process parameters. The common assumption for the most recent efficient simulation method is the modeling of the individual laser scan line is no longer required, but approximations to simplify the analysis can be used. Carraturo et al. [153] used the finite cell method for a part-scale simulation of an LPBF process by means of a layer-by-layer activation process. The simulation was validated by experimental measurements of an Inconel 625 cantilever structure showing a maximum error of 4.72% and a very good correlation between experimental and numerical data. A technique called process agglomeration has been used by Hodge et al. [154] where the layers are modeled with a bigger scale equal to 20 times the actual layer thickness. The models have been validated with experimental measurements performed by Wu et. al [155] on relatively small components made of stainless steel 316L. The simulation required high-performance clusters and the surface deformations were measured via digital image correlation (DIC), while interior stresses were measured via neutron diffraction. The deformations predicted with the numerical method were good in terms of magnitude, but the with high discrepancies in the distribution. Other approaches operate by activation of a group of layers or single full layers at high temperatures. The activation temperature can be determined with an analytical thermal load calculation and then the mechanical

response is determined with a coupled thermo-mechanical calculation. Zaeh and Branner [156] simulated the production of a T-shaped cantilever beam made with tool steel 1.2709 (X3NiCoMoTi18- 9-5) and verified the deformations with experimental results obtained with a coordinate measuring machine (CMM). They showed that the method captured the trend of distortions, but the absence of a moving heat source model caused considerable overestimation of the peak distortion by 22.8%. Papadakis et al. [157] predicted the residual stress and distortion of an Inconel 718 cantilever using a reduced thermal input method, however, the peak distortion was overestimated by 26%. Inherent strain models are another approach to AM process simulations. They rely on the assumption that the plastic strain developed during the process is uniform [158]. Inherent strain models need two fundamental steps, the plastic strain calculation and the plastic strain application [146]. The first step is usually achieved with several experimental builds [159] which can be time and cost-consuming. Another drawback of the inherent strain theory is the hypothesis of plastic strain homogeneity, this means that any difference in the plastic strain field caused by different geometries is neglected [159].

An advanced method for LPBF simulation is multi-scale modeling, where the results of the simulation of micro-scale physical phenomena are used as input for bigger-scale simulations. Li et al. [160] developed a multi-scale model with multiple stages. The first step is a micro-scale simulation of a moving heat source which generates an integrated heat input. This input is used for a meso-scale thermo-mechanical analysis of a larger volume for the residual stress tensor calculation. The last step consist of mapping the residual stress tensor into a macro-scale model. The research showed good agreement between predicted and measured distortions, but the model was limited to simple geometries. Another study of the same author [161] used a multi-scale model for the simulation of an AlSi10Mg cantilever beam production, reporting an error equal to 28% for the peak deformation.

It is worth mentioning that most of the models present in the literature consider only simple geometries. This allows for more accurate results but limits the understanding of the capabilities of FEM AM process simulation. One of the research studies that considers complex geometries has been proposed by Gouge et al. [162]. They used small-scale analysis results as input for the part-scale analysis of a small thin-walled Inconel 625-compliant cylinder, a small Inconel 718 build with both very thin and very thick sections, and an industrial-scale part formed from AlSu10Mg. The multi-scale model proposed showed a good correlation with the experimental re-

sult with a maximum error of 13% for the peak distortion and a minimum correlation
of 90.5%.

8.2   Thermal-Mechanical Model

The strategy adopted for the LPBF process simulation performed in this research is
a thermal-mechanical model developed by ITACAe S.r.l and SimTech Simulation
et Technologie SARL. The model is implemented into a platform of software tools
called AMTOP® developed to analyze and optimize additive manufacturing products
and processes. The platform is based on several algorithms for the evaluation of
stresses and distortions through a layer-by-layer approach, consisting of loops of
coupled thermal structural analysis [163, 164]. AMTOP® calculates the temperature,
stress, and displacements history of the different equivalent layers at the end of
the LPBF process. The equivalent layers consist of bundles of actual layers. The
software can compute the distortions that occur after the removal of the supports and
the component from the base plate. The process parameters needed for the simulation
are laser speed, laser power, laser path, layer thickness, hatch distance, material
mechanical properties, base plate temperature, environment temperature, shape, and
dimensions of the supports. The latest are particularly important because they affect
considerably the distortion mechanism and therefore the manufacturability of the
component. The finite element analysis (FEA) is performed with the external solver
Calculix. The FEA consists of a series of thermal-mechanical simulations for each
layer bundle, the results computed for each bundle constitute the initial conditions of
the subsequent one. Once the simulation is complete and the part is fully built, it is
possible to determine the deformed geometry. A scheme of the analysis workflow is
reported in Figure 8.1 and the correlation between the phases of the process and the
corresponding modeling is resumed in Table 8.1

The physical process parameters are critical for an accurate simulation, however,
there are also numerical parameters that need to be set up to guarantee the best
compromise between calculation time and accuracy. The mesh size significantly
affects this aspect of the simulation through the beam diameter scale (DIASCALE)
and the layer thickness scale (LAYTHKSCALE) that determine the actual size of
the mesh and the layer bundle height. The assumption is that the size of the laser
dot can be considered negligible if compared with the dimensions of the component.

Table 8.1 Modeling of the physical process.

Process Phase	Simulation Phase
Part orientation and placement.	AMTOP® can suggest the best orientation strategy. Process parameters need to be assigned and a mesh sensitivity study performed.
Layer 1: fusion of the powder for the first layer bundle.	The model calculates the temperature of the first bundle of layers. The model requires the temperature field as the initial condition for the FEM solver and the geometry of the first layer bundle.
Recoating: deposition of the powder for the next layer	At each layer, the calculation provides stress, displacement, and temperature field that depends on the results of the previous layer which are the initial condition of the current one.
Layer 1+n: fusion of the powder for the first layer.	At each layer, the calculation provides stress, displacement, and temperature field that depends on the results of the previous layer which are the initial condition of the current one.
Cutting from the plate and the supports.	The cutting removes elements (supports + plate) that do not belong to the printed part. In this phase, AMTOP® calculates the final distortion.
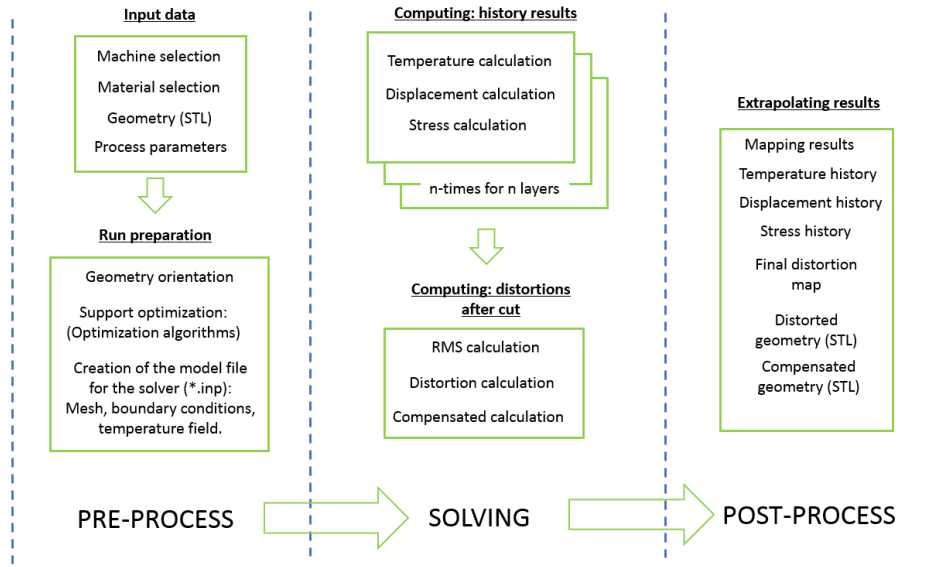
Fig. 8.1 AMTOP® workflow scheme.

During the pre-processing phase, an algorithm prepares the FE model starting from the triangle tessellated boundary surface of the surface mesh of the part with a voxel meshing of the domain. The voxel sizes are multiples of DIASCALE and LAYTHKSCALE. The model is based upon the simplification that the laser energy is instantaneously absorbed into the system for each voxel layer. Therefore, the new layer elements are associated with a temperature higher than the melting temperature of the material considered.

The coupled thermal-mechanical analysis at the macro scale level follows the governing equation for transient heat conduction

$$\nabla\left(-\kappa\nabla T\right)+\rho c\dot{T}=\rho h \tag{8.1}$$

with

$$-\kappa\nabla T = q - h_c(T-T_0) - \sigma_e\varepsilon(T^4-T_0^4) \tag{8.2}$$

where T is the temperature, κ is the thermal conductivity of the material, ρ is the material density, h is the heat generation per unit of mass, q is the input heat flux, h_c is the heat transfer coefficient under natural convection, σ_e is the Stefan-Boltzmann constant, T_0 is the ambient temperature, and ε is the emissivity. The deformations of

the component are calculated with a quasi-static mechanical analysis. The results of the thermal analysis constitute the thermal load for the mechanical analysis. The governing stress equilibrium equation is

$$\nabla\sigma = 0 \tag{8.3}$$

where σ is the mechanical stress which follows the Hook's Law

$$\sigma = C\varepsilon \tag{8.4}$$

C is the isotropic material stiffness tensor and ε is the total strain which includes the elastic strain ε_e, the plastic strain ε_p, and the thermal strain ε_T the thermal strain is computed as

$$\varepsilon_T = \alpha(T)(T - T_{ref}) \tag{8.5}$$

with $\alpha(T)$ the temperature dependent thermal expansion coefficient of the material and T_{ref} is the environment temperature.

8.3   Application to Stiffened Panels

The advantages of additive manufacturing technologies can be exploited the most when complex geometries are considered. Stiffened metallic panels can be machined from a metallic bar with great costs and material waste. The introduction of curvilinear stiffeners or complex stiffener sections can further increase these costs or make traditional manufacturing technologies obsolete. Additive manufacturing is unlikely to reduce production costs unless nesting strategies are introduced, however, it allows for more design opportunities.

Large flat and thin surfaces are not always easy to manufacture with AM technologies because the thermal stresses can easily deform the structure. Another drawback of the production of panel structures are the support structures. A solution for this problem can be the vertical or lateral positioning of the panel to eliminate the need for support. Another aspect to consider is the increment of the panel thickness to make the structure less prone to deformation and able to stand on one of its
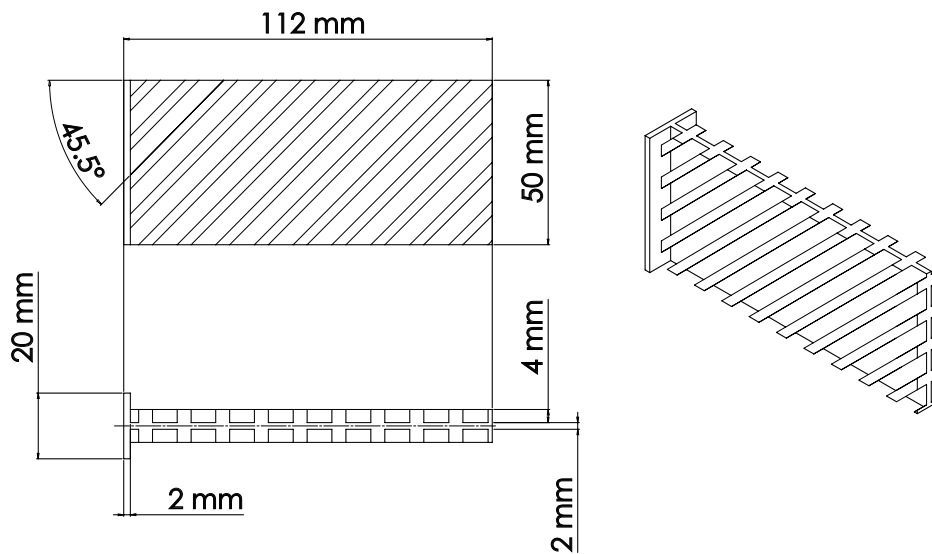
Fig. 8.2 Portion of curvilinear stiffener panel

sides. However, it is not necessary to increase the thickness too much, because the symmetric configuration of the stiffeners can be used to support the whole structure. The presence of support structures in the undercuts formed by the oriented stiffeners can be undesired due to the additional machining cost, the problem can be avoided by limiting the design domain to orientations that create an undercut with an angle bigger than $40°$.

These considerations have been taken into account for the optimization performed in Chapter 6. The result of the optimization was a stiffened panel box-beam structure with slightly curvilinear stiffeners. A portion of the stiffened panel has been designed for additive manufacturing production (Figure 8.2). The model has been simulated with AMTOP® to obtain the residual deformations caused by an LPBF process. The process parameters used for the simulation are summarized in Table 8.2. The resulting finite element model is represented in Figure 8.3.

8.3.1 Stiffened Panel Simulation results

The results of the additive manufacturing process simulation performed with AM-TOP® are reported in Figures 8.4-8.7. The software performs the thermal-mechanical

Table 8.2 Process Parameters

Property	Value
Laser Power	370 W
Platform Temperature	160 $^\circ C$
Scan Speed	1200 mm/s
Layer Thickness (LT)	0.03 mm
Hatch Distance	0.2 mm
Laser Diameter (LD)	0.1 mm
Element Width	10×LD
Element Height	50×LT
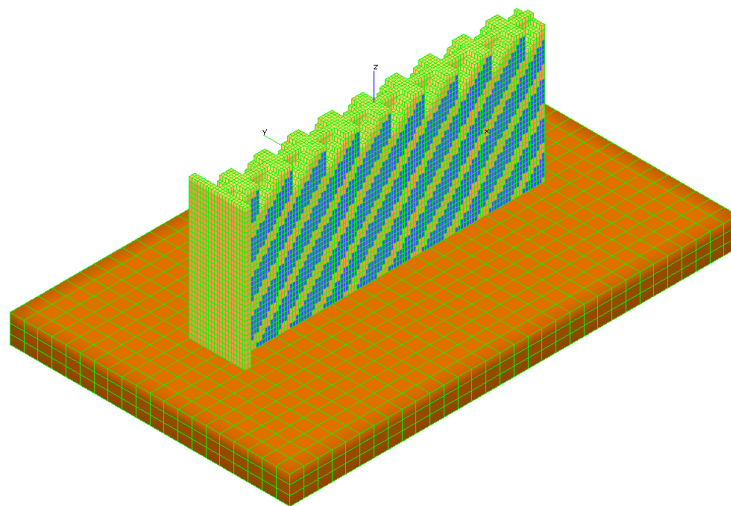
Fig. 8.3 Finite element model for LPBF process simulation

simulation and computes the residual stresses, then simulates the release of the stresses caused by the base plate and support structure removal. The chosen process parameters and the designed geometry did not generate support structures minimizing the post-production machining. The represented results are the nodal displacements in the principal directions with respect to the initial conditions. The simulation showed that the part could be produced with LPBF, obtaining a component with deformations lower than 0.82 mm.
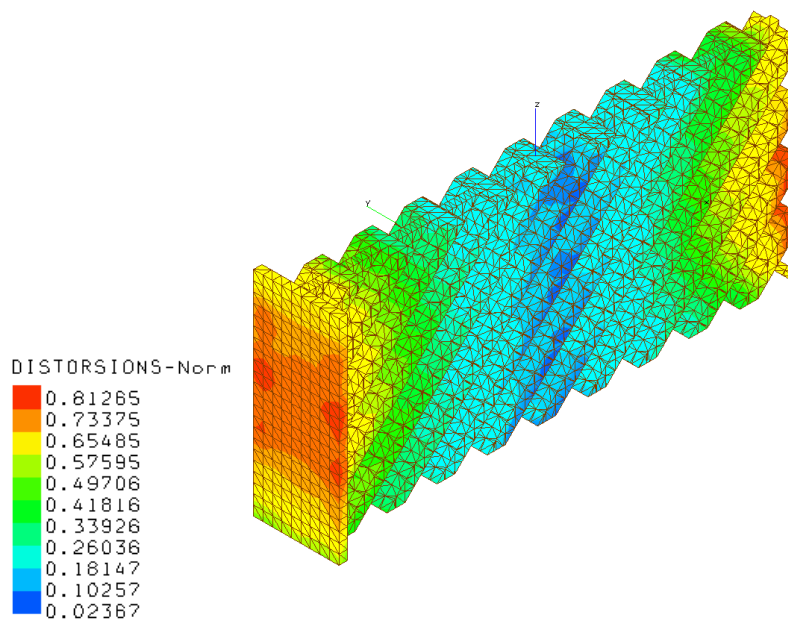
Fig. 8.4 Deformation magnitudes for the AM component.
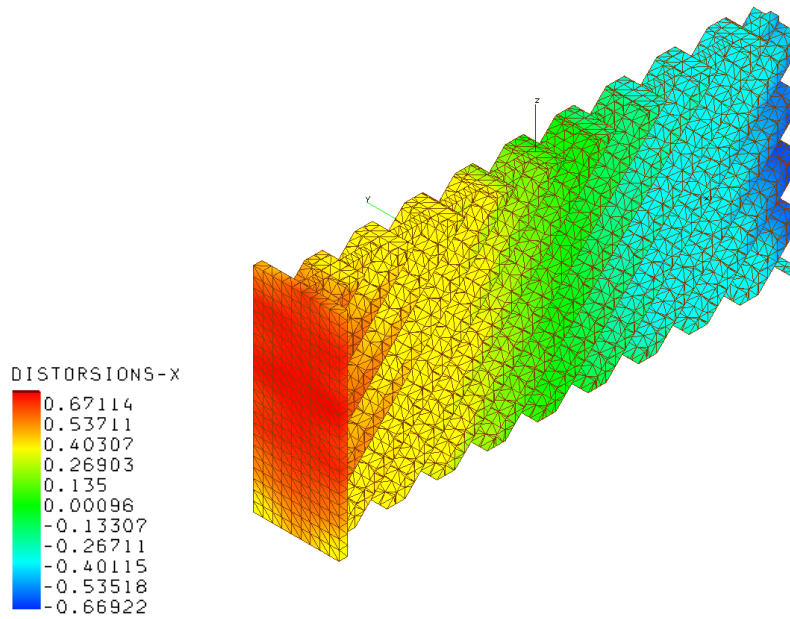
Fig. 8.5 Deformations in the x-direction for the AM component.
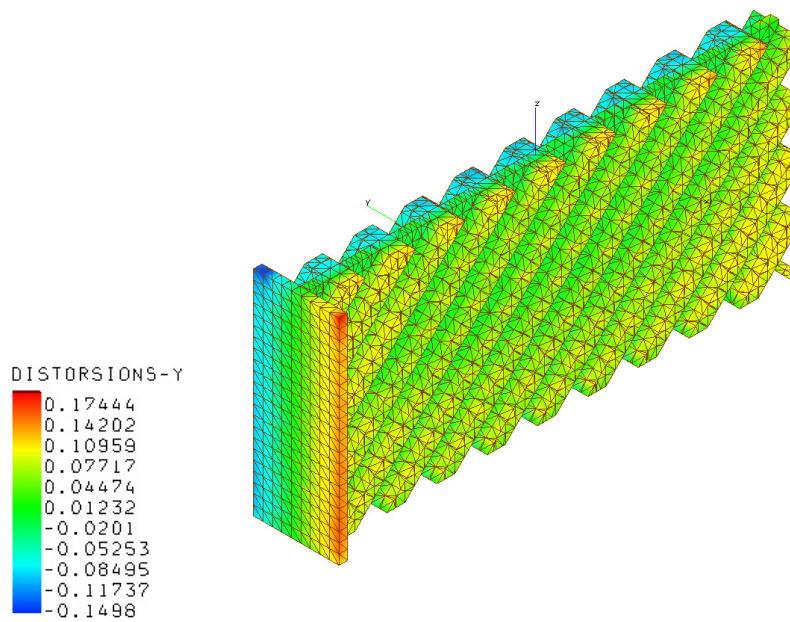
Fig. 8.6 Deformations in the y-direction for the AM component.

DISTORSIONS-Z
0.50472
0.43943
0.37415
0.30887
0.24359
0.1783
0.11302
0.04774
-0.01754
-0.08283
-0.14811
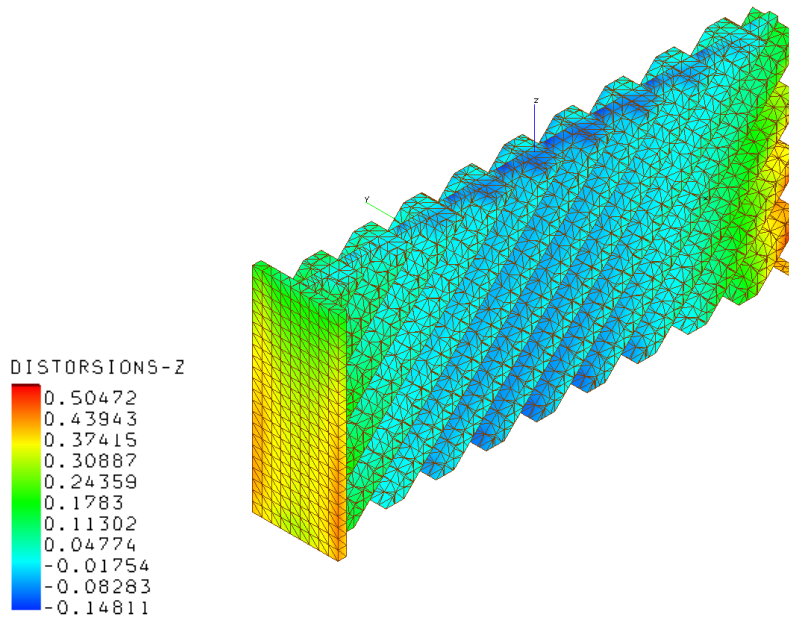
Fig. 8.7 Deformations in the z-direction for the AM component..

8.4 Test Artifact

The geometry of the component is based on the calibrating features present in the regulation ISO/ASTM 52902:2019. In addition, some novel features like freeform shapes, lattice structures, and cavities have been included. All the features have been merged together to obtain a single artifact, due to the complexity of the new features introduced, non-standard measurement methods are needed for the evaluation of the deformations and the dimensional tolerances.

The material considered for the component production was an AlSi10Mg alloy powder 20–60 μm, and printed with a layer thickness of 0.03 mm with one Yb (Ytterbium) fiber laser IR. The AlSi10Mg alloy has been chosen due to its popularity in the AM industry and the literature abundance of thermal and physical properties data necessary for AM process simulation. The artifact has been manufactured with a Print Sharp 250 EP-M250 by Prima Additive and with process parameters listed in Table 8.3. The process parameters have been determined by the manufacturer based on several tests and studies performed during their activity. The result of the AM process is represented in Figure 8.9.
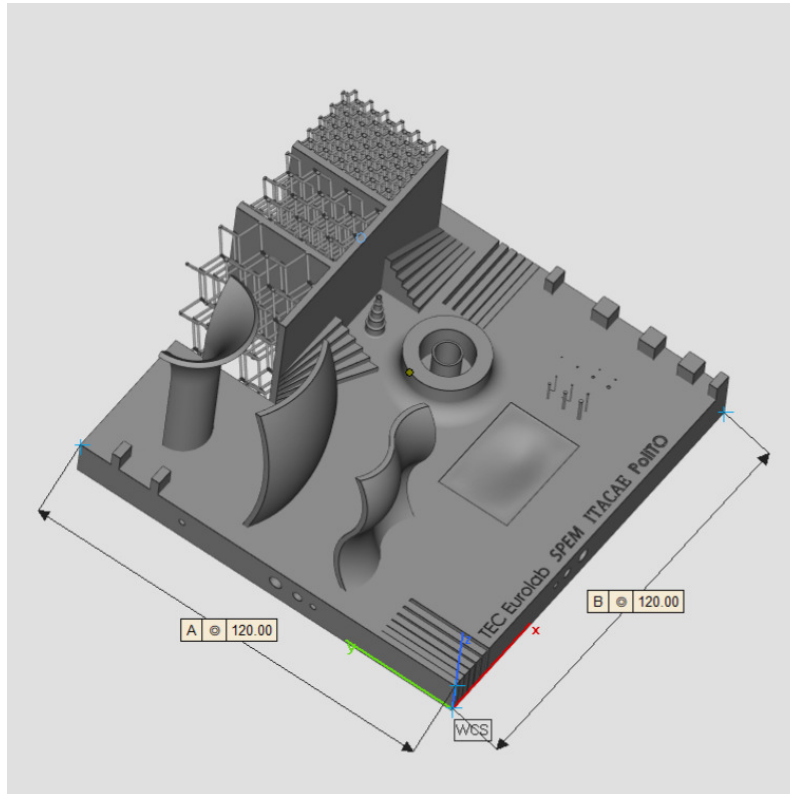
Fig. 8.8 Test artifact

Table 8.3 Process Parameters

Property	Value
Laser Power	370 W
Platform Temperature	120 $^\circ C$
Scan Speed	1300 mm/s
Scan Strategy	10 mm Stripes
N° of Contour	2
Spot (Laser)	0.11 mm
Gas Type	N_2
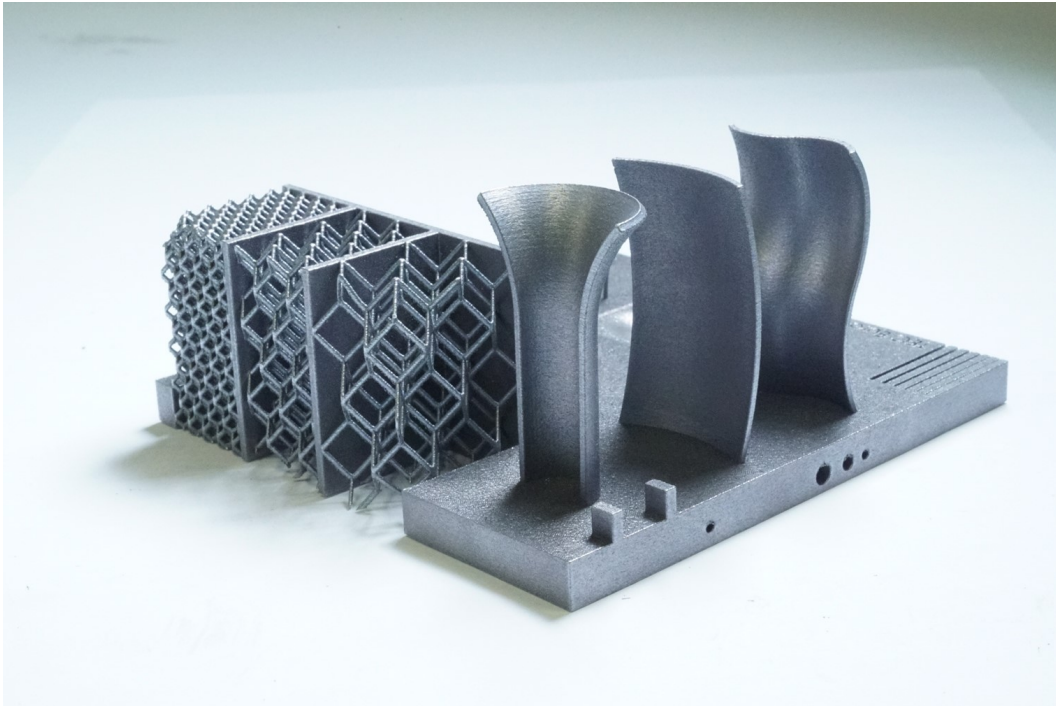
Fig. 8.9 Result of the AM process

8.5   Finite Element Model and iCT

The finite element model created with AMTOP®, represented in Figure 8.10, includes different properties to describe the components of the simulation. For an AM process simulation, the software groups the elements with the same characteristics identifying the base plate, the component, the powder, and the supports. The base plate is considered undeformable, but its temperature influences the thermal analysis. The elements of the component present the thermal-mechanical properties of the chosen material and are added layer by layer. The supports are defined with degraded properties and with custom geometries, the elements can be removed after the simulation to calculate the deformations of the component. The powder elements in this simulation are introduced for numeric purposes and do not affect the simulation. The selected geometry presents lattice structures with very small pillars, a high fidelity representation of these structures implies a high number of elements which results in an excessive computational time. However, the two volumes with bigger lattice cells probably do not influence heavily the thermal-mechanical analysis, since the solidified material is scarce. On the other hand, the volume with smaller cells presents a
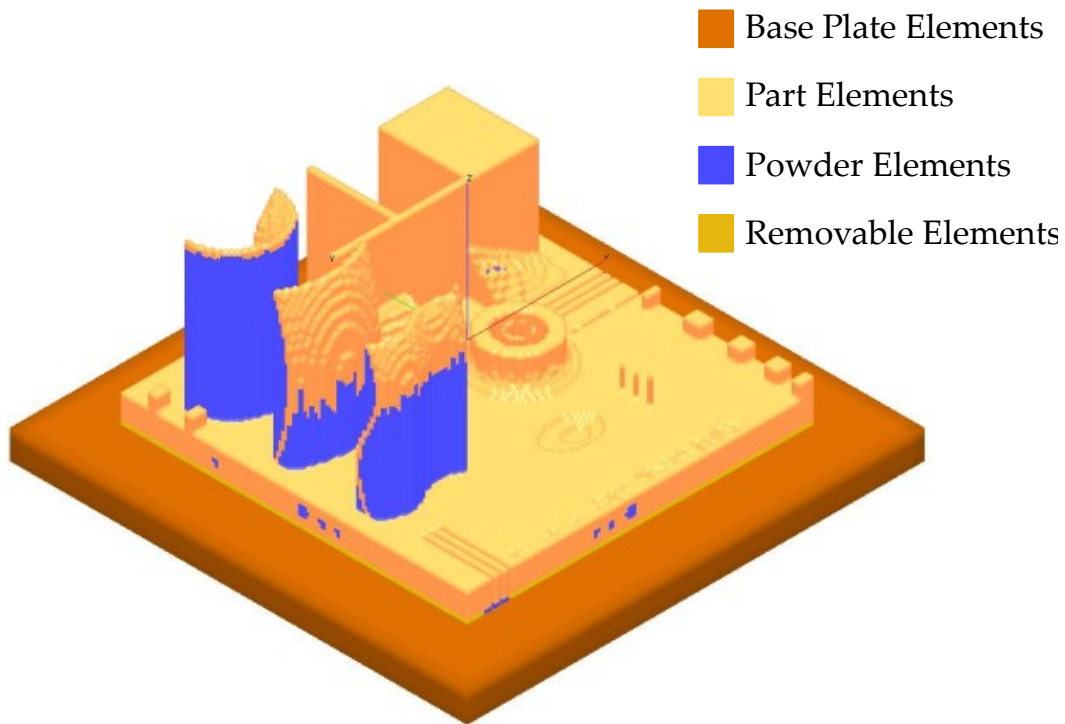
Fig. 8.10 AMTOP® Voxel Meshing

higher quantity of melted powder and its influence can not be neglected. A possible solution to avoid the full representation of the lattice geometry could be the modelization of the lattice volume with a full volume and equivalent thermal-mechanical properties. The equivalent properties could be computed with the rule of mixtures considering the volume ratio between lattice structures and powder. However, the software does not implement this feature yet, for this reason, the volumes with bigger cell size have been considered void, while the volume with bigger cell size has been considered a solid volume with mechanical properties equal to the rest of the artifact. With this approximation, the information on the deformations of the details of the lattice structures is not available, but it allows for the global deformation of the component in a few hours.

The actual component went through the removal of material during the base plate separation process, quantified in 1.5 mm of thickness of the bottom surface. A first simulation, SIM1 from hereinafter, has been performed considering a perfect separation of the artifact from the base plate and neglecting advanced thermal parameters such as convection and radiation heat exchange. Then a second simulation, SIM2, was prepared considering the additional heat exchange sources and

including the removal of 1,5 mm of material. This operation has been achieved by creating support structures with a height of 1,5 mm and with mechanical properties and geometry equivalent to a solid volume. With this method, the mechanical and thermal properties of the removed volume are preserved, but the software identifies the corresponding elements as supports and removes them during the base plate removal procedure. The process parameters considered for the simulation are the same used for the actual part reported in Table 8.3. The convective heat transfer coefficient is $h_c = 10/m^2K$ [165], while the thermophysical temperature-dependent properties of the AlSi10Mg alloy used for the simulation can be found in [166].

The deformations obtained with the FE simulations have been compared to the experimental measurements of an iCT. During an iCT scan using an X-ray system, multiple projections are taken systematically. The images are acquired from several different viewing angles obtained with the rotation of the sample. It is possible to obtain radiographic imaging due to different X-ray attenuation coefficients of materials, and the X-ray linear attenuation coefficients are represented as different iCT grey values. From these values, it is possible to obtain a virtual three-dimensional volume of a sample via reconstruction algorithms. The obtained volume could be used for different purposes: One of the main applications of iCT volume is defect analysis, where all kinds of indications are analyzed looking for defects according to the requirements. iCT volume is also used in the field of metrology validation because it is the only non-destructive testing (NDT) technique that allows for having the full geometries of an internal feature. In this research, the NSI X5000 TEC Eurolab system was used for the metrological analysis of the designed artifact. The device is a Microfocus system with a Flat Panel detector, specifically designed to check components manufactured with light alloys or composite materials, for which a high resolution is required. iCT Volume could also be used for failure analysis, reverse engineering, and FEM simulation [167]. The scan was performed at 0.094 mm of resolution, 240 kV, and 430 μA. After the surface calculation, the reference element and the analyzed surface/STL file were aligned through a best-fit registration.

8.6   Residual Deformations Comparison

The result of the iCT consists of a cloud of points where the geometry is reconstructed by an algorithm. The iCT can be aligned to the 3D model with the nominal geometry
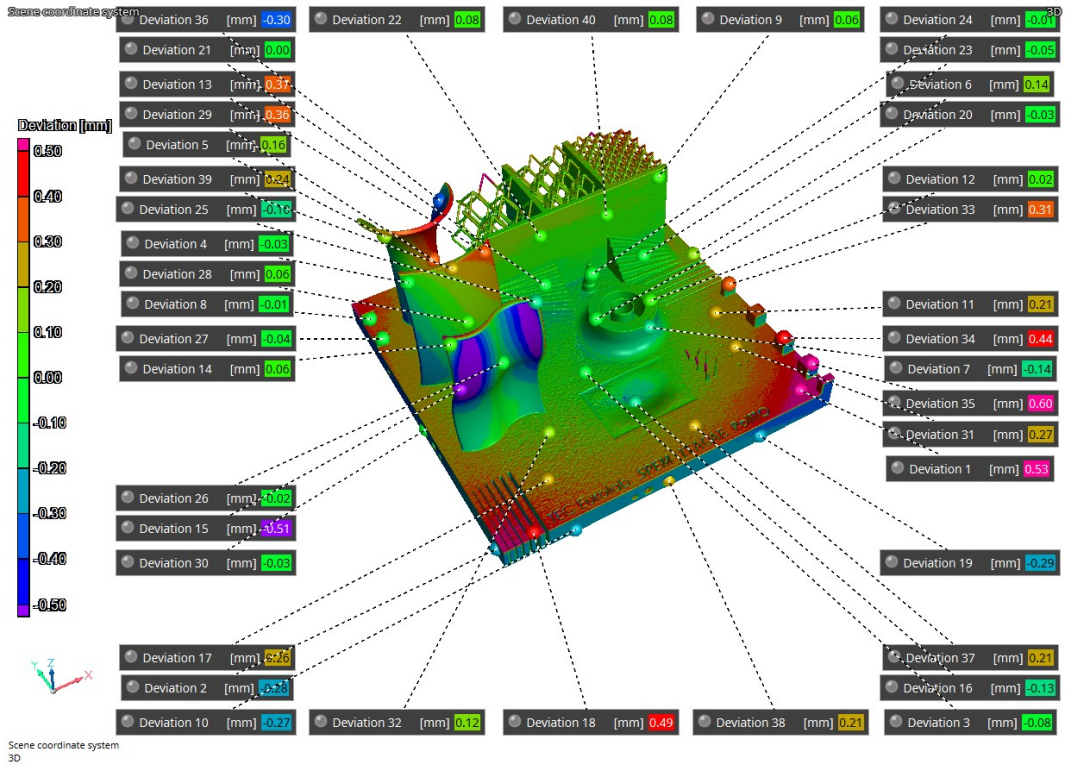
Fig. 8.11 NG-iCT comparison, top view

(NG) for a direct comparison of the deviations. The strategy used for the models alignment can affect the results and should be chosen carefully, in this case, the minimum square error strategy has been used to align the models. The deviations highlighted by the comparison between the NG and the iCT volume, summarized in Table 8.4, are represented in Figures 8.11 to 8.13.
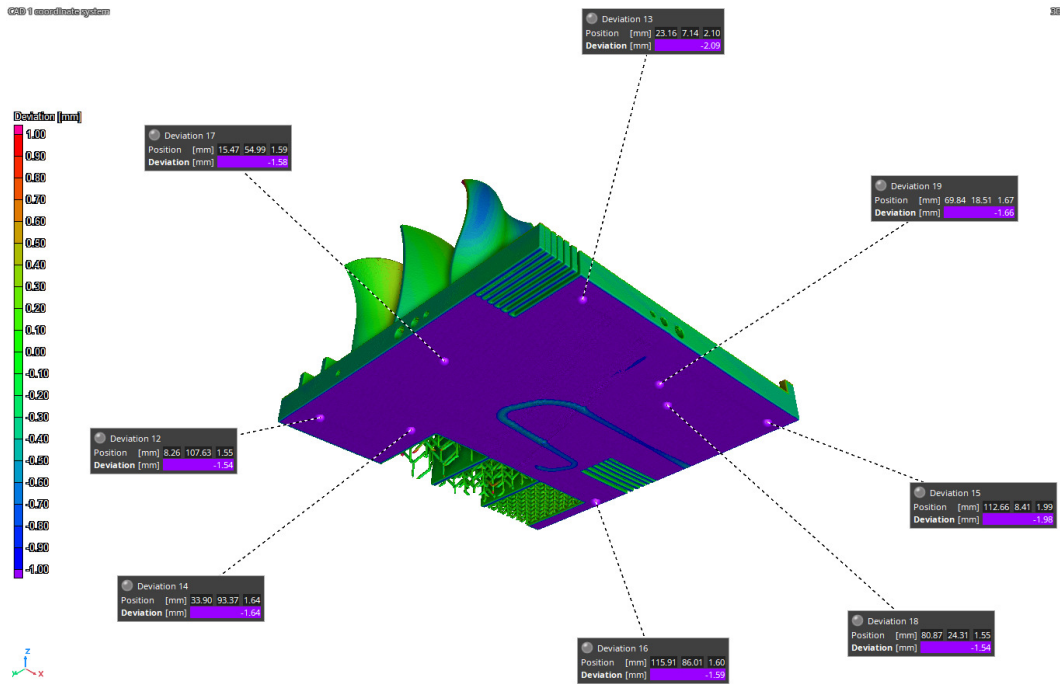
Fig. 8.12 NG-iCT comparison, bottom view
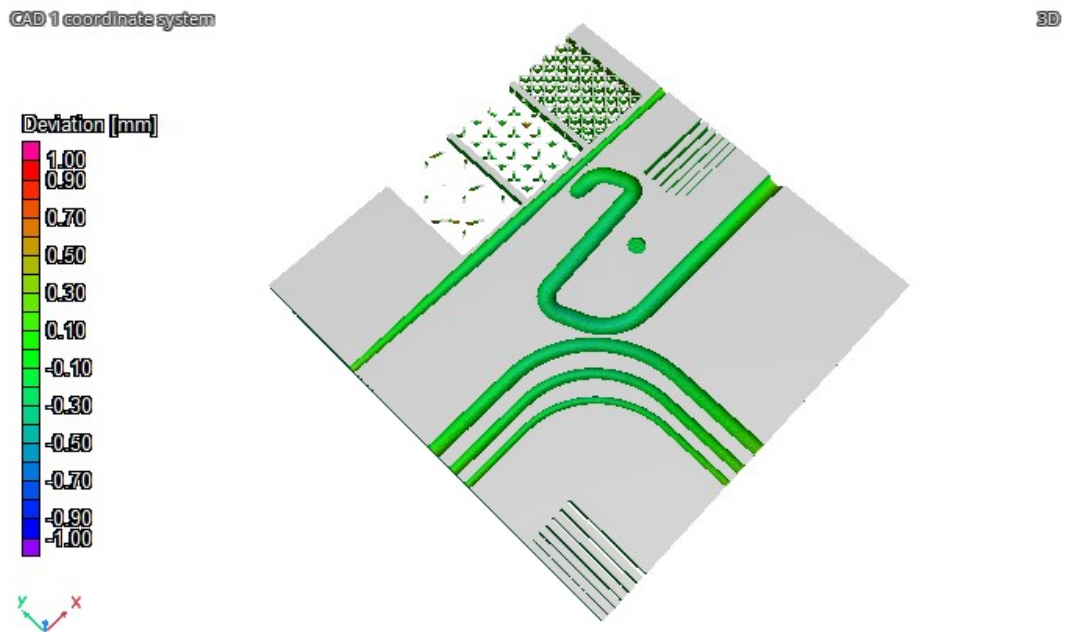
Fig. 8.13 NG-iCT comparison, internal view

Table 8.4 Results of iCT volume comparison with respect to the initial geometry and with respect to SIM2 results.

Point	NG-iCT [mm]	NG-SIM2 [mm]	iCT-SIM2 [mm]
1	0.53	0.34	-0.20
2	-0.28	-0.48	-0.20
3	-0.08	0.08	0.11
4	-0.03	-0.43	-0.40
5	0.16	-0.26	-0.41
6	0.14	0.37	0.23
7	-0.14	-0.29	-0.15
8	-0.01	0.34	0.34
9	0.06	0.34	0.27
10	-0.27	-0.64	-0.37
11	0.21	0.20	0.00
12	0.02	0.01	0.00
13	0.37	0.02	-0.35
14	0.06	-0.35	0.42
15	-0.51	-0.28	-0.23
16	-0.13	0.04	0.17
17	0.26	0.13	-0.12
18	0.49	0.89	0.40
19	-0.29	-0.57	-0.28
20	-0.03	-0.03	0.00
21	0.00	0.01	0.01
22	0.08	0.10	0.02
23	-0.05	0.05	0.10
24	-0.01	0.06	0.07
25	-0.10	-0.15	-0.25
26	-0.02	0.28	0.30
27	-0.04	0.21	0.24
28	0.06	0.03	-0.03
29	0.36	0.42	0.06
30	-0.03	0.08	0.11
31	0.27	0.13	-0.14
32	0.12	0.05	-0.07
33	0.31	0.27	-0.04
34	0.44	0.27	-0.17
35	0.60	0.36	-0.24
36	-0.30	-0.64	-0.44
37	0.21	0.14	-0.07
38	0.21	0.39	0.18
39	0.24	-0.01	-0.25
40	0.08	0.26	0.18
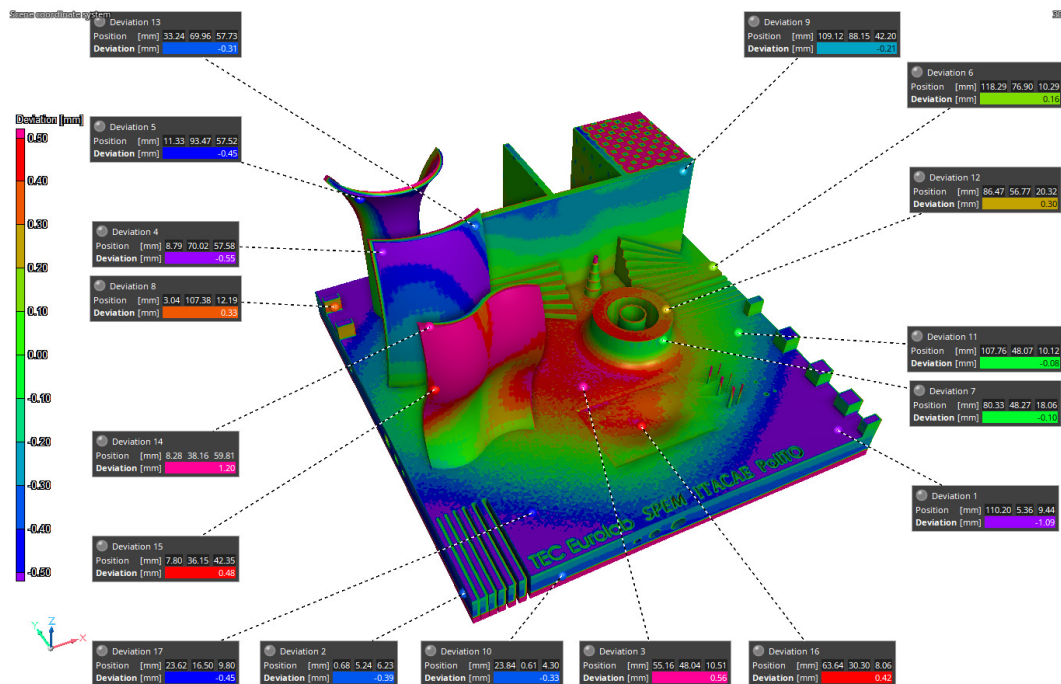
Fig. 8.14 SIM1-iCT comparison

The first simulation performed with AMTOP® has been compared with the iCT volume, the deviations are reported in Figure 8.14 and in Table 8.5. The comparison revealed differences in the deformations with respect to the iCT up to 1.20 mm. Moreover, the concavity of the bottom surface is opposite to the one observed in the manufactured part. For this reason, only 17 reference points have been considered, and the results of the first simulation have not been compared with the NG since the deformation pattern was clearly different. These differences can be attributed to the hypothesis of perfect separation from the base plate and the neglect of convective heat exchange.

The second simulation considered convection heat exchange and the removal of 1.5 mm of material during the separation from the base plate to improve the correlation with the manufactured part. In this case, the concavity was the same as observed with the iCT and the differences between the manufactured part and the predicted results are comparable and below 0.44 mm as reported in Figure 8.15 and in Table 8.4. Moreover, Figures 8.11 and 8.16 present the comparison of the iCT and SIM2 with the initial geometry, respectively. The comparison revealed a common deformation pattern with similar deviations for the actual part and the digital twin as reported in Table 8.4. However, some differences are present, and the

Table 8.5 Results of iCT volume comparison with respect to SIM1

Point	iCT-SIM1[mm]
1	-1.09
2	-0.39
3	0.56
4	-0.55
5	-0.45
6	0.16
7	-0.10
8	0.33
9	-0.21
10	-0.33
11	-0.08
12	0.30
13	-0.31
14	1.20
15	0.48
16	0.42
17	-0.45

hypothesis considered for the lattice structures reduced considerably the calculation time, but the absence of the features determined some discrepancies in the results. In general, the numerical model and the voxel discretization introduce approximations that contribute to reducing the simulation accuracy; moreover, the comparison with the best-fitting alignment of the volumes can introduce small differences in the deviations.

The accuracy of the simulations can be quantified using two metrics, percent error of peak displacement, and by calculating the correlation over a field of representative points. The peak displacement evaluation would give an indication of how well the model predicts the most severe distortion. However, the base plate removal caused the loss of material, and for this reason, when comparing the iCT volume to the NG, the bottom of the artifact is the area indicated as the most distorted, but the discrepancies are not caused by the stress-induced deformations but by the absence of material. The same situation is present in the lattice structure area. For this reason, it is not possible to locate the actual peak distortion of the artifact. On the other hand, correlation gives a more global indication of how accurate the model is. Correlation is calculated between two sets of data A and B with Equation 8.6
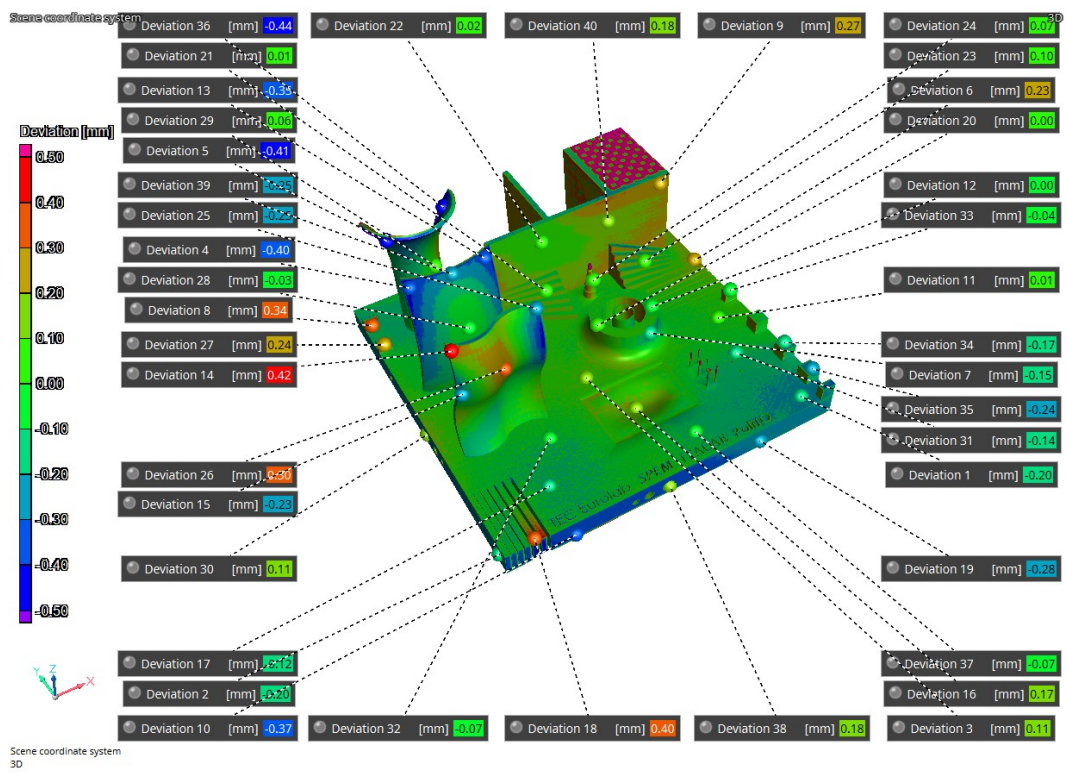
Fig. 8.15 SIM2-iCT comparison
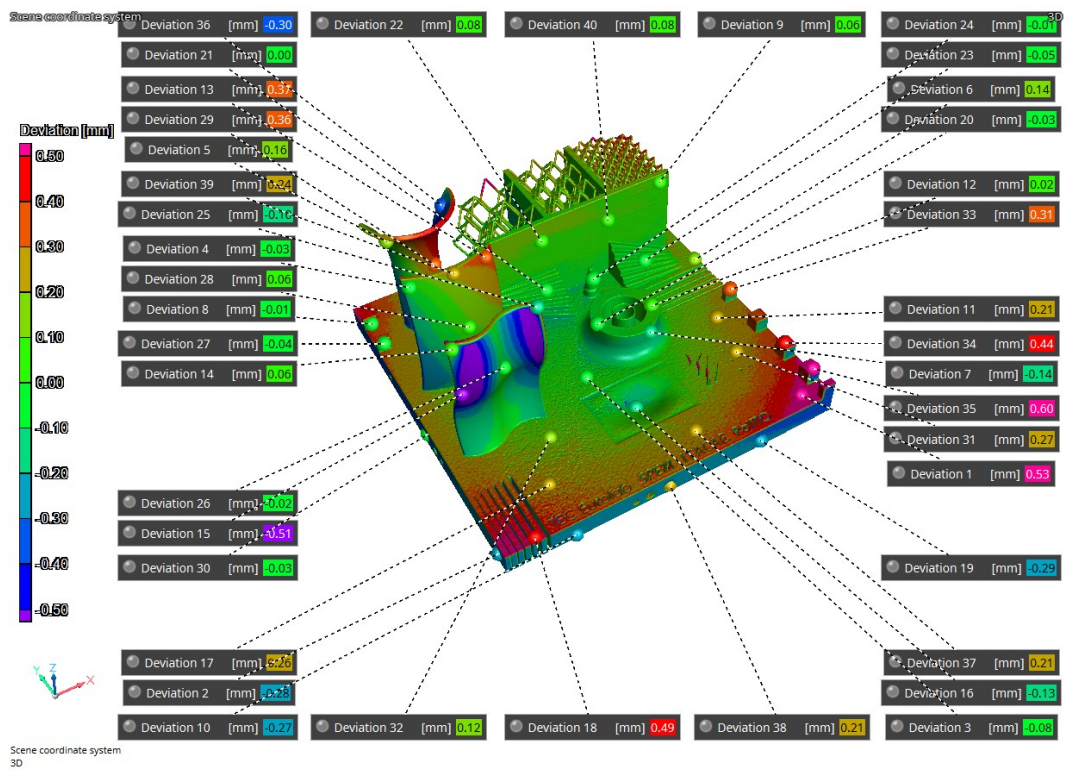
Fig. 8.16 SIM2-NG comparison
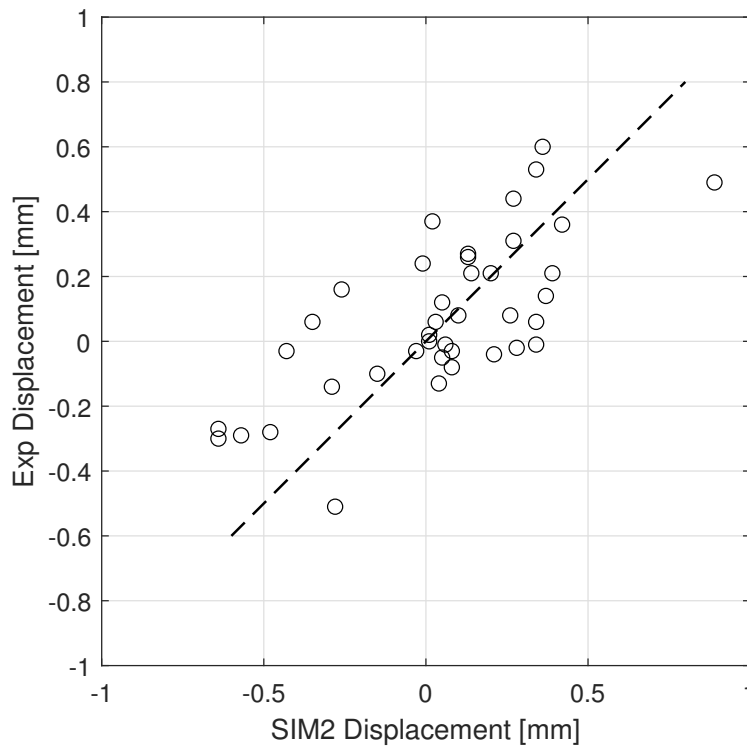
Fig. 8.17 Comparison of 40 individual simulation-measurement points

$$Correlation(A, B)\% = \frac{\sum (a - \bar{a})(b - \bar{b})}{\sqrt{\sum (a - \bar{a})^2 \sum (b - \bar{b})^2}} \tag{8.6}$$

where a and b are the members of the sets A and B, respectively, while $\bar{a}$ and $\bar{b}$ are the mean of A and B. The correlation between the two sets of data has been computed with Equation 8.6, revealing a value of 71%. This value does not reach the level of accuracy reported in other works. For example, Gouge et al. [162] reported a minimum correlation of 90.5% for a more sophisticated model. Considering the complexity of the studied geometry and the approximations introduced during the simulation phase, the correlation obtained is encouraging and can be further improved by increasing the number of reference points. The predicted and measured displacements taken at the 40 locations on the artifact surface are reported in Figure 8.17. The trend line represents the exact correspondence between predicted and measured displacements. The trend line plot indicates a good agreement between the simulation and the iCT volume.

8.7   Summary and Conclusions

In this chapter AM process simulation has been discussed and applied. An optimal configuration addressing geometric constraints for AM production, featuring a self-supporting structure to minimize post-production machining, was investigated. AMTOP® thermo-mechanical simulations revealed residual stress-induced deformations smaller than 0.82 mm on the final component, affirming the feasibility of AM production for such high-performance beam structures. In addition, this chapter presented an artifact geometry featuring lattice structures, freeform structures, and cavities. The designed geometry was manufactured using AlSi10Mg powder. The manufactured part underwent analysis with iCT. An FE model was employed to simulate the manufacturing process, with simplifying hypotheses introduced to enhance computational efficiency for industrial applications. These assumptions included lattice structure homogenization and the neglect of emissivity effects. In the initial simulation, convection heat exchange and the removal of 1.5 mm of material from the bottom surface of the part to simulate the manufacturer's cutting procedure were not considered. However, a subsequent simulation incorporated convection and material removal, demonstrating significant differences in the investigated points and overall deformation compared to the first simulation. The second simulation exhibited a correlation of 71%, indicating good agreement. The implementation of the simulation methodology within the process engineering workflow offers numerous advantages to manufacturers. These include reduced time to market and costs, enhanced geometrical and structural properties, accelerated learning processes, and the establishment of a robust design methodology, facilitated by a deeper understanding of technology-based physical phenomena through software tools.

Chapter 9

Summary and outlook

9.1 Contribution to knowledge

The major contributions are summarized below.

- **Contribution 1**: The derivation of a beam finite element with bending-torsion coupling formulation for static and dynamic analysis of box-beam structures with rectilinear or curvilinear stiffened panels or composite fibers.

  Chapter 2 introduces a novel beam finite element that predicts both static and dynamic behaviors of beam structures with bending-torsion coupling. The derived model establishes a relationship between the bending and torsional nodal degrees of freedom within a two-node beam element. Equilibrium equations are derived by neglecting nonlinear terms, while stiffness and mass matrices are obtained using Galerkin's method. Shape functions are determined based on Timoshenko's hypothesis, assuming constant torsional moment along the element.

- **Contribution 2**: The derivation of two models for the dynamic analysis of box-beam structures with bending-torsion couplings in the presence of geometric non-linearities.

  Chapter 3 introduces two dynamic analysis models for beam structures incorporating bending-torsion coupling and geometric nonlinearities. The first model adjusts the orientation of the beam finite element based on a known

equilibrium deformation, addressing geometric effects. The second model considers nonlinear terms in the stiffness matrix derivation by assuming small perturbations from an equilibrium configuration under static load, with Hamilton's Principle used to derive the stiffness matrix. Experimental tests were conducted to determine the extent of deflection necessary for noticeable nonlinear effects and to evaluate the accuracy of the models in nonlinear analysis with bending-torsion coupling effects.

- **Contribution 3**: The experimental validation of an equivalent single layer for dynamic analysis of beams with stiffened panels. The validation showed good accuracy and extended the use of this model also for the modal analysis of stiffened panels box-beam structures.

Chapter 4 examines the vibration response of box beams with bending-torsion coupling for aero-structural applications through experimental and numerical analyses. Validation of prior static results is provided, complemented by dynamic analysis. Comparison of experimental and numerical results includes natural frequencies, mode shapes, and modal assurance criterion (MAC) matrices, with good accuracy in all cases. The study demonstrates achieving desired dynamic coupling through oriented fibers or metallic stiffeners, applicable in wing box design to prevent aeroelastic instability. Finally, agreement with experimental tests and equivalent single-layer model results underscores the methodology's value in the early design stages of metal wing boxes, significantly reducing structural complexity and computational costs while maintaining satisfactory accuracy.

- **Contribution 4**: The experimental and numerical validation of the derived finite element for the static and dynamic problems of composite beams, stiffened and composite thin-walled box-beam, variable stiffness beam and, pre-deformed beams.

In Chapter 5, the present model underwent validation for static scenarios by simulating an aluminum beam with stiffened panels in a cantilever configuration, subject to three different load configurations at its free end. The inclusion of oriented stiffeners enabled the achievement of a notable bending-torsion coupling effect, accurately represented in both static and modal analyses. Validation extended to dynamic scenarios via modal analysis in the cantilever configuration. Results were compared with experimental and TETRA10 FE model

data, confirming the accuracy of the finite element. Further testing involved modal analysis of an NREL 5MW HAWT blade and a CAS graphite/epoxy cantilever box beam with varied layups. Natural frequencies exhibited good alignment with numerical and experimental results, affirming the compatibility of the BTCE model with these structural classes. The coupled beam finite element, incorporating oriented stiffeners or composite materials, demonstrates versatility beyond box-section beams. It holds promise for nonlinear static and dynamic analyses, as well as applications in aeroelasticity with fluid-structure interactions and aerodynamic tailoring. Experimental tests were conducted to verify the level of deflection necessary to observe appreciable nonlinear effects and assess the accuracy of nonlinear analysis with the nonlinear BTCE models. Results indicated that geometric non-linearities had minor effects on the structure's characteristic frequencies, however, nonlinear couplings induced significant differences in mode shapes, accurately predicted by the derived nonlinear BTCE models. These models hold potential for studying the aeroelastic performance of wing structures and optimizing material orientation for desired dynamic properties, even in the presence of geometric non-linearities.

- **Contribution 5**: The development of an optimization procedure for the design of box-beam structures with curvilinear stiffness in the presence of bending-torsion performance constraints as well as AM constraints.

In Chapter 6 The derived finite element has been used for optimizing stiffener paths in box-beam structures with curvilinear stiffened panels. Three distinct load cases, including one reflecting manufacturing geometric constraints in the AM process, were considered. The optimization aimed to maximize strain energy under prescribed loads, while adhering to constraints on maximum vertical deflection and minimum torsional angle, in other cases the goal was to minimize bending-torsion effects and achieve maximum strain energy, with zero torsional angle at the tip. BTCE demonstrated potential as both an optimization and static analysis tool for beam structures with curvilinear stiffeners. It also showcased the capability to tailor configurations to enhance or diminish bending-torsion effects as desired. Furthermore, optimization was performed for geometric constraints related to AM production, aiming for a self-supporting structure to minimize post-production machining.

- **Contribution 6**: A procedure for divergence analysis of composite wing structures using the derived finite element and an aerodynamic analysis performed with the Vortex Lattice Method. The results obtained have been validated with experimental results.

The objective of Chapter 7 was to demonstrate the capabilities of the derived finite element for static aeroelastic analysis. The methodology, comprising structural analysis using a BTCE model and aerodynamic analysis based on VLM, was validated against experimental and analytical data from existing literature. The predicted divergence velocities closely matched experimental results, although discrepancies were noted in tip deflection and rotation in one of the cases studied. The methodology was applied to various curvilinear laminations to assess their impact on static aeroelastic analysis outcomes and the potential use of BTCE. The versatility of BTCE was evident, as it seamlessly integrated into aerodynamic analysis and facilitated static aeroelastic analysis. Furthermore, its incorporation with curvilinear lamination introduced design variables capable of achieving specific aeroelastic performance objectives. This methodology holds promise for further development through optimization algorithms to tackle optimization challenges and can be extended to flutter analysis for comprehensive aeroelastic assessment.

- **Contribution 7**: The validation of an AM process simulation algorithm with experimental results obtained with an industrial computed tomography.

The aim of Chapter 8 was to validate the theory behind the software AM-TOP®, an artifact geometry that included key features such as lattice structures, freeform structures, and cavities was presented. The designed geometry has been manufactured with AlSi10Mg powder and has been analyzed with an iCT. An FE model has been implemented to simulate the process considering the removal of 1.5 mm of material from the bottom surface of the part to replicate the manufacturer's cutting procedure. The second simulation revealed good accordance with a correlation equal to 71%. Thanks to the contribution of the software tool to the knowledge of the technology-based physical phenomenon, the implementation of the simulation methodology in the process engineering workflow can show several advantages to the manufacturer. These can be revealed in the reduction of time to market and costs, improvement of geomet-

rical and structural properties, acceleration of the learning process, and the definition of a robust design methodology.

9.2 Outlook

The present work set the basis for a comprehensive aeroelastic tailoring design and optimization tool. The linear model has been validated for many structures and analyses, however further investigation could be done to improve the accuracy for the torsional frequencies. The non-linear model can be enriched with experimental validation of composite structures and can be extended to include higher order effects and consider also large deformations.

The optimization procedure for curvilinear stiffeners can be extended to dynamic optimization, where the curvilinear path is determined under constraints on characteristic frequencies. Moreover, the optimization can be coupled with the divergence analysis algorithm to perform aeroelastic optimization of stiffeners or fibers orientation. The effectiveness of the model for divergence analysis can be further demonstrated with wind-tunnel tests on composite and stiffened structures.

The mass matrices derived for the linear and nonlinear beam finite element, allow also for the analysis of flutter speed. The extension of the BTCE to a flutter analysis application alongside an experimental validation would complete the analysis framework.

Additive manufacturing presented great opportunities for aeroelastic tailoring. This thesis focused on the effect of stiffened orientation on aeroelastic performances, however, the stiffeners design parameters are numerous and each one can be optimized to achieve the desired effects. The capabilities of these technologies allows also for non-conventional stiffeners shape and sections giving an additional design degree of freedom which should be further explored. The simulation of the AM process can be further optimized with an increased comprehension of physical phenomena given by further experimental campaigns.

References

[1] Dominik Eisenhut, Nicolas Moebs, Evert Windels, Dominique Bergmann, Ingmar Geiß, Ricardo Reis, and Andreas Strohmayer. Aircraft requirements for sustainable regional aviation. *Aerospace*, 8(3), 2021.

[2] Airbus. Airbus global market forecast 2021 - 2040, 2021.

[3] Boeing. Commercial market outlook 2021-2040, 2021.

[4] E.M. Greitzer, P.A. Bonnefoy, D.K. Hall, R.J. Hansman, J.I. Hileman, R.H. Liebeck Liebeck, J. Lovegren, P. Mody, J.A. Pertuze, S. Sato, Z.S. Spakovszky, C.S. Tan, J.S. Hollman, J.E. Duda, N. Fitzgerald, J. Houghton, J.L. Kerrebrock, G.F. Kiwada, D. Kordonowy, J.C. Parrish, E.A. Tylko, and J. Wen. N+3 aircraft concept designs and trade studies, final report. *NASA Glenn Research Center, Cleveland, Ohio 44135*, 2010.

[5] European Commission. Flightpath 2050: Europe's vision for aviation, advisory council for aeronautics research in europe. Brussels, Belgium, 2021.

[6] Grewe Volker, Arvind Gangoli Rao, Tomas Grönstedt, Carlos Xisto, Florian Linke, Joris Melkert, Jan Middel, Barbara Ohlenforst, Simon Blakey, Simon Christie, Sigrun Matthes, and Katrin Dahlmann. Evaluating the climate impact of aviation emission scenarios towards the paris agreement including covid-19 effects. *Nature Communications*, 12, 06 2021.

[7] Yiyuan Ma and Ali Elham. Designing high aspect ratio wings: A review of concepts and approaches. *Progress in Aerospace Sciences*, 145, 02 2024.

[8] Sergio Ricci, Luca Marchetti, Francesco Toffol, Jacopo Beretta, and Nicola Paletta. Aeroelastic optimization of high aspect ratio wings for environmentally friendly aircraft. 01 2022.

[9] Gaetan Kenway and Joaquim Martins. Multi-point high-fidelity aerostructural optimization of a transport aircraft configuration. *Journal of Aircraft*, 51:144–160, 01 2014.

[10] Joaquim Martins, Graeme Kennedy, and Gaetan Kenway. High aspect ratio wing design: Optimal aerostructural tradeoffs for the next generation of materials. 01 2014.

[11] Nils Beck, Tim Landa, Arne Seitz, Loek Boermans, Yaolong Liu, and Rolf Radespiel. Drag reduction by laminar flow control. *Energies*, 11:252, 01 2018.

[12] Yiyuan Ma, Stanislav Karpuk, and Ali Elham. Conceptual design and comparative study of strut-braced wing and twin-fuselage aircraft configurations with ultra-high aspect ratio wings. *Aerospace Science and Technology*, 121, 01 2022.

[13] M.K. Bradley, C.K. Dorney, and T. Allen. Subsonic ultra green aircraft research: Phase ii – volume i – truss braced wing design exploratio. 2015.

[14] C. Hofacker. Aerospace america (2023). https://aerospaceamerica.aiaa.org/departments/the-bridge-to-net-zero/. Accessed: 2024-04-07.

[15] M.K. Bradley and C.K. Dorney. Subsonic ultra green aircraft research: Phase i final report. 2011.

[16] C.K. Dorney, A.J. Sclafani, N.A. Harrison, A.D. Grash, and M.D. Beyar. Subsonic ultra green aircraft research: Phase iii – mach 0.75 transonic truss-braced wing design, boeing research and technology. 2020.

[17] G. Warwick. Nasa picks boeing's transonic truss-based wing for sustainable x-plane | aviation week network, aviation week network (2023). https://aviationweek.com/air-transport/aircraft-propulsion/nasa-picks-boeings-transonic-truss-based-wing-sustainable-x-plane. Accessed: 2024-04-07.

[18] Pier Davide Ciampa, Prajwal Shivaprakasha, Francesco Torrigiani, Jan-Niclas Walther, Thierry Lefebvre, Nathalie Bartoli, Huub Timmermans, Pierluigi Vecchia, Luca Stingo, Darwin Rajpal, Imco van Gent, Gianfranco La Rocca, Marco Fioriti, Giovanni Cerino, Reinhold Maierl, Dominique Charbonnier, Aidan Jungo, Benedikt Aigner, Kirill Anisimov, and M. Voskuijl. Streamlining cross-organizational aircraft development: Results from the agile project. 06 2019.

[19] Sergio Ricci, Nicola Paletta, Sebastien Defoort, Emmanuel Benard, Je Cooper, and Barabinot Philippe. U-harward: a cs2 eu funded project aiming at the design of ultra high aspect ratio wings aircraft. 01 2022.

[20] Giulio Romeo and Giacomo Frulla. HELIPLAT: design of high altitude very-long endurance solar powered platform for telecommunication and earth observation. In R. A. Harris, editor, *Data Systems in Aerospace*, volume 509 of *ESA Special Publication*, page 54.1, July 2002.

[21] John Gundlach, Frank Gern, Bernard Grossman, Rakesh Kapania, Andy Ko, William Mason, Amir Nagshineh-Pour, Joseph Schetz, and Philippe-André Tétrault. Conceptual design studies of a strut-braced wing transonic transport. *Journal of Aircraft - J AIRCRAFT*, 37:976–983, 11 2000.

[22] Martin Sohst, J. Lobo do Vale, Frederico Afonso, and Afzal Suleman. Optimization and comparison of strut-braced and high aspect ratio wing aircraft configurations including flutter analysis with geometric non-linearities. *Aerospace Science and Technology*, 124:107531, 04 2022.

[23] Nicholas Meadows, Joseph Schetz, Rakesh Kapania, Manav Bhatia, and Guclu Seber. Multidisciplinary design optimization of medium-range transonic truss-braced wing transport aircraft. *Journal of Aircraft*, 49:1844–1856, 11 2012.

[24] Ohad Gur, Manav Bhatia, William Mason, Joseph Schetz, Rakesh Kapania, and Taewoo Nam. Development of framework for truss-braced wing conceptual mdo. *Structural and Multidisciplinary Optimization*, 44:277–298, 08 2011.

[25] G. Gould. A future aircraft design, supercomputed, nasa (2023). https://www.nasa.gov/image-article/future-aircraft-design-supercomputed. Accessed: 2024-04-07.

[26] Timothy Chau and David Zingg. Fuel burn evaluation of a transonic strut-braced-wing regional aircraft through multipoint aerodynamic optimisation. *Aeronautical Journal -New Series-*, 127, 06 2022.

[27] Timothy Chau and David Zingg. Aerodynamic design optimization of a transonic strut-braced-wing regional aircraft. *Journal of Aircraft*, 59:1–19, 08 2021.

[28] Frederico Afonso, José Vale, Éder Oliveira, Fernando Lau, and Afzal Suleman. A review on non-linear aeroelasticity of high aspect-ratio wings. *Progress in Aerospace Sciences*, 89:40–57, 2017.

[29] Dewey Hodges and E.H. Dowell. Nonlinear equations of motion for the elastic bending and torsion of twisted nonuniform rotor blades. 01 1975.

[30] Peter Dunn and John Dugundji. Nonlinear stall flutter and divergence analysis of cantilevered graphite/epoxy wings. *AIAA Journal*, 30:153–162, 01 1992.

[31] In Lee. Aeroelasticity research and development activities in korea. 05 2009.

[32] Todd Quackenbush, Jeffery Keller, Alexander Boschitsch, Glen Whitehouse, and Robert Mckillip. Modeling tools for real time aeroservoelastic simulation with nonlinear aerodynamics. 08 2009.

[33] David Lucia. The sensorcraft configurations: A non-linear aeroservoelastic challenge for aviation. volume 3, 04 2005.

[34] Changchuan Xie and Chao Yang. Linearization method of nonlinear aeroelastic stability for complete aircraft with high-aspect-ratio wings. *Science China Technological Sciences*, 54:403–411, 02 2011.

[35] Giacomo Frulla. Aeroelastic behaviour of a solar-powered high-altitude long endurance unmanned air vehicle (hale-uav) slender wing. *Proceedings of The Institution of Mechanical Engineers Part G-journal of Aerospace Engineering - PROC INST MECH ENG G-J A E*, 218:179–188, 06 2004.

[36] Michael Shirk, Terrence Hertz, and Terrence Weisshaar. Aeroelastic tailoring - theory, practice, and promise. *Journal of Aircraft*, 23, 02 1986.

[37] Masaki Kameyama and Hisao Fukunaga. Optimum design of composite plate wings for aeroelastic characteristics using lamination parameters. *Computers and Structures*, 85:213–224, 02 2007.

[38] Terrence Weisshaar. Aeroelastic tailoring of forward swept composite wings. *Journal of Aircraft - J AIRCRAFT*, 18:669–676, 08 1981.

[39] Z. Gürdal, B.F. Tatting, and K. Wu. Variable stiffness composite panels: Effects of stiffness variation on the in-plane and buckling response. *Composites Part A: Applied Science and Manufacturing*, 39:911–922, 05 2008.

[40] Rakesh Kapania, Jing Li, and Hitesh Kapoor. Optimal design of unitized panels with curvilinear stiffeners. 09 2005.

[41] S.U Benscoter and R.H. MacNeal. Equivalent plate theory for a straight multicell wing. *NACA TN*, (2786), Hanover,MD, USA, September 1952.

[42] Navin Jaunky, Norman Knight, and Damodar Ambur. Formulation of an improved smeared stiffener theory for buckling analysis of grid-stiffened composite panels. *Composites Part B: Engineering*, 27:519–526, 12 1996.

[43] C.V. Jutte and B.K. Stanford. Aeroelastic tailoring of transport aircraftwings: State-of-the-art and potential enabling technologies. *NASA TM*, (218252), Hanover, MD, USA, 1 April 2014.

[44] Francesco Danzi, E. Cestino, Giacomo Frulla, and James Gibert. Numerical and experimental validation of unitized box beam model. 09 2018.

[45] E. Cestino, Giacomo Frulla, and Pier Marzocca. A reduced order model for the aeroelastic analysis of flexible wings. *SAE International Journal of Aerospace*, 6:447–458, 07 2013.

[46] Davide Locatelli, Sameer Mulani, and Rakesh Kapania. Wing-box weight optimization using curvilinear spars and ribs (sparibs). *Journal of Aircraft*, 48:1671–1684, 09 2011.

[47] Michael Shirk, Terrence Hertz, and Terrence Weisshaar. Aeroelastic tailoring - theory, practice, and promise. *Journal of Aircraft*, 23, 02 1986.

[48] M.M. Munk. Propeller containing diagonally disposed fibrous material, U.S. Patent 2, 484, 308, 1111, Oct. 1949.

[49] ME Waddoups. Composite wing for transonic improvements, composite wing aeroelastic response study. *AFFDL-TR-71-24*, 1972.

[50] Jr Krone. Forward swept wing flight demonstrator. 08 1980.

[51] R Lynch and W Rogers. Aeroelastic tailoring of composite materials to improve performance. In *17th Structures, Structural Dynamics, and Materials Conference*, page 1505, 1976.

[52] Liviu Librescu and Ohseop Song. On the static aeroelastic tailoring of composite aircraft swept wings modeled as thin-walled beam structures. *Composites Engineering*, 2:497–512, 12 1992.

[53] Byron Blakey-Milner, Paul Gradl, Glen Snedden, Michael Brooks, Jean Pitot, Elena Lopez, M. Leary, Filippo Berto, and Anton Du Plessis. Metal additive manufacturing in aerospace: A review. *Materials and Design*, 209:110008, 07 2021.

[54] Dirk Herzog, Vanessa Seyda, Eric Wycisk, and Claus Emmelmann. Additive manufacturing of metals. *Acta Materialia*, 117:371–392, 2016.

[55] Atin Angrish. A critical analysis of additive manufacturing technologies for aerospace applications. pages 1–6, 03 2014.

[56] A. A. Shapiro, J. P. Borgonia, Q. N. Chen, R. P. Dillon, B. McEnerney, R. Polit-Casillas, and L. Soloway. Additive manufacturing for aerospace flight applications. *Journal of Spacecraft and Rockets*, 53(5):952–959, 2016.

[57] Jacob C. Snyder and Karen A. Thole. Effect of Additive Manufacturing Process Parameters on Turbine Cooling. *Journal of Turbomachinery*, 142(5):051007, 04 2020.

[58] Fabio Kerstens, Angelo Cervone, and Paul Gradl. End to end process evaluation for additively manufactured liquid rocket engine thrust chambers. *Acta Astronautica*, 182:454–465, 2021.

[59] Malte Gebler, Anton J.M. Schoot Uiterkamp, and Cindy Visser. A global sustainability perspective on 3d printing technologies. *Energy Policy*, 74:158–167, 2014.

[60] B. Dutta and Francis H. (Sam) Froes. 24 - the additive manufacturing (am) of titanium alloys. In Ma Qian and Francis H. (Sam) Froes, editors, *Titanium Powder Metallurgy*, pages 447–468. Butterworth-Heinemann, Boston, 2015.

[61] A. Barz, T. Buer, and H.-D. Haasis. A study on the effects of additive manufacturing on the structure of supply networks. *IFAC-PapersOnLine*, 49(2):72–77, 2016. 7th IFAC Conference on Management and Control of Production and Logistics MCPL 2016.

[62] Lawrence Murr. *Handbook of Materials Structures, Properties, Processing and Performance*, pages 969–984. 01 2015.

[63] Harry Bikas, Panagiotis Stavropoulos, and George Chryssolouris. Additive manufacturing methods and modeling approaches: A critical review. *The International Journal of Advanced Manufacturing Technology*, 83, 07 2015.

[64] Steven Hollowell and John Dugundji. Aeroelastic flutter and divergence of stiffness coupled, graphite/epoxy cantilevered plates. *Journal of Aircraft - J AIRCRAFT*, 21:69–76, 01 1984.

[65] Chang-Ho Hong and Inderjit Chopra. Aeroelastic stability analysis of a composite rotor blade. *Journal of The American Helicopter Society - J AMER HELICOPTER SOC*, 30, 04 1985.

[66] Erkan Dokumaci. An exact solution for coupled bending and torsion vibrations of uniform beams having single cross-sectional symmetry. *Journal of Sound and Vibration*, 119:443–449, 12 1987.

[67] J.R. Banerjee. Coupled bending–torsional dynamic stiffness matrix for beam elements. *International Journal for Numerical Methods in Engineering*, 28:1283 – 1298, 06 1989.

[68] J.R. Banerjee and F. Williams. Free vibration of composite beams - an exact method using symbolic computation. *Journal of Aircraft*, 32:636–642, 04 1995.

[69] Edward Smith and Inderjit Chopra. Formulation and evaluation of an analytical model for composite box-beams. *Journal of the American Helicopter Society*, 36, 02 1990.

[70] Ramesh Chandra and Inderjit Chopra. Experimental and theoretical analysis of composite i-beams with elastic couplings. *Aiaa Journal - AIAA J*, 29:2197–2206, 04 1991.

[71] Ramesh Chandra and Inderjit Chopra. Experimental-theoretical investigation of the vibration characteristics of rotating composite box beams. *Journal of Aircraft - J AIRCRAFT*, 29:657–664, 07 1992.

[72] Seyed Hashemi and Marc Richard. A dynamic finite element (dfe) method for free vibrations of bending-torsion coupled beams. *Aerospace Science and Technology - AEROSP SCI TECHNOL*, 4:41–55, 01 2000.

[73] Sung Jung, Inderjit Chopra, and V. Nagaraj. Refined structural model for thin and thick-walled composite rotor blades. *Aiaa Journal - AIAA J*, 40:105–116, 01 2002.

[74] Wenbin Yu, Dewey Hodges, Vitali Volovoi, and Carlos Cesnik. On timoshenko-like modeling of initially curved and twisted composite beams. *International Journal of Solids and Structures*, 39:5101–5121, 09 2002.

[75] Foudil Mohri, Abderrahman Ed-dinari, Noureddine Damil, and Michel Potier-Ferry. A beam finite element for non-linear analyses of thin-walled elements. *Thin-Walled Structures*, 46:981–990, 07 2008.

[76] Pavel Babuska, Richard Wiebe, and Michael R. Motley. A beam finite element for analysis of composite beams with the inclusion of bend-twist coupling. *Composite Structures*, 189:707–717, 2018.

[77] Ali Nayfeh and Perngjin Pai. *Linear and Nonlinear Structural Mechanics*. 01 2004.

[78] Dewey Hodges and G. Pierce. *Introduction to Structural Dynamics and Aeroelasticity*. 01 2011.

[79] Mayuresh Patil and Dewey Hodges. On the importance of aerodynamic and structural geometrical nonlinearities in aeroelastic behavior of high-aspect-ratio wings. *Journal of Fluids and Structures*, 19:905–915, 08 2004.

[80] Mayuresh Patil, Dewey Hodges, and Carlos Cesnik. Characterizing the effects of geometrical nonlinearities on aeroelastic behavior of high-aspect ratio wings. pages 501–510, 01 1999.

[81] Dewey Hodges. Geometrically exact, intrinsic theory for dynamics of curved and twisted anisotropic beams. *AIAA Journal*, 41:1131–1137, 06 2003.

[82] Dewey H. Hodges. A mixed variational formulation based on exact intrinsic equations for dynamics of moving beams. *International Journal of Solids and Structures*, 26(11):1253–1273, 1990.

[83] Ryan Kitson, Christopher Lupp, and Carlos Cesnik. Modeling and simulation of flexible jet transport aircraft with high-aspect-ratio wings. 01 2016.

[84] Jessica Jones and Carlos Cesnik. Nonlinear aeroelastic analysis of the x-56 multi-utility aeroelastic demonstrator. 01 2016.

[85] Mark Drela. Integrated simulation model for preliminary aerodynamic, structural, and control-law design of aircraft. volume 3, 04 1999.

[86] Mayuresh Patil and Dewey Hodges. Flight dynamics of highly flexible flying wings. *Journal of Aircraft - J AIRCRAFT*, 43, 11 2006.

[87] Markus Ritter, Jessica Jones, and Carlos Cesnik. Enhanced modal approach for free-flight nonlinear aeroelastic simulation of very flexible aircraft. 01 2016.

[88] Renato Medeiros, Carlos Cesnik, and Etienne Coetzee. Computational aeroelasticity using modal-based structural nonlinear analysis. *AIAA Journal*, 58:1–10, 10 2019.

[89] C. Bruni, E. Cestino, G. Frulla, and P. Marzocca. Nonlinear slender beam-wise schemes for structural behaviour of flexible uas wings". *SAE Technical Paper 2015-01-2462*, 2015.

[90] D Paavani, Aswathy M., Arun C O, and Praveen I R. Analysis of geometrically nonlinear euler-bernoulli beam using efgm. *IOP Conference Series: Materials Science and Engineering*, 936:012050, 10 2020.

[91] T. Yang and Sunil Saigal. A simple element for static and dynamic response of beams with material and geometric nonlinearities. *International Journal for Numerical Methods in Engineering*, 20:851 – 867, 05 1984.

[92] K. Surana and Robert Sorem. Geometrically non-linear formulation for three dimensional curved beam elements with large rotations. *International Journal for Numerical Methods in Engineering*, 28:43 – 73, 01 1989.

[93] Jin Duan and Yun Li. A beam element for geometric nonlinear dynamical analysis. *Advanced Materials Research*, 919-921:1273–1281, 04 2014.

[94] E. Cestino, Giacomo Frulla, M Spina, D Catelani, and M Linari. Numerical simulation and experimental validation of slender wings flutter behaviour. *Proceedings of the Institution of Mechanical Engineers. Part G: Journal of Aerospace Engineering*, 233(16):5913–5928, 2019.

[95] Cesare Patuelli, Alessandro Polla, Enrico Cestino, and Giacomo Frulla. Experimental and numerical dynamic behavior of bending-torsion coupled box-beam. *J. Vib. Eng. Technol.*, 2022.

[96] Francesco Danzi, E. Cestino, Giacomo Frulla, and James Gibert. Equivalent plate model of curvilinear stiffened panels. In *PROCEEDINGS M2D2017, Albufeira (Algarve)/Portugal*, pages 553–568, 07 11-15 June 2017. ISBN: 978-989-98832-7-7.

[97] E. Cestino and Giacomo Frulla. Analysis of slender thin-walled anisotropic box-beams including local stiffness and coupling effects. *Aircraft Engineering and Aerospace Technology: An International Journal*, 86, 07 2014.

[98] Michael Nemeth. Nasa/tp-20- a treatise on equivalent-plate stiffnesses for stiffened laminated-composite plates and plate-like lattices. Technical report, 02 2011.

[99] E. Cestino, Giacomo Frulla, Paolo Piana, and Renzo Duella. Numerical/experimental validation of thin-walled composite box beam optimal design. *Aerospace*, 7:111, 07 2020.

[100] D. Ewins. *Modal Testing, Theory, Practice and Application*. Research Studies Press LTD., Baldock; Hertfordshire; England, 2 edition, 2000.

[101] Erian Armanios and Ashraf Badir. Free vibration analysis of anisotropic thin-walled closed-section beams. *Aiaa Journal - AIAA J*, 33:1905–1910, 10 1995.

[102] Jonkman JM, S. Butterfield, W. Musial, and G. Scott. Definition of a 5mw reference wind turbine for offshore system development. *National Renewable Energy Laboratory (NREL)*, 01 2009.

[103] AMNA ALGOLFAT, Weizhuo Wang, and A. Albarbar. Dynamic responses analysis of a 5mw nrel wind turbine blade under flap-wise and edge-wise vibrations. *Journal of Dynamics, Monitoring and Diagnostics*, 09 2022.

[104] Min-Soo Jeong, Myung-Chan Cha, Sang-Woo Kim, In Lee, and Taeseong Kim. Effects of torsional degree of freedom, geometric nonlinearity, and gravity on aeroelastic behavior of large-scale horizontal-axis wind turbine blades under varying wind speed conditions. *Journal of Renewable and Sustainable Energy*, 6:1–19, 03 2014.

[105] Zhan-Wei Li, Binrong Wen, Xing-Jian Dong, Z. Peng, Yegao Qu, and W. Zhang. Aerodynamic and aeroelastic characteristics of flexible wind turbine blades under periodic unsteady inflows. *Journal of Wind Engineering and Industrial Aerodynamics*, 2020:105057, 12 2019.

[106] E. Cestino, Giacomo Frulla, E. Perotto, and Pier Marzocca. Experimental slender wing model design by the application of aeroelastic scaling laws. *Journal of Aerospace Engineering*, 27:112–120, 01 2014.

[107] Raphael Haftka. Parametric constraints with application to optimization for flutter using a continuous flutter constraint. *AIAA Journal*, 13, 05 1975.

[108] Joaquim Martins, Juan Alonso, and James Reuther. High-fidelity aero-structural design optimization of a supersonic business jet. 12 2002.

[109] W. Stroud, T. Krishnamurthy, Brian Mason, Steven Smith, and Ahmad Naser. Aiaa-2002-1464 probabilistic design of a plate-like wing to meet flutter and strength requirements. 07 2002.

[110] Kurt Maute and Matthew Allen. Conceptual design of aeroelastic structures by topology optimization. *Structural and Multidisciplinary Optimization*, 27:27–42, 01 2004.

[111] K. Chauncey Wu, Zafer Gurdal, and James H. Starnes. Structural response of compression-loaded, tow-placed, variable stiffness panels. 04 2002.

[112] Dan Wang and Mostafa Abdalla. Global and local buckling analysis of grid-stiffened composite panels. *Composite Structures*, 119:767–776, 01 2015.

[113] Dan Wang and Mostafa Abdalla. Buckling optimization of steering stiffeners for grid-stiffened composite structures. 07 2015.

[114] V. Sherrer, T. Hertz, and M. Shirk. Wind tunnel demonstration of aeroelastic tailoring applied to forward swept wings. *Journal of Aircraft - J AIRCRAFT*, 18:976–983, 11 1981.

[115] Shijun Guo. Aeroelastic optimization of an aerobatic aircraft wing structure. *Aerospace Science and Technology*, 11:396–404, 06 2007.

[116] Chao Li, Michael Gouge, Erik Denlinger, Jeff Irwin, and Pan Michaleris. Estimation of part-to-powder heat losses as surface convection in laser powder bed fusion. *Additive Manufacturing*, 26, 02 2019.

[117] Renato Medeiros, Carlos Cesnik, and Etienne Coetzee. Computational aeroelasticity using modal-based structural nonlinear analysis. *AIAA Journal*, 58:1–10, 10 2020.

[118] Bret Stanford, Carol Wieseman, and Christine Jutte. Aeroelastic tailoring of transport wings including transonic flutter constraints. 01 2015.

[119] Chris Pettit and Ramana Grandhi. Optimization of a wing structure for gust response and aileron effectiveness. *Journal of Aircraft - J AIRCRAFT*, 40:1185–1191, 11 2003.

[120] Peter Dunning, Bret Stanford, H Alicia Kim, and Christine Jutte. Aeroelastic tailoring of a plate wing with functionally graded materials. *Journal of Fluids and Structures*, 51, 11 2014.

[121] Liviu Librescu and Karam Maalawi. Material grading for improved aeroelastic stability in composite wings. *Journal of Mechanics of Materials and Structures*, 2:1381–1394, 09 2007.

[122] M.W. Tosh and Donald Kelly. On the design, manufacture and testing of trajectorial fibre steering for carbon fibre composite laminates. *Composites Part A: Applied Science and Manufacturing*, 31:1047–1060, 10 2000.

[123] Lars Bernhammer, Roeland De Breuker, and Moti Karpel. Geometrically nonlinear structural modal analysis using fictitious masses. *IFASD 2013 - International Forum on Aeroelasticity and Structural Dynamics*, 55, 01 2013.

[124] Etay Kantor, Daniella Raveh, and Rauno Cavallaro. Nonlinear structural, nonlinear aerodynamic model for static aeroelastic problems. *AIAA Journal*, 57:1–13, 02 2019.

[125] Ariel Drachinsky and Daniella Raveh. Modal rotations: A modal-based method for large structural deformations of slender bodies. *AIAA Journal*, 58:1–15, 05 2020.

[126] Terrence Weisshaar and Brian Foist. Vibration tailoring of advanced composite lifting surfaces. *Journal of Aircraft*, 22, 03 1985.

[127] Matthew Kramer, Zhanke Liu, and Yin Lu Young. Free vibration of cantilevered composite plates in air and in water. *Composite Structures*, 95:254–263, 01 2013.

[128] R.L. Bisplinghoff, H. Ashley, and R.L. Halfman. *Aeroelasticity*. Dover Books on Aeronautical Engineering. Dover Publications, 2013.

[129] Steven J. Hollowell. *Aeroelastic flutter and divergence of graphite/epoxy cantilevered plates with bending-torsion stiffness coupling*. Phd thesis, Massachusetts Institute of Technology. Department of Aeronautics and Astronautics, January 1981.

[130] Nagesha BK, Dhinakaran Veeman, Varsha Mahesh, K.P. Kumar, Damodar Chalawadi, and T. Sathish. Review on characterization and impacts of the lattice structure in additive manufacturing. *Materials Today: Proceedings*, 21, 08 2019.

[131] Dieter Radaj. Heat effects of welding. 01 1992.

[132] G. Servetti and Xiang Zhang. Predicting fatigue crack growth rate in a welded butt joint: The role of effective r ratio in accounting for residual stress effect. *Engineering Fracture Mechanics - ENG FRACTURE MECH*, 76:1589–1602, 07 2009.

[133] William Frazier. Metal additive manufacturing: A review. *Journal of Materials Engineering and Performance*, 23, 06 2014.

[134] Z. Duriagina, I. Lemishka, A. Trostianchyn, Volodymyr Kulyk, s Shvachko, Tetiana Tepla, E. Pleshakov, and Taras Kovbasyuk. The effect of morphology and particle-size distribution of vt20 titanium alloy powders on the mechanical properties of deposited coatings. *Powder Metallurgy and Metal Ceramics*, 57, 04 2019.

[135] Ali Gökhan Demir and Barbara Previtali. Investigation of remelting and preheating in slm of 18ni300 maraging steel as corrective and preventive measures for porosity reduction. *The International Journal of Advanced Manufacturing Technology*, 93:2697–2709, 11 2017.

[136] Paras Shah, Radu Racasan, and Paul Bills. Comparison of different additive manufacturing methods using computed tomography. *Case Studies in Nondestructive Testing and Evaluation*, 6, 05 2016.

[137] Hao-Jie Jiang and Hong-Liang Dai. Effect of laser processing on three dimensional thermodynamic analysis for hsla rectangular steel plates. *International Journal of Heat and Mass Transfer*, 82:98–108, 03 2015.

[138] Aniruddha Gaikwad, Richard Williams, Harry Winton, Benjamin Bevans, Ziyad Smoqi, Prahalada Rao, and Paul Hooper. Multi phenomena melt pool sensor data fusion for enhanced process monitoring of laser powder bed fusion additive manufacturing. *Materials & Design*, 221:110919, 07 2022.

[139] J. P. Oliveira, A.D. LaLonde, and Ji Ma. Processing parameters in laser powder bed fusion metal additive manufacturing. *Materials & Design*, 193:108762, 04 2020.

[140] Gunther Mohr, Simon Altenburg, and Kai Hilgenberg. Effects of inter layer time and build height on resulting properties of 316l stainless steel processed by laser powder bed fusion. *Additive Manufacturing*, 32:101080, 03 2020.

[141] Xiaoqing Wang, Tahmina Keya, and Kevin Chou. Build height effect on the inconel 718 parts fabricated by selective laser melting. *Procedia Manufacturing*, 5:1006–1017, 11 2016.

[142] Mangesh Pantawane, Yee-Hsien Ho, Sameehan Joshi, and Narendra Dahotre. Computational assessment of thermokinetics and associated microstructural evolution in laser powder bed fusion manufacturing of ti6al4v alloy. *Scientific Reports*, 10, 05 2020.

[143] I.A. Roberts, Chang Wang, R. Esterlein, M. Stanford, and Diane Mynors. A three-dimensional finite element analysis of the temperature field during laser melting of metal powders in additive layer manufacturing. *International Journal of Machine Tools and Manufacture*, 49:916–923, 10 2009.

[144] Kenneth Cooper, Phillip Steele, Bo Cheng, and Kevin Chou. Contact-free support structures for part overhangs in powder-bed metal additive manufacturing. *Inventions*, 3:2, 12 2017.

[145] Claire Bruna-Rosso and Ali Gökhan Demir. Selective laser melting finite element modeling: Validation with high-speed imaging and lack of fusion defects prediction. *Materials & Design*, 156, 06 2018.

[146] Y. Huang, Lijun Yang, Xiaoze Du, and Y.P. Yang. Finite element analysis of thermal behavior of metal powder during selective laser melting. *International Journal of Thermal Sciences*, 104:146–157, 06 2016.

[147] Zhibo Luo and Yaoyao Zhao. Efficient thermal finite element modeling of selective laser melting of inconel 718. *Computational Mechanics*, 65:1–25, 03 2020.

[148] Ruwei Geng, Jun Du, Zhengying Wei, Siyuan Xu, and Ninshu Ma. Modelling and experimental observation of the deposition geometry and microstructure evolution of aluminum alloy fabricated by wire-arc additive manufacturing. *Journal of Manufacturing Processes*, 64:369–378, 04 2021.

[149] Alberto Cattenone, Simone Morganti, Gianluca Alaimo, and Ferdinando Auricchio. Finite element analysis of additive manufacturing based on fused deposition modeling (fdm): distortion prediction and comparison with experimental data. *Journal of Manufacturing Science and Engineering*, 141, 10 2018.

[150] Xu Song, Stefanie Feih, Wei Zhai, Chen-Nan Sun, Feng Li, Raj Maiti, J. Wei, Yangzhan Yang, V. Oancea, León Romano Brandt, and Alexander Korsunsky. Advances in additive manufacturing process simulation: Residual stresses and distortion predictions in complex metallic components. *Materials & Design*, 193:108779, 05 2020.

[151] Laurent van Belle, Guillaume Vansteenkiste, and Jean Boyer. Comparisons of numerical modelling of the selective laser melting. *Key Engineering Materials*, 504-506:1067–1072, 02 2012.

[152] Steven Price, Bo Cheng, James Lydon, Kenneth Cooper, and Kevin Chou. On process temperature in powder-bed electron beam additive manufacturing: Process parameter effects. *Journal of Manufacturing Science and Engineering*, 136:061019, 12 2014.

[153] Massimo Carraturo, John Jomo, Stefan Kollmannsberger, Alessandro Reali, Ferdinando Auricchio, and Ernst Rank. Modeling and experimental validation of an immersed thermo-mechanical part-scale analysis for laser powder bed fusion processes. *Additive Manufacturing*, 36:101498, 08 2020.

[154] N.E. Hodge, Robert Ferencz, and R.M. Vignes. Experimental comparison of residual stresses for a thermomechanical model for the simulation of selective laser melting. *Additive Manufacturing*, 12, 05 2016.

[155] Amanda Wu, Don Brown, Mukul Kumar, Gilbert Gallegos, and Wayne King. An experimental investigation into additive manufacturing-induced residual stresses in 316l stainless steel. *Metallurgical and Materials Transactions A*, 45, 12 2014.

[156] Michael Zaeh and Gregor Branner. Investigations on residual stresses and deformations in selective laser melting. *Production Engineering*, 4:35–45, 02 2009.

[157] Loucas Papadakis, Andreas Loizou, Jeroen Risse, and Johannes Schrage. Numerical computation of component shape distortion manufactured by selective laser melting. *Procedia CIRP*, 18:90–95, 12 2014.

[158] P. Michaleris, L. Zhang, S. Bhide, and P. Marugabandhu. Evaluation of 2d, 3d and applied plastic strain methods for predicting buckling welding distortion and residual stress. *Science and Technology of Welding & Joining*, 11:707–716, 11 2006.

[159] Matteo Bugatti and Quirico Semeraro. Limitations of the inherent strain method in simulating powder bed fusion processes. *Additive Manufacturing*, 23, 06 2018.

[160] Chao Li, Chenhao Fu, Y.B. Guo, and Fengzhou Fang. A multiscale modeling approach for fast prediction of part distortion in selective laser melting. *Journal of Materials Processing Technology*, 229:703–712, 10 2015.

[161] Chao Li, Jingfu Liu, X. Fang, and Y.B. Guo. Efficient predictive model of part distortion and residual stress in selective laser melting. *Additive Manufacturing*, 17:157–168, 09 2017.

[162] Michael Gouge, Erik Denlinger, Jeff Irwin, Chao Li, and Pan Michaleris. Experimental validation of thermo-mechanical part-scale modeling for laser powder bed fusion processes. *Additive Manufacturing*, 29, 06 2019.

[163] Nils Keller, Fabian Neugebauer, H Xu, and Vasily Ploshikhin. Thermo-mechanical simulation of additive layer manufacturing of titanium aerospace structures. 09 2013.

[164] Fabian Neugebauer, Nils Keller, Hongxiao Xu, Christian Kober, Vasily Ploshikhin, et al. Simulation of selective laser melting using process specific layer based meshing. In *Proc. Fraunhofer Direct Digital Manufacturing Conf.(DDMC 2014), Axel Demmer, Aachen, Germany*, pages 297–302, 2014.

[165] Liwei Chen, Hui Li, Sheng Liu, Shengnan Shen, Tao Zhang, Yicang Huang, Zhang Guoqing, Yunfan Zhang, Bo He, and Chongkun Yang. Simulation of surface deformation control during selective laser melting of alsi10mg powder using an external magnetic field. *AIP Advances*, 9:045012, 04 2019.

[166] Xiaochuan Zhang, Jin-wu Kang, Yiming Rong, Pengyue Wu, and Tao Feng. Effect of scanning routes on the stress and deformation of overhang structures fabricated by slm. *Materials*, 12:47, 12 2018.

[167] F. Esposito, Andrea Gatto, Elena Bassoli, and Lucia Phd. A study on the use of xct and fea to predict the elastic behavior of additively manufactured parts of cylindrical geometry. *Journal of Nondestructive Evaluation*, 37, 09 2018.